UC Berkeley
UC Berkeley Electronic Theses and Dissertations

Title

Transport and Spectral Functions in Low-dimensional Quantum Spin Systems

Permalink

https://escholarship.org/uc/item/5587q7bn

Author

Sherman, Nicholas Edward

Publication Date

2023

Peer reviewed|Thesis/dissertation

Transport and Spectral Functions in Low-dimensional Quantum Spin Systems

by

Nicholas E. Sherman

A dissertation submitted in partial satisfaction of the

requirements for the degree of

Doctor of Philosophy

in

Physics

in the

Graduate Division

of the

University of California, Berkeley

Committee in charge:

Professor Joel E. Moore, Chair
Professor Joseph Orenstein
Professor Daryl Chrzan

Summer 2023

Transport and Spectral Functions in Low-dimensional Quantum Spin Systems

Abstract

Transport and Spectral Functions in Low-dimensional Quantum Spin Systems

by

Nicholas E. Sherman

Doctor of Philosophy in Physics

University of California, Berkeley

Professor Joel E. Moore, Chair

Non-equilibrium properties of quantum materials are examined in low-dimensional systems using matrix product state (MPS) simulations. The spectral function known as the dynamical structure factor, which is directly observed in neutron scattering experiments, is studied for two classes of novel quantum systems. First, recent work has demonstrated that the Heisenberg spin chain exhibits anomalous super-diffusive transport at infinite temperature called Kardar-Parisi-Zhang (KPZ) hydrodynamics. Here, it is demonstrated that signatures of KPZ physics are present in the low-energy spectrum at experimentally relevant temperatures, and this has been detected in $KCuF_3$ with neutron scattering. The crossover from the ground state physics described by the Tomonaga-Luttinger liquid theory to KPZ hydrodynamics at high temperatures is explored.

Second, the spectral function of the $J_1 - J_2$ Heisenberg model is studied using MPS simulations. Signatures for the three primary classes of quantum spin liquid (QSL) states in the spectral function are discussed. Our findings point to a U(1) Dirac spin liquid ground state in this model. The calculated spectrum is then compared with the triangluar lattice compounds $KYbSe_2$ and $YbZn_2GaO_5$. We find that $KYbSe_2$ is well modelled by the $J_1 - J_2$ Heisenberg model in close proximity to the QSL phase. Additionally, we find that the QSL phase of the $J_1 - J_2$ Heisenberg model captures the essential features of the $YbZn_2GaO_5$, suggesting a realization of a Dirac spin liquid in this material.

Lastly, the effect of using an MPS to study quantum dynamics is explored. Using an MPS places a restriction on the entanglement in the system, and we study how this modifies time dynamics in a Kibble-Zurek process. We derive that the effect of finite entanglement on a Kibble-Zurek process is captured by a dimensionless scaling function of the ratio of two length scales, one determined dynamically and one by the entanglement restriction. This result is verified numerically in the transverse field Ising model and the 3-state Potts model.

Contents

List of Figures

List of Tables

Acknowledgments

I actually did it. After dropping out of high school, I had this wild dream to become a physicist, and I actually did it. I have been blessed with great people in my life, and I would not be here without their support. First, I want to thank my parents for bringing me into this world, and believing in me. For sacrificing so much for me and my brother, and loving us when we made it difficult. I also want to thank my brother for being my best friend throughout my life, and not letting our disagreements divide us.

I had a humble beginning at Solano Community College, and had some of my greatest teachers there. I want to thank Randy Robertson, Zak Hannan, Daryl Allen, and Melanie Lutz for all their guidance and support. I am grateful for Parsa Mahmoudieh, Andrew Cloud, and Rustin Domingos for helping to cultivate my passion for learning early on, and remaining good friends over the years.

I want to thank Rajiv Singh for introducing me to computational condensed matter physics, and continuing to work with me during my time at UC Davis. Rajiv mentored me from a complete novice to a published scientist, and I will be eternally grateful. I also want to thank Bruno Nachtergaele for reinvigorating my interest in physics during my senior thesis, and having confidence in my ability as a researcher when I was questioning it.

I thank my collaborators, Alexander Avdoshkin, Allen Scheie, Alan Tennant, and Sara Harivafard for stimulating conversations, and interesting collaborative projects. I want to thank Maxime Dupont for all his help and guidance during my Ph.D.

I want to thank my friends along the way that were there for me when I wanted to throw in the towel. Specifically Kunal Marwaha, Michael Bachman, and Nicolina Gallo. I have a Ph.D because of you, and more importantly, I am a better person because of you. A special thank you to Nicolina for showing me agape, and guiding me to God. I would also like to thank my therapist, Thomas Michahelles, for his unbelievable patience, and quite frankly, for changing my life.

I especially want to thank my advisor Joel Moore. It has been a real pleasure having Joel as a mentor. His ability to identify interesting research projects is admirable, and being a part of cutting edge research was an honor. Most of all, I appreciate how kind and supportive Joel has been through this process. I began graduate school feeling like an imposter, and left feeling like a scientist, and Joel is a big part in that transformation. Thank you.

Lastly, I want to thank God. Thank you for never giving up on me, even when I gave up on you. Thank you for showing me the light when I was lost in the dark. Thank you for guiding me to this point, and I am looking forward to what the future holds.

Chapter 1

Introduction

The development of Quantum Mechanics was a real quantum leap in our conception of the physical world. Beyond the serious philosophical difficulties of the theory, such as the indeterministic nature of physics, the theory demonstrates that there is a vibrant microscopic world that is governed by seemingly completely separate laws of physics. Particles behave differently if you look at them or if you do not, they can act as though they are in multiple places at once, and particles can be correlated over even immense distances between them through quantum entanglement. This raises the question of why is the macroscopic world around us so "normal" if the quantum world is so "weird".

One key theme in condensed matter physics is the idea of *emergence*, and understanding how the world around us emerges from a microscopic picture in terms of atoms. Prior to quantum mechanics, there were successful *classical* theories, such as thermodynamics and hydrodynamics, describing systems with many particles. Forming a bridge between these macroscopic theories, and the microscopic theory of quantum mechanics, has been a major effort in modern physics. This bridge has been difficult to form due to the complexity of the microscopic description of the physical world. A typical chunk of material that can fit in your hand has on the order of $\sim 10^{23}$ atoms, which is essentially impossible to describe exactly.

To understand how complex the macroscopic world is, let us look at spin systems, which will be the focus of this work, and is also among the simplest quantum systems. If we have a spin$-1/2$ particle, then the spin degree of freedom has a local Hilbert space of dimension 2. If we have N such particles in our system, then the Hilbert space dimension is exponentially large and given by $d = 2^N$. If we want to represent a generic state in a system with 30 spins on a computer, this would require roughly 8 Gb of storage. Each additional spin added to the system will double this requirement, exceeding the storage possible on even the worlds largest computers with only 40 or so spins. This is only to store the state of the system, but we often wish to calculate quantities such as the energy, which requires a Hamiltonian with d^2 elements. If the full spectrum of the Hamiltonian is needed, such as when looking at dynamical systems, the number of operations needed scales as d^3. Given that a real material has $N \sim 10^{23}$ particles, an exact description is virtually hopeless.

What is surprising is that the macroscopic world often has a much simpler description. For example if we are looking at a gas of particles at equilibrium, then we only need to know a small

number of properties about the system, such as the pressure, temperature, and volume, to fully specify the thermodynamic properties of the system. Or in hydrodynamics, we can treat the fluid as a continuum, and keeping track of a small number of local densities is sufficient. One goal of this thesis, and condensed matter theory broadly, is to understand how these simple descriptions emerge from the complicated quantum mechanical description. A second goal, and perhaps a more interesting goal, is to identify what new materials can we predict or understand because of such a quantum mechanical understanding. These materials are often called *quantum materials*, as they require quantum mechanics to understand their behaviors. An example of a quantum material is a superconductor, which the Bardeen–Cooper–Schrieffer (BCS) theory explains by the condensation of Cooper pairs [19], a mechanism with no classical analog.

To bridge the microscopic and macroscopic worlds, we need a way to propose a microscopic model, and produce a macroscopic observable. One way to do this is to make approximations, that hopefully preserve the essential physical features of the material, that simplify the theory enough to perform calculations. The concept of universality is useful to this end, where certain quantities have features that are identical for large classes of systems. For example, the phase diagram for the transition between a paramagnet and a ferromagnet, tuned by the temperature T, is identical for every ferromagnetic material. Specifically, near the transition temperature T_c, the magnetization M scales as

$$|M| \sim |T - T_c|^{\alpha}, \tag{1.1}$$

and α is the same for every material with this phase transition. Therefore if we are interested in a universal quantity, such as the critical exponent α, then any model with this phase transition is sufficient, no matter how simple or complicated it is. Not every quantity of interest is universal though, or if it is, we do not always know a simple model that enables us to extract such information analytically.

In recent years, the use of numerical simulations has become a power-house in connecting theory and experiment, and is the primary technique used in this thesis. To overcome the exponential wall of complexity, clever techniques have been developed to either recast the problem into a different framework that requires less parameters, or to perform minimal approximations that do not lose essential features of the microscopic model. For example, certain classes of states permit efficient representations even though representing a generic state requires an exponentially large amount of memory. Ground states, for example, are often states that have low-entanglement, and a matrix product state (MPS) is an ansatz that can efficiently represent low-entangled states. Matrix product states are the primary tool used in this thesis, and are discussed at length in Chapter 2.

The focus of this thesis is on studying quantum materials, and specifically identifying experimentally relevant signatures of these exotic states. I focus on MPS simulations, mostly to calculate spin spectral functions, which are directly probable with neutron scattering experiments. There are two classes of quantum systems I look at in this work. First, a one-dimensional quantum magnet that exhibits an anomalous spin transport that is super-diffusive, known as Kardar-Parisi-Zhang (KPZ) hydrodynamics. Secondly, I look at quantum spin liquids (QSL), which have a lack of long-range order even down to $T = 0$, and posses exotic quasi-particle excitations such as magnetic monopoles,

or anyons[1]. Lastly, I examine the effect that MPS simulations, and specifically the entanglement restrictions imposed by the ansatz, has on the dynamics of systems near criticality.

In the remainder of this chapter, I will provide a very brief introduction to hydrodynamics and the KPZ universality class, as well as quantum spin liquids. Then, I will briefly discuss neutron scattering experiments, and how to compare them with theoretical calculations of spectral functions. I will end this chapter with an outline for the remainder of this thesis.

1.1 Hydrodynamics in Spin Systems

1.1.1 Classical Hydrodynamics

From a classical perspective, we can view hydrodynamics as a course-grained description of Newton's laws for the dynamics of many interacting point-like particles. Generically, if we write Newton's Laws down for N particles, then the equation for the nth particle would take the form

$$m_n \ddot{x}_n = \sum_{i \neq n} F_{ni}(x_n, x_i) + F_{\text{ext}} \tag{1.2}$$

Where the left hand side is the mass and acceleration of the nth particle, and the right is the interaction between all other particles, and possibly also some external forces such as gravity, or electromagnetic fields. On our scale, a hydrodynamical system would have $N \sim 10^{23}$ particles, making this approach hopeless.

What Hydrodynamics effectively provides is a simplification of Newton's laws in the appropriate limits. One key insight is that systems tend towards a state of equilibrium, where on average, observables become constant in time. So, if we knock a system out of equilibrium at $t = 0$, it will eventually return to equilibrium, although possibly a different state than where it started. Initially, the system will experience transient behavior, and then it sets into a hydrodynamical regime after a time τ, as it flows to equilibrium at $t = \infty$. A cartoon of this behavior is shown in Fig. 1.1.

This time scale τ that separates transient dynamics and hydrodynamics is characterized by the relaxation time of observables that are not conserved. Generic quantities will relax back to equilibrium quickly, where conserved quantities are constrained, and have a longer relaxation time. Hydrodynamics is about discussing the flow of such conserved quantities. In classical hydrodynamics, there are typically three conserved quantities, the energy E, the momentum P, and the particle number N.

In the continuum limit, for any extensive quantity Q, we can define a local density ρ, such that

$$Q(t) = \int dx \rho(x, t) \tag{1.3}$$

If Q is conserved, then even though ρ is time dependent, Q is not. The continuity equation states that for a conserved quantity,

$$\frac{\partial}{\partial t} \rho_i(x, t) = -\nabla \cdot J_i(x, t) \tag{1.4}$$

---

[1] Anyons are particles with exchange statistics that are neither fermionic nor bosonic.
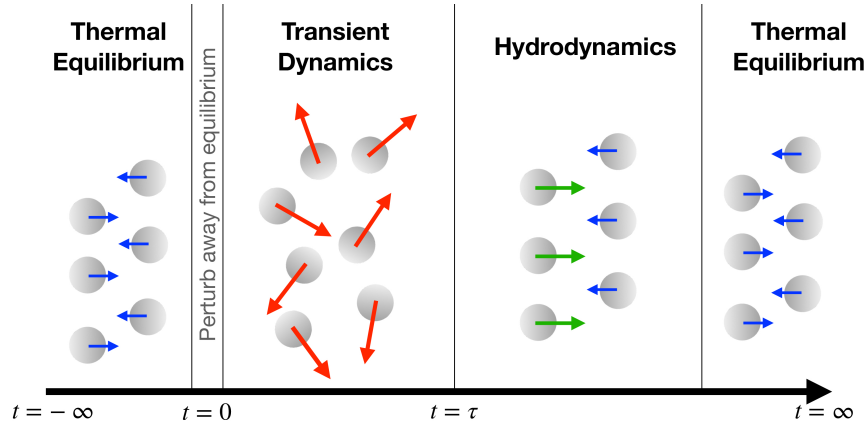
Figure 1.1: A depiction of how a system that is knocked out of equilibrium relaxes back to equilibrium.

Where J is a current density, and the index i labels one of a collection of conserved quantities $\{\rho_i\}$. The continuity equation alone is not sufficient to solve for the densities, and additional information relating the densities back to the currents is needed.

A common way to close Eq. (1.4) is to assume that the conserved quantities are independent, and that they satisfy Fick's First Law [107]

$$J = -D\nabla\rho. \tag{1.5}$$

For simplicity, let us look at the particle number N with density $n(x, t)$ in only one dimension. This gives rise to the diffusion equation

$$\frac{\partial}{\partial t}n(x, t) - D\frac{\partial^2}{\partial x^2}n(x, t) = 0 \tag{1.6}$$

If we assume that all N particles start at the origin, i.e. $n(x, t = 0) = N\delta(x)$, then the solution is given by

$$n(x, t) = \frac{N}{\sqrt{4\pi Dt}}\exp\left(-\frac{x^2}{4Dt}\right). \tag{1.7}$$

If we look at the form of Eq. (1.7), there is a particular structure that will be useful later. Note that we can write

$$n(x, t) \sim t^{-1/2} f_{\text{Gaussian}}(xt^{-1/2}). \tag{1.8}$$

This is a universal scaling relation for the diffusion universality class. Diffusion describes a wide range of systems from how heat flows through a material, to how electrons flow through a conducting wire, as well as random walk processes. All systems exhibiting diffusive transport have a local density that takes the form of Eq. (1.8). What this means is if we could somehow gain access to $n(x, t)$, and it scaled as Eq. (1.8), then we can say that the transport is diffusive. This will be helpful in the quantum case, as we do not have direct access to the simplified macroscopic transport equations.

1.1.2   Spin Transport

The universal nature of the diffusion equation suggests that we would also anticipate diffusive transport to emerge from a quantum mechanical perspective. In the quantum mechanical case, an observable O evolves via

$$\frac{\partial}{\partial t} O = \frac{i}{\hbar}[H, O] + \frac{\partial O}{\partial t} \tag{1.9}$$

Where $\hbar$ is Planck's constant (which is likely to be set to 1 most places), and H is the Hamiltonian for the system. For simplicity, let us look at a spin chain, governed by the Heisenberg Hamiltonian

$$H = J \sum_n \vec{S}_n \cdot \vec{S}_{n+1}. \tag{1.10}$$

The magnetization is a conserved quantity of this Hamiltonian, defined by

$$M^z(t) = \sum_x \langle S_x^z(t) \rangle. \tag{1.11}$$

Through analogy with the diffusion example, we can say that $\langle S_x^z(t) \rangle$ plays the role of the local density. This quantity in fact has trivial time-dependence, and so we examine density-density correlations instead. Classically, we would look at

$$C(x, t) = \rho(x, t)\rho(0, 0), \tag{1.12}$$

which has the same scaling behavior as the density itself. The quantum analog is a two-point correlation function of the form

$$G(x, t) = \langle S_x^z(t) S_0^z(0) \rangle. \tag{1.13}$$

To test for the emergence of diffusive transport, we can examine the long-time and long-distance behavior of this correlation function. In particular, if

$$G(x, t) \stackrel{?}{\sim} t^{-1/2} f_{\text{Gaussian}}(xt^{-1/2}) \tag{1.14}$$

then this would be evidence of diffusive spin transport.

More generally, hydrodynamical scaling of the two-point correlation function would look like

$$G(x, t) \sim t^{-1/z} f_z(xt^{-1/z}), \tag{1.15}$$

where z is called the dynamical critical exponent, and f_z is some universal function that does not depend on the microcsopic details. This expression serves as a test for the emergence of a simplified hydrodynamical description in quantum spin systems.

We can also examine the Fourier transform, called the dynamical structure factor

$$S(q, \omega) = \frac{1}{N} \sum_x \int \frac{dt}{2\pi} e^{i(qx-\omega t)} G(x, t). \tag{1.16}$$

Combining Eq. (1.15) and (1.16), the scaling form of $S(q, \omega)$ is given by

$$S(q, \omega) \sim q^{-z} \tilde{f}_z(\omega q^{-z}), \tag{1.17}$$

where $\tilde{f}_z$ is the Fourier transform of f_z. The dynamical structure factor is directly probed with neutron scattering experiments, enabling experimental validation of emergent spin hydrodynamics as well (see Sec. 1.3 for more details).

1.1.3 Kardar-Parisi-Zhang Hydrodynamics

Here I will briefly discuss the Kardar-Parisi-Zhang (KPZ) Equation. This equation originated as a model for the evolution of the profile of a growing interface [190], and takes the form,

$$\partial_t h(x, t) - D \nabla^2 h(x, t) = \frac{\lambda}{2} \left(\nabla h(x, t) \right)^2 + \eta(x, t). \tag{1.18}$$

Here, $h(x, t)$ is the height of the growing interface, and $\eta(x, t)$ is a stochastic noise term satisfying

$$\langle \eta(x, t) \eta(x', t') \rangle \propto \delta(x - x') \delta(t - t'). \tag{1.19}$$

Note that the left hand side of the KPZ equation is just the diffusion equation, and the additional terms are the simplest non-linearity, and a noise term. Beyond the original system of a growing interface, KPZ dynamics has been found in a wide range of systems from disordered conductors [343], quantum fluids [203], quantum circuits [252], and traffic flow [122], and was recently predicted also to appear in the high-temperature dynamics of some one-dimensional integrable quantum magnets [229, 80, 92, 83]. In particular, it was observed in Ref. [229] that in the Heisenberg Hamiltonian of Eq. (1.10), at infinite temperature that

$$G(x, t) \sim t^{-2/3} f_{\text{KPZ}}(xt^{-2/3}) \tag{1.20}$$

where f_{KPZ} is the scaling function for the KPZ universality class which is known numerically [280]. From the numerical result, it is possible to calculate the KPZ scaling function expected for the dynamical structure factor $S(q, \omega)$ via Fourier transformation. This then enables a direct method to look for KPZ hydrodynamics using neutron scattering experiments. I will discuss this further in Chapter 3.
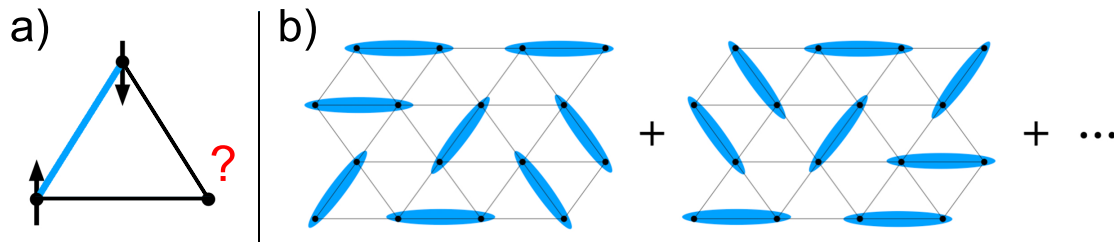
Figure 1.2: a) Picture of a triangle in the triangular lattice showing geometric frustration. b) Picture of the resonating valence bond solid introduced by Phil Anderson [14].

1.2 Quantum Spin Liquids

It is quite difficult to give a precise definition of a quantum spin liquid (QSL), but loosely it is a system that has strong correlations between the spins of a system, yet does not exhibit long range order, even down to $T = 0$. This definition makes it difficult to identify such phases, as it only tells us what the spins do *not* do. Rather than trying to be very precise in the definition, I will discuss some of the important features of many QSL states, and why these states are quite exotic and a vibrant area of research.

The literature on QSLs dates back to the 1970s, with Phil Anderson's work looking at the antiferromagnetic Heisenberg model on the triangular lattice [14]. The Hamiltonian is given by

$$H = J \sum_{\langle i,j \rangle} \vec{S}_i \cdot \vec{S}_j, \tag{1.21}$$

where the sum runs over all nearest neighbor pairs on the triangular lattice. This model has *geometric frustration*, meaning the terms in the Hamiltonian can not all be satisfied simultaneously. Since the coupling is anti-ferromagnetic, neighboring spins want to be anti-parallel. As shown in Fig. 1.2 a), once two spins are fixed to be anti-parallel, then either orientation of the third spin will frustrate one of the bonds.

Due to the frustration, Anderson proposed that the ground state was a *resonating valence bond* (RVB) state, where the ground state is a super-position over all possible dimer-coverings in the lattice [14]. A cartoon of the RVB state is shown in Fig. 1.2 b). This state would be an example of a QSL, as the ground state lacks long range order, due to quantum fluctuations. In particular, the massive super-position present in such a state is one of the hallmarks of a QSL state, which corresponds to an anomalously large degree of entanglement [305].

After further investigations over a few decades, it has been shown that the ground state of Eq. (1.21) does in fact order, and is not the RVB state discussed by Anderson [167, 188, 338, 66, 27, 52, 430, 387]. A modification to Eq. (1.21), adding a second-neighbor interaction, does in fact possess a QSL ground state [434, 163, 174, 299, 389, 124, 160]. The exact nature of the ground state of this model is still an open question, and this will be a large focus of Chapter 4.
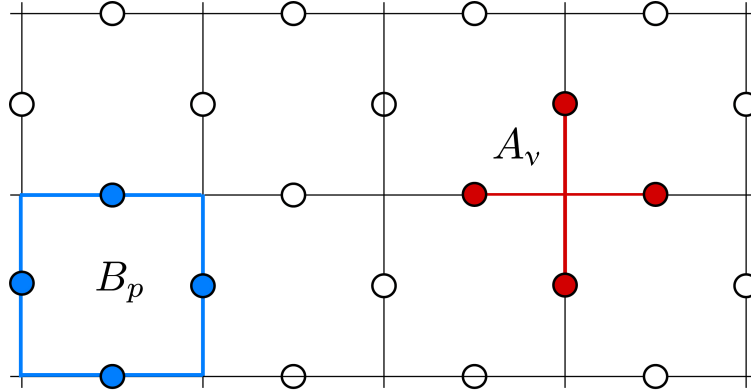
Figure 1.3: Image displaying the terms in the toric code Hamiltonian given by Eq. (1.22).

1.2.1 Toric Code and Anyons

A different, but relatively simple model known as the toric code model, does in fact possess a QSL ground state that is known analytically [198]. The Hamiltonian is given by

$$H_{\text{tc}} = -\sum_v A_v - \sum_p B_p \tag{1.22}$$

$$A_v = \prod_{n\sim v} \sigma_n^x \quad ; \quad B_p = \prod_{n\sim p} \sigma_n^z. \tag{1.23}$$

The degrees of freedom lie on the edges of a square lattice, A_v is a product of σ^x on the edges touching vertex v, and B_p is a product of σ^z over the edges on the boundary of the plaquette p. A picture is shown in Fig. 1.3 demonstrating these terms.

The full spectrum of this model is known exactly, and the ground state is known as a gapped $\mathbb{Z}_2$ QSL. In particular, the ground state is given by

$$|\Omega\rangle = \prod_v \left(\frac{\mathbb{1} + A_v}{2} \right) |\uparrow \cdots \uparrow\rangle_z . \tag{1.24}$$

To understand this state, first consider a ferromagnetic state $|\uparrow \cdots \uparrow\rangle_z$. The action of A_v on such a state is to flip all spins connected to the vertex v, creating a star pattern of flipped spins. The state in Eq. (1.24) is thus a massive super-position over all combinations of having stars of flipped spins at each vertex or not. This structure is reminiscent of the RVB state proposed by Anderson [14], and is a hallmark of QSL states.

There are two types of quasi-particle excitations in the toric code, call them ϵ and μ particles, know as anyons. Anyons have exchange statistics that fall outside of the fermion-boson paradigm, and can be utilized for quantum-information processing [38, 363]. This is an example of *fraction-alization* which is another key aspect of QSL states. If you consider a bound state of an ϵ and a μ

state, this is in fact a fermionic particle. So you can think of the excitations as a result of a fermion *fractionalizing* into two anyons. Another example of fractionalization is the idea of spin-charge separation [364, 232, 141], where in particular materials, the electron 'splits' into a chargeless spin-1/2 *spinon*, and a spinless charged *chargon*.

1.2.2 Classification of Quantum Spin Liquids

Quantum spin liquids are quite exotic states, often possessing massive super-positions in the ground state, and fractionalized quasi-particle excitations. There are three main categories of QSL states that are distinguished by the low-energy physics. The broad idea is that we start with some Hamiltonian for the spin degrees of freedom, but the low-energy physics is governed by a gauge-theory with both matter and gauge fields, similar to quantum electrodynamics (QED). To see how this may be possible, we look at the *parton construction*, which is an exact mapping between spin opertors and fermions [305]. This mapping is given by

$$S^i = \frac{1}{2} f_\alpha^\dagger \sigma_{\alpha\beta}^i f_\beta, \quad f_\alpha^\dagger f_\alpha = 1, \tag{1.25}$$

where σ^i is the i^{th}Pauli matrix, the indices α, β run over the spin orientations $\uparrow, \downarrow$, and repeated indices are summed over. This mapping is also possible with bosons rather than fermions, and takes the same form. We note that the local Hilbert space for the spin system has dimension two, but the fermion Hilbert space has dimension four, as there are two fermions corresponding to $\uparrow$ and $\downarrow$. To make this exact, we must also include the half-filling constraint in Eq. (1.25).

Note that this mapping has a redundancy in terms of the fermion operators called *spinons*. In particular, the transformation

$$f_\alpha \longrightarrow e^{i\phi} f_\alpha \tag{1.26}$$

$$f_\alpha^\dagger \longrightarrow e^{-i\phi} f_\alpha \tag{1.27}$$

leaves the spin operator invariant. This is a $U(1)$ redundancy, and if we fix $\phi = \pm\pi$, then we would have a $\mathbb{Z}_2$ redundancy. We can upgrade this redundancy to a gauge symmetry of the underlying theory, and couple the fermions to a gauge field obeying the symmetry. This leads to three distinct classes of QSLs, defined by the gauge symmetry. The first two are $\mathbb{Z}_2$, and $U(1)$ QSLs. The $\mathbb{Z}_2$ QSL is said to be "toric code like", while the $U(1)$ QSL is said to be "QED like". The last option is to have only matter fields, and no gauge field at all. This theory is described by fermions with a half-filling constraint, which is "metal like". This often leads to a fermi-surface for the spinons, and this state is called a spinon fermi surface (SFS) state.

1.3 Neutron Scattering and Spectral Functions

Since neutrons are chargeless particles, they are quite insensitive to the electronic structure of the material. However, since neutrons carry spin, they interact with the atomic nuclei, and probe the magnetic properties of the material. This makes neutron scattering an excellent probe of the magnetic excitations of a material.

In a neutron scattering experiment, a neutron with a fixed wavevector is scattered off of a material, and a detector on the other side of the material captures where the scattered neutron ends up. After scattering many neutrons with different wavevectors, an interference pattern forms, which encodes properties of the magnetic structure of the material in question.

Mathematically, we start with an incident neutron with wavevector $\mathbf{k}_i$, that scatters off a material, producing a neutron with a final wavevector $\mathbf{k}_f$. Due to this, there is a momentum $\mathbf{q} = \hbar \mathbf{k}_i - \hbar \mathbf{k}_f$ transferred to the material. The energy difference between the incoming and outgoing neutron is $\hbar \omega$. I will set $\hbar = 1$ in the remainder of this discussion.

The neutron scattering cross-section is directly probed by the dynamical structure factor $S(\mathbf{q}, \omega)$[366, 353, 350]. For a spin system with N lattice sites, the dynamical structure factor is defined as

$$S(\boldsymbol{q}, \omega) = \frac{1}{N} \sum_{\boldsymbol{x}} \int_0^{+\infty} \frac{\mathrm{d}t}{2\pi} e^{i(\omega t - \boldsymbol{q} \cdot \boldsymbol{x})} G(\boldsymbol{x}, t), \tag{1.28}$$

where $\mathbf{x}$ denotes the location of a site in the lattice, and $G(\boldsymbol{x}, t)$ is a two-point spin-spin correlation function. In particular, we define

$$G(\mathbf{x}, t) = \langle \mathbf{S}_{\mathbf{x}}(t) \cdot \mathbf{S}_0(0) \rangle \tag{1.29}$$

Where $\mathbf{S_x}$ is the operator valued spin-vector at site $\mathbf{x}$, and $\langle \cdot \rangle$ denotes the thermal expectation value. The dot product of the spin operators in Eq. (1.29) produces a sum of multiple terms, so we will define

$$G^{\alpha\beta}(\boldsymbol{x}, t) = \langle S_{\mathbf{x}}^{\alpha}(t) S_0^{\beta}(\mathbf{0}) \rangle \tag{1.30}$$

where $S_{\mathbf{x}}^{\alpha}$ is the α component of the spin operator at the site $\mathbf{x}$. We allow α, β to be different, as using spin raising and lowering operators S^+, S^- is often advantageous. Let us also define $S^{\alpha\beta}(\mathbf{q}, \omega)$ in terms of $G^{\alpha\beta}(\mathbf{x}, t)$.

The thermal expectation value of the operator O is defined as

$$\langle O \rangle := \mathrm{Tr}\left[e^{-H/k_b T} O \right] / Z \quad , \quad Z = \mathrm{Tr}\left[e^{-H/k_b T} \right] \tag{1.31}$$

where H is the Hamiltonian for the system, and T is the temperature. Often we examine this expecation value at $T = 0$, which is equivalent to calculating the expectation value in the ground state of H. Lastly, the time dependence in Eq. (1.30) is interpreted in the Heisenberg picture as

$$O(t) = e^{iHt} O e^{-iHt}. \tag{1.32}$$

If we have access to the full spectrum of H, with eigenvectors $|n\rangle$ and eigenvalues E_n, then we can write

$$S^{\alpha\beta}(\mathbf{q}, \omega) = \sum_{n,m} \frac{e^{-E_n/k_b T}}{Z} \langle n | S_{-\mathbf{q}}^{\alpha} | m \rangle \langle m | S_{\mathbf{q}}^{\beta} | n \rangle \, \delta(\omega - [E_n - E_m]), \tag{1.33}$$

with

$$S_{\mathbf{q}}^{\alpha} = \frac{1}{N} \sum_{\mathbf{x}} e^{i\mathbf{q} \cdot \mathbf{x}} S_{\mathbf{x}}^{\alpha}. \tag{1.34}$$

To gain some intuition about the dynamical structure factor, let us explore further the structure of Eq. (1.33). For simplicity, let us look at the $T = 0$ spectral function, which yields

$$S^{\alpha\beta}(\mathbf{q}, \omega) = \sum_m [\langle\Omega|S^{\alpha}_{-\mathbf{q}}|m\rangle\langle m|S^{\beta}_{\mathbf{q}}|\Omega\rangle] \, \delta(\omega - [E_0 - E_m]), \qquad (1.35)$$

where $|\Omega\rangle$ is the ground state of H. This expression consists of two terms. First, the delta function is a density of states type term, and the term in brackets is a selection rule term. If the selection rule term were not present, then this quantity would count the number of energy eigenstates with an energy ω above the ground state. The term in brackets imposes an additional constraint, to only look for states with a particular form. For example, if we consider a ferromagnetic ground state $|\Omega\rangle = |\downarrow \cdots \downarrow\rangle$, and take $\alpha = \beta = x$, then the bracketed term takes the form

$$\langle\Omega|S^x_{-\mathbf{q}}|m\rangle\langle m|S^x_{\mathbf{q}}|\Omega\rangle \qquad (1.36)$$

This term is only non-zero if the state $|m\rangle$ is of the form

$$|m(\mathbf{q})\rangle = \frac{1}{\sqrt{N}} \sum_x e^{i\mathbf{q}\cdot\mathbf{x}} S^+_x| \downarrow \cdots \downarrow\rangle. \qquad (1.37)$$

Such a state is a spin-wave state in the one-magnon sector. Treating a magnon as a quasi-particle, created by a spin flip in a ferromagnetic background, then this state represents a single magnon with a momentum $\mathbf{q}$. Looking at Eq. (1.35), we then see that the dynamical structure factor in this example is non-zero when there is a magnon eigenstate with energy ω and momentum $\mathbf{q}$. Therefore, $S(\mathbf{q}, \omega)$ is probing the dispersion relation $\omega(\mathbf{q})$ of the magnon excitations in the system. This intuition is useful for more complicated systems as well.

In a real material with interactions, these spin-wave excitations are not exact eigenstates, and this will lead to more broad spectral features, and a continuum at higher energies. When the low-energy excitations in the system are not magnons, then the dispersion relation interpretation of $S(\mathbf{q}, \omega)$ begins to break down. This is the case in quantum spin liquids for example, where the low-energy excitations are spinons, which are fractionalized magnons. In such a case, the dynamical structure factor is actually probing bound-states of spinons. This will lead to distinct features in the dynamical structure factor, and will be discussed further in Chapter 4.

1.4 Outline

The outline for this thesis is the following.

In Chapter 2, I discuss the numerical technique used throughout the rest of the thesis known as matrix product states (MPS). I discuss the basic framework of MPS, as well as common algorithms for finding ground states and performing time evolution. Lastly, I discuss how we can work directly in the thermodynamic limit, and the concept of finite-entanglement scaling.

In Chapter 3, I discuss emergent hydrodynamics in the Heisenberg spin chain. Recent work demonstrated that the spin transport at $T = \infty$ is part of the Kardar-Parisi-Zhang (KPZ) universality class, rather than diffusion. I show that this finding is robust down to temperatures that are experimentally relevant, as well as identify signatures detectable with neutron scattering experiments. I discuss a collaboration with the neutron scattering group at Oak Ridge National Lab detecting these signatures in the compound $KCuF_3$. I then discuss the crossover from the Tomonaga-Luttinger liquid physics in the ground state of this model, to the KPZ dynamics at finite temperature. This chapter is based on these papers [93, 308].

In Chapter 4, I examine the $J_1 - J_2$ Heisenberg model on the triangular lattice, which is a well known model with a quantum spin liquid (QSL) ground state. I discuss the main different types of candidate QSL states for this model, and the unique signatures they predict in the dynamical structure factor. Using an MPS based approach, I calculate the dynamical structure factor, and suggest that the result are most consistent with a U(1) Dirac quantum spin liquid. Then I discuss two collaborations with neutron scattering experimental groups in the triangular lattice QSL candidate materials $KYbSe_2$ and $YbZn_2GaO_5$. This chapter is based on these papers [309, 331, 399].

Lastly, in Chapter 5, I look at how time evolution of a state that is represented by an MPS with a fixed bond-dimension at all times deviates from the exact time evolved state. In particular, I examine a time evolution process known as the Kibble-Zurek mechanism. I derive that the effect of finite entanglement on a Kibble-Zurek process is captured by a dimensionless scaling function of the ratio of two length scales, one determined dynamically and one by the entanglement restriction from the MPS ansatz. This scaling behavior is then demonstrated numerically for the quantum Ising model, and the 3-state Potts model. This chapter is based on this paper [330].

Chapter 2

Matrix Product States Background

2.1 Matrix Product States and Operators

2.1.1 Matrix Product States

The fundamental object representing the pure state of a system is a *ket* $|\psi\rangle$, which is a unit vector in a Hilbert space $\mathcal{H}$. We can express the state in an orthonormal basis as

$$|\psi\rangle = \sum_{\sigma} C_{\sigma} |\sigma\rangle . \tag{2.1}$$

If the dimension of the Hilbert space is d, then $|\psi\rangle$ can be represented as a list of d complex numbers.

When studying a system with N degrees of freedom, then the Hilbert space for the composite system is determined by the tensor product. If $\mathfrak{h}_x$ is the local Hilbert space for a site at position x, then the composite Hilbert space is given by

$$\mathcal{H} = \otimes_x \mathfrak{h}_x \tag{2.2}$$

A generic state in the composite Hilbert space can be written

$$|\psi\rangle = \sum_{\sigma_1 \cdots \sigma_N} C_{\sigma_1 \cdots \sigma_N} |\sigma_1 \cdots \sigma_N\rangle . \tag{2.3}$$

If the local Hilbert space is dimension d, then the state can be represented as a list of d^N complex numbers. This is the exponential wall of many-body physics, and this quickly becomes intractable. The matrix product state (MPS) ansatz circumvents this issue, and provides an efficient representation for states with low entanglement (see Sec. 2.1.3 for more details about why).

The idea of an MPS is to consider the following ansatz for the coefficients of Eq. (2.3)

$$C_{\sigma_1 \cdots \sigma_N} = \sum_{\alpha_0 \cdots \alpha_N} M^{\sigma_1}_{\alpha_0, \alpha_1} M^{\sigma_2}_{\alpha_1, \alpha_2} \cdots M^{\sigma_N}_{\alpha_{N-1}, \alpha_N} \tag{2.4}$$

Where M^{σ_i} is a matrix with indices α_{i-1}, α_i, and the expression is just a sequence of matrix multiplications. These matrices do not all need to be the same, but I leave out an additional index identifying the site when it is clear to do so. The upper index, σ_i is called the physical index, and α_{i-1}, α_i are called virtual indices. The dimension of the largest virtual index is called the bond-dimension, and is denoted by χ. The first and last virtual indices, α_0 and α_N, set the boundary conditions of the Ansatz. For open boundary conditions, we drop these indices (or we can take them to be dimension 1), and for periodic boundary conditions, α_0 and α_N are contracted, leading to

$$C_{\sigma_1\cdots\sigma_N} = \text{Tr}\left[M^{\sigma_1}\cdots M^{\sigma_N}\right]. \tag{2.5}$$

This ansatz is complete, in that any state in a finite Hilbert space can be expressed as an MPS if χ is large enough [316].

It is common to use diagrams to represent an MPS. First, we can draw a single tensor as

$$\tag{2.6}$$

Then, the coefficient matrix in Eq. (2.4) can be drawn diagramatically as

$$\tag{2.7}$$

This diagram is an MPS for a state $|\psi\rangle$, with open boundary conditions. The line connecting adjacent tensors means to contract the connected indices. For Periodic boundary conditions, there would be an additional line connecting the left of the first tensor to the right of the last tensor.

Let us return to Eq. (2.4), and omit the virtual indices.

$$C_{\sigma_1\cdots\sigma_N} = M^{\sigma_1}M^{\sigma_2}M^{\sigma_3}\cdots M^{\sigma_N} \tag{2.8}$$

I want to note that the choice of matrices is not unique. In particular, for some invertible matrix X, we can write

$$C_{\sigma_1\cdots\sigma_N} = M^{\sigma_1}M^{\sigma_2}XX^{-1}M^{\sigma_3}\cdots M^{\sigma_N}, \tag{2.9}$$

and the result is left invariant. From here, we could define

$$\tilde{M}^{\sigma_2} = M^{\sigma_2}X \tag{2.10}$$

$$\tilde{M}^{\sigma_3} = X^{-1}M^{\sigma_3}, \tag{2.11}$$

and arrive at

$$C_{\sigma_1\cdots\sigma_N} = M^{\sigma_1}\tilde{M}^{\sigma_2}\tilde{M}^{\sigma_3}\cdots M^{\sigma_N}. \tag{2.12}$$

This produces the same coefficient matrix, except the tensor at site 2 and site 3 are different. This is called a *gauge transformation*.

2.1.2 Canonical Forms

In the previous section, we saw that the coefficient matrix is left invariant under a gauge transformation by an invertible matrix X. Here, we will use this gauge freedom to define useful *canonical forms* for an MPS. To do this, let us take the singular value decomposition (SVD) of one of the tensors M. Using diagrams, we can write

$$\alpha_{i-1} - \boxed{M} - \alpha_i \quad = \alpha_{i-1} - \boxed{A} - \boxed{S} - \boxed{V} - \alpha_i \qquad (2.13)$$

Since the left and right singular matrices are unitary, we conclude that A satisfies the property

$$\sum_{\sigma_i, \alpha_{i-1}} A^{\sigma_i}_{\alpha_{i-1}, \mu} \bar{A}^{\sigma_i}_{\alpha_{i-1}, \nu} = \delta_{\mu, \nu} \qquad (2.14)$$

Where the index μ is the index contracted with S in Eq. (2.13). Diagramtically, we would write this as

$$\left(\begin{array}{c} \boxed{A} \\ | \\ \boxed{\bar{A}} \end{array} \right) = \left(\right. \qquad (2.15)$$

What this means is that if A and $\bar{A}$ are contracted from the left, then the result is a new tensor, that acts like an identity matrix.

If we return to Eq. (2.13), we can absorb S, V into the next tensor in the MPS, defining a new $M^{\sigma_{i+1}}$. If we perform this process, starting on the left most site, all the way to the last site, then we would say that the MPS is in *left canonical form*, denoted by

$$\boxed{A} - \boxed{A} - \cdots - \boxed{A} \qquad (2.16)$$

Where the letter A signifies that the tensors are in left canonical form.

We could also perform an SVD from the right, expressing M as

$$\alpha_{i-1} - \boxed{M} - \alpha_i \quad = \alpha_{i-1} - \boxed{U} - \boxed{S} - \boxed{B} - \alpha_i \qquad (2.17)$$

Where the B matrices satisfy a similar relation given by

$$\left. \begin{array}{c} \boxed{B} \\ | \\ \boxed{\bar{B}} \end{array} \right) = \left. \right). \qquad (2.18)$$

Then, we say that an MPS is in *right canonical form* if every tensor satisfies this relation.

We could also put an MPS into a *mixed canonical form*, where we fix a central site c, and then every tensor to the left (right) of c is in left (right) canonical form. Such an MPS takes the form

$$
\boxed{A} - \cdots - \boxed{A} - \boxed{C} - \boxed{B} - \cdots - \boxed{B} \, , \tag{2.19}
$$

where the C tensor is at site c. Note that c does not have to be the exact center site, it can be placed anywhere, it just indicates the site separating left and right canonical form tensors. If we perform an SVD on C, we can write

$$
- \boxed{A} - \boxed{S} - \boxed{V} - = - \boxed{C} - = - \boxed{U} - \boxed{S} - \boxed{B} - . \tag{2.20}
$$

If we take the left (right) side of the equation, we can absorb the V (U) tensor into the B (A) tensor to the right (left). Such a gauge transformation preserves the left (right) canonical form, since the left (right) and physical indices are not effected by this transformation. With this implicit gauge transformation in mind, we can then write

$$
- \boxed{A} - \diamond{S} - = - \boxed{C} - = - \diamond{S} - \boxed{B} - . \tag{2.21}
$$

We use a diamond shape for the S tensor to highlight that it is a diagonal tensor with only two indices. Putting this altogether, we can then write an MPS in mixed canonical form as

$$
\boxed{A} - \cdots - \boxed{A} - \diamond{S} - \boxed{B} - \cdots - \boxed{B} \, . \tag{2.22}
$$

2.1.3 Advantage of Matrix Product States

Let us consider an MPS in mixed canonical form, given by Eq. (2.22). Mathematically, this state takes the form

$$
|\psi\rangle = \sum_{\alpha=1}^{\chi} s_\alpha \, |\alpha\rangle_A \, |\alpha\rangle_B \tag{2.23}
$$

We note that this state is already in the form of a Scmidt decomposition, for the partition separating the system into a left part A, and a right part B. The Schmidt coefficients are precisely the singular values of the tensor S. We note that the number of Schmidt values, called the Schmidt rank, is precisely the bond-dimension χ.

In this form, we can compute the reduced density matrix easily. In particular

$$
\rho_A = \text{Tr}_B \left[|\psi\rangle\langle\psi| \right] = \sum_{\alpha=1}^{\chi} s_\alpha^2 \, |\alpha\rangle_A \, \langle\alpha|_A \tag{2.24}
$$

$$
\rho_B = \text{Tr}_A \left[|\psi\rangle\langle\psi| \right] = \sum_{\alpha=1}^{\chi} s_\alpha^2 \, |\alpha\rangle_B \, \langle\alpha|_B \tag{2.25}
$$

From this form, we can read off the entanglement entropy directly

$$S_{A|B}(|\psi\rangle) = -\operatorname{Tr}[\rho_A \log \rho_A] = -\operatorname{Tr}[\rho_B \log \rho_B] \tag{2.26}$$

$$= -\sum_{\alpha=1}^{\chi} s_\alpha^2 \log\left(s_\alpha^2\right). \tag{2.27}$$

Computing the reduced density matrix depends on the bipartition into subsystems A, B, and the initial pure state $|\psi\rangle$. This quantity is typically computationally intensive to compute, but arises naturally from an MPS in mixed canonical form.

The potency of the MPS ansatz is contained within Eq. (2.27), as the Schmidt rank is given by χ, which controls the number of parameters needed to specify a given state. Therefore, if a state has "small" entanglement, then it can be represented by an MPS with "small" χ. The main advantage arises when we look at one-dimensional systems. In particular, the ground state of one-dimensional gapped systems satisfy an entanglement area law [147]. This means the entanglement does not scale with the system size L. Moreover, what this means is that the maximum χ needed to represent a state remains finite, and independent of L. For open boundary conditions, this means that the number of parameters P_L needed to specify such a low entanglement state of length L scales as

$$P_L \sim O(\chi^2 L) \tag{2.28}$$

Since χ is finite, the scaling with L is linear rather than exponential.

If we are studying a system with translational invariance, then we can bake this into the MPS ansatz by repeating the same tensor for every site (or a few tensors if the unit-cell is larger than one site). Then, we can represent the ground state of a gapped one-dimensional system exactly, even in the thermodynamic limit, with a finite number of parameters. This realization has revolutionized the numerical study of many-body systems. We will discuss working in the thermodynamical limit, as well as gapless systems in Sec. 2.4.1.

2.1.4 Thermal States

Often we are interested in studying mixed rather than pure states, such as studying the effect of temperature with a thermal state. One way to do this within the MPS framework is via the purification method [370], and I will briefly discuss this technique here.

When studying a mixed state, the state of the system is now represented by a density matrix ρ. The density matrix for a pure state $|\psi\rangle$ is given by

$$\rho = |\psi\rangle\langle\psi|. \tag{2.29}$$

In the case of a general mixed state, we can write

$$\rho = \sum_n P_n |\psi_n\rangle\langle\psi_n|. \tag{2.30}$$

The interpretation is that the system has a classical probability P_n of being in the quantum pure state $|\psi_n\rangle$. If the state $|\psi\rangle$ is a d dimensional vector, note that ρ is a $d \times d$ dimensional matrix. If we think of ρ as actually a d^2 dimensional vector, then this suggests that we can treat ρ as a pure state in an enlarged Hilbert space. This is the idea of the purification method [370].

In the case of thermal states, the density matrix we are interested in is given by

$$\rho_T = e^{-\frac{H}{k_b T}}/Z \tag{2.31}$$

$$Z = \text{Tr}\left[e^{-\frac{H}{k_b T}}\right] \tag{2.32}$$

where T is the temperature, and H is the Hamiltonian of the system. We can write a mixed thermal state ρ_T as a pure state $|\psi_T\rangle$ in an enlarged Hilbert space,

$$\mathcal{H} \rightarrow \mathcal{H}_P \otimes \mathcal{H}_A \tag{2.33}$$

where H_P is the physical Hilbert space of interest, and H_A is an auxiliary Hilbert space of the same size. Then the density matrix is retrieved by the relation

$$\rho_T = \text{Tr}_A |\psi_T\rangle\langle\psi_T| . \tag{2.34}$$

The state $|\psi_T\rangle$ is defined by

$$|\psi_T\rangle = \exp\left(-\frac{H}{2k_b T}\right)|\psi_\infty\rangle \tag{2.35}$$

with $H = H_P \otimes I_A$ the physical Hamiltonian acting only on the physical subspace, and I_A the identity acting on the auxiliary space. The state $|\psi_\infty\rangle$ can be expressed exactly as an MPS by forming maximally entangled pairs between one site in the physical Hilbert space and one site in the auxiliary space.

Expectation values are computed via

$$\langle O\rangle_T = \langle\psi_T| O \otimes I |\psi_T\rangle \tag{2.36}$$

Where the identity on the Auxiliary space makes this equivalent to

$$\langle O\rangle_T = \text{Tr}\left[\rho_T O\right] . \tag{2.37}$$

Note that if we apply a unitary operation to the auxiliary degrees of freedom, then expectation values for observables on the physical degrees of freedom are left invariant. This is often useful when computing time dependent quantities such as two-point correlation functions of the form

$$\langle A(t)B\rangle_T = \langle\psi_T| e^{i[H\otimes I]t} A e^{-i[H\otimes I]t} B |\psi_T\rangle \tag{2.38}$$

We can evolve the auxiliary states backwards in time to write

$$\langle A(t)B\rangle_T = \langle\psi_T| e^{-i[I\otimes H]t} e^{i[H\otimes I]t} A e^{-i[H\otimes I]t} B e^{i[I\otimes H]t} |\psi_T\rangle \tag{2.39}$$

$$= \langle\psi_T| e^{i\mathcal{L}t} A e^{-\mathcal{L}t} B |\psi_T\rangle , \tag{2.40}$$

where we have defined the Louivillian operator

$$\mathcal{L} = H \otimes I - I \otimes H. \tag{2.41}$$

This is the same result as working directly with open systems, and treating density matrices as super-kets $|\rho_T\rangle\rangle$ where the dynamics are generated by the super-operator $\mathcal{L}$ [243]. This means studying the dynamics of a thermal state numerically requires only minor adaptations from working with pure states. Essentially the Hamiltonian is replaced by the Louivillian, and a system of length L is described by an MPS with $2L$ sites.

2.1.5 Matrix Product Operators

We can also write operators, such as a Hamiltonian H, in the MPS framework. Such an operator is called a *matrix product operator* (MPO). Mathematically, we express an MPO as

$$H = \sum_{\vec{\sigma},\vec{\sigma}'} W^{\sigma_1}_{\sigma_1'} \cdots W^{\sigma_N}_{\sigma_N'} |\vec{\sigma}\rangle \langle\vec{\sigma}'| \tag{2.42}$$

where $\vec{\sigma} = (\sigma_1, \cdots, \sigma_N)$. Diagramatically, we can express an MPO by

$$\tag{2.43}$$

Representing Local Hamiltonians as a Matrix Product Operator

Let us start with a concrete example of the transverse field Ising model (TFIM) with Hamiltonian

$$H = -J \sum_i \sigma^z_i \sigma^z_{i+1} - h \sum_i \sigma^x_i. \tag{2.44}$$

If we only look at the terms involving site i, this include the terms

$$H_i = -J\sigma^z_{i-1}\sigma^z_i - J\sigma^z_i\sigma^z_{i+1} - h\sigma^x_i \tag{2.45}$$

Since the Hamiltonian acts on a composite Hilbert space, say of N sites, then these terms are really given by

$$H_i = -J[I \otimes \cdots \otimes I \otimes \sigma^z \otimes \sigma^z \otimes I \otimes I \otimes \cdots \otimes I] \tag{2.46}$$
$$-J[I \otimes \cdots \otimes I \otimes I \otimes \sigma^z \otimes \sigma^z \otimes I \otimes \cdots \otimes I] \tag{2.47}$$
$$-h[I \otimes \cdots \otimes I \otimes I \otimes \sigma^x \otimes I \otimes I \otimes \cdots \otimes I] \tag{2.48}$$
$$\tag{2.49}$$

These three terms can be thought of as a particular string of fixed length N, where the first term would correspond to the string "$I \cdots IZZI \cdots I$". Then, the Hamiltonian is the set of strings satisfying the rule that it includes ever string that has two Z's appearing next to each other, and every string with a single X, with every other slot occupied by an I. From this interpretation, this set of strings can be generated, using a finite-state machine [316]. For the TFIM Hamiltonian, the state machine would look like

$$
\begin{array}{c}
q_1 \\
-J\sigma^z \nearrow \quad \searrow \sigma^z \\
q_0 \xrightarrow{-h\sigma^x} q_2 \\
\circlearrowleft \qquad \circlearrowleft \\
I \qquad\qquad I
\end{array}
\tag{2.50}
$$
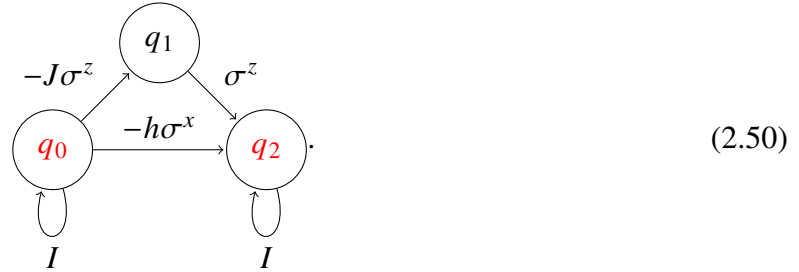
To understand how to look at this, imagine the rule that you must start at node q_0, and end at node q_2, and you must perform N transitions. Each time you perform a transition, record the expression next to the transition arrow. The string

$$
-J\sigma^z \otimes \sigma^z \otimes I \cdots
\tag{2.51}
$$

would be the path through the state machine of

$$
q_0 \xrightarrow{-J\sigma^z} q_1 \xrightarrow{\sigma^z} q_2 \xrightarrow{I} q_2 \xrightarrow{I} \cdots .
\tag{2.52}
$$

Where the string

$$
I \otimes I \otimes -J\sigma^z \otimes \sigma^z \otimes I \cdots
\tag{2.53}
$$

is given by the path

$$
q_0 \xrightarrow{I} q_0 \xrightarrow{I} q_0 \xrightarrow{-J\sigma^z} q_1 \xrightarrow{\sigma^z} q_2 \xrightarrow{I} q_2 \xrightarrow{I} \cdots .
\tag{2.54}
$$

Similarly, a path that connects $q_0 \to q_2$ would correspond to a string including $-h\sigma^x$. From this, it is hopefully clear that all possible strings of length N that this state machine can generate corresponds to all the terms in the TFIM Hamiltonian of Eq. (2.44). Then, the MPO tensor W that represents the Hamiltonian H is given by the adjacency matrix of the state machine. For the TFIM, the MPO tensor would be

$$
W = \begin{pmatrix} I & -J\sigma^z & -h\sigma^x \\ 0 & 0 & \sigma^z \\ 0 & 0 & I \end{pmatrix}.
\tag{2.55}
$$

If we multiply two W matrices together, where the muplication operation is taken to mean tensor product, the we find

$$
W - W = \begin{pmatrix} I \otimes I & -J(I \otimes \sigma^z) & -J(\sigma^z \otimes \sigma^z) - h(\sigma^x \otimes I + I \otimes \sigma^x) \\ 0 & 0 & \sigma^z \otimes I \\ 0 & 0 & I \otimes I \end{pmatrix},
\tag{2.56}
$$

and notice the top right element is precisely the Hamiltonian density for the TFIM of Eq. (2.45). Generalizing to other local Hamiltonians is straightforward.

Suppose we wanted to add a long-range interaction of the form

$$\sum_{n,m} \gamma^{m-n} A_m B_n, \quad 0 < \gamma < 1, \tag{2.57}$$

to the TFIM, then the state machine would be updated to look like

(2.58)
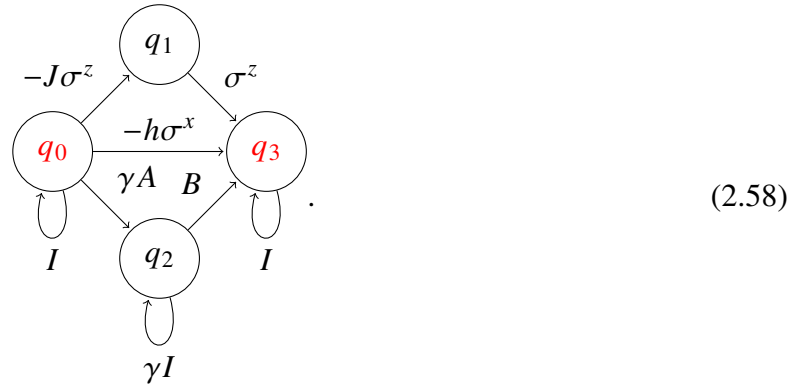
The corresponding MPO tensor W would take the form

$$W = \begin{pmatrix} I & -J\sigma^z & \gamma A & -h\sigma^x \\ 0 & 0 & 0 & \sigma^z \\ 0 & 0 & \gamma I & B \\ 0 & 0 & 0 & I \end{pmatrix}. \tag{2.59}$$

2.2 Basic Operations

Here I will discuss some basic operations with matrix product states. First, let us define a "bra" MPS written as

(2.60)

where $\bar{M}$ means the complex conjugate of all the elements of M. Then, if we have two states $|\psi(M)\rangle$ and $|\phi(N)\rangle$, then the overlap is given by

(2.61)

Note that the overlap has no free indices, and thus produces a number, as desired.

Expectation Values of Local Operators

Let us look at the expectation value of an on-site operator O at site x. Then, if we put an MPS into mixed canonical form, with the center site at x, then the overlap is given by

$$\langle O_x \rangle = \quad (2.62)$$

Using the left (right) canonical form properties of Eq. (2.15) and (2.18), this then reduces to

$$\langle O_x \rangle = \quad (2.63)$$

Where the only contractions needed to compute are the ones that occur at site x.

If we wish to compute correlation functions of two on-site operators separated by a distance r, then this is also simple. For simplicity, let us define the *transfer matrices*

$$\quad (2.64)$$

Then, a two-point correlation function would take the form

$$\langle O_0 O_{r+1} \rangle = \quad (2.65)$$

Where we inserted r copies of the transfer matrix to connect sites 0 and $r + 1$[1]. There is an analogous expression using the T_A transfer matrix, with C on the right, and A on the left. More complicated expectation values, such as for N-point (N>2) correlation functions, or local but not on-site operators, can be treated in a similar way.

---

[1]The expression for $\langle O_0 O_{r+1} \rangle$ true for a translationally symmetric state. For an open system, the transfer matrix T_B will be different at each site, and will require the multiplication of these r different matrices.

This expression for the correlation function allows us to extract the correlation length ξ quite easily. To see this, we first note that if r is large, then

$$\langle O_0 O_r \rangle \sim e^{-r/\xi} \tag{2.66}$$

When looking at the transfer matrix, if we apply r copies of the tensor with itself, then what survives are only the largest eigenvectors. Due to normalization, the largest eigenvalue must be 1, and this is uninteresting. However, the first eigenvalue less than 1, call it λ_T will encode the decay of the correlation function. Thus, from the MPS representation of the correlation function, we also have for large r that

$$\langle O_0 O_r \rangle \sim \lambda_T^r \tag{2.67}$$

Comparing these, we find

$$\xi \sim -\frac{1}{\ln \lambda_T}. \tag{2.68}$$

.

Note that the structure of Eq. (2.65) necessitates the the long distance form given in Eq. (2.66). This means that systems which exhibit power-law scaling in their correlations can not be represented exactly by an MPS. An important example of such systems are critical systems, where the correlation length diverges. I will discuss this further in Sec. 2.4.2.

2.2.1 Addition of MPS

Let us suppose we have two MPS with periodic boundary conditions taking the form

$$|\psi\rangle = \sum_{\vec{\sigma}} \text{Tr} \left(A^{\sigma_1} \cdots A^{\sigma_N} \right) |\vec{\sigma}\rangle, \quad |\phi\rangle = \sum_{\vec{\sigma}} \text{Tr} \left(B^{\sigma_1} \cdots B^{\sigma_N} \right) |\vec{\sigma}\rangle, \tag{2.69}$$

where $\vec{\sigma}$ is a short hand for $\sigma_1, \cdots, \sigma_N$, and we do not assume any particular canonical form. Then we seek to find the MPS that represents

$$|\psi\rangle + |\phi\rangle = \sum_{\vec{\sigma}} \text{Tr} \left(C^{\sigma_1} \cdots C^{\sigma_N} \right) |\vec{\sigma}\rangle. \tag{2.70}$$

Note that if we write

$$C^{\sigma_i} = \begin{pmatrix} A^{\sigma_i} & 0 \\ 0 & B^{\sigma_i} \end{pmatrix} \tag{2.71}$$

then, we can see that

$$\text{Tr} \left(C \cdots C \right) = \text{Tr} \begin{pmatrix} A \cdots A & 0 \\ 0 & B \cdots B \end{pmatrix} = \text{Tr} \left(A \cdots A \right) + \text{Tr} \left(B \cdots B \right). \tag{2.72}$$

Thus, Eq. (2.72) produces the correct coefficient in the summed state. If we work with open boundary conditions, the result is essentially the same, but the boundary tensors have to be handled with care [316].

One thing to note is that if the bond-dimension of $|\psi\rangle$ is χ_A, and of $|\phi\rangle$ is χ_B, then the bond-dimension of the sum is $\chi_C = \chi_A + \chi_B$. This has two implications. First, that the set of MPS with bond-dimension χ is not closed under addition. Second, the operation of addition increases the computational complexity of any subsequent operations. For this reason, it is best to avoid the operation of addition where possible within the MPS framework. If a sequence of additions is needed in a calculation, then often we will need to compress the resulting MPS, to get a close approximation that is computationally efficient. We will discuss compression in Sec. 2.2.3.

2.2.2 MPO-MPS product

Let us examine the action of an MPO on an MPS, and the structure of the resulting MPS. Suppose we have an MPS $|\psi\rangle$, and MPO H taking the form

$$|\psi\rangle = \sum_{\vec{\sigma}} \text{Tr}\left(M^{\sigma_1} \cdots M^{\sigma_N}\right) |\vec{\sigma}\rangle \tag{2.73}$$

$$H = \sum_{\vec{\sigma},\vec{\sigma}'} W^{\sigma_1}_{\sigma_1'} \cdots W^{\sigma_N}_{\sigma_N'} |\vec{\sigma}\rangle \langle\vec{\sigma}'| . \tag{2.74}$$

Then the resulting state $|\phi\rangle = H |\psi\rangle$ takes the form

$$|\phi\rangle = H |\psi\rangle = \left[\sum_{\vec{\sigma},\vec{\sigma}'} W^{\sigma_1}_{\sigma_1'} W^{\sigma_2}_{\sigma_2'} \cdots W^{\sigma_N}_{\sigma_N'} |\vec{\sigma}\rangle \langle\vec{\sigma}'|\right]\left[\sum_{\vec{\sigma}'} M^{\sigma_1'} M^{\sigma_2'} \cdots M^{\sigma_N'} |\vec{\sigma}'\rangle\right] \tag{2.75}$$

$$= \sum_{\vec{\sigma},\vec{\sigma}'} \left[W^{\sigma_1}_{\sigma_1'} M^{\sigma_1'}\right] \cdots \left[W^{\sigma_N}_{\sigma_N'} M^{\sigma_N'}\right] |\vec{\sigma}\rangle \tag{2.76}$$

$$:= \sum_{\vec{\sigma}} \Phi^{\sigma_1} \cdots \Phi^{\sigma_N} |\vec{\sigma}\rangle \tag{2.77}$$

Where the resulting MPS tensor at site i is the product of the two tensors coming from H and $|\psi\rangle$. Let us look at the ith new tensor diagramatically

$$\tag{2.78}$$

From this image, we interpret $\gamma_i = (\alpha_i, \beta_i)$ as a super index, obtained by the tensor product of M with W. This means that the bond-dimension of $|\phi\rangle$, is the product of the bond-dimension of M and W, $\chi_\phi = \chi_M \cdot \chi_W$.

This is a striking result when contrasted against traditional representations of linear algebra using vectors and matrices. Many state of the art linear algebra algorithms are based on repetitve applications of matrix-vector multiplications, such as Krylov-subspace based methods [298]. For example, a ground state search using the Lanczos algorithm [206] can find the ground state of a Hamiltonian H accurately with on the order of $10^1 - 10^2$ applications of H on some random starting vector. However, here, if we perform N matrix multiplications with an MPO with bond-dimension χ_W, on a starting state with bond-dimension χ_M, then the resulting state will have bond-dimensions $\chi \sim O(\chi_W^N \chi_M)$, which is exponential in χ_W. For this reason, these common algorithms are not well suited for the MPS framework, and other methods are preferred.

2.2.3 Compression

Often in the MPS framework, we have an MPS with bond-dimension χ, and we wish to compress the state down to an MPS with bond-dimension $\tilde{\chi} < \chi$. One option is to perform an SVD, and only keep the $\tilde{\chi}$ largest singular values and singular vectors for a given tensor. This is often done in combination with bringing a state into a particular canonical form, as we discussed in Sec. 2.1.2. Bringing a state into, say, left canonical form requires a sequence of SVD starting with site 1, and ending on site N. While doing this, we can keep only the $\tilde{\chi}$ largest singular values at each step, effectively compressing the MPS.
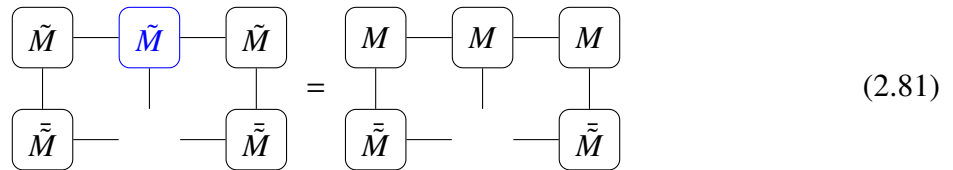
The problem with performing this sequence of SVDs with truncations is that it will propagate errors through the MPS. On the first site, there is some error from the compression, which then gets absorbed into the second tensor before performing the SVD and compressing it further. Another procedure is to say we desire a state $|\tilde{\psi}\rangle$ with bond-dimension $\tilde{\chi}$ such that $|\tilde{\psi}\rangle$ minimizes $\left\||\psi\rangle - |\tilde{\psi}\rangle\right\|^2$. We can write

$$\left\||\psi\rangle - |\tilde{\psi}\rangle\right\|^2 = \langle\psi|\psi\rangle + \langle\tilde{\psi}|\tilde{\psi}\rangle - \langle\tilde{\psi}|\psi\rangle - \langle\psi|\tilde{\psi}\rangle \tag{2.79}$$

Then the optimum would be the solution to system of equations

$$\frac{\partial}{\partial\bar{M}^{(i)}}\left[\langle\tilde{\psi}|\tilde{\psi}\rangle - \langle\tilde{\psi}|\psi\rangle\right] = 0, \tag{2.80}$$

where the derivative is interpreted element-wise. For simplicity, let us look at a system with $N = 3$, but larger N is straightforward. Diagramatically, this equation takes the form

$$\tag{2.81}$$

This can be interpreted as an equation solving for the tensor at site i $\tilde{M}^{(i)}$ shown in blue. If $\tilde{M}^{(i)}$ is removed from the left hand side, define the remainder of the network P. Define the right hand side as the three index tensor N. Then, this is equivalent to the system of equations

$$P\tilde{M}^{(i)} = N \tag{2.82}$$

which can be solved with typical linear algebra algorithms such as the conjugate gradient method.

We can simplify this, however, if we put the MPS for the state $|\tilde{\psi}\rangle$ into mixed canonical form first, with tensors A, C, B as discussed in Sec. 2.1.2. Using Eq. (2.15) and Eq. (2.18), then Eq. (2.81) would take the form

$$
\boxed{\tilde{C}} \quad = \quad \begin{array}{c} \boxed{M}-\boxed{M}-\boxed{M} \\ \boxed{\bar{\tilde{A}}} \qquad \boxed{\bar{\tilde{B}}} \end{array}, \tag{2.83}
$$

which gives $\tilde{C}^{(i)}$ directly.

In practice, we start with some initial guess for the MPS $|\tilde{\psi}\rangle$, put the state into left canonical form, and then update the first tensor using Eq. (2.83). With the updated tensor, use that to update the tensor at site two, and continue through the full network forward and backward. This process is called a *sweep*, and this idea is a common aspect of MPS algorithms. After a full sweep, you have a new updated approximation to the compressed state. Then iterate on this process until convergence is reached.

2.3 Algorithms

2.3.1 Ground State Search: Density Matrix Renormalization Group

The density matrix renormalization group (DMRG) is an algorithm for calculating the ground state of a Hamiltonian within the MPS framework. It is a variational algorithm over the set of MPSs at a fixed bond-dimension χ. In particular, we seek to solve

$$
\min_{|\psi\rangle \in \mathcal{H}_\chi} \left[\langle\psi| H |\psi\rangle - \lambda \langle\psi|\psi\rangle \right], \tag{2.84}
$$

where $\mathcal{H}_\chi$ is the manifold of states that can be represented with a bond-dimension at most χ, and the second term is a Lagrange multiplier to enforce normalization. We will convert this into a matrix equation, by differentiating one tensor at a time to get a sequence of equations. If ψ has tensor $M^{(i)}$ at site i, then we can write that the solution to Eq. (2.84) would satisfy

$$
\frac{\partial}{\partial \bar{M}^{(i)}} \left[\langle\psi| H |\psi\rangle - \lambda \langle\psi|\psi\rangle \right] = 0 \tag{2.85}
$$

where the derivative is interpreted element-wise. Diagramatically, this equation takes the form

$$
\begin{array}{c} \boxed{M}-\boxed{M}-\boxed{M} \\ \boxed{W}-\boxed{W}-\boxed{W} \\ \boxed{\bar{M}} \qquad \boxed{\bar{M}} \end{array} = \lambda \begin{array}{c} \boxed{M}-\boxed{M}-\boxed{M} \\ \boxed{\bar{M}} \qquad \boxed{\bar{M}} \end{array} \tag{2.86}
$$

We can think of the terms on both sides of the equation as linear operators acting on the tensor $M^{(i)}$ shown in blue. If $M^{(i)}$ is removed from the left side, define the remainder of the network as H_i, and similarly on the right side defining S_i, then this is equivalent to writing

$$\tilde{H}_i M^{(i)} = \lambda \tilde{S}_i M^{(i)}. \tag{2.87}$$

If we treat $M^{(i)}$ as a vector, then we can interpret this as a generalized eigenvector problem to solve for $M^{(i)}$.

Similarly to the case of compression, this expression can be simplified if we work in mixed canonical form, and expressing $|\psi\rangle$ in terms of the tensors A, C, B. This results in the following diagram equation

which simplifies Eq. (2.87) to

$$\tilde{H}_i C^{(i)} = \lambda C^{(i)} \tag{2.89}$$

which is now a simple eigenvector problem. Solving this for each site i would then produce the lowest energy state.

One subtlety is that $\tilde{H}_i$ depends on the other optimized tensors $M^{(j)}$ when contracting the network. Because of this, in practice, we sweep through the system in a manner similar to the case of compression. We start at site 1, and solve for an updated tensor $M^{(1)}$, which is used to create $\tilde{H}_2$ to update $M^{(2)}$, and then both updated tensors are used to create $\tilde{H}_3$ and so on. We continue this process through the full network forward and then backward, for a single sweep. After each sweep, we check for convergence, and stop the algorithm when the convergence criteria is met.

This local optimization procedure does not guarantee convergence to the true ground state, and can get caught in local minima. Modifications of this algorithm have been proposed to help address the local minima problem, and are discussed in Ref. [316].

2.3.2 Time Evolution: Time-Evolving Block Decimation

The problem of interest is finding a state $|\psi(t)\rangle$ given some starting state $|\psi(0)\rangle$. The starting point for this problem is Schrodinger's equation

$$i\partial_t |\psi(t)\rangle = H(t) |\psi(t)\rangle. \tag{2.90}$$

In the most general case, where H is a time-dependent Hamiltonian, without further structure, the solution takes the form

$$|\psi(t)\rangle = U(t) |\psi(0)\rangle \tag{2.91}$$

$$U(T) = \mathcal{T} \exp\left(-i \int_0^T dt\, H(t)\right) \tag{2.92}$$

where $\mathcal{T}(\cdot)$ is the time ordering operator. If we write $t_n = n\Delta t$, and $T = t_N$, then this is equivalent to writing

$$U(t) = \lim_{N \to \infty} \left[e^{-iH(t_N)\Delta t} \cdots e^{-iH(t_0)\Delta t} \right]. \tag{2.93}$$

Conceptually, this amounts to treating the Hamiltonian as piecewise constant over an interval of size Δt, and the exact time evolution is found in the limit that $\Delta t \to 0$. For finite Δt, treating the Hamiltonian as piecewise constant produces an error of order $O(\Delta t)$.

Since we can treat a time-dependent Hamiltonian as piece-wise constant, we will only look at time evolution for constant Hamiltonians. We will look at a simple and widely used approach to time evolution know as the time-evolving block-decimation (TEBD) algorithm [375, 316]. This technique is most applicable for Hamiltonians with nearest neighbor interactions, and I will only look at that case here.

We start with a general, nearest-neighbor Hamiltonian in one-dimension,

$$H = \sum_n h_{n,n+1}. \tag{2.94}$$

From here, we rearrange the Hamiltonian into two separate terms, corresponding to sums over even and odd bonds

$$H = H_O + H_E := \sum_{n\,\text{odd}} h_{n,n+1} + \sum_{n\,\text{even}} h_{n,n+1} \tag{2.95}$$

The trick is that now these two terms separately, are sums of commuting terms, even though $[H_O, H_E] \neq 0$ in general. Then we can approximate the full evolution by

$$e^{-iH\Delta t} = e^{-iH_O\Delta t} e^{-iH_E\Delta t} + O(\Delta t). \tag{2.96}$$

Higher order decompositions are also possible, leading to reduced errors [113].

Looking at the odd term, we find that

$$e^{-iH_O\Delta t} = \prod_{n\,\text{odd}} U_{n,n+1}(\Delta t) \tag{2.97}$$

$$U_{n,n+1}(\Delta t) = e^{-i\Delta t h_{n,n+1}} \tag{2.98}$$

since all the terms in H_O commute. An analogous expression is found by looking at the even term. The $U_{n,n+1}(\Delta t)$ term only acts on a single bond, and is often called a Trotter gate.

Let us look closer at applying a single Trotter gate to an MPS. Let us assume that an MPS is in mixed canonical form, where the Trotter gate is being applied to the center bond. Let us define the result of a Trotter gate as the tensor Θ which takes the form

$$
\tag{2.99}
$$

The resulting tensor Θ is a two-site wave-function. To decompose this into separate tensors for each site, we can perform an SVD resulting in

$$
\tag{2.100}
$$

yielding updated tensors $\tilde{A}, \tilde{S}, \tilde{B}$. We then can repeat this procedure for each bond to complete a full time step.

As the state time evolves, the entanglement in the system grows, and so compression often becomes necessary. This can be achieved by truncating the SVD needed in Eq. (2.100), or by performing a sweep compression after a full time step is complete ((see Sec. 2.2.3 for more details).

the TEBD algorithm can also be used to perform imaginary time evolution. In particular, calculating a state of the form

$$|\psi(\tau)\rangle = e^{-H\tau} |\psi(0)\rangle \tag{2.101}$$

This can serve as a ground state calculator by noting that

$$|\psi_0\rangle = \lim_{\tau \to \infty} e^{-H\tau} |\psi(0)\rangle . \tag{2.102}$$

The equation for a thermal state in Eq. (2.35) is of the same form, and thus TEBD can be used to calculate such a state as well.

Another useful time evolution algorithm is the time-dependent variational principle (TDVP). I will skip the technical details of this technique here, but the interested reader can learn more in Ref. [137, 135, 138, 367, 412]. One major advantage of TDVP is that it performs the time-evolution using an MPO representation of H, rather than using Trotter gates. This means that it naturally handles long-range interactions, so long as an MPO representation is available. This is especially useful when working with two-dimensional systems that are curled into a cylinder, and then mapped to quasi-one-dimensional system producing long range interactions.

2.4 Infinite MPS and Finite Entanglement Scaling

2.4.1 Infinite MPS

Often in the thermodynamic limit, the state of interest is a translationally invariant state. If this is the case, then we could represent the state with an infinite matrix product state (iMPS). An iMPS is a generalization of Eq. (2.4), where we keep track of a tensor for each site in the unit-cell, and then repeat that unit-cell everywhere. The infinite number of tensors is only considered analytically, where algorithms only keep track of a single unit-cell. For simplicity, we will assume the unit-cell is one site in the discussions here, but extending this to larger unit cells is straightforward.

Let us look at some of the operations discussed for an MPS to see how they are modified for an iMPS. We can write an iMPS as

$$|\psi(M)\rangle = \sum_{\cdots \sigma_n, \sigma_{n+1}, \cdots} \text{Tr} \left[\cdots M^{\sigma_n} M^{\sigma_{n+1}} \cdots \right] |\cdots, \sigma_n, \sigma_{n+1}, \cdots\rangle. \qquad (2.103)$$

If we have another iMPS $|\phi(N)\rangle$, then the overlap of two iMPS takes the form

$$\langle\phi(N)|\psi(M)\rangle = \qquad\qquad\qquad = \lim_{L\to\infty} \text{Tr}\left(\left[\begin{array}{c} M \\ \bar{N} \end{array}\right]^L\right). \qquad (2.104)$$

If λ_{NM} is the largest eigenvalue of the tensor in the brackets, then this expression becomes

$$\langle\phi(N)\psi(M)\rangle = \lim_{L\to\infty} \lambda_{NM}^L. \qquad (2.105)$$

Note that if the states are normalized, then $\lambda_{NM} \leq 1$. Thus, taking the limit of $L \to \infty$, we have that

$$\langle\phi(N)|\psi(M)\rangle = \begin{cases} 1 & \text{if } |\phi(N)\rangle = |\psi(M)\rangle \\ 0 & \text{otherwise} \end{cases}. \qquad (2.106)$$

This is an interesting result, saying that any two iMPS are either equal, or orthogonal.

If we wish to calculate expectation values of local observables using iMPS, then the results are identical to those found in Sec. 2.2. This is because the use of canonical forms will truncate the infinite contractions to either side of the local operators in an analogous way.

We can define an iMPO as the generalization of Eq. (2.42) to the thermodynamic limit, analogous to how we define an iMPS. Computing the expectation value of an iMPO H in the iMPS $|\psi\rangle$, this is a bit more tricky to work with. Let us assume the iMPS is in mixed canonical form, then we have

$$\langle\psi|H|\psi\rangle = \qquad\qquad\qquad\qquad\qquad\qquad\qquad\qquad\qquad. \qquad (2.107)$$

We can define the tensors L (R) as the result of the semi-infinite contraction to the left (right), and then we have

$$\langle\psi|H|\psi\rangle = \boxed{\begin{array}{c} L \end{array}}\; \boxed{\begin{array}{c} C \\ W \\ \bar{C} \end{array}}\; \boxed{\begin{array}{c} R \end{array}}\;. \tag{2.108}$$

The tensor L can be found by repeated application of the transfer matrix $A - W - \bar{A}$ until converged. However, as the number of contractions gets large, this will converge to the leading eigenvector of the transfer matrix. Thus, L can be found via

$$\boxed{\begin{array}{c} L \end{array}}\; \boxed{\begin{array}{c} A \\ W \\ \bar{A} \end{array}}\; = \; \boxed{\begin{array}{c} L \end{array}} \tag{2.109}$$

This can be solved numerically, via an eigensolver. Moreover, for specific forms of the Hamiltonian, such as local Hamiltonians with an MPO as discussed in Sec. 2.1.5, an analytical expression is known [272]. An analogous procedure can be done to compute R. With L and R, this enables constructing an effective Hamiltonian, similar to H_i in Eq. (2.86) for performing DMRG directly in the thermodynamic limit [316]. The TEBD algorithm is almost identical in the thermodynamic limit, since the Trotter gates only act on two sites at a time [316].

2.4.2 Finite Entanglement Scaling

In Sec. 2.1.3, we discussed that the bond-dimension χ for an MPS is related to the entanglement in the state that is being represented. Additionally, for gapped one-dimensional local Hamiltonians, the ground state satisfies an area-law [147], permitting exact MPS representations, even in the thermodynamic limit. However, for gapless systems, such as critical systems, the entanglement often diverges logarithmically [374]. Although this forbids an exact MPS representation, if one performs multiple simulations at different χ, then a scaling analysis is possible. This is the so called *finite entanglement scaling*, and is analogous to finite size scaling [53]. This work has been examined in depth in a series of papers [357, 277, 274], and I will discuss the highlights here.

When a system is perturbed away from criticality, it develops a length scale ξ, and the entanglement entropy scales as [47]

$$S \sim \frac{c}{6} \log \xi, \tag{2.110}$$

where c is the central charge of the conformal field theory (CFT) describing the low-energy physics of the critical theory.

Such a scaling relation seems plausible when examining how the entanglement entropy scales with the bond-dimension χ. Looking at Eq. (2.26), we have that a maximally entanglement state scales as

$$S \sim \log \chi \tag{2.111}$$

which suggests a connection between χ, and some length scale introduced, call it ξ_χ. Tagliacozzo et al. [357] found numerically that in the quantum ising model, the entropy at the critical point scaled as

$$S \sim \frac{c}{6} \log \chi^\kappa \tag{2.112}$$

with $\kappa \approx 2.011$. Matching this with Eq. (2.110), we find

$$\xi_\chi \sim \chi^\kappa. \tag{2.113}$$

This result suggests that the effect of finite χ when representing the critical ground state is to effectively introduce a length scale ξ_χ into the problem, analogous to finite-size scaling, or the effect of a relevant perturbation.

A followup by Pollman et al. [277] used general results about CFT to pin down the exponent κ, conjecturing that

$$\kappa = \frac{6}{c \left[\sqrt{\frac{12}{c}} + 1 \right]}. \tag{2.114}$$

Combining Eq. (2.112) and Eq. (2.114) yields

$$S = \frac{1}{\sqrt{\frac{12}{c}} + 1} \log \chi, \tag{2.115}$$

which they verified numerically in several critical spin chains.

These results suggest that representing a critical state with an MPS at finite χ has an effect analogous to a relevant perturbation, introducing a length scale $\xi_\chi \sim \chi^\kappa$, and κ only depends on the central charge c of the critical theory. This both provides a means to extract the central charge through such a finite entanglement scaling analysis, as well as provides a means to extrapolate to the $\chi = \infty$ result. I will discuss these ideas further in a dynamical context for a Kibble-Zurek process in Chapter 5.

Chapter 3

Kardar-Parisi-Zhang Hydrodynamics in the Heisenberg Spin Chain

In this chapter, I discuss a form of emergent hydrodynamics in one-dimensional quantum magnets, known as Kardar-Parisi-Zhang (KPZ) hydrodynamics. In particular, KPZ hydrdoynamics is present in the spin transport of the one-dimensional spin-1/2 Heisenberg model at high temperatures. This model is one of the most well studied models of a quantum magnet, and yet the emergence of such an anomalous spin transport remained unnoticed until recently [229]. Typically, the high temperature regime behaves classically, as the thermal fluctuations tend to drown out any present quantum fluctuations. However, in the classical Heisenberg spin chain, where the spins are modelled by unit vectors, the spin transport is governed by diffusion rather than KPZ. Moreover, at low temperatures, this model is governed by the Tomonaga-Luttinger liquid (TLL) theory [142, 119], which does not exhibit KPZ hydrodynamics. This makes the presence of KPZ hydrodynamics, in the spin-1/2 Heisenberg model at high temperatures, surprising, and fundamentally a quantum phenomena.

In Sec. 3.1, I discuss the signatures of KPZ hydrdoynamics in the neutron scattering cross-section. I then discuss a collaboration with the neutron scattering group at Oak Ridge National Lab to detect these signatures experimentally in the material $KYbSe_2$. In Sec. 3.2, I discuss the crossover between the TLL physics exhibited at low temperatures, and the recently discovered high temperature KPZ hydrodynamics.

3.1 Detection of Kardar-Parisi-Zhang hydrodynamics in a quantum Heisenberg spin-$1/2$ chain

3.1.1 Introduction

Classical hydrodynamics is a remarkably versatile description of the coarse-grained behavior of many-particle systems once local equilibrium has been established [207]. The form of the hydrodynamical equations is determined primarily by the conserved quantities present in a system. Some quantum spin chains are known to possess, even in the simplest cases, a greatly expanded

set of conservation laws, and recent work suggests that these laws strongly modify collective spin dynamics even at high temperature [54, 30]. Here, by probing the dynamical exponent of the one-dimensional Heisenberg antiferromagnet $KCuF_3$ with neutron scattering, we find evidence that the spin dynamics are well described by the dynamical exponent $z = 3/2$, which is consistent with the recent theoretical conjecture that the dynamics of this quantum system are described by the Kardar-Parisi-Zhang universality class [190, 229]. This observation shows that low-energy inelastic neutron scattering at moderate temperatures can reveal the details of emergent quantum fluid properties like those arising in non-Fermi liquids in higher dimensions.

Interacting magnetic moments ("spins") governed by the laws of quantum mechanics can exhibit a vast set of complex phenomena such as Bose-Einstein condensation and superfluidity [121], topological states of matter [143], and exotic phase transitions [300, 103]. Understanding quantum magnets is therefore a challenging task, connecting experiments with intensive theoretical modeling and state-of-the-art numerical simulations. In that respect, linear arrangements of spins ("spin chains") at temperatures close to absolute zero have been influential because the one-dimensional (1D) setting produces especially prominent quantum fluctuations [120].

The most celebrated model magnetic system realized in nature is the Heisenberg spin-half chain, where isotropic magnetic moments are coupled by a nearest-neighbor antiferromagnetic exchange interaction of strength J. It is characterized by fractional quasiparticles excitations called spinons (Fig. 3.1b) with a dispersion relation given by $\hbar\omega(Q) = J\frac{\pi}{2}|\sin(Qa)|$, where a is the lattice spacing unit (following convention for 1D chains, we set $a = 1$ in this study). They are responsible for the physical properties of the system and can be identified by the dynamical spin response function, as measured in inelastic neutron spectroscopy. Spinons are created in pairs, leading to a continuum in the neutron scattering spectrum, and interact with one another. In fact, in the ground state, two-spinon states accounting for 71% of the total spectral weight have an upper bound $\hbar\omega(Q) = J\pi|\sin(Q/2)|$, which gives its distinctive shape to the spectrum (Fig. 3.2a), and including the four-spinon contribution on top of the two-spinon exhausts 98% of the weight [55], etc.

As temperature increases and many spins are excited, the spin dynamics at frequencies $\hbar\omega \ll k_B T$ is usually thought of in terms of collective thermal rather than quantum effects. This high-temperature regime has not been the focus of experimental study, but recent theoretical progress in 1D quantum systems suggests that it nevertheless holds precious information on the underlying quantum features [54, 30, 45]. One can make an analogy with the phenomenological derivation of the equations of fluid dynamics, based on the continuity equations of conserved quantities (such as mass, energy, or momentum): depending on the intrinsic quantum conservation laws of the system, one expects the emergence of different kinds of coarse-grained hydrodynamic behaviors for the spins at high-temperature. Remarkably, some 1D quantum systems, known as integrable — including the Heisenberg spin-half chain — possess an infinite number of nontrivial conserved quantities. They strongly constrain the overall dynamics of integrable systems and can endow them with peculiar hydrodynamic properties, some of which have been observed experimentally in a 1D cloud of trapped ^{87}Rb atoms [314]. In the case of magnets, three universal regimes have been identified [92, 83] and are classified by the dynamical exponent z, governing the length-time
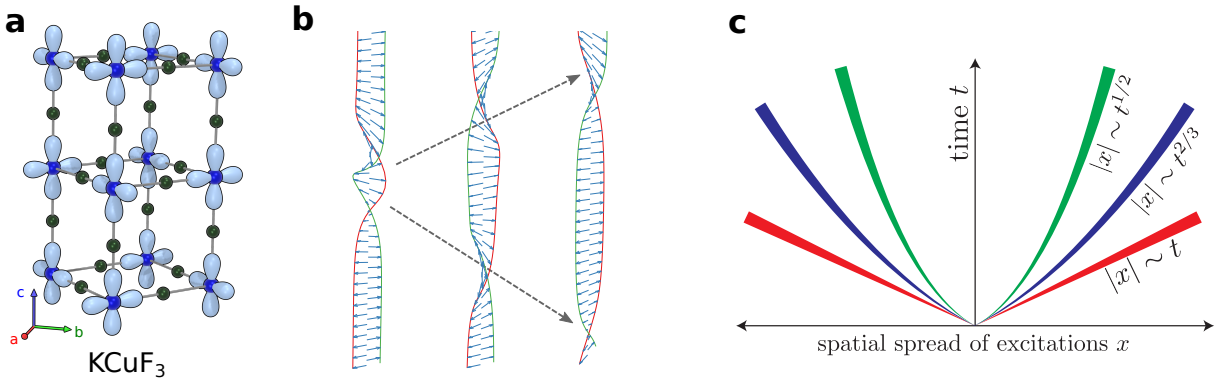
Figure 3.1: 1D physics in $KCuF_3$. **a** Crystal structure of $KCuF_3$, showing the orbital order of the Cu $x^2 - y^2$ orbitals. This order leads to strong magnetic exchange interactions along the c (vertical) axis and weak exchange interactions along a and b, such that the Cu^{2+} ions effectively make 1D chains. **b** Schematic illustration of spinon excitations in a 1D Heisenberg antiferromagnet (based on Ref. [143]). **c** Schematic illustration of three possible length-time scaling behaviors $|x| \sim t^{1/z}$ observed at high temperature in 1D quantum magnets, classified by the dynamical exponent z: $z = 2$ corresponds to diffusion (green curve), $z = 3/2$ to superdiffusive (blue curve) and $z = 1$ to ballistic dynamics.

scaling, i.e., LENGTH $\sim$ TIME$^{1/z}$: $z = 2$ corresponds to diffusion, $z = 1$ to ballistic, and $z = 3/2$ to superdiffusive dynamics (Fig. 3.1c).

The presence of ballistic spin dynamics in integrable systems is theoretically established by showing that at least part of the spin current $\hat{j}_s$ in an initial state persists to infinite time, resulting in an infinite spin dc conductivity. Quantitatively, this can be achieved by looking at the long-time asymptote of the spin current-current correlation $\lim_{t \to \infty} \langle \hat{j}_s(t) \hat{j}_s(0) \rangle$, where saturation to a nonzero value signals ballistic spin transport and a nonzero Drude weight. Although challenging for many-body quantum systems, the Drude weight can be accessed numerically [191] and a lower bound can often be obtained analytically [438, 282]. Diffusive behavior, one of the other universal regimes, is typically recovered for systems with zero Drude weight, which implies eventual relaxation of spin currents and finite transport coefficients. Unexpectedly, an intermediate scenario was recently unveiled [172, 229, 127, 80]: a zero Drude weight but a slowly decaying (typically algebraically with time) spin current-current correlation, giving rise to superdiffusive dynamics with $z = 3/2$. The intermediate scenario was found numerically [229] by calculation of the full scaling function to belong to the Kardar-Parisi-Zhang (KPZ) universality class in 1+1 dimension, reproduced in Sec. 3.3.2; a theoretical scenario for how KPZ dynamics emerges in the Heisenberg chain has been proposed [44].

This universality class originates from the classical non-linear stochastic partial differential equation of the same name [190], initially introduced to describe the evolution in time of the profile of a growing interface. Generally speaking, a system is considered to be in the KPZ universality class
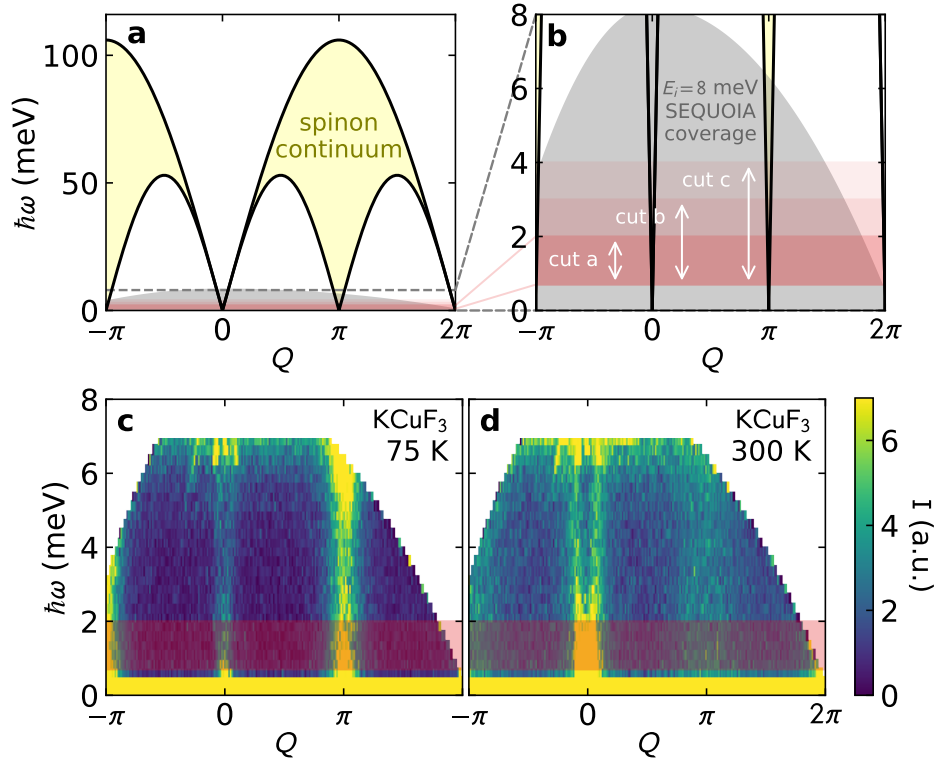
Figure 3.2: Measured neutron spectrum of $KCuF_3$. **a** Cartoon of the $KCuF_3$ spinon spectrum. The gray region at the bottom shows the region measured. **b** Zoom in on the region measured in the SEQUOIA experiment, also showing three cuts (cut a, cut b, and cut c) used to approximate the $\hbar\omega \to 0$ scattering. **c** and **d** show measured spectra at 75 K and 100 K, respectively. Cut a is indicated by the horizontal red bar. It is not possible to directly measure the magnetic scattering at $\hbar\omega \to 0$ due to the strong elastic incoherent scattering. Therefore, we take the lowest energy cuts where magnetic scattering dominates, cut a, as shown in Fig. 3.4.

if its long-time dynamics shows the same scaling laws as appear in the KPZ equation itself. Besides interface growth [358], such scaling has been found in disordered conductors [343], quantum fluids [203], quantum circuits [252], traffic flow [122], and was recently predicted also to appear in the high-temperature dynamics of some one-dimensional integrable quantum magnets [229, 80, 92, 83], although its exact microscopic origin is still under active research in this case.

Here, using neutron scattering experiments on $KCuF_3$[1] , which realizes a nearly ideal quantum Heisenberg spin-half chain, we report on the observation of KPZ dynamics at various temperatures in the range $T = 75$ K to $T = 300$ K. Combining experimental measurements with extensive numerical simulations based on a microscopic description of the system, we identify a characteristic

---

[1]The experiments of $KCuF_3$ were conducted by my collaborators at Oak Ridge National Lab. See Ref. [308] for more information about the researchers and their contributions.

power-law $\propto Q^{-3/2}$ behavior in the neutron scattering spectrum, in agreement with the KPZ universality class predictions [280].

3.1.2 Methods

Here I will discuss the methods used to perform the numerical simulations. Additional information about the experimental setup can be found in Sec. 3.3.1. The numerical simulations are based on a matrix product state (MPS) method [316] using the ITensor library [108] to simulate the finite-temperature spin dynamics of the 1D quantum Heisenberg spin-half chain of Eq. (3.6). We use the purification method to represent the finite-temperature quantum state $\hat{\rho}_T$ (mixed state) as a pure state $|\psi_T\rangle$ in an enlarged Hilbert space [370]. The construction of $|\psi_T\rangle$ is done using the time-evolving block decimation (TEBD) algorithm [375] along with a fourth order Suzuki-Trotter decomposition [113]. Details about constructing $|\psi_T\rangle$ and the TEBD algorithm can be found in Chapter 2.

When the state $|\psi_T\rangle$ is obtained and normalized such that $\langle\psi_T|\psi_T\rangle = 1$ (this corresponds to setting the partition function of the system to 1), we use a method expanding the desired spectral function $\mathcal{S}(Q, \omega)$ in terms of Chebyshev polynomials [157, 390]. The dynamics is generated by the Louivillian operator $\hat{\mathcal{L}} = \hat{\mathcal{H}}_\mathsf{P} \otimes \hat{I}_\mathsf{Q} - \hat{I}_\mathsf{P} \otimes \hat{\mathcal{H}}_\mathsf{Q}$, i.e., the dynamical structure factor is expressed directly in frequency space as [20, 362],

$$\mathcal{S}(Q, \omega) = \left\langle \hat{\boldsymbol{S}}_{-Q} \delta\left(\hbar\omega - \hat{\mathcal{L}}\right) \cdot \hat{\boldsymbol{S}}_Q \right\rangle, \tag{3.1}$$

with the momentum space spin operators defined by,

$$\hat{\boldsymbol{S}}_Q = \sqrt{\frac{2}{L+1}} \sum_{r=1}^{L} \sin(Qr)\hat{\boldsymbol{S}}_r, \tag{3.2}$$

with L the total number of spins in the system with lattice spacing taken equal to unity; r labels the spin index on the chain. Because MPS are more efficient at simulating systems with open boundary conditions, we have used a slightly different version of the Fourier transform in the above equation compared to the usual definition [25]; both are equivalent in the thermodynamic limit $L \to +\infty$. Here, the allowed momentum by the finite-length geometry are $Q = k\pi/(L+1)$ with $k = 1, 2, \ldots, L$. Because the Heisenberg model is isotropic with respect to the different spin components, we can make the substitution $\langle\hat{\boldsymbol{S}}_{-Q}\delta(\omega - \hat{\mathcal{L}}) \cdot \hat{\boldsymbol{S}}_Q\rangle \to 3\langle\hat{S}^\alpha_{-Q}\delta(\omega - \hat{\mathcal{L}})\hat{S}^\alpha_Q\rangle$ and only compute the dynamics associated with the $\alpha \in [x, y, z]$ spin component. In practice we choose $\alpha \equiv z$, and ignore the factor of 3 as the overall scale is adjusted to compare with experiments whose spectral intensity is in arbitrary units (a.u.).

To compute the spectral function numerically, we expand the delta function of Eq. (3.1) in a Chebyshev series [157, 390]. An expansion in Chebyshev polynomials, $T_n(x) = \cos\left[n \arccos(x)\right]$, is only permitted for $x \in [-1, 1]$. Thus, we rescale the spectrum of $\hat{\mathcal{L}}$ and ω by an amount W to ensure that the spectral function $\mathcal{S}(Q, \omega)$ is only non-zero in the range $\omega \in [-1 + \epsilon, 1 - \epsilon]$. Using a small $\epsilon > 0$ helps with numerical stability. The rescaled quantities are defined by,

$$\hat{\mathcal{L}}' = \hat{\mathcal{L}}/W, \quad \omega' = \omega/W. \tag{3.3}$$

Then, the dynamical structure factor is written

$$S(Q, \omega) = \frac{1}{W\pi\sqrt{1 - \omega'^2}} \sum_{n=0}^{\infty} (2 - \delta_{n0})\mu_n(Q)T_n(\omega'), \tag{3.4}$$

with $\mu_n(Q) = \langle t_0|t_n\rangle$ the Chebyshev moments and $|t_n\rangle = T_n(\hat{\mathcal{L}}')\hat{S}_Q^z|\psi_T\rangle$ the Chebyshev vectors. They can be calculated iteratively by

$$|t_n\rangle = 2\hat{\mathcal{L}}'|t_{n-1}\rangle - |t_{n-2}\rangle, \tag{3.5}$$

with $|t_0\rangle = \hat{S}_Q^z|\psi_T\rangle$ and $|t_1\rangle = \hat{\mathcal{L}}'|t_0\rangle$ as a starting point. For comparison between experiments and numerical simulations, we use a system size of $L = 128$ spins, a bond dimension $\chi = 256$, and the order of the Chebyshev expansion is $N = 3000$. We chose $W = L/2(1 - \epsilon)$ together with $\epsilon = 0.0125$ for this work.

3.1.3 Searching for Kardar-Parisi-Zhang Hydrodynamics

$KCuF_3$ has long been studied as a model of 1D Heisenberg antiferromagnetism with $S = 1/2$ spins borne by Cu^{2+} ions [152, 360, 204]. Due to the Cu^{2+} $d_{x^2-y^2}$ orbital order (Fig. 3.1a), the magnetic exchange interaction is limited to nearest-neighbor spins and is spatially anisotropic. It is dominant along the c axis ($J_c = 33.5$ meV) while the interchain coupling is much weaker ($J_{a,b} = -1.6$ meV), leading to effective one-dimensional c axis spin-half chains. Although the system magnetically orders at $T_N = 39$ K due to the inherent presence of a finite exchange interaction $J_{a,b}$, its behavior for $T \gtrsim T_N$ is a good approximation to an ideal 1D Heisenberg antiferromagnet which can be modeled by the following Hamiltonian,

$$\hat{\mathcal{H}} = J_c \sum_n \hat{\boldsymbol{S}}_n \cdot \hat{\boldsymbol{S}}_{n+1}, \tag{3.6}$$

with $\hat{\boldsymbol{S}}_n$ the spin-1/2 operator on the site index n.

At equilibrium, the spin dynamics can be characterized through the correlation function between two spatially separated spins at different moments in time, and whose Fourier transform to momentum and frequency spaces is the dynamical spin structure factor $\mathcal{S}(Q, \omega)$. This quantity is directly proportional to the measured inelastic neutron scattering intensity, and can be computed numerically for the model (3.6) using matrix product state (MPS) techniques (See Sec. 3.1.2), allowing for a direct comparison between theory and experiments. Especially, the universal dynamical exponent z is expected to manifest itself in the form [280],

$$\mathcal{S}(Q, \omega \to 0) \sim Q^{-z}, \tag{3.7}$$

in the limit of small momentum Q and vanishing energy $\hbar\omega$, with KPZ behavior identified by $z = 3/2$.
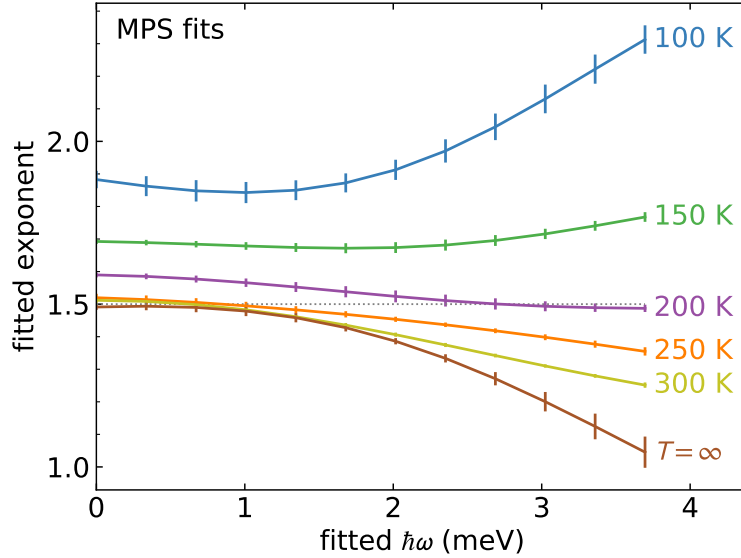
Figure 3.3: Deviations from $Q^{-3/2}$ KPZ behavior at finite temperature and finite energy transfer. Each curve shows the fitted exponent for the MPS simulated low-Q scattering as a function of energy. At infinite temperature and $\hbar\omega = 0$, the exponent is $-3/2$. As temperature decreases, the exponent generally increases. However, above 200 K, the KPZ behavior is still dominant. Error bars indicate one standard deviation.

The simple scaling behavior of Eq. (3.7) is only exact as $\hbar\omega \rightarrow 0$. However, elastic incoherent scattering prevents the experiment from isolating the magnetic scattering at $\hbar\omega \rightarrow 0$, so we take the $0.7 < \hbar\omega < 2$ meV scattering to be an approximation to the $\hbar\omega \rightarrow 0$ spectrum. To evaluate the robustness of this approximation, we consider three different energy ranges with $\hbar\omega > 0.7$ meV (this is empirically where elastic incoherent scattering background is negligible), as indicated in Fig. 3.2. Due to this experimental limitation, we examine the effect of the power-law behavior within this energy range using MPS simulations. We still find a power-law region in the MPS simulations, and we examine how the exponent depends on the energy window used, as well as the temperature in Fig. 3.3. The main take away from this is that, for temperatures of 200 K and above, the exponent drops as the frequency window increases, and as $\hbar\omega \rightarrow 0$, the $z = 3/2$ exponent is recovered. Therefore an exponent close to, but lower than, $z = 3/2$ would be consistent with KPZ scaling.

3.1.4   Results

A quantitative test to distinguish different kinds of hydrodynamics is the scattering intensity behavior at small energy versus Q near the ferromagnetic wavevector $Q = 0$, see Eq. (3.7). We first compare these data to MPS simulations integrated over the same energy range in Fig. 3.4. There is a very good agreement between the two, with deviations only appearing at the low temperature (mainly 75 K). This discrepancy is attributed to the inherent interchain couplings (not present in the pure
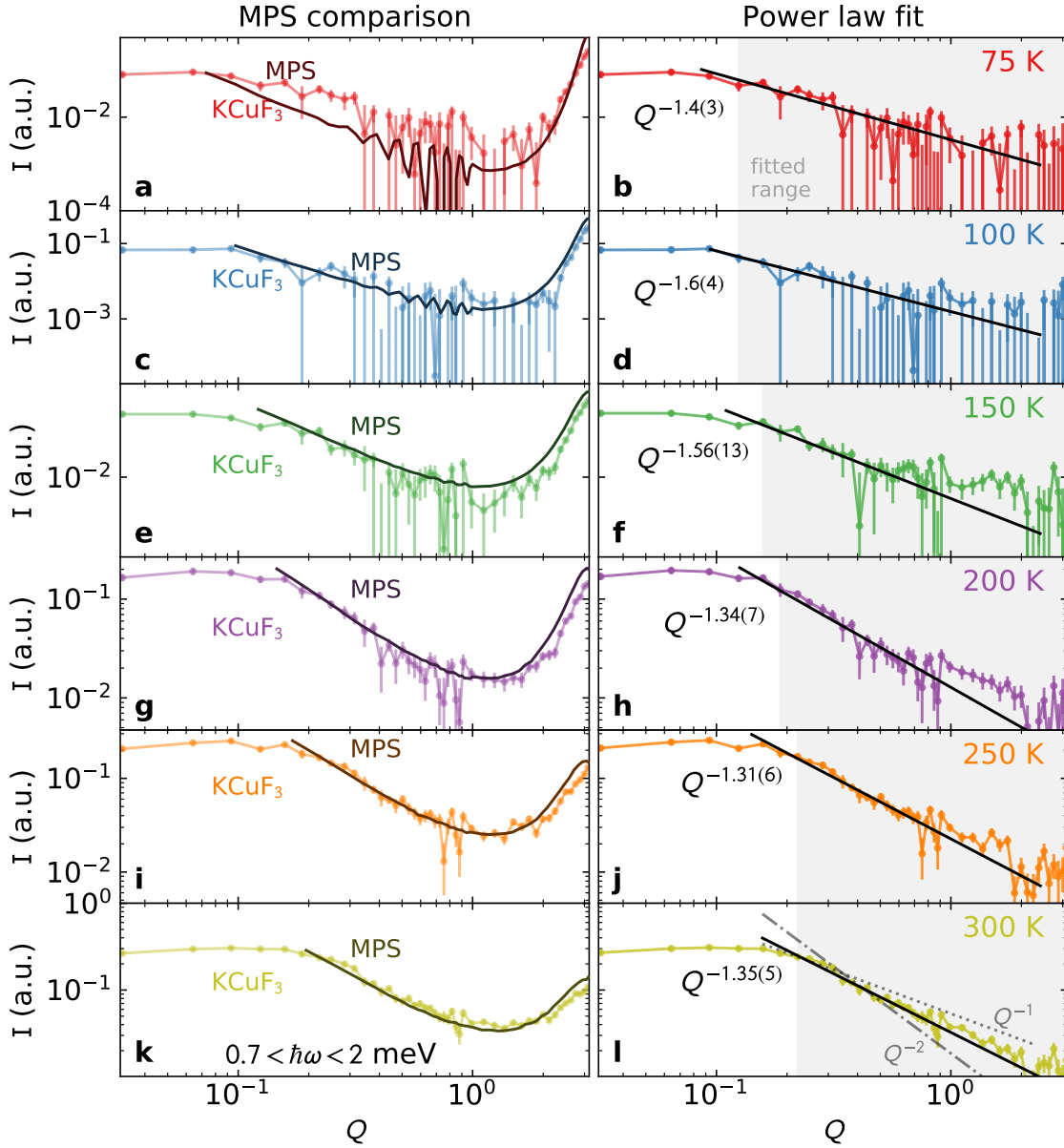
Figure 3.4: Power law behavior of $KCuF_3$ around $Q = 0$. The left column shows experimental data integrated over $0.7 < \hbar\omega < 2$ meV (cut a in Fig. 3.2) symmetrized about $Q = 0$ compared with the MPS simulations. The same multiplicative scaling factor is used for all temperatures, and the agreement is quite good above $Q \approx 0.2$, below which finite-size effects are significant for MPS (see Sec. 3.3.2). The right column shows the data fitted to a phenomenological power law. As a part of the fit, the $Q = \pi$ peak was also fitted to a power law and subtracted off as background. The fitted power is very close to $-3/2$ at all temperatures. Comparison to $z = 2$ and $z = 1$ exponents are given in panel l. (Note that Q is unitless $0 \to 2\pi$ as in Fig. 3.2.) Error bars indicate one standard deviation.

1D model), and which lead to antiferromagnetic ordering at $T_N = 39$ K. In fact, it was theoretically shown [94] that for dynamical quantities, the 1D temperature crossover in quasi-one-dimensional systems such as $KCuF_3$ is spoiled for $T \lesssim 3T_N$. Furthermore the spectral intensity at low-energy in a strictly 1D system away from $Q \to \pm 0$ and $\pm \pi$ is greatly suppressed with temperature, making an accurate estimation from numerical simulations difficult; hence the non-physical oscillatory behavior in the MPS data of Fig. 3.4 at 100 K and 75 K for intermediate Q values. The $Q \lesssim 0.1$ experimental data deviates from power law behavior, partly because of Q resolution broadening, and partly because of the dispersion peaking away from $Q = 0$ at finite energy. Moreover, the numerical simulations do not allow us to reliably access the $Q \lesssim 0.2$ regime: this is because simulations are performed on finite-length chains (typically a hundred spins on the lattice) which introduces an artificial cutoff at low Q as $\hbar\omega \to 0$ when it comes to the dynamics, as compared to a system in the thermodynamic limit (see Sec. 3.3.2 for more details).

Having identified the temperature window where 1D physics take place, we consider in Fig. 3.4 the same experimental data from which a phenomenological $Q = \pi$ power-law background is subtracted. This highlights the $Q \to 0$ regime, where power-law fits of the form $\propto Q^{-z}$ give an exponent close to $z \approx 1.5$ at all temperatures. Note that fits without this phenomenological background yield results which are equivalent to within uncertainty, and are discussed further in the Appendix 3.3.1. (Also note that experimental resolution broadening increases the fitted power by 2-3%, also shown in Sec. 3.3.1, so the true 300 K exponent may be closer to $Q^{-1.31(5)}$). This correction notwithstanding, the fitted exponent, while not $Q^{-3/2}$ exactly, is clearly closer to that value than to either Q^{-1} (ballistic) or Q^{-2} (diffusive). See Fig. 3.4l for a comparison between the three cases. At $T = 300$ K, the discrepancy between the expected $Q^{-3/2}$ behavior and the experimental fit $Q^{-1.35(5)}$ can be explained by the fact that we are not measuring at exactly $\hbar\omega = 0$. This effect is experimentally unavoidable, and we thus consider our experimental results, in conjunction with a comprehensive numerical study observing the same trend, to be clearly more consistent with the KPZ universality class behavior than either of the conventional possibilities, ballistic or diffusive behavior. A different experiment (e.g., with polarized neutrons or a spin-echo spectrometer) may be able to measure the magnetic scattering at the elastic line.

In measuring the low-energy $KCuF_3$ neutron spectrum, we also noticed a previously unreported feature, shown in Fig. 3.5: as temperature increases, the dispersion around $Q = 0$ softens. In other words, the split between $\pm Q$ modes increases, showing a decreased dispersion velocity: 190(20) meV·Å at 100 K (within uncertainty of the theoretical $T = 0$ velocity 207 meV·Å) to 84(9) meV·Å at 300 K. This feature is also captured by the MPS simulations, as shown in Fig. 3.5g-l. This temperature dependent mode softening has not been noticed before, and indicates that the excitation velocity is renormalized by interaction with other quasiparticles; such spin wave velocity renormalization also exists in the two-dimensional quantum Heisenberg antiferromagnet.[56] We leave it an open question whether this mode softening may relate to KPZ physics or be an apparent shift from broadening by material-dependent damping.
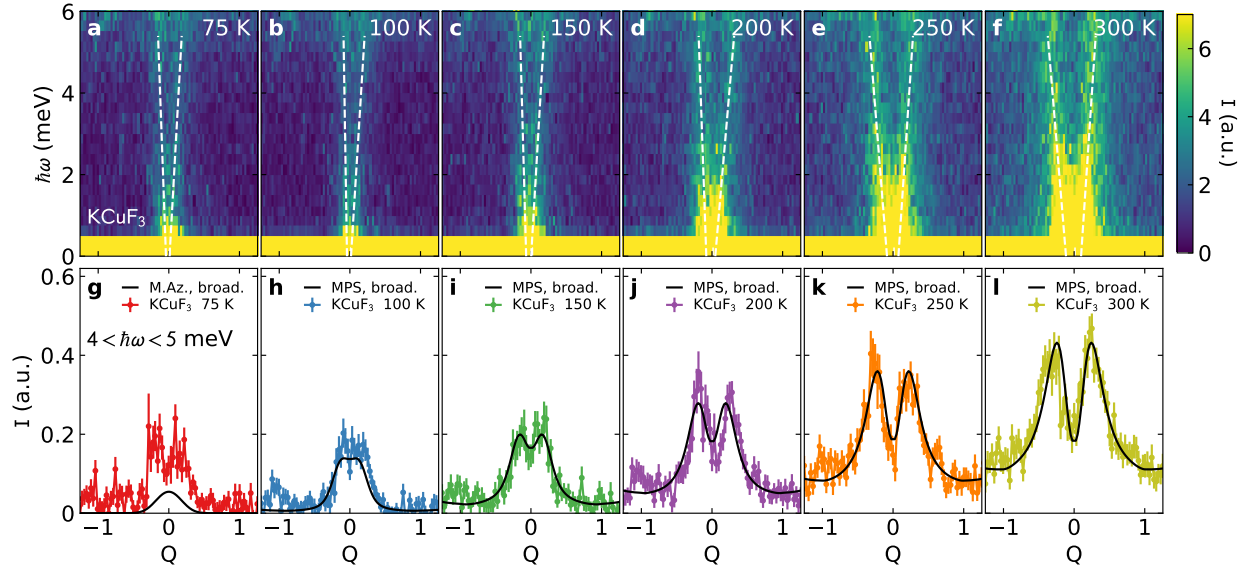
Figure 3.5: Temperature evolution of the KCuF$_3$ neutron spectra around $Q = 0$. (Q units are defined in Fig. 3.2.) Panels **a** - **f** show colormap plots of the spectra (white dashed lines are fitted linear dispersions), and panels **g** - **l** show constant energy cuts of $4 < \hbar\omega < 5$ meV. The lower panel also includes theoretical curves for comparison. (Panel **g** shows the zero-temperature Müller ansatz [250] scaled to match the $Q = \pi$ intensities, the rest show the MPS calculations. Resolution broadening has been applied to the theoretical curves, see Sec. 3.3.2 for details.) These show the spinon modes splitting more as temperature increases, indicating a significant mode softening. Error bars indicate one standard deviation.

3.1.5 Conclusion

Our results experimentally show the presence of KPZ-like physics in KCuF$_3$, characterized by the dynamical exponent $z = 3/2$. The observation of this superdiffusive scaling in the high-temperature dynamics of a Heisenberg chain demonstrates that inelastic neutron scattering can complement transport as a probe of quantum coherent collective phenomena, even when those phenomena do not have an interpretation in terms of a small number of quasiparticles. In some situations transport measurements are prohibitively difficult, like in many non-chiral 1D systems where even trace impurities or small defects simply interrupt macroscopic transport. In such cases, neutron scattering can probe subtle fluid properties where the dynamical exponent z around the low-energy dispersion reveals the nature of the collective quasiparticle flow.

In higher dimensions, this approach can provide insight into analogues of non-Fermi liquid scaling and other behaviors hypothesized to exist from transport, with the advantage of an increased degree of quantum coherence and a precise characterization of the model Hamiltonian. In one dimension, this work goes significantly beyond previous efforts with other techniques to see generalized hydrodynamics from integrability by revealing a different scaling regime. Theoreti-

cally, there remain important questions to be understood, such as how to characterize the crossover regime when integrability is broken by interchain couplings or other residual interactions (discussed further in Sec. 3.2). In particular, there are spin chains where the field-theory description at low temperatures shows emergent integrability but the lattice-scale physics is not integrable, unlike for the Heisenberg model, and it should be possible to apply our combined experimental and computational approach to this category of systems as well.

3.2 Spatiotemporal Crossover Between Low- and High-Temperature Dynamical Regimes in the Quantum Heisenberg Magnet

3.2.1 Introduction

At low temperatures, reduced spatial dimensionality greatly enhances quantum fluctuations in physical systems, giving rise to exotic properties. In that regard, one-dimensional (1D) quantum many-body systems have always been influential and generically fall into two classes [142, 119]: on the one hand, gapless low-energy excitations described in the framework of Tomonaga-Luttinger liquid (TLL), and on the other, a gapped behavior. Theoretical predictions have been intensively checked by experiments in various contexts, ranging from ultracold atom setups to quantum magnets [118, 388].

At energy $\hbar\omega \ll k_{\mathrm{B}}T$, the physics is usually thought of in terms of thermal rather than quantum effects. This regime had not been thought to hold phenomena as compelling as its low-temperature counterpart until very recently. Indeed, recent theoretical progress suggests that the equilibrium and out-of-equilibrium dynamics of some 1D quantum systems can exhibit peculiar behaviors and contain information about the intrinsic quantum features, even at very high temperatures [30, 54, 45].

While such many-particle systems are governed at the microscopic level by the Schrödinger equation, they display in the long-time and long-wavelength limits an emergent coarse-grained hydrodynamic behavior. An analogy can be made with classical fluid dynamics: one does not describe individual particles with Newton's laws of motion but relies instead on phenomenological continuous differential equations, ideally more amenable. The derivation of hydrodynamic equations is based essentially on continuity equations of conserved quantities (e.g., mass, energy, etc.), assuming local equilibrium [207].

Quantum systems also possess conservation laws, and depending on those, one expects the emergence of different kinds of coarse-grained hydrodynamic descriptions. Singularly in 1D, a class of quantum systems—known as integrable—has an infinite set of nontrivial conserved quantities that can lead to anomalous dynamical behaviors [438, 339, 340, 282, 437, 192, 171, 30, 54, 45, 79, 129, 254, 9, 229, 80, 127, 9, 128, 92, 83, 82, 111, 10, 173, 44, 29, 231, 81, 308].

Integrable systems are typically described by very fine-tuned models but some of them can be reliably realized in the lab (e.g., the Lieb-Liniger model representing a gas of one-dimensional bosons with contact repulsion [226, 225]) and found with high fidelity in nature (e.g., the spin-1/2 Heisenberg chain of magnetic moments coupled by a nearest-neighbor exchange interaction [119]). In that context, some of the theoretical predictions have been successfully tested on 1D cloud of trapped ^{87}Rb [314, 239] and ^{7}Li [184] atoms for out-of-equilibrium dynamics and by neutron scattering on the quantum magnet $KCuF_3$ at thermal equilibrium [308].

In the case of quantum magnets, it has been numerically conjectured, based on microscopic simulations, that in the limit of infinite temperature, the spin dynamics of the $S = 1/2$ Heisenberg chain is anomalous and belongs to the Kardar-Parisi-Zhang (KPZ) universality class in $1 + 1$ dimensions [190, 229]. It is characterized by a dynamical exponent $z = 3/2$, controlling the length-time scaling of the dynamical properties. This exponent has been recently observed in the high-temperature neutron spectrum of $KCuF_3$ [308] (discussed in Sec. 3.1), which is directly proportional to the dynamical structure factor, probing spin-spin correlations.

Here, we seek to reconcile the low-temperature physics of the $S = 1/2$ Heisenberg chain, falling within the gapless TLL category, with the recently found infinite-temperature KPZ hydrodynamics. Whereas both regimes have been studied independently, no work has attempted to bring them together. We precisely define the long-time and long-wavelength limits for the emergence of anomalous dynamics versus the temperature. We find that these limits define a spatiotemporal crossover beyond which hydrodynamics take place. As the temperature is lowered, the crossover is pushed toward infinity and eventually disappears at exactly zero temperature, see Fig. 3.6. This scenario allows one to recover the well-known zero temperature results where KPZ hydrodynamics is absent. Moreover, because experimental dynamical condensed matter probes such as neutron scattering or nuclear magnetic resonance (NMR) work for all practical purposes at a finite frequency and finite temperatures, it is paramount to better understand and quantitatively define the theoretical limits. We discuss the implication of our results for experiments and confront our findings to earlier high-temperature NMR experiments on the nearly ideal Heisenberg spin-1/2 compound Sr_2CuO_3 [361].

3.2.2 Model and Method

The 1D spin-1/2 Heisenberg model is described by the lattice Hamiltonian,

$$\hat{\mathcal{H}} = J \sum_j \hat{\boldsymbol{S}}_j \cdot \hat{\boldsymbol{S}}_{j+1}, \tag{3.8}$$

with $\hat{\boldsymbol{S}}_j = (\hat{S}_j^x, \hat{S}_j^y, \hat{S}_j^z)$ and $J > 0$ the nearest-neighbor antiferromagnetic exchange. To investigate the thermal equilibrium spin dynamics, we consider the time-dependent spin-spin correlation function

$$C(T, x, t) = \text{tr}\left[\hat{\boldsymbol{S}}_x(t) \cdot \hat{\boldsymbol{S}}_0(0) \, \hat{\rho}_T\right] \in \mathbb{C}, \tag{3.9}$$
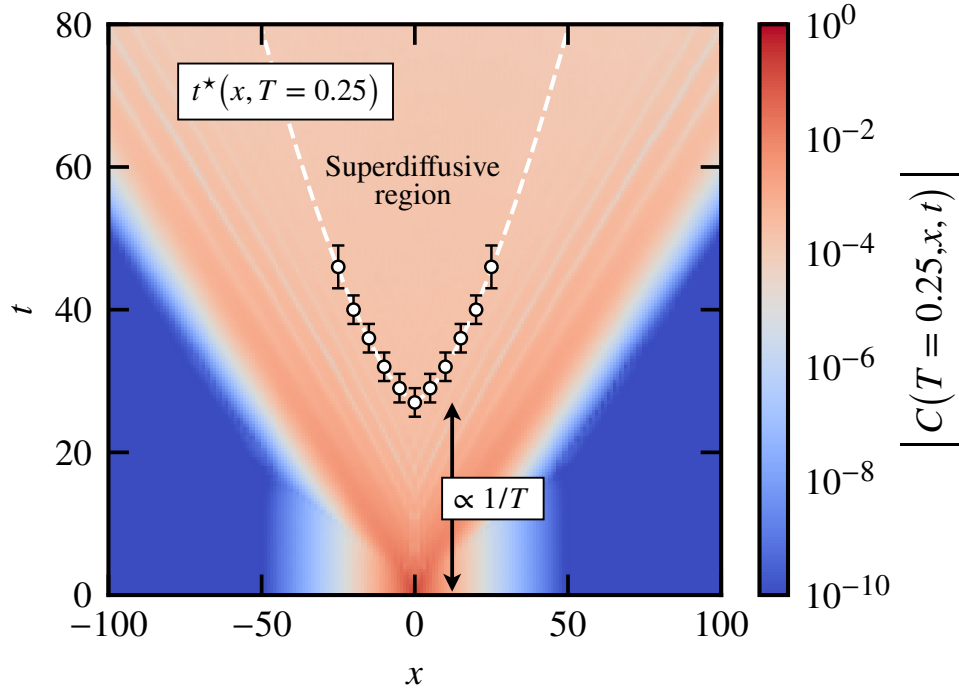
Figure 3.6: Log-scale intensity plot of the Euclidean norm of the spin-spin correlation (3.9) at $T = 0.25$. Simulation obtained for $L = 256$ with $\chi = 1024$. The goal of this Letter is to determine and study the superdiffusive region delimited by the spatiotemporal crossover $t^\star$ of Eq. (3.10) versus the temperature (white circles and dashed white line). As the temperature is decreased, we find that the superdiffusive region is shifted vertically to longer and longer times by a factor $\propto 1/T$, and eventually disappears at exactly zero temperature.

with $\hat{\rho}_T = \mathrm{e}^{-\hat{\mathcal{H}}/k_\mathrm{B}T}/\mathrm{tr}(\mathrm{e}^{-\hat{\mathcal{H}}/k_\mathrm{B}T})$ as the thermal density matrix of the system at temperature T and $\hat{S}_j(t) = \mathrm{e}^{i\hat{\mathcal{H}}t/\hbar}\hat{S}_j\mathrm{e}^{-i\hat{\mathcal{H}}t/\hbar}$ as the time-dependent spin operator in the Heisenberg picture. We set $J = k_\mathrm{B} = \hbar = 1$ in the following. We compute the correlation function (3.9) based on a numerical matrix product state (MPS) approach [315, 108], where we represent the mixed state as a pure state in an enlarged Hilbert space [371, 440]. We use the time-evolving block decimation algorithm [376] along with a fourth-order Trotter decomposition [148] to handle the exponential operators [1].

At fixed distance x and temperature T, the hydrodynamics regime is characterized by an algebraic decay of the Euclidean norm of the spin-spin correlation (3.9) function at long time,

$$\left|C(T, x, t)\right| \propto t^{-1/z} \quad \text{for } t \gtrsim t^\star(x, T), \tag{3.10}$$

with z as the dynamical exponent. The long-time limit is denoted by the crossover time $t^\star$, which we aim to identify, see Fig. 3.6. Depending on the microscopic model, three values for the exponent z have been reported for 1D quantum magnets: $z = 3/2$ corresponding to superdiffusion, $z = 1$
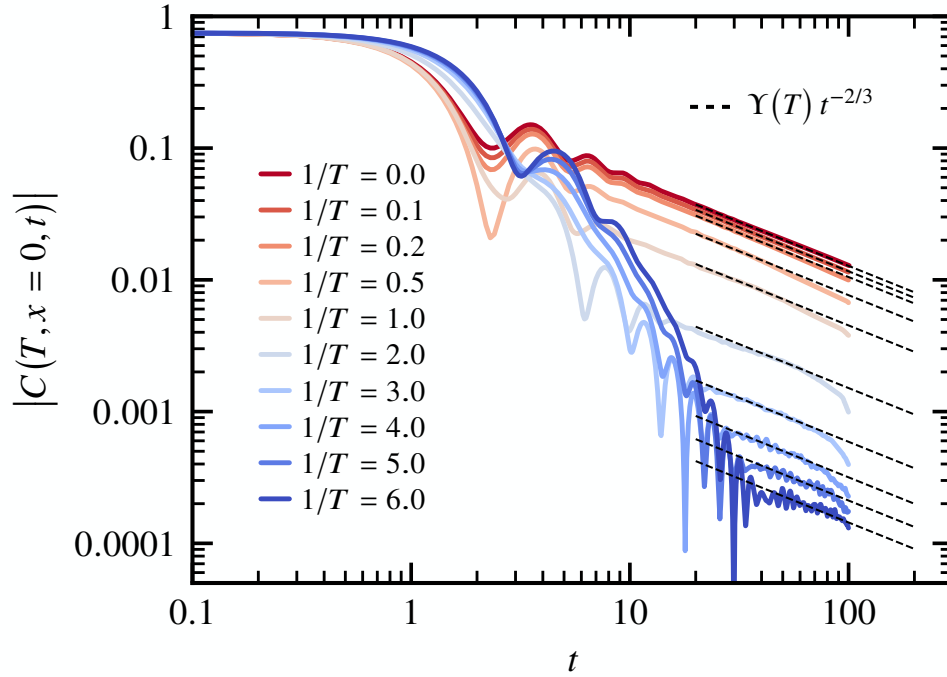
Figure 3.7: Time dependence of the norm of the spin-spin correlation (3.9) at $x = 0$ for various temperatures T. Simulations obtained for $L = 256$ with $\chi = 1024$. At long time, it displays an algebraic decay with time, according to Eq. (3.10). It is well fitted by the form $\Upsilon(T) \, t^{-2/3}$ with $\Upsilon(T)$, a temperature-dependent prefactor decreasing with the temperature reported in Fig. 3.8(b). The deviation from the genuine power law at long time is the result of the bond dimension being too small.

for ballistic, and $z = 2$ for diffusion [92, 83]. Superdiffusion is expected for the isotropic spin-1/2 Heisenberg model of Eq. (3.8).

3.2.3 Autocorrelation

We first consider the autocorrelation function ($x = 0$) versus time for different temperatures, as plotted in Fig. 3.7. Two regimes are clearly visible, delimited by the crossover time $t^{\star}(x = 0, T)$ (see Sec. 3.3.4 for more details). Beyond the crossover time and for all temperatures, one finds the expected power-law decay $\propto t^{-2/3}$ of superdiffusive hydrodynamics. Note that the rapid change of slope from the genuine power-law, at the longest times displayed, is the result of the bond dimension being too small and not a physical effect.

With high-temperature physics beyond $t^{\star}$, one can suspect low-temperature features at shorter times. For instance, the oscillating behavior observed in the norm of the autocorrelation is rem-

iniscent of a change of sign in the real and imaginary part (see Sec. 3.3.4 for more details), signaling antiferromagnetic correlations as the temperature is lowered. The long-time asymptotic of $C(T = 0, x = 0, t)$ has been studied at exactly zero temperature [271, 270]. It is composed by several power-law decaying contributions with the slowest one being $\propto t^{-1}$ (up to logarithmic corrections inherent to the isotropic spin-1/2 Heisenberg antiferromagnet [6, 258, 100, 359, 7, 24, 23, 90]). We cannot identify this regime in Fig. 3.7, which we attribute to insufficiently low temperatures, and discussed further in Sec. 3.3.4.

We now turn our attention to the temperature dependence of the crossover time $t^\star(x = 0, T)$. It is plotted in Fig. 3.8(a) versus the inverse temperature and shows a linear dependence. It can be understood as follows. It is well known that a finite temperature induces a thermal correlation length ξ which diverges as $T \to 0$ as $\propto u/T$ (up to logarithmic corrections [258]) with u the velocity of low-energy excitations in the spin-1/2 chain. Moreover, the dynamical correlation function (3.9) can also be thought of as measuring the spreading of a spin excitation. In this picture, the system behaves like a TLL for $t \lesssim \xi/u$, which can be identified as the crossover time $t^\star(x = 0, T) \propto 1/T$. Hence, the onset of superdiffusive hydrodynamics simply takes place as the low-energy physics gets suppressed by the finite temperature. It is only at zero temperature that the system is strictly critical and thus does not display any sign of anomalous high-energy dynamics. In addition to the linear dependence with $\propto 1/T$, there is an $O(1)$ constant in Fig. 3.8(a) that coincides with the very short-time dynamics where $|C(T, x = 0, t \simeq 0)| \simeq 0.75$.

At infinite temperature, it has been established that the dynamics belong to the $1 + 1$ KPZ universality class [190, 229], as it shows the same scaling laws as appear in the KPZ equation itself: $\partial_t h = \frac{1}{2}\lambda(\partial_x h)^2 + \nu\partial_x^2 h + \sqrt{\sigma}\eta$ with $h \equiv h(x, t)$, $\eta \equiv \eta(x, t)$ a normalized Gaussian white noise, and λ, ν, and σ parameters. It is a Langevin equation, with no quantum roots—and which makes the observation of its physics in a quantum magnet rather puzzling. In the right limits, the noise-averaged slope correlations behave as [349, 348]

$$C_{\text{KPZ}}(x, t) \simeq \chi_{\text{s}}(\lambda_{\text{KPZ}}t)^{-2/3} f_{\text{KPZ}}\left[x(\lambda_{\text{KPZ}}t)^{-2/3}\right], \tag{3.11}$$

with $\chi_{\text{s}} = \sigma/2\nu$ as the static spin susceptibility, $\lambda_{\text{KPZ}} = \sqrt{2}\lambda$, and f_{KPZ} as the KPZ scaling function [280]. The numerical observation of the scaling (3.11) for the Heisenberg spin chain through the spin-spin correlation (3.9) served as a conjecture regarding the nature of its dynamics [229]. A theoretical scenario for how KPZ hydrodynamics emerges in the Heisenberg chain has been advanced [44]. A relation between the parameters of the KPZ equation with those of the microscopic quantum model has been proposed [82]. Here, by identifying the prefactor of $C_{\text{KPZ}}(x = 0, t)$ in Eq. (3.11) with the prefactor $\Upsilon(T)$ of the power-law decay $\propto t^{-2/3}$ shown in Fig. 3.8(b), we are able to report on the temperature dependence of the parameters. The high-temperature data points are compatible with Ref. [82]. In addition, for $T \lesssim 1$, we find that $\Upsilon(T) = 0.13(1)T^2$, and therefore that $\chi_{\text{s}}\lambda_{\text{KPZ}}^{-2/3} f_{\text{KPZ}}(0) \propto T^2$. We argue in Sec. 3.3.3 that this behavior is compatible with earlier NMR experiments on Sr_2CuO_3 [361].

The definition of the crossover time $t^\star$ in Eq. (3.10) for the onset of superdiffusion is related to the power-law dependence $\propto t^{-2/3}$ and not f_{KPZ} of Eq. (3.11). It is well known that unambiguously identifying the scaling function from microscopic simulations with f_{KPZ} requires great numerical
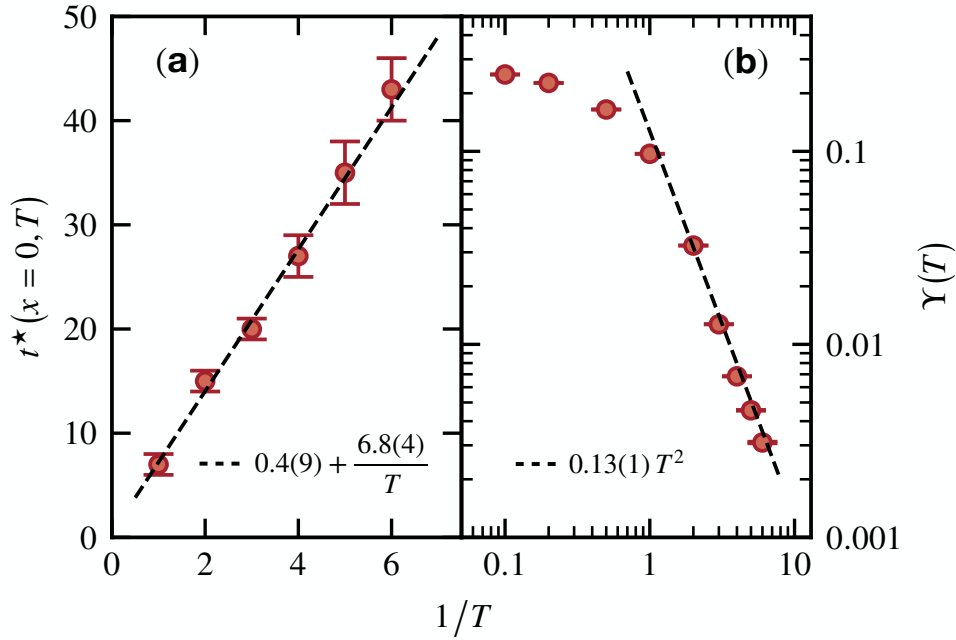
Figure 3.8: The data points are extracted from Fig. 3.7. (a) Temperature dependence of the crossover timescale $t^\star(x = 0, T)$ beyond which the algebraic decay $\propto t^{-2/3}$ for superdiffusive hydrodynamics emerges, see Eq. (3.10). It shows a linear dependence with the inverse temperature (dashed line). (b) Temperature dependence of the prefactor $\Upsilon(T)$ of the algebraic decay $\propto t^{-2/3}$ for superdiffusive hydrodynamics. At low temperatures $T \lesssim 1$, it follows a quadratic dependence $\propto T^2$ (dashed line).

precision and long-time data for all distances x [229]. This is beyond the capability of our simulations at low temperatures. Instead, we consider the spatial dependence of $t^\star$ for $|x| > 0$.

3.2.4 Spatiotemporal Crossover

The time-dependent spin-spin correlation function (3.9) is associated with a light-cone structure and we therefore expect $t^\star(x, T)$ to be an increasing function with the distance $|x|$. It is verified in Fig. 3.9(a) where we plot its time dependence at fixed temperature ($T = 0.25$). As $|x|$ increases, the onset of superdiffusion takes place at longer and longer times, and we display the crossover timescale in Fig. 3.9(b) for different temperatures. Because we can only reliably estimate it for $|x| \lesssim 30$, it is difficult to draw a definite conclusion on its scaling. Nevertheless it is compatible with a superdiffusive length-time scaling of the form,

$$t^\star(x, T) = 0.4(9) + \frac{6.8(4)}{T} + 0.17(3) |x|^{3/2}, \tag{3.12}$$
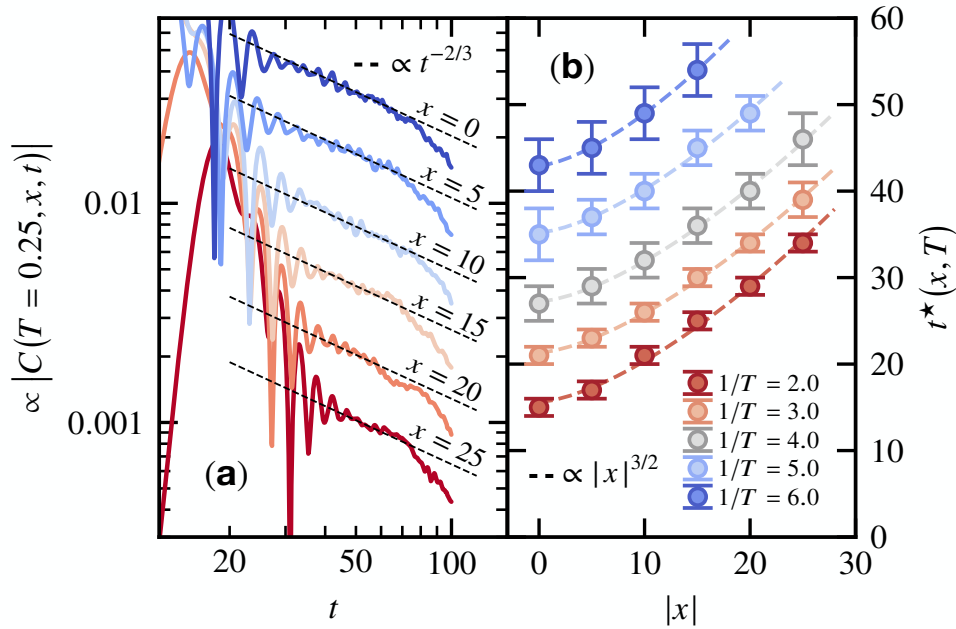
Figure 3.9: (a) Time dependence of the norm of the spin-spin correlation (3.9) at $T = 0.25$ for various distances x. Simulations obtained for $L = 256$ with $\chi = 1024$. The curves have been shifted vertically for visibility. At long time, it displays an algebraic decay with time, according to Eq. (3.10), well fitted by the form $\propto t^{-2/3}$. The deviation from the genuine power law at long time is the result of the bond dimension being too small. (b) Spatial dependence of the crossover time $t^{\star}(x, T)$ beyond which the algebraic decay $\propto t^{-2/3}$ for superdiffusive hydrodynamics emerges, see Eq. (3.10). The dashed lines are fits of the form $A + B|x|^{3/2}$ with $A \equiv t^{\star}(0, T)$ and $B = 0.17(3)$ found to be temperature independent (see Sec. 3.3.4 for more details).

with the first two terms obtained from the $t^{\star}(x = 0, T)$ data, see Fig. 3.8(a). The prefactor of $|x|^{3/2}$ is found independent of the temperature (see Sec. 3.3.4 for more details). The reported numerical parameters are obtained by least-square fitting. The spatiotemporal crossover time (3.12) is plotted on top of the norm of the spin-spin correlation in Fig. 3.6 for $T = 0.25$. Note that based on this picture, we expect logarithmic corrections for the temperature dependence, but they are not detectable from our simulations [2].

3.2.5 Experimental Consequences

Although we have focused on the norm of the spin-spin correlation (3.9), we find that

$$|\mathfrak{Im}\, C(T, x, t)| \ll |\mathfrak{Re}\, C(T, x, t)| \quad \text{for } t \gtrsim t^{\star}, \tag{3.13}$$

and that the superdiffusive power law $\propto t^{-2/3}$ only holds for the real part, which therefore hosts the relevant high-temperature physics. For instance, superdiffusion was observed in $KCuF_3$ by neutron scattering in the limit of small momentum and vanishing frequency [308], which probes the Fourier transform to momentum and frequency spaces of $C(T, x, t)$.

Another promising experimental technique for investigating high-temperature hydrodynamics is NMR, which has been successfully used to characterize the low-temperature TLL regime in numerous spin compounds [199, 36, 182, 183, 90, 71, 28, 94, 159]. Nuclear spins are polarized via a static magnetic field (ideally weak) and then perturbed by an electromagnetic pulse of frequency ω_0, chosen to target specific nuclei as per the Zeeman splitting. Following the perturbation, the nuclear spins relax over time with an energy transfer to the electrons. When the nuclear and electronic spins belong to the same atom, the relaxation rate is related to the autocorrelation function, $1/T_1 \sim \int_0^{1/\omega_0} \Re\mathfrak{e}\, C(T, x = 0, t)\, dt$ [4, 158, 341]. With ω_0 of the order of a few mK, it usually leads to a frequency-independent $1/T_1$ as long as the correlation decays quickly enough. Here, the hydrodynamics regime should lead instead to $1/T_1 \propto \omega_0^{1/z-1}$ and give access to z in the right frequency regime. According to Eq. (3.12), the corresponding crossover frequency scale $\omega^\star \sim 1/t^\star$ goes as $\propto T$, and superdiffusion will be visible if $\omega_0 \ll \omega^\star \sim T$. Considering the experimental range of ω_0, this condition is fulfilled even at low temperatures, where measurements are often less noisy and less subject to spoiling effects such as phonons.

Thus, the existence of a finite spatiotemporal crossover $t^\star(x, T)$ in the form of Eq. (3.12) confirms that superdiffusive hydrodynamics is within the experimentally relevant window of parameters with respect to temperatures, time and length scales for quantities involving $\Re\mathfrak{e}\, C(T, x, t)$.

In fact, a power-law behavior of the form $1/T_1 \propto \omega_0^{-\alpha}$ has been reported in the nearly ideal spin-1/2 Heisenberg antiferromagnet Sr_2CuO_3 ($J \simeq 2200$ K) at $T = 295$ K a couple of decades ago [361]. NMR was performed on the ^{17}O, coupled symmetrically to the Cu^{2+} carrying the relevant electronic spin, which filtered out the $q = \pm\pi$ contributions in the $1/T_1$ due to form factors, but not the long-wavelength modes $q = 0$ holding hydrodynamics. Although the measurement accuracy was not sufficiently precise to extract the exponent α, the results are compatible with $\alpha \approx 0.33$, which corresponds to $z = 3/2$. In addition, the authors find that at fixed frequency, the NMR relaxation rate may be approximated by an empirical form $1/T_1 T \approx a + bT$ for $T \ll J$ with a and b fitting constants. When dropping a, this is compatible with $\Upsilon(T) \propto T^2$ reported in Fig. 3.8(b), which relates to the temperature dependence of the parameters of the KPZ equation.

Today's theoretical understanding of the dynamics of 1D quantum systems and our results call for new NMR experiments on spin chains at high temperatures. It would provide a complementary probe to neutron scattering [308] to access anomalous spin transport in quantum materials.

3.2.6   Conclusion

Building on large-scale MPS calculations, we reconciled the well-established low-temperature dynamics of the quantum Heisenberg spin-1/2 chain with the recently predicted high-temperature superdiffusive regime related to KPZ hydrodynamics. We have found that both coexist, and the transition from one to the other takes the form of a spatiotemporal crossover. The crossover is

controlled by the temperature: as the temperature is lowered, the growing quantum correlations between degrees of freedom push the onset of superdiffusion to longer length and timescales as $\propto 1/T$. We also reported on the temperature dependence of the parameters of the KPZ equation, which should provide useful guidance in relating them to the microscopic parameters of the quantum model. We also showed that only the real part of the spin-spin correlations holds the superdiffusive hydrodynamics. Finally, we discussed the experimental consequences of our results for condensed matter probes. We motivated NMR experiments as a great way to measure spin transport in quantum materials and showed that earlier results are compatible with the current theoretical understanding yet calling for new experiments in quantum spin chains. Because NMR requires the use of a static magnetic field to polarize the nuclear spins, it would be insightful to study the effect of this perturbation on the dynamics of the $S = 1/2$ Heisenberg chain studied in this Letter. We believe that it would induce another crossover from superdiffusion to ballistic dynamics, which needs to be characterized.

3.3 Appendix

3.3.1 Experimental Details

In this section of the appendix, I discuss additional information regarding the experiment conducted in $KCuF_3$ by my collaborators at Oak Ridge National Lab. I was not involved directly with conducting the experiments, but the experimental detection of KPZ hydrodynamics is an important part of this thesis work, and so I include additional details here.

Data collection

To search for effects of KPZ behavior, we measured the inelastic $KCuF_3$ neutron spectrum using the SEQUOIA spectrometer at the Spallation Neutron Source at Oak Ridge National Laboratory. Our sample was a 6.86 g $KCuF_3$ single crystal mounted with the c axis perpendicular to the incident beam. To probe hydrodynamic signatures, we focused on the low-energy part of the spectrum. We measured with an incident energy $E_i = 8.2$ meV, which gives access to the very bottom of the spectrum (the total $KCuF_3$ bandwidth is 105 meV [204]), as shown in Fig. 3.2, with a resolution full width at half maximum 0.25 meV.

We measured six temperatures of $KCuF_3$ with the c axis perpendicular to the incident neutron beam, and an incident energy of $E_i = 8.2$ meV, shown in Fig. 3.10. Data were integrated over all directions perpendicular to L [205]. At each temperature, the spectra was measured for eight hours at nominal 1.4 Mw operation [244], with choppers set to 120 Hz (SEQ-100-2.0-AST chopper with 2 mm slit spacing). Data were corrected for the form factor by calculating the magnitude of Q for each pixel and dividing by the anisotropic $d_{x^2-y^2}$ Cu^{2+} form factor [32, 415]:

$$f(\mathbf{Q}) = \langle j_0 \rangle + \frac{5}{7}(3\cos^2\beta - 1)\langle j_2 \rangle + \frac{3}{56}(35\cos^4\beta - 30\cos^2\beta + 35\sin^4\beta\cos 4\alpha + 3)\langle j_4 \rangle \quad (3.14)$$
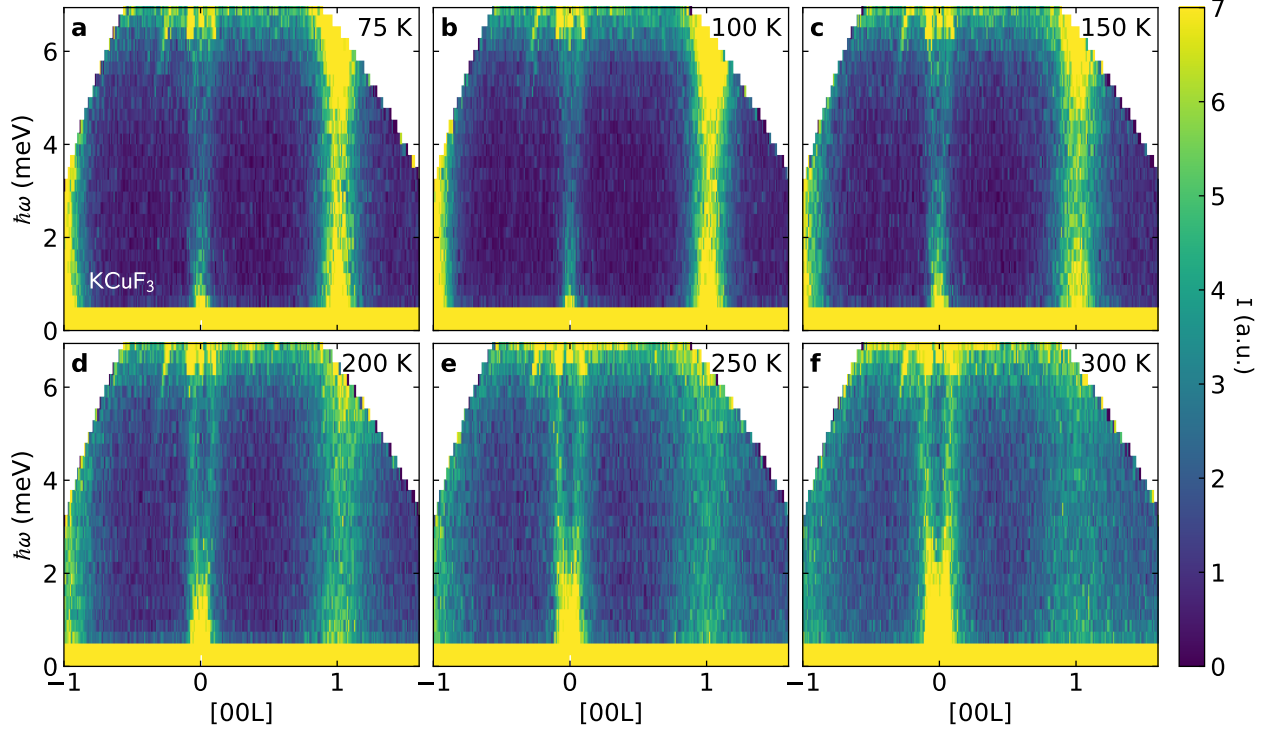
Figure 3.10: Temperature dependent neutron spectra of KCuF$_3$.

where β is the angle between **Q** and the z axis of the $d_{x^2-y^2}$ orbital, and α is the xy-plane angle from the x axis. We used Cu^{2+} $\langle j_n \rangle$ constants from Ref. [41]. As shown in Fig. 3.11, each pixel at nonzero Q_L (along the chain) or $\hbar\omega$ includes a nonzero Q_{HH} component

$$Q_{HH} = \sqrt{k_f^2 - Q_L^2} - k_i \qquad (3.15)$$

where k_f and k_i are the magnitudes of the incident and final neutron wavevectors. Taking this into account, we calculated the anisotropic form factor for the two $d_{x^2-y^2}$ orbital orientations shown in Fig. 1(a) in the main text, averaging over both orientations. The final calculated form factor for this geometry is in Fig. 3.11b. Fig. 3.12 compares the isotropic and anisotropic Cu^{2+} form factors: the difference is noticeable but small. The fitted 300 K dynamic exponent is 1.36(5) with the isotropic form factor correction, and 1.35(5) with the anisotropic form factor correction: no difference to within uncertainty.

In order to estimate the experimental resolution of the SEQUOIA spectrometer for this experiment, we simulated an antiferromagnetic linear chain spin wave dispersion with a bandwidth 52.7 meV (the lower bound of the spinon continuum) using MCViNE virtual neutron experiment [227]. The Monte Carlo ray tracing simulations of SEQUOIA [130] were run using McVine for 2×10^{10} incident neutron packets using the exact incident energy and chopper settings used during
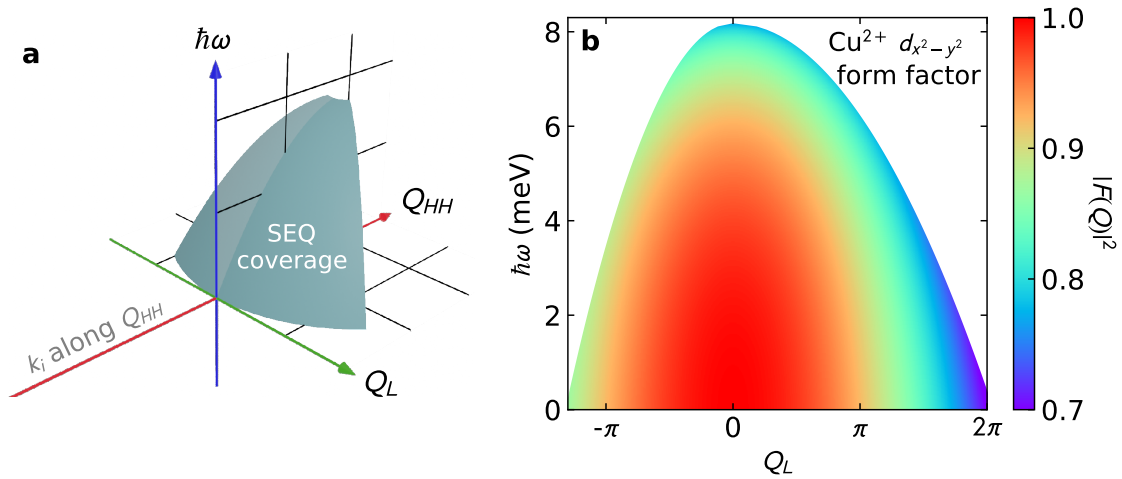
Figure 3.11: Form factor correction for $KCuF_3$ SEQUOIA experiment. Panel **a** shows the coverage in reciprocal space and energy. Because of the instrument geometry, any finite energy or momentum transfer also involves a finite momentum transfer along the $(h, h, 0)$ direction. This leads to the Cu^{2+} $d_{x^2-y^2}$ form factor correction shown in panel **b**, which is calculated based off $\vec{Q}$.
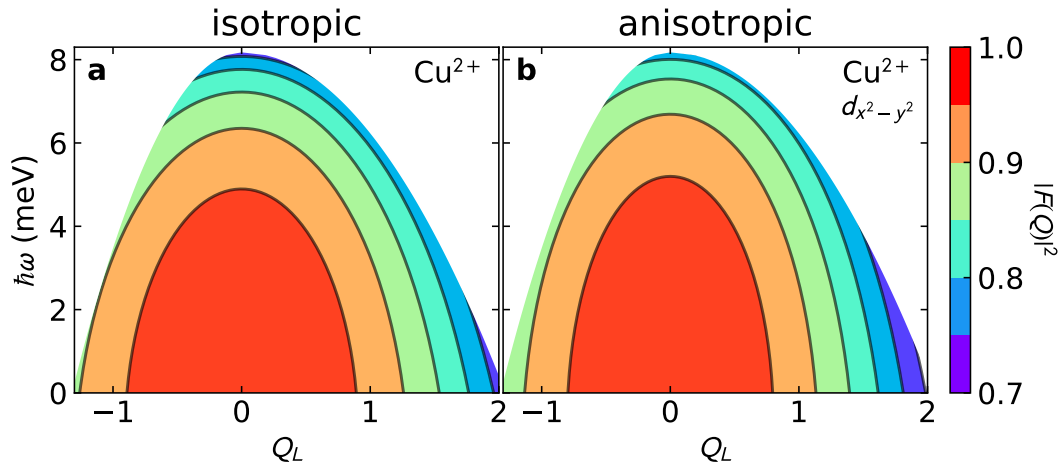
Figure 3.12: Comparison of the isotropic Cu^{2+} to the anisotropic Cu^{2+} form factor. **a** Color contour map of the isotropic Cu^{2+} form factor compared to **b** the anisotropic $d_{x^2-y^2}$ Cu^{2+} form factor for $KCuF_3$. The differences are subtle: the anisotropic form factor falls off faster with Q_L but more gradually with $\hbar\omega$ than the isotropic form factor.
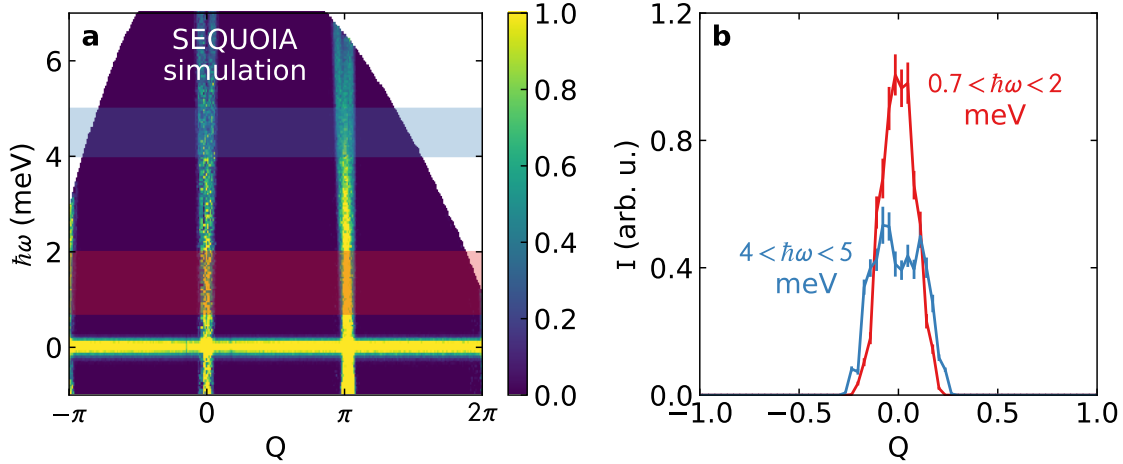
Figure 3.13: Simulated neutron spectrum of a 1D antiferromagnetic spin chain in the SEQUOIA experiment, in order to show resolution width. The inelastic spectra is assumed to be the semi-classical linear spin wave theory dispersion, and the Q resolution has a FWHM 0.08. Panel **a** shows the spectrum, and panel **b** shows constant-energy cuts. At 4.5 meV, the two modes of the dispersion are just barely distinguishable.

the experiment. The results are shown in Fig. 3.13, and indicate a Q resolution has a FWHM 0.08. Note that the finite-temperature mode softening and the power law in Q are absent from this simulated data, indicating that they are intrinsic to $KCuF_3$ and not resolution effects.

To estimate the impact of experimental resolution on the fitted power law, we used the resolution function defined by the MCViNE simulations in Fig. 3.13, and convolved the 300 K MPS data with a Gaussian resolution width, shown in Fig. 3.14. We find that the fitted exponent of the broadened data increases slightly (by 2.7%) because of the sharp $Q = 0$ feature becoming smoothed out to higher Q. This means that the experimental fits slightly overestimate the dynamic exponent: the true 300 K $KCuF_3$ dynamic exponent may be closer to 1.31(5) than 1.35(5).

Data fitting

We show the power law fit for different choices of the energy window at the temperatures relevant for experiments in Fig. 3.17, analogous to Fig. 3.16. In this case, the trends are more clear: at lower temperatures, the fitted power is larger, and larger energy windows suppresses the fitted power at high temperatures, and enhances the fitted power at the lowest temperatures.

In Fig. 3.4, we subtract a phenomenological power law at $Q = \pi$ in order to isolate the power law at $Q = 0$. The fitted power laws are shown in Fig. 3.15, showing that the power near $Q = \pi$ dramatically varies with temperature both in theory and experiment. We also chose the lowest energy window ("cut a" in Fig. 3.2) to approximate the $\hbar\omega = 0$ scattering. If we do not do this, but instead define a constant background based off the lowest temperature data, the fitted exponents are
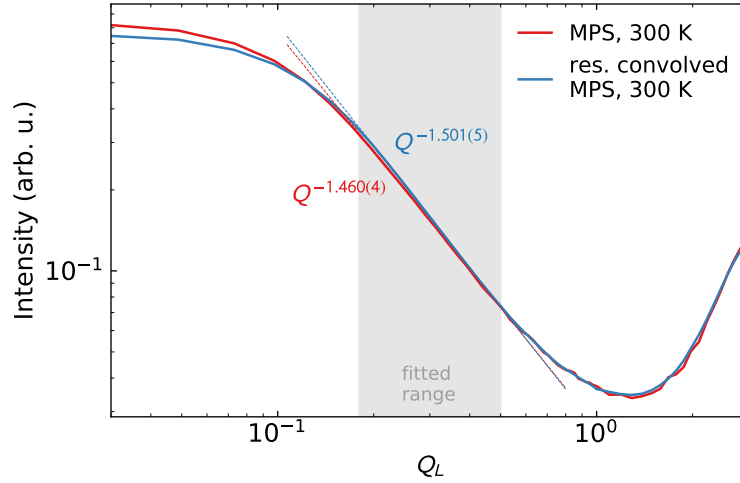
Figure 3.14: Effect of resolution broadening on the fitted power law, demonstrated using the MPS 300 K simulation. The resolution-broadened fit increases the fitted exponent by 2.7%, which means that the fitted experimental data slightly overestimates the dynamic exponent.

shown in Fig. 3.16. We also show the results of fits to cuts b and c. Forgoing the phenomenological background means that the power law is visible over a narrower range in Q, but in nearly every case the fitted powers agree to within uncertainty. Meanwhile, an increase in the energy window yields slightly different fitted powers, generally decreasing as the window increases. All fits were performed with the scipy least squares routine [378].

3.3.2 Spectral Function Additional Information

Gaussian broadening

Extracting an analytic spectral function from simulations is difficult due to the discrete spectrum for any finite system. A common technique is to broaden the delta functions with a smooth distribution, such as a Gaussian. Here, this is achieved by scaling the moments, $\mu_n(Q)$, by a damping factor g_n that also smooths out the Gibbs oscillations that occur from truncating the series in Eq. (3.4) to a finite value N. This can be achieved via Jackson damping [383], with

$$g_n = \frac{N-n+1}{N+1} \cos\left(\frac{\pi n}{N+1}\right) + \frac{1}{N+1} \sin\left(\frac{\pi n}{N+1}\right) \cot\left(\frac{\pi}{N+1}\right). \tag{3.16}$$

Note that g_n is a monotonic function of n that decays from 1 to 0, and in the limit $N \rightarrow +\infty$, $g_n \rightarrow 1$ for all n. Jackson damping has the effect of smoothing out the finite system spectral peaks with a Gaussian with an ω dependent width. This Gaussian broadening procedure is used in Figs. 3.22, 3.21, and 3.5.
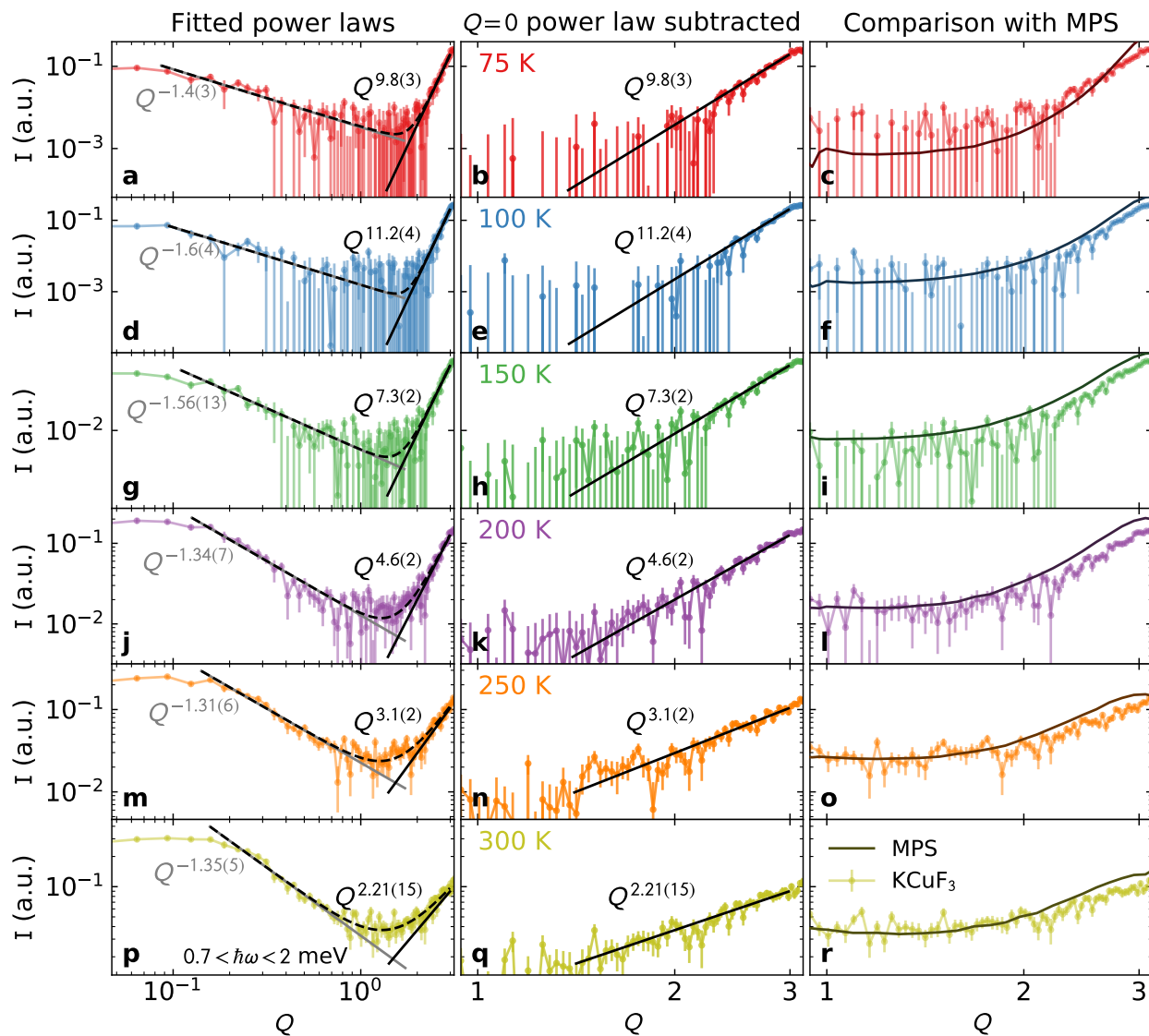
Figure 3.15: Power law fits for $KCuF_3$ scattering showing the fitted phenomenological power law at $Q = \pi$. The left column shows the data with the $Q = 0$ and $Q = \pi$ fitted power laws, the middle column shows the $Q = \pi$ power law with the $Q = 0$ (dynamic exponent) subtracted, and the right column shows the experimental data compared to MPS simulations in the vicinity of $Q = \pi$. The data near $Q = \pi$ follows a power law very well, but it dramatically varies with temperature. The right column shows this is the case for both theory and experiment. Error bars indicate one standard deviation.
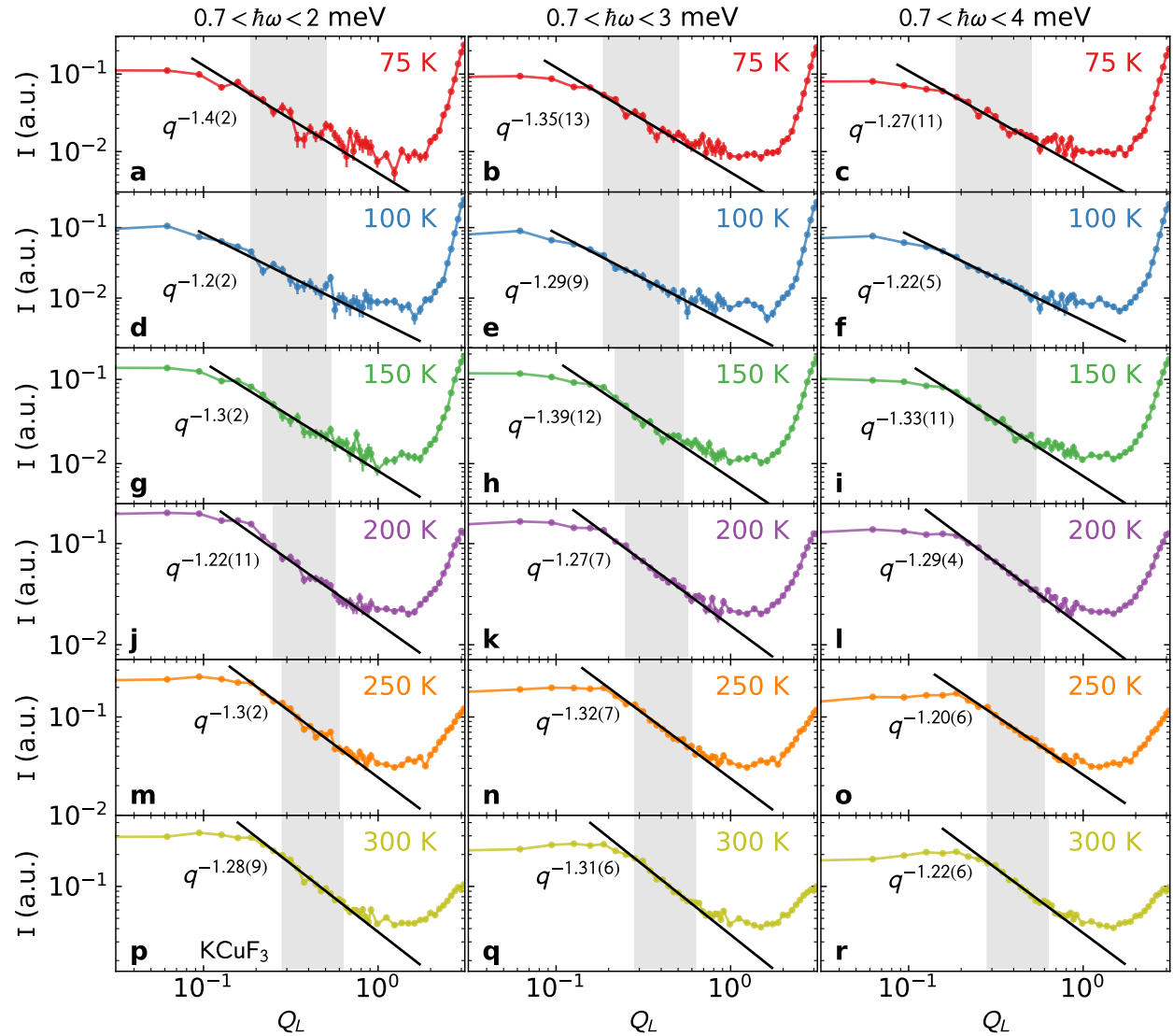
Figure 3.16: Power law fits for low-Q KCuF$_3$ scattering for three different energy windows: $0.7 < \hbar\omega < 2$ meV (cut a, left column), $0.7 < \hbar\omega < 3$ meV (cut b, middle column), and $0.7 < \hbar\omega 4$ meV (cut c, right column). No background has been subtracted, and the window where data was fitted is indicated in gray. Note that these powers, in most cases, agree to within uncertainty with those in Fig. 4 in the main text. Error bars indicate one standard deviation.
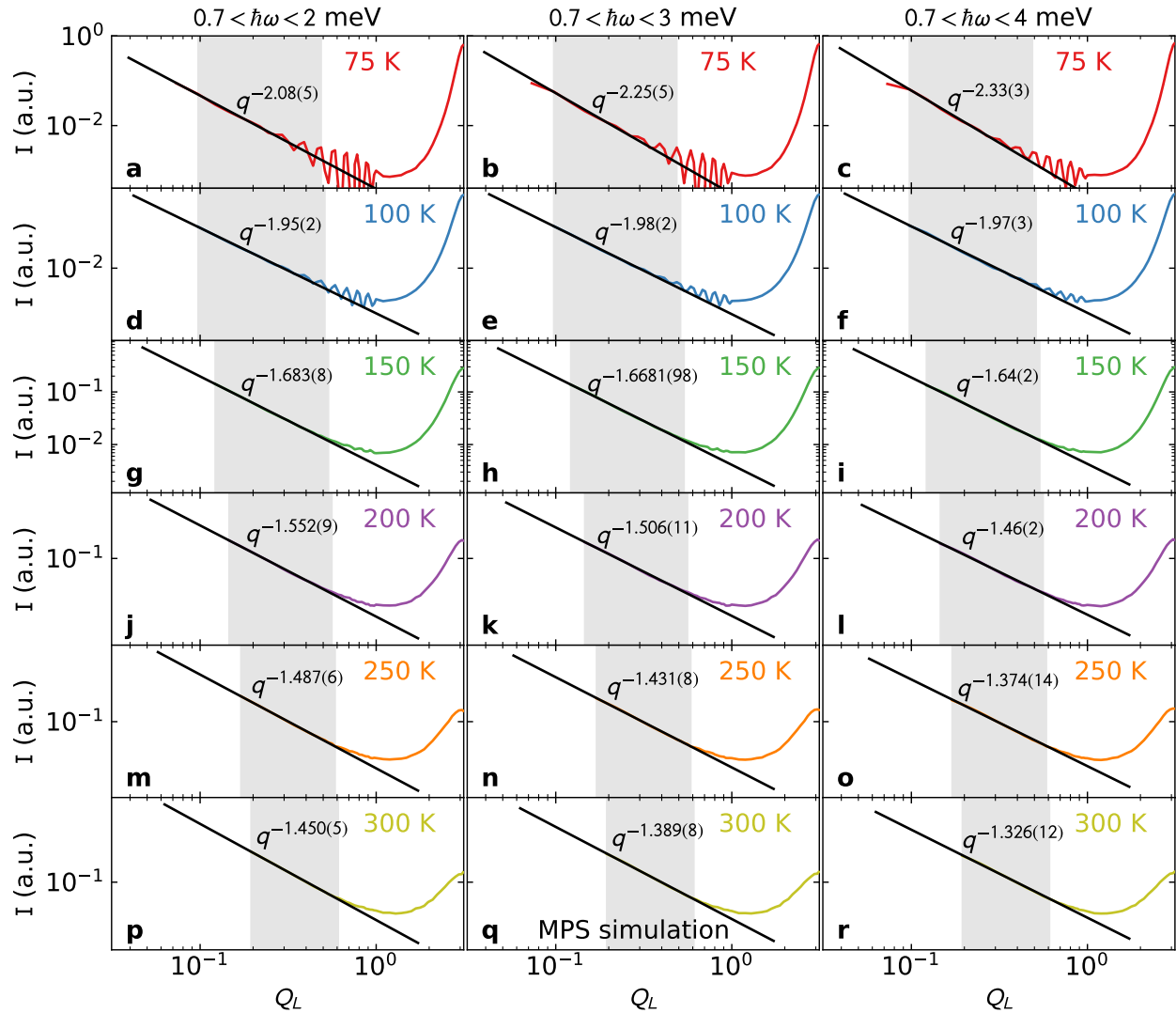
Figure 3.17: Power law fits to the low-Q MPS simulated spectrum for three different energy windows: $0.7 < \hbar\omega < 2$ meV (cut a, left column), $0.7 < \hbar\omega < 3$ meV (cut b, middle column), and $0.7 < \hbar\omega < 4$ meV (cut c, right column). The window where data was fitted is indicated in gray. Note that the finite energy transfer causes the exponent to deviate from the $\hbar\omega = 0$ value of $z = 3/2$: too large at low temperatures, and too high at high temperatures. Also note that the exponent magnitude is suppressed as the energy transfer window increases.
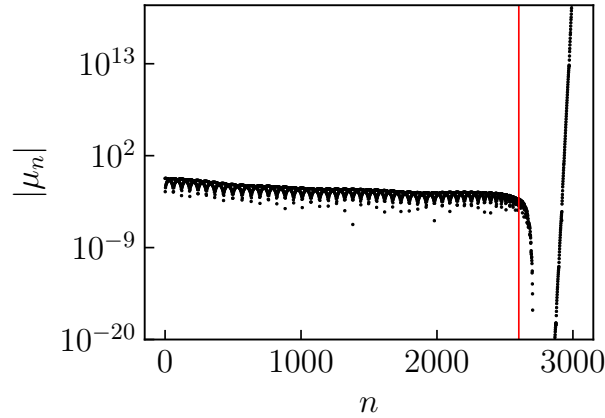
Figure 3.18: The absolute value of the Chebyshev moments, $|\mu_n|$, as a function of n for the case of $T = 75$ K, and $Q = 1.680$. The vertical line in red illustrates N^*, the value of n for which we terminate the series in Eq. (3.4).

Chebyshev moments and convergence

The Chebyshev moments, $\mu_n(Q)$, are the expansion coefficients in Eq. (3.4), and dictate the convergence of the numerical simulations. The moments have an envelope that decays exponentially [390], and if $\mu_n(Q)$ is not "sufficiently close to zero", then our simulations are unreliable. We fit the envelope of the moments to a decaying exponential of the form $\propto e^{-n/\xi}$, and if $\xi > 500$, we say the moments are not converged. This procedure defines a minimum Q value, $Q_{\min}$, and we don't show $Q < Q_{\min}$ when comparing with experiments. Numerical error can spoil the iterative process of Eq. (3.5), and can cause μ_n to rapidly drop to near zero, and then diverge for values of $n > N^*$. When this happens, we zero out the moments for all $n > N^*$ when computing $\mathcal{S}(Q,\omega)$ in the sum of Eq.(3.4), effectively truncating the series at N^*. This occurs only at $T = 100$ K, and $T = 75$ K, and for Q values larger than the power law region. The lowest value of N^* used is 2600, and we show in Fig. 3.18 the moments for this case.

We include $N = 3000$ terms in Eq. (3.4) for comparison with experiments. N/W is a pseudo-time parameter in this method, and larger values produce greater ω resolution. The Q dependence at small ω is illustrated in Fig. 3.20 and Fig. 3.19, where we see the simulations are well converged in the region where comparison with experiments is made. Convergence is not found for very small $Q < Q_{\min}$, which is understood when making the analogy between N and time t. Exactly at $Q = 0$, then $\hat{S}^z_{Q=0}$ is a conserved quantity, and so for very low Q, very large t (and equivalently very large N) is needed to accurately resolve the ω dependence.
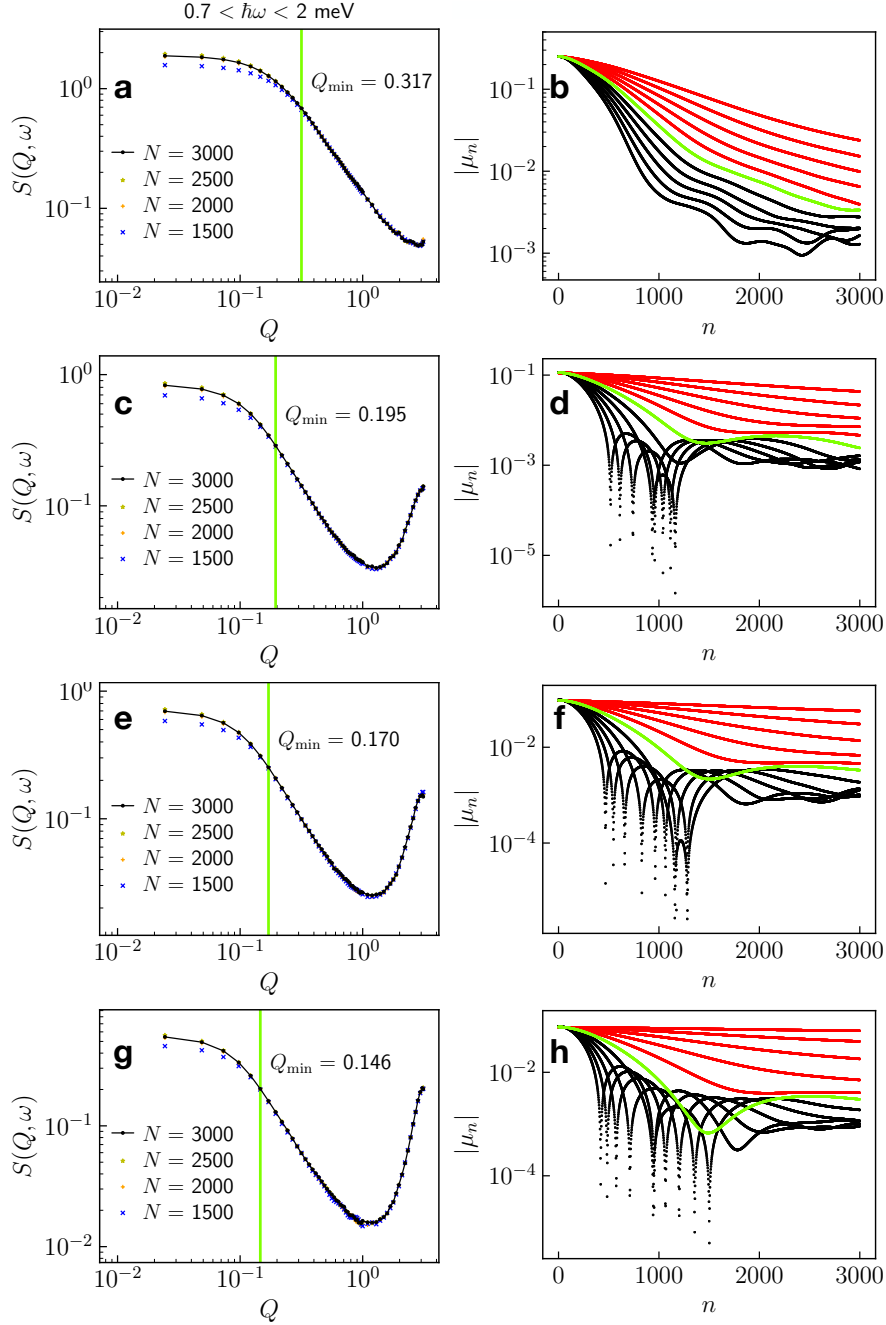
Figure 3.19: The left columns shows the Q dependence of $\mathcal{S}(Q, \omega)$ for $0.7\hbar\omega < 2$ meV with different choice of the number of terms, N, used in Eq. (3.4). The vertical green line corresponds to the value $Q = Q_{\min}$. The right column is the absolute value of the Chebyshev moments appearing in Eq. (3.4) as a function of the number of iterations n for several values of Q. Only the moments with even values of n are shown for clarity. The green curve in each plot depicts $Q = Q_{\min}$, the red curves are $Q < Q_{\min}$, and the black curves are $Q > Q_{\min}$. The temperatures shown are **a**, **b** $T = +\infty$, **c**, **d** 300 K, **e**, **f** 250 K, and **g**, **h** 200 K.
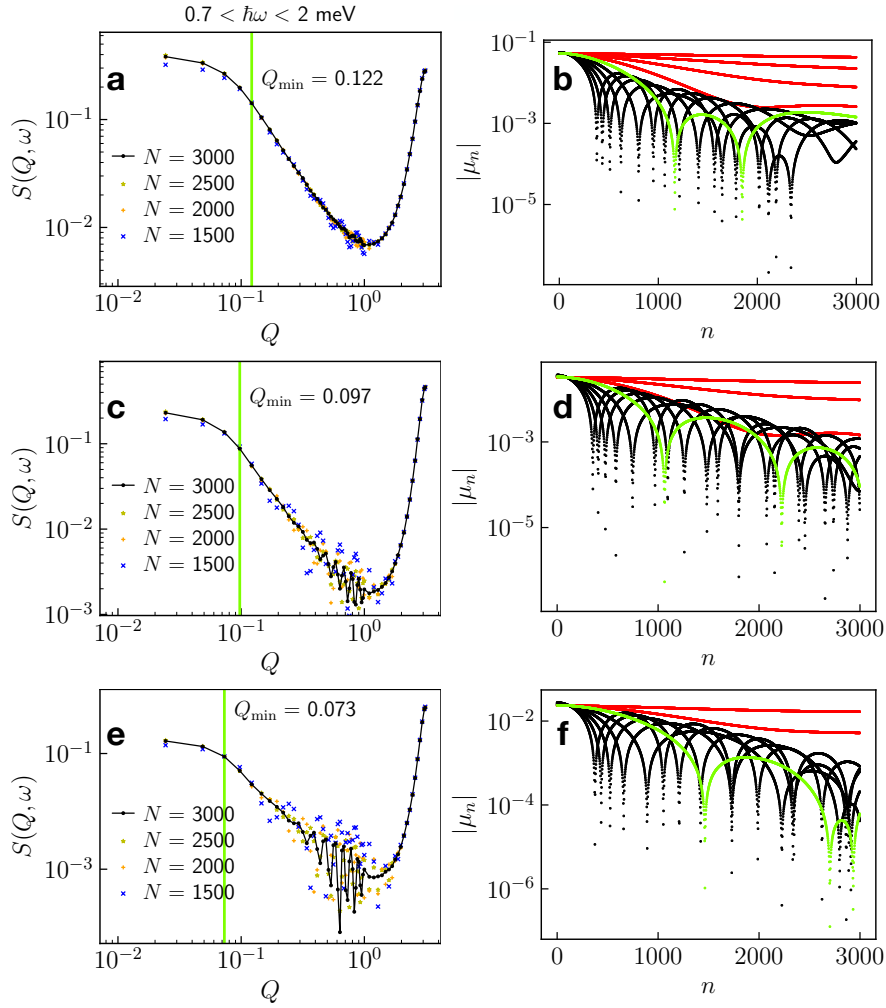
Figure 3.20: The left columns shows the Q dependence of $\mathcal{S}(Q,\omega)$ for $0.7 < \hbar\omega < 2$ meV with different choice of the number of terms, N, used in Eq. (3.4). The vertical green line corresponds to the value $Q = Q_{\min}$. The right column is the absolute value of the Chebyshev moments appearing in Eq. (3.4) as a function of the number of iterations n for several values of Q. Only the moments with even values of n are shown for clarity. The green curve in each plot depicts $Q = Q_{\min}$, the red curves are $Q < Q_{\min}$, and the black curves are $Q > Q_{\min}$. The temperatures shown are **a**, **b** $T = 150$ K, **c**, **d** 100 K, and **e**, **f** 75 K.

Full spectral function temperature dependence

The full ω dependence of $S(Q, \omega)$ is computed, and shown in Fig. 3.21 and Fig. 3.22 for various temperature values. Jackson damping is used in these figures [383]. As temperature is lowered, agreement with the low-energy spectrum is observed. The region near $(Q, \omega) = (0, 0)$ relevant for the neutron scattering experiments is also shown. We see strong intensity at $(Q, \omega) = (0, 0)$ with bifurcating dispersion lines emerging as we move away from this point. We note that the bifurcation point appears to occur at finite ω from the numerical data, but this is a finite size effect, and does not seem to occur in the experimental data. To verify this, we show the frequency bifurcation, ω_c as a function of the Chebyshev expansion order N in Fig. 3.23. As $N \to +\infty$, we're approaching the thermodynamic limit, and we see this bifurcation point tends towards $\omega_c = 0$.

Kardar-Parisi-Zhang scaling function

The scaling function for the $1 + 1$ KPZ universality class $f(\cdot)$ is known numerically exactly [280] in real space x and time t. In particular, Ref. [280] provides raw data for the scaling function $f(y)$ with $y \propto xt^{-2/3}$, and following this work, we Fourier transform this data to arrive at the scaling function $\mathring{f}(\cdot)$ in momentum Q and frequency ω space. The relation to the spectral function, in the hydrodynamic regime is given by

$$S(Q, \omega) = c_1 Q^{-3/2} \mathring{f}\left(c_2 \omega Q^{-3/2}\right), \tag{3.17}$$

where c_1 and c_2 are system-dependent constants that we use as fitting parameters to compare with the numerical simulations. We found $c_1 \simeq 0.026$ and $c_2 \simeq 0.639$ by fitting $\mathring{f}$ to the numerical data at $T = +\infty$ and $Q = Q_{\min}$ for the optimum simulation parameters used in this work. Comparison with our numerical simulations and the scaling functions for KPZ are shown in Fig. 3.24.

3.3.3 Revisiting Experimental NMR Data for Sr_2CuO_3

Characterizing anomalous spin transport

We revisit in Fig. 3.25 the experimental data of Fig. 3(d) in Ref. [361]. In this work, a power-law behavior of the form $1/T_1 \propto H^{-\alpha}$ assuming $\alpha = 0.5$ (corresponding to diffusion) was reported for the nearly ideal spin-1/2 Heisenberg antiferromagnets Sr_2CuO_3. Here, in addition to the diffusive behavior, we show the best superdiffusive fit of the form $\propto H^{-1/3}$, which is the expected behavior for the quantum spin-1/2 Heisenberg chain, based on today's knowledge. We also show the best constant fit of the form $\propto H^0$ corresponding to ballistic transport.

From a purely theoretical perspective, we expect ballistic spin transport in the infinite time limit due to the external magnetic field. However, the magnetic field being extremely small (14 T) compared to the spin exchange coupling in this compound ($J \simeq 2200$ K), the crossover might happen beyond the timescale related to the NMR frequency, making the dynamics look effectively supper-diffusive. The effect of the magnetic field needs to be precisely studied and we leave that for future work. For instance, for the low-energy physics studied in Refs. [361] and [359], the effect of the magnetic field was irrelevant.
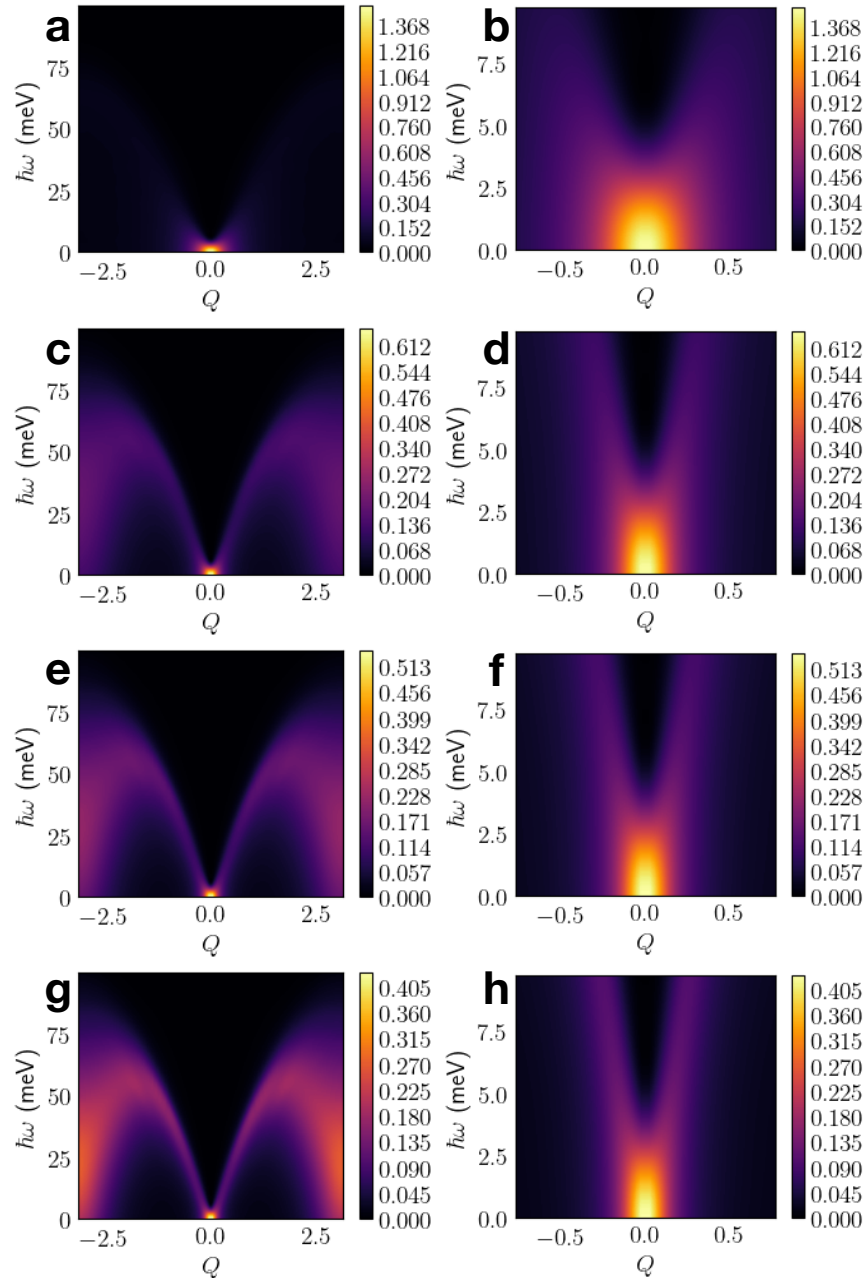
Figure 3.21: The spectral function, $\mathcal{S}(Q, \omega)$ at **a**, **b** $T = +\infty$, **c**, **d** 300 K, **e**, **f** 250 K, and **g**, **h** 200 K. The left column illustrates the full spectrum, and the right column zooms in around $(Q, \omega) = (0, 0)$, the region relevant for comparison with experiments.
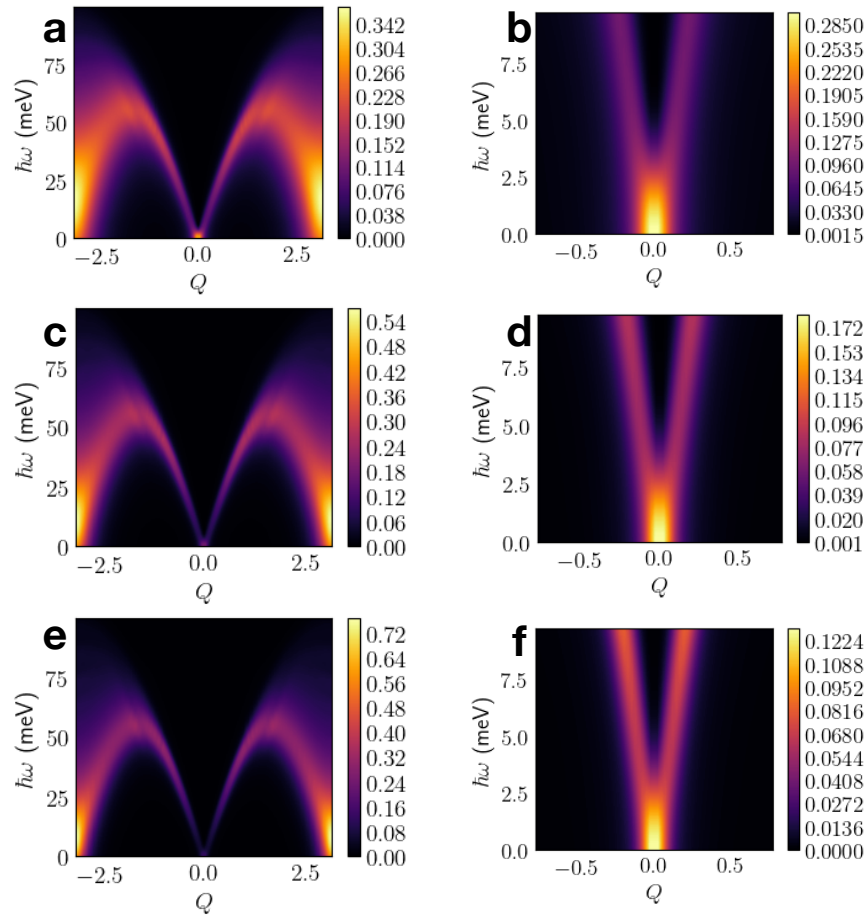
Figure 3.22: The spectral function, $\mathcal{S}(Q, \omega)$ at **a**, **b** $T = 150$ K, **c**, **d** 100 K, and **e**, **f** 75 K. The left column illustrates the full spectrum, and the right column zooms in around $(Q, \omega) = (0, 0)$, the region relevant for comparison with experiments.
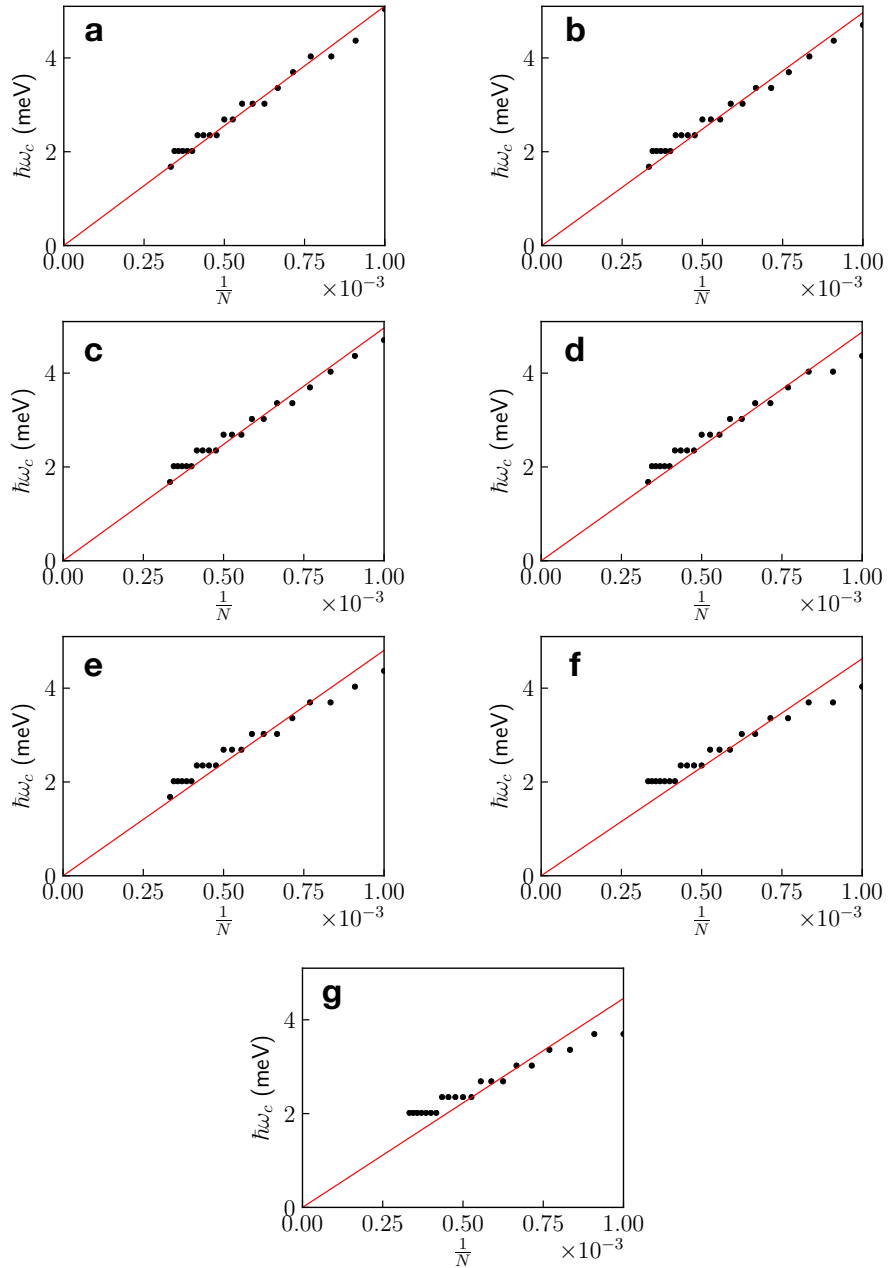
Figure 3.23: The value of $\hbar\omega_c$ at which the spinon mode splitting occurs at $Q = 0$ versus the inverse of the number of terms used in the sum of Eq. (3.4). The different subplots correspond to **a** $T = +\infty$, **b** 300 K, **c** 250 K, **d** 200 K, **e** 150 K, **f** 100 K, and **g** 75 K.
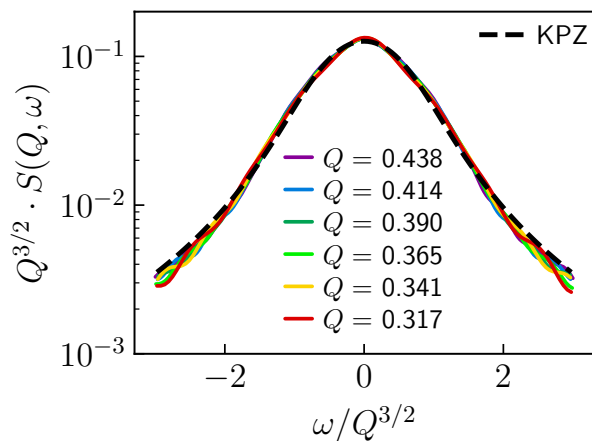
Figure 3.24: The KPZ scaling function plotted against the numerical data for various values of Q
at $T = +\infty$.
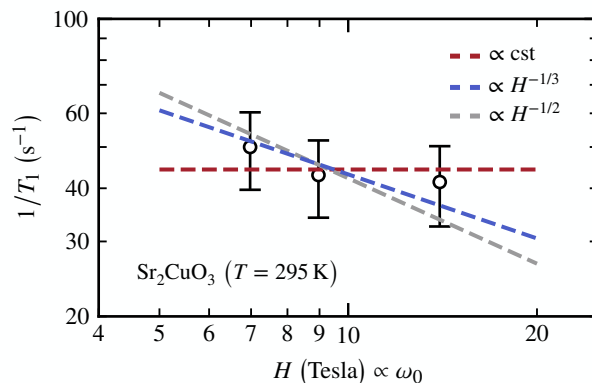
Figure 3.25: The data reported on this figure is extracted from Fig. 3(d) of Ref. [361]. It corresponds
to the NMR relaxation rate $1/T_1$ versus the strength of the applied external magnetic field H for
Sr_2CuO_3 at $T = 295$ K (the exchange coupling is $J \simeq 2200$ K). The NMR was performed on the ^{17}O
nuclei, coupled symmetrically to the Cu^{2+} ions carrying the relevant electronic spins $S = 1/2$. As a
result, the NMR relaxation rate $1/T_1$ filters out $q = \pm\pi$ components but conserves nonetheless the
long-wavelength modes $q = 0$ holding hydrodynamics. The applied field is directly proportional to
the NMR frequency ω_0 as per the Zeeman splitting.

In any case, three data points are not enough to unambiguously identify the correct behavior,
calling for new and dedicated NMR experiments on the issue of anomalous spin transport in one-
dimensional spin chains. In particular, we believe that the present numerical abilities to efficiently

simulate the microscopic dynamics of interacting 1D quantum models could greatly help in guiding experiments.

The behavior $\Upsilon(T) \propto T^2$ for $T \ll J$ is compatible with experimental observations

We approximate the real part of the spin-spin correlation $\mathfrak{Re}\, C(T, x = 0, t)$ by $\Upsilon(T)t^{-2/3}$, which is the correct behavior in the long-time limit, see Fig. 2 in the main text. We get for the NMR relaxation rate,

$$\frac{1}{T_1} \sim \int_0^{1/\omega_0} \mathfrak{Re}\, C(T, x = 0, t)\, \mathrm{d}t \ \sim \ \Upsilon(T)\omega_0^{-1/3} \implies \frac{1}{T_1} \sim T^2 \omega_0^{-1/3} \ \text{ for } \ T \ll J, \qquad (3.18)$$

where we found that $\Upsilon(T) \sim T^2$ for $T \ll J$, see Fig. 3(b) in the main text. As discussed in the main text, $\Upsilon(T)$ relates to the temperature dependence of the parameters of the KPZ equation: $\chi_s \lambda_{\mathrm{KPZ}}^{-2/3} f_{\mathrm{KPZ}}(0) \sim \Upsilon(T)$.

In Fig. 4(a) of Ref. [361], the authors find that for $T \ll J$, the NMR relaxation rate of Sr_2CuO_3 at fixed frequency ω_0 may be approximated by an empirical form $1/T_1 \approx aT + bT^2$ for $T \ll J$ with a and b fitting constants. Up to the term with linear temperature dependence aT, this is the behavior obtained in Eq. (3.18).

Neglecting the experimental data points for very low temperatures ($T \lesssim 100\,\mathrm{K}$), the experimental data of Fig. 4(a) in Ref. [361] is compatible with $1/T_1 \sim T^2$. Substituting the real part of the correlator by its asymptotic behavior in Eq. (3.18) becomes less and less valid at very low temperatures: the low-temperature physics of the real part of the correlator, not taken into account in the approximation of Eq. (3.18) becomes dominant over high-temperature superdiffusive regime. In other words, in the time window $t \in [0, 1/\omega_0]$, the two regimes coexist with the low-temperature one for $t \lesssim t^\star$ and the high-temperature one for $t \gtrsim t^\star$, with $t^\star \sim 1/T$ (see main text). In Eq. (3.18), it is assumed that the high-temperature regime is dominant. In this picture, we interpret the small flattening observed for very low temperatures ($T \lesssim 100$ K) in Fig. 4(a) of Ref. [361], and which gives rise to the linear term aT, as the onset of low-temperature physics characterized by $1/T_1 \simeq \ln^{-1/2}(J/T)$ [359, 23, 90]. In fact, this logarithmic divergence was reported in Ref. [359] for the same compound (Sr_2CuO_3) for temperatures $T/J \lesssim 0.05$, corresponding to $T \simeq 100$ K, i.e., the regime where a linear term aT is necessary to fit the experimental $1/T_1$ data.

For these reasons, we believe that the behavior $1/T_1 \sim T^2$ reported in Eq. (3.18) is compatible with earlier experimental measurements on Sr_2CuO_3 [361], and relates to the temperature dependence of the parameters of the KPZ equation.

3.3.4 KPZ Crossover Parameter Fitting

Real part versus imaginary part of the dynamical spin-spin correlation

While we display the norm of the spin-spin correlation function in the main text, we compute both the real and imaginary parts. We show them independently in Fig. 3.26. We observe that the real
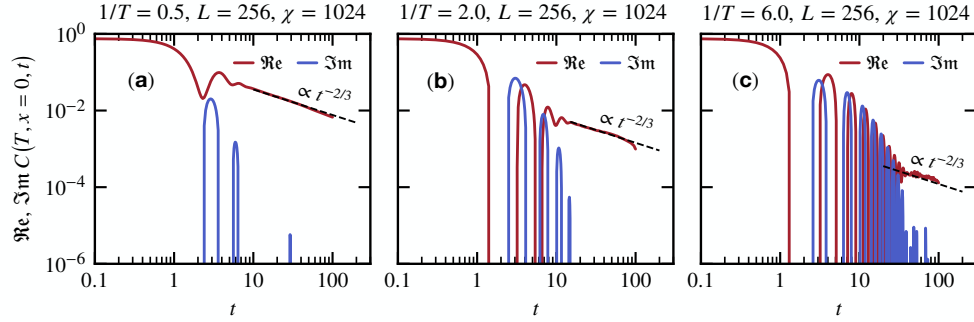
Figure 3.26: Time dependence of the real part "$\mathfrak{Re}$" and imaginary part "$\mathfrak{Im}$" part of the spin-spin correlation of Eq. (2) in the main text at $x = 0$. Simulations obtained for $L = 256$ and $\chi = 1024$ at three different temperatures (**a**) $1/T = 0.5$, (**b**) $1/T = 2.0$, and (**c**) $1/T = 6.0$. We observe that the superdiffusive power-law regime $\propto t^{-2/3}$ only holds for the real part (dashed black line) and that in this regime we have $|\mathfrak{Im}\, C(T, x = 0, t)| \ll |\mathfrak{Re}\, C(T, x = 0, t)|$.

part hosts the characteristic power-law dependence $\propto t^{-2/3}$, not the imaginary part. In fact, in the hydrodynamics regime, we find that $|\mathfrak{Im}\, C(T, x, t)| \ll |\mathfrak{Re}\, C(T, x, t)|$, meaning that at long time, the imaginary part plays no role in the superdiffusive dynamics of the spin-1/2 Heisenberg chain.

Low-temperature versus zero temperature

By plotting the different system sizes for the spin-spin correlation of Eq. (2) in the main text at $x = 0$ and $T = 0$, see Fig. 3.27(e) we show that the "flattening" observed at long times is a finite size effect. In Figs. 3.27(a)–3.27(d) we show the effect of the finite bond dimension, which is qualitatively very small.

Our data confirm the $\propto 1/t$ decay (up to logarithmic corrections) of the $x = 0$ spin-spin correlation at zero temperature for the spin-1/2 Heisenberg chain [271, 270] in Fig. 3.27(e). Including logarithmic corrections, the decay follows $\propto \ln^{1/2}(t/t_0)/t$, with $t_0 \approx 0.5$ a fitting parameter.

We also confirm that the finite-temperature data (down to $1/T = 6.0$ in the main text) is actually not small enough to observe the genuine low-temperature dynamics. We see in Fig. 3.28 that at least $1/T \gtrsim 20.0$ is required to have an overlap between zero-temperature and finite-temperature data in a reasonable time window. This rather slow convergence of the finite-temperature data onto the zero-temperature ones is also observed for the spatial dependence at $t = 0$ in Fig. 3.29(a). It is understood from the absolute value of the thermal correlation length of Eq. (3.19).

Note that the numerical simulations for zero temperature $T = 0$ are carried out with a slightly different method than for $T > 0$. In particular, we do not need to use the trick representing a mixed state as a pure state in an enlarged Hilbert space, the state at $T = 0$ being a pure state (it is the ground state). The ground state is obtained with the density matrix renormalization
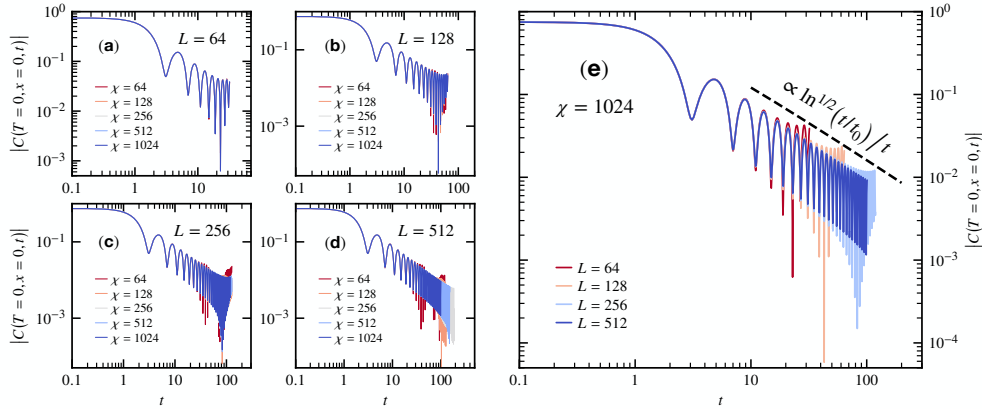
Figure 3.27: Time dependence of the norm of the spin-spin correlation of Eq. (2) in the main text at $x = 0$ for various system sizes $L = 64, 128$, and 256 and bond dimensions $\chi = 64, 128, 256, 512$, and 1024 at zero temperature ($T = 0$). **(a)** $L = 64$, **(b)** $L = 128$, **(c)** $L = 256$, and **(d)** $L = 512$ for various bond dimensions χ. **(e)** $\chi = 1024$ for various system sizes L. The dashed line is a fit of the form $\propto \ln^{1/2}(t/t_0)/t$, with $t_0 \approx 0.5$ a fitting parameter.

group algorithm [385, 316, 108], and the time evolution is then performed using time-evolving block decimation algorithm [376] along with a fourth-order Trotter decomposition [148] with step $\delta = 0.1$ leading to a negligible discretization error $O(\delta^5)$.

Temperature dependence of the correlation length

The thermal correlation length ξ of the spin-1/2 Heisenberg chain diverges at low temperature as $1/T$, plus additional log corrections which at first order gives [258],

$$\xi \simeq \frac{1}{2T}\left[1 + \frac{1}{2\ln(T/T_0)}\right]^{-1}, \tag{3.19}$$

with $T_0 \approx 2.68$ a nonuniversal constant. Here, we have used the value of T_0 obtained in Ref. [258] computed by the thermal Bethe ansatz. The agreement in Fig. 3.29 is extremely good for $1/T \gtrsim 5$. Yet, for the range of temperatures considered in this work, the data could be fitted equally well without the log corrections.

The data of Fig. 3.29 together with Eq. (3.19) shows why one needs to go to extremely low temperatures to observe the genuine low-temperature physics of the spin-1/2 Heisenberg chain: the prefactor of the temperature dependence of the correlation length $\xi \simeq 1/2T$ is small. It explains why in the time-dependent data of Fig. 3.28 it is difficult to observe a good overlap between zero-temperature and finite-temperature data for the temperatures accessible in this work; this overlap is equally hard to observe for the spatial dependence in Fig. 3.29(a).
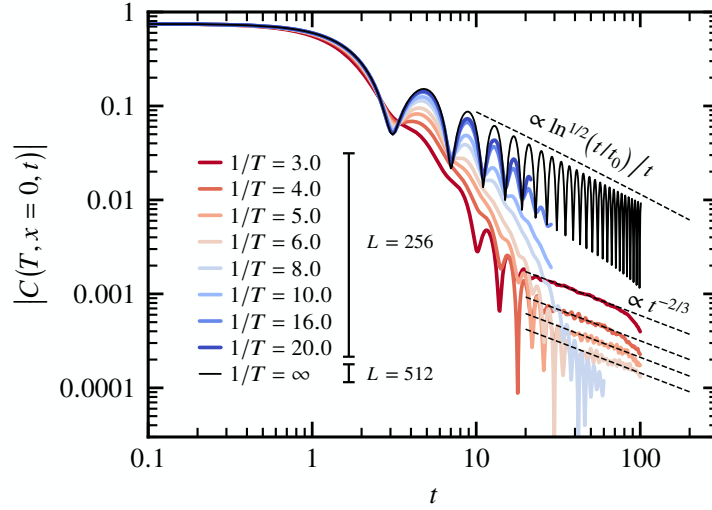
Figure 3.28: Time dependence of the norm of the spin-spin correlation of Eq. (2) in the main text at $x = 0$ for various temperatures T. Simulations obtained for $L = 256$ with $\chi = 1024$ at finite temperature and for $L = 512$ with $\chi = 1024$ at zero temperature. Same data as in Fig. 2 of the main text plus the zero temperature ($1/T = \infty$), $1/T = 8.0$, $1/T = 10.0$, $1/T = 16.0$, and , $1/T = 20.0$ data. The dashed line next to the zero temperature data is a fit of the form $\propto \ln^{1/2}(t/t_0)/t$, with $t_0 \approx 0.5$ a fitting parameter.

Temperature dependence of the parameters of the KPZ equation

By identifying the prefactor of $C_{\mathrm{KPZ}}(x = 0, t)$ of Eq. (4) in the main text with the prefactor $\Upsilon(T)$ of the power-law decay $\propto t^{-2/3}$ shown in Fig. 3.30(a), we find $\Upsilon(T) = 0.13(1)T^2$ for $T \lesssim 1$, and therefore that $\chi_{\mathrm{s}} \lambda_{\mathrm{KPZ}}^{-2/3} f_{\mathrm{KPZ}}(0) \propto T^2$. It is established that in this temperature range, the static spin susceptibility of the spin-1/2 Heisenberg chain takes the form [100],

$$\chi_{\mathrm{s}}(T) = \sum_x \left\langle \hat{\boldsymbol{S}}_x \cdot \hat{\boldsymbol{S}}_0 \right\rangle \simeq \frac{3T}{\pi^2} \left[1 - \frac{1}{2\ln(T/T_0')} \right], \tag{3.20}$$

with $T_0' \approx 7.7$ a nonuniversal constant obtained in Ref. [100] through Bethe ansatz (there are also higher order log corrections). The form of Eq. (3.20) is verified in Fig. 3.30(b). Isolating λ_{KPZ}, we find that,

$$\lambda_{\mathrm{KPZ}}(T) = \left(\frac{\Upsilon}{\chi_{\mathrm{s}} f_{\mathrm{KPZ}}(0)} \right)^{-3/2} \simeq \left\{ \frac{0.13(1)T\pi^2}{3 f_{\mathrm{KPZ}}(0)} \left[1 - \frac{1}{2\ln(T/T_0')} \right]^{-1} \right\}^{-3/2}, \tag{3.21}$$

which we plot in Fig. 3.30(c). The high-temperature data points are compatible with Ref. [82].
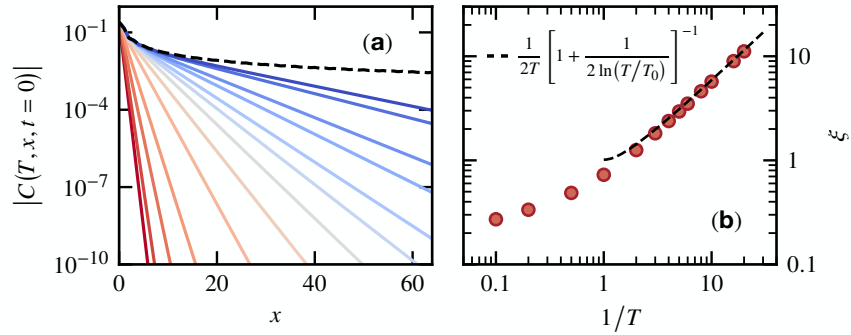
Figure 3.29: (**a**) Spatial dependence of the norm of the spin-spin correlation of Eq. (2) in the main text at $t = 0$ for system size $L = 256$ and bond dimension $\chi = 1024$. From the lower left corner to the upper right one, the solid lines correspond to the following temperatures: $1/T = 0.1, 0.2, 0.5, 1.0, 2.0, 3.0, 4.0, 5.0, 8.0, 10.0, 16.0,$ and 20.0. The dashed line is the zero temperature data ($1/T = \infty$). Except for the zero temperature data which decay as $\propto \ln^{1/2}(x/x_0)/x$, the finite temperature data decay exponentially at long distance x. A fit of the form $\propto \exp(-x/\xi)$ gives access to the correlation length ξ. (**b**) Correlation length ξ plotted versus the inverse temperature $1/T$. The dashed line is the expression of Eq. (3.19) valid as $T \to 0$ and derived in Ref. [258] with $T_0 \approx 2.68$.
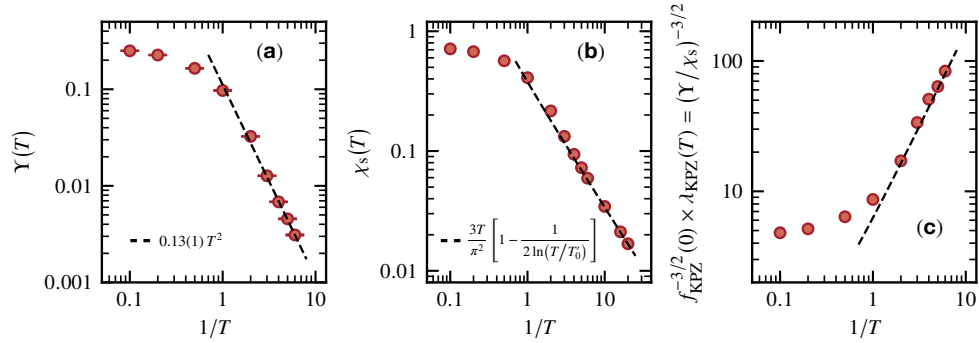
Figure 3.30: (**a**) Same as Fig. 3(a) in the main text. Temperature dependence of the prefactor $\Upsilon(T)$ of the algebraic decay $\propto t^{-2/3}$ for superdiffusive hydrodynamics at $x = 0$. At low temperatures $T \lesssim 1$, it follows a quadratic dependence $\propto T^2$ (dashed line). (**b**) Temperature dependence of the static spin susceptibility $\chi_s(T)$ defined in Eq. (3.20). The dashed line is the expression reported in Eq. (3.20) valid as $T \to 0$ and derived in Ref. [100] with $T_0' \approx 7.7$. (**c**) By identifying $\Upsilon(T) = \chi_s \lambda_{\text{KPZ}}^{-2/3} f_{\text{KPZ}}(0)$, we get $f_{\text{KPZ}}^{-3/2}(0) \times \lambda_{\text{KPZ}}(T) = (\Upsilon/\chi_s)^{-3/2}$, and plot its temperature dependence. Based on the reported results for $\Upsilon(T)$ and $\chi_s(T)$, the dashed line has a dominant $\propto T^{-3/2}$ behavior plus additional log corrections originating from $\chi_s(T)$, see Eq. (3.21).

Spatial dependence of the crossover time

We show in Fig. 3.31 the temperature dependence of the prefactor of the spatial dependence of $t^\star(x, T)$ of Eq. (5) in the main text, i.e., the term $\propto |x|^{3/2}$. It is extracted from a least-square fitting of the data of Fig. 4(b) of the main text. While it fluctuates slightly from one temperature to the next, there is no clear trend observed, and the data is consistent with a constant prefactor with value 0.17(3).
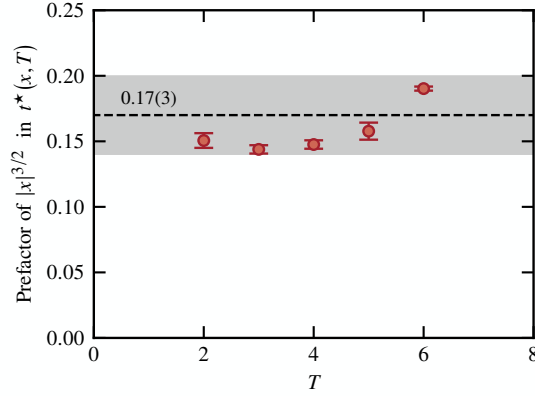
Figure 3.31: Temperature dependence of the prefactor of the spatial dependence of $t^\star(x, T)$ of Eq. (5) in the main text. The prefactor, which is plotted here, is extracted from a least-square fitting of the data of Fig. 4(b) of the main text. It is roughly independent of temperature with a value compatible with 0.17(3).

Extraction of the crossover time from the microscopic simulations

There is a degree of appreciation in defining the crossover time $t^\star(T, x)$ from the numerical simulations, precisely because it is related to a crossover and not, e.g., a sharp transition. We have defined two quantities to extract $t^\star(T, x)$,

$$\mathsf{R}_\mathsf{A}(T, x, t) = \overline{\left[\frac{\left|\left|C(T, x, t)\right| - \Upsilon(T, x)t^{-3/2}\right|}{\left|C(T, x, t)\right|}\right]}^{t\pm 2} \quad , \text{ and } \quad \mathsf{R}_\mathsf{B}(T, x, t) = \overline{\left|\frac{\Im\mathfrak{m}\ C(T, x, t)}{\mathfrak{Re}\ C(T, x, t)}\right|}^{t\pm 2}. \quad (3.22)$$

The first one returns the relative difference between the norm of the spin-spin correlation of Eq. (2) in the main text with the superdiffusive decay $\Upsilon(T, x)t^{-3/2}$. The second one returns the relative weight of the imaginary part $\Im\mathfrak{m}$ versus the real part $\mathfrak{Re}$ of the spin-spin correlation of Eq. (2) in the main text. In Eq. (3.22), T and x are set to given values and the quantities are looked at versus the time t. The symbol $\overline{(-)}^{t\pm 2}$ means that the data at time t actually corresponds an average from

the range $\in [t-2, t+2]$. The effect is to smoothen the local oscillations in $C(T, x, t)$, and make the extraction more reliable.
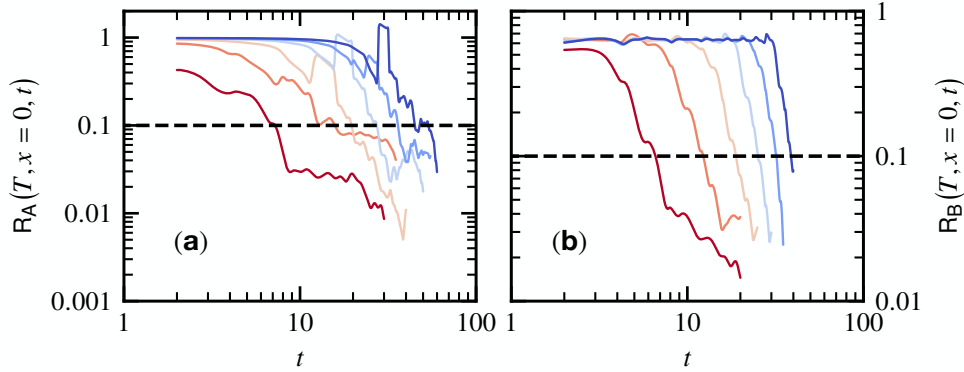
Figure 3.32: Panels (**a**) and (**b**) correspond to the quantities $R_A(T, x = 0, t)$ and $R_B(T, x = 0, t)$ of Eq. (3.22), respectively. The system size is $L = 256$ and the bond dimension $\chi = 1024$. From the lower left corner to the upper right one, the solid lines correspond to the following temperatures: $1/T = 1.0, 2.0, 3.0, 4.0, 5.0$, and 6.0. The intersection of the data with the horizontal dashed line at $R_{A,B}(T, x = 0, t) = 0.1$ is used to extract the crossover time $t^\star(T, x)$.

The time at which $R_A(T, x, t)$ and $R_B(T, x, t)$ hit the value 0.1 is used as the definition of the crossover time $t^\star(T, x)$. The definition of $R_B(T, x, t)$ uses the fact that in the hydrodynamics regime we have $|\Im C(T, x, t)| \ll |\Re C(T, x, t)|$. Both quantities lead to comparable estimates of $t^\star(T, x)$. The error bar reported on $t^\star(T, x)$ reflects the small difference between the two estimates. As an example, we show $R_A(T, x, t)$ and $R_B(T, x, t)$ for $x = 0$ in Fig. 3.32. The corresponding value $t^\star(T, x = 0)$ is reported in Fig. 3(a) in the main text.

Chapter 4

Quantum Spin Liquids and Triangular Lattice Compounds

In this chapter, I discuss quantum spin liquids (QSL), with a focus on those found in triangular lattice models and materials. A QSL is an exotic phase of matter with no long-range order even down to zero temperature. In the triangular lattice systems studied here, the antiferromagnetic coupling, together with the lattice geometry, gives rise to frustration in the spins. Specifically, once one spin of a triangle is fixed, the antiferromagnetic coupling leads to anti-parallel neighbors, but the triangular lattice forbids this pattern. The result is a state with strong quantum fluctuations, often times with fractionalized quasi-particle excitations, where the properties of these materials require a quantum mechanical description.

In Sec. 4.1 I discuss the so-called $J_1 - J_2$ Heisenberg model, which hosts a QSL phase as one of the three ground state phases in the model. I primarily examine the dynamical structure factor $S(q, \omega)$, the quantity relevant for neutron scattering experiments. I further discuss the technique used to calculate $S(q, \omega)$ within the MPS framework, and how to overcome some of the hurdles present in simulating two-dimensional systems. In Sec. 4.2, I discuss a collaboration with the neutron scattering group at Oak Ridge National Lab examining the triangular lattice compound $KYbSe_2$. Lastly, in Sec. 4.3 I discuss a collaboration with a neutron scattering group at Duke examining the triangular lattice compound $YbZn_2GaO_5$.

4.1 Spectral Function of the $J_1 - J_2$ Heisenberg Model on the Triangular Lattice

4.1.1 Introduction

Two-dimensional quantum systems host exciting physics: reduced dimensionality leads to strong quantum fluctuations, yet provides more possibilities than in one dimension as continuous symmetry can be spontaneously broken and lead to long-range order [245, 155, 248, 120, 300]. While such conventional ordered states of matter are fairly well understood, some disordered states remain

elusive. Among those are quantum spin liquids (QSL) found in frustrated quantum magnets [305, 200, 322, 39] as a result of competing ordered phases. These states possess no long-range order, even at zero temperature, and often result in fractionalized excitations with non-trivial statistics.

One of the most promising geometries for realizing a QSL phase is the triangular lattice, which has a rich history starting with Anderson's proposed resonating valence bond state [14]. However, the simplest lattice spin model, namely the spin-1/2 nearest-neighbor antiferromagnetic Heisenberg model, has been shown to have 120° magnetic long-range ordering [167, 188, 338, 66, 27, 52, 430, 387]. Yet, quantum fluctuations lead to the order parameter magnitude being significantly smaller than its classical value, implying the order is weak and potentially easy to disrupt. For instance, with the introduction of a small next-nearest-neighbor interaction, this model exhibits a QSL phase [434, 163, 174, 299, 389, 124, 160]. Early studies using the density matrix renormalization group (DMRG) [386] suggested that the QSL phase was a $\mathbb{Z}_2$ gapped QSL [434, 163, 299]. This was later challenged by simulations using variational quantum Monte Carlo (QMC), which found that a gapless $U(1)$ Dirac spin liquid was most energetically favorable [174]. This was later supported by a DMRG study on an infinite cylinder with an external Aharonov-Bohm flux, claiming unambiguous evidence for a gapless $U(1)$ Dirac spin liquid [160]. However, this has been challenged by a recent DMRG study [186], as well as by Schwinger-boson theory [117], suggesting the phase is a gapped $\mathbb{Z}_2$ QSL.

The simplicity and realistic form of the Hamiltonian has attracted many experiments to probe triangular lattice materials, in the quest for a realization of such a QSL phase. Experiments conducted on triangular lattice systems range from organic compounds such as $k-(\text{BEDT-TTF})_2\text{Cu}_2(\text{CN})_3$, $\text{Et}_n\text{Me}_{4-n}\text{Sb}[\text{Pd}(\text{DMIT})_2]_2$, and other similar structures [409, 276, 240, 3, 319, 333, 273, 102, 253, 112, 275, 402, 247, 265, 297, 177, 114, 242, 201, 251, 146, 208, 240, 179, 178, 115, 37, 405, 193, 257, 406, 408, 407, 241], to $\text{Ba}_3\text{CoSb}_2\text{O}_9$ [334, 354, 255, 202, 284, 233, 176, 189, 211, 237, 419], and many Yb^{3+}-based materials [217, 222, 219, 400, 215, 262, 214, 221, 422, 18, 328, 423, 85, 33, 289, 287, 303, 416, 224, 336, 336, 396, 87, 238, 394, 17, 418, 133, 428, 268, 398, 74, 397, 234, 393, 291, 235, 313]. In particular, recent neutron scattering data in KYbSe_2 has shown that the material is well modelled by a spin one-half Heisenberg model on a triangular lattice with nearest- and next-nearest-neighbor antiferromagnetic interactions, i.e., a $J_1 - J_2$ Heisenberg model [313] (further details in Sec. 4.2). The authors also found critical scaling in the dynamical structure factor near the corner of the Brillouin zone, suggesting the close proximity of this material to a second-order quantum phase transition.

Despite a plethora of experimental studies in triangular lattice compounds, the presence and nature of a QSL phase is still under debate, as smoking-gun signals for such phases are challenging to identify. One main signature is a lack of long-range order, which is also present in other phases such as spin-glass states [98, 292]. In fact, the actively studied spin liquid candidate YbMgGaO_4 has been conjectured to be a spin-glass, based on susceptibility measurements in its sister compound YbZnGaO_4 [235]. Another key signature is the presence of fractionalized quasi-particles which are hard to detect directly. Recent proposals to look at the entanglement content of the triangular lattice compound KYbSe_2 [313], through the quantum Fisher information [169, 149] and other entanglement measures [43, 70, 13, 295, 21, 12], may prove fruitful. This challenge calls for

further theoretical understanding, and improved numerical simulations of experimentally relevant quantities to identify signatures of QSL phases.

Neutron scattering is potentially an excellent experimental tool to detect quantum spin liquid physics, as it directly probes the excitations in the system through the spin-spin correlation function [366, 353]. On the theoretical side, making a direct comparison with neutron scattering experiments requires calculating the dynamical structure factor, which is notoriously difficult to compute. QMC struggles to probe this quantity directly, and relies on analytic continuation from imaginary time simulations [181]. However, analytic continuation is numerically ill-posed due to the inherent statistical uncertainty of Monte Carlo sampling. Nevertheless, QMC supplemented by the maximum entropy method [337, 132] for analytic continuation or the stochastic analytic continuation [323] is still the dominant method to probe spectral functions in two- and higher-dimensional systems, with reliable results obtained in various frustration-free contexts [283, 324, 94, 335, 51, 164]. Unfortunately, frustrated systems, such as the triangular lattice Heisenberg model, plague QMC with the infamous sign problem, preventing efficient simulations [230, 365].

In one dimension, DMRG [386], and the later reformulation in terms of matrix product states (MPS) [315], have been revolutionary. Their main success is due to the entanglement area-law in gapped systems, which leads to a finite entanglement entropy even in the thermodynamic limit [147]. Even for gapless one-dimensional systems, the deviations from the exact answer are understood through a finite-entanglement scaling analysis [278]. However, in two dimensions, an area law state still has an entanglement entropy that grows with the system size, which makes standard MPS calculations struggle to capture the thermodynamic limit. Other tensor-network-based approaches, such as projected entangled pair states (PEPS) [370, 68, 67], have been proposed to work in higher dimensions. Recent work using PEPS to study the dynamical structure factor in a model near a QSL phase [64], has found great accuracy in comparison with neutron scattering experiments in $Ba_3CoSb_2O_9$ [237]. Other methods for two-dimensional spectral functions include higher-order spin wave theory [62, 351, 63, 249], series expansion methods [431, 429], and variational QMC [106, 104].

Utilizing DMRG on the triangular lattice wrapped into a cylinder, yielding a quasi-one-dimensional system, has proven useful in studying static properties of QSL states [434, 163, 299, 160, 123, 356, 8, 72, 355, 187, 186]. We focus on this approach in this study, and extend this work into the realm of dynamics, with a similar method as was used in Ref. [368]. We use this approach to examine the full phase diagram of the $J_1 - J_2$ Heisenberg model on the triangular lattice.

4.1.2 Models, Definitions, and Methods

In this work, we primarily focus on the spin one-half Heisenberg model with nearest and next-nearest neighboring interactions on the triangular lattice,

$$H = J_1 \sum_{\langle i,j \rangle} \boldsymbol{S}_i \cdot \boldsymbol{S}_j + J_2 \sum_{\langle\langle i,j \rangle\rangle} \boldsymbol{S}_i \cdot \boldsymbol{S}_j, \tag{4.1}$$
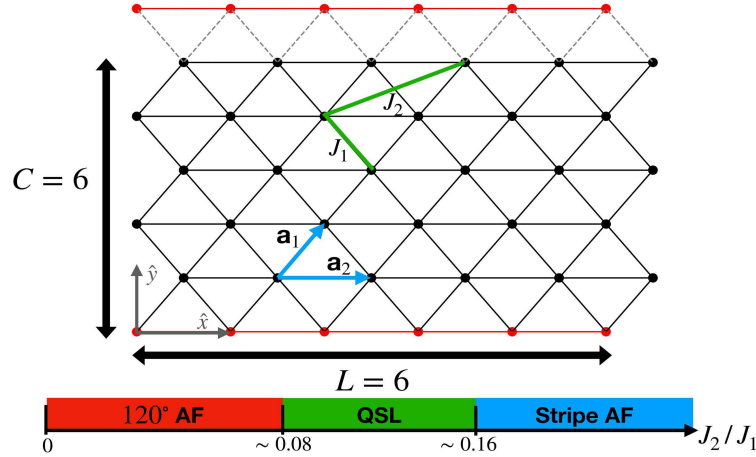
Figure 4.1: A 6×6 triangular lattice illustrating the relevant parameters used in this work. An example of a nearest neighbor couplings J_1 and next-nearest neighbor couplings J_2 are shown in green. We also show the circumference C, length L. The lattice vectors $\boldsymbol{a_1} = (1/2, \sqrt{3}/2)$ and $\boldsymbol{a_2} = (1, 0)$ are shown in blue. We also show the three expected phases of the Hamiltonian given in Eq. (4.1) and the approximate phase boundaries [174].

where $\boldsymbol{S}_i = (S_i^x, S_i^y, S_i^z)$ are spin-$1/2$ operators; $\langle i, j \rangle$ and $\langle\langle i, j \rangle\rangle$ denote nearest- and next-nearest neighbor exchange interactions, respectively. We show in Fig. 4.1 the lattice with circumference C (we will use periodic boundary conditions along this direction in the following), length L, lattice vectors $\boldsymbol{a_1}$ and $\boldsymbol{a_2}$, the couplings J_1 and J_2, and the three expected phases of this model [434, 163, 174, 299, 389, 124, 160]. We also examine the same Hamiltonian on the square lattice with only nearest-neighbor interactions ($J_2 = 0$, Heisenberg model) which serves as a benchmark to compare our results against quantum Monte Carlo supplemented by analytic continuation following Ref. [324]. We set $\hbar = J_1 = 1$ in the following.

Spectral Function

The spectral function of interest in this study is the dynamical spin structure factor, relevant for neutron scattering experiments [366, 353], defined by

$$S(\boldsymbol{q}, \omega) = \frac{1}{N} \sum_{\boldsymbol{x}} \int_0^{+\infty} \frac{\mathrm{d}t}{2\pi} e^{i(\omega t - \boldsymbol{q} \cdot \boldsymbol{x})} G(\boldsymbol{x}, t), \tag{4.2}$$

with N the number of sites in the lattice. $G(\boldsymbol{x}, t)$ is a two-point spin-spin correlation function defined by

$$G(\boldsymbol{x}, t) = \langle \Omega | \boldsymbol{S_x}(t) \cdot \boldsymbol{S_c}(0) | \Omega \rangle, \tag{4.3}$$

with $\boldsymbol{c}$ being the center site in the lattice taken to be the origin when defining $\boldsymbol{x}$, and $|\Omega\rangle$ the ground state of the Hamiltonian H with energy E_0.

Another useful related quantity we examine is the static spin structure factor defined by

$$S(\boldsymbol{q}) = \frac{1}{N} \sum_{\boldsymbol{x}} \cos(\boldsymbol{q} \cdot \boldsymbol{x}) G(\boldsymbol{x}, t = 0). \tag{4.4}$$

Since the Hamiltonian we examine is rotationally invariant and the ground state on a finite system cannot spontaneously break the continuous SU(2) symmetry of the model (4.1), it suffices to just consider the z-component of the spin. Hence, what we compute in this study reduces to

$$G(\boldsymbol{x}, t) = 3 \langle \Omega | S_{\boldsymbol{x}}^z(t) S_{\boldsymbol{c}}^z | \Omega \rangle . \tag{4.5}$$

We drop the factor of 3 in this work. There are methods to compute the frequency dependence of Eq. (4.2) directly, such as the correction vector method [256], and the Chebyshev expansion method [157, 391]. However, both of these methods require many operator-state products between some initial state and the Hamiltonian H. In two dimensions, the bond dimension of the matrix product operator (MPO) representation of H is large, making such operations quite inefficient.

Instead, we compute the correlation functions directly by writing,

$$\begin{aligned} G(\boldsymbol{x}, t) &= \langle \Omega | e^{iHt} S_{\boldsymbol{x}}^z e^{-iHt} S_c^z | \Omega \rangle \\ &= e^{iE_0 t} \langle \Omega | S_{\boldsymbol{x}}^z e^{-iHt} S_c^z | \Omega \rangle . \end{aligned} \tag{4.6}$$

Then the computation of $G(\boldsymbol{x}, t)$ is reduced to finding the ground state $|\Omega\rangle$, time evolving the state $S_c^z |\Omega\rangle$, and then computing its matrix elements of $S_{\boldsymbol{x}}^z$ with the ground state for all positions $\boldsymbol{x}$.

In the definition of $S(\boldsymbol{q}, \omega)$ in Eq. (4.2), formally infinite time and infinite space data is required, but this is not possible numerically. This forces us to truncate at a maximum distance $\boldsymbol{R}_{\max}$ and time $T_{\max}$. Introducing such a cutoff is not unique, and we discuss practical advice on how to extract the dynamical structure factor from only finite data in the following.

Finite Geometry

How to approximately represent the infinite system with a finite one is not unique, and each representation has its own pros and cons. Possibly the first choice to consider is just a finite patch of the infinite system, which we will call open boundary conditions. When using MPS, we need to represent the finite system as a quasi-one-dimensional system, and doing this creates long-range interactions. If the two-dimensional system has a depth C and a length $L \geq C$, then the long-range interactions are at best $O(C)$. If we use the the standard Schur form to represent H as an MPO [246], then the bond dimension will also be $O(C)$. If we roll the lattice into a cylinder with circumference C, this causes a minimal decrease in computational efficiency as compared to open boundary conditions. Since this partially restores the translation symmetry of the infinite system with a marginal penalty, this is considered standard practice. Due to computational limitations, C is quite small, and so we take $L \gg C$.
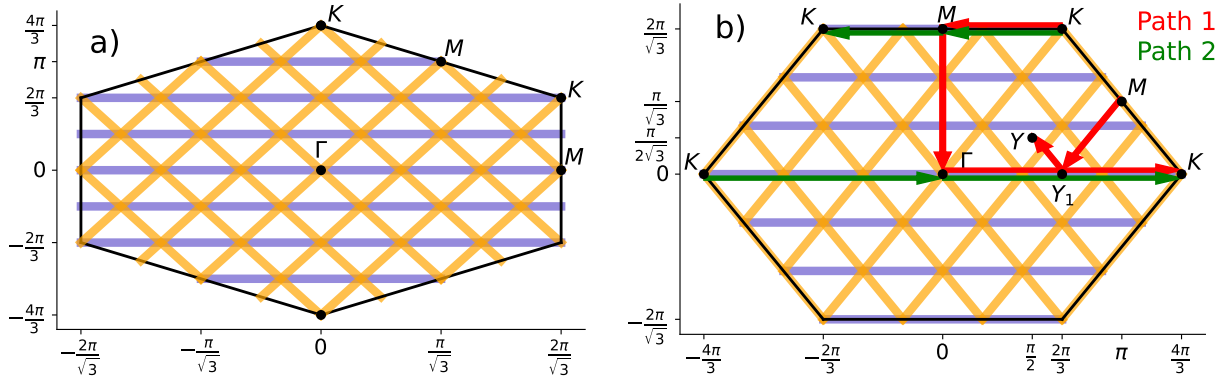
Figure 4.2: Allowed q values highlighted in blue for the triangular lattice wrapped into a cylinder with a circumference $C = 6$. We form the cylinder using YC boundary conditions in a) and XC boundary conditions in b). The orange lines in both figures are the q values that are rotations of the allowed q values by the C_6 symmetry of the triangular lattice. In green and red are the two paths through the Brillouin zone that we examine. We note that $Y = M/2$ and $Y_1 = K/2$.

Since C is small, this restricts the allowed q values quite dramatically. How one forms a cylinder out of the triangular lattice is subtle, as the choice of boundary conditions modifies which momenta in the Brillouin zone are allowed. In the literature, there are two primary boundary conditions for the triangular lattice denoted as the XC and YC geometries [356]. The boundary conditions in Fig. 4.1 is the XC boundary condition, and the YC boundary condition would be if we identified the left and right edges rather than the top and bottom. In Ref. [356], the authors recommend the YC boundary conditions generically, as the circumference is larger in units of the lattice spacing for the same number of lattice points. However, by examining Fig. 4.2, we see that the q values permitted by these two geometries are dramatically different. Since most of the high symmetry q values are permitted by the XC geometry, we use the XC geometry throughout this work.

To find the allowed $q = (q_x, q_y)$ values for the XC geometry, we note that two conditions need to be met due to the periodic boundary conditions along the circumference and open boundary conditions along the length. For the periodic boundary conditions, we need

$$e^{iq \cdot C a_1} = e^{iq \cdot \frac{C}{2} a_2} \implies e^{i\frac{\sqrt{3}}{2} C q_y} = e^{i2\pi n} \tag{4.7}$$

$$q_y = \frac{4\pi}{\sqrt{3}C}n, \quad n \in \left(-\frac{C}{2}, \frac{C}{2}\right] \cap \mathbb{Z} \tag{4.8}$$

The allowed values for q_x are the standard allowed values for a system with length L, meaning

$$q_x = \frac{2\pi}{L}n, \quad n \in \left(-\frac{L}{2}, \frac{L}{2}\right] \cap \mathbb{Z}. \tag{4.9}$$

We can improve upon the heavily restricted allowed $\boldsymbol{q}$ values by generating other points in the Brillouin zone by rotating the $\boldsymbol{q}$ value by a symmetry in the lattice, as discussed in Ref. [368]. In particular, if R is a rotation that leaves the lattice invariant, then in the thermodynamic limit any momentum resolved operator O satisfies

$$O(R\boldsymbol{q}) = O(\boldsymbol{q}). \tag{4.10}$$

We use this relation when examining quantities on the entire Brillouin zone, to fill in much of the Brillouin zone to gain a better glimpse into the thermodynamic result. We show the allowed $\boldsymbol{q}$ values in blue, and the additional $\boldsymbol{q}$ values generated in this manner in orange in Fig. 4.2.

Other geometries are possible, but we have found these choices the most relevant. Other possible procedures to form a cylinder out of the infinite plane are discussed in Ref. [356].

Time Evolution

The standard MPS time evolution procedure in one dimension is the Time-Evolving Block Decimation (TEBD) method [375]. This method expresses the time evolution operator in terms of unitary gates acting only on the bonds in the model. This method is exceptionally well-suited for models with only nearest neighbor interactions, but the quasi-one-dimensional systems we study here have long-range interactions. One can implement swap gates to bring distant sites near each other, and then apply the unitary gate, but this becomes inefficient rapidly as the circumference C is increased. Moreover, each time step in this method increases the bond dimension, which then requires a truncation of the resulting state, which introduces errors.

An in-depth discussion of the most common time evolution techniques for MPS can be found in Ref. [266]. In this work, we opt to use the Time-Dependent Variational Principle (TDVP) [137, 135, 138, 367, 412] to implement the time evolution. This method automatically finds the optimum time-evolved state at the given bond dimension, and obeys conservation laws such as energy.

For any finite system, Eq. (4.2) will be come a finite sum of delta functions, as opposed to an analytical function in the thermodynamic limit. To remedy this, we broaden the peaks by convolution with a distribution, typically a Gaussian. This also doubles to serve the role of controlling the truncation of the infinite time integral in a smooth way rather than a sharp cutoff at some max time $T_{\max}$. Formally, we write

$$G(\boldsymbol{x}, t) \longrightarrow f_\eta(t) G(\boldsymbol{x}, t) \tag{4.11}$$

Then we can choose f_η to be a properly normalized dampening factor. The typical choices for dampening are

$$f_\eta(t) = \begin{cases} \Theta\left(t - \eta^{-1}\right) & \text{Sharp} \\ e^{-\eta^2 t^2} & \text{Gaussian} \\ e^{-\eta|t|}/\pi & \text{Lorentzian} \end{cases} \tag{4.12}$$

The dampening factor labelled sharp is equivalent to truncation of the time integration in Eq. (4.2) at a maximum time $T_{\max} = \eta^{-1}$. The broadening factor is an inverse time scale that is taken to be $\eta \sim O(T_{\max}^{-1})$, where $T_{\max}$ is the maximum times reliably obtained during the time evolution process. The choice of dampening factor to use depends on the problem of interest, but the general purpose choice is the Gaussian dampening. Note though, that the introduction of broadening by a Gaussian will modify the intensity and sharpness of peaks in the spectrum, and so if precision in the peaks is required, using the sharp cutoff can be useful [308].

We want to note that there is nothing that prevents one from time evolving to arbitrarily large times, as this just requires longer run times of the simulations. However, it is not the case that the data is necessarily reliable for these larger times. To determine the reliability of the time evolved data, we use a physically motivated criterion, namely that the spectral function must be positive for all frequencies. We broaden the spectral function using the Gaussian dampening factor in Eq. (4.12), and we choose η as small as possible so that the spectral function is positive. The maximum time $T_{\max}$ for which the correlation function is reliable is approximated by $T_{\max} \sim \eta^{-1}$.

Fourier Transform

There are two Fourier transforms necessary to achieve $S(\boldsymbol{q}, \omega)$, one in space and one in time. Since we only have data for finite time and finite space, we must truncate the integrals in Eq. (4.2). One issue with just naively truncating Eq. (4.2) is that $S(\boldsymbol{q}, \omega)$ generically will acquire a non-zero imaginary part that is not physical. From there, one could only look at the real part, or the magnitude, but we propose an alternative that enforces reality of $S(\boldsymbol{q}, \omega)$.

If we have a translationally invariant system, then we have the following properties,

$$G(-\boldsymbol{x}, t) = G(\boldsymbol{x}, t) \text{ and } G(\boldsymbol{x}, -t) = G(\boldsymbol{x}, t)^*. \tag{4.13}$$

With these properties, we can write

$$S(\boldsymbol{q}, \omega) = \frac{1}{\pi N} \int_0^\infty \mathrm{d}t \sum_{\boldsymbol{x}} \cos(\boldsymbol{q} \cdot \boldsymbol{x})$$
$$\times \Big(\cos(\omega t)\mathsf{Re}G(\boldsymbol{x}, t) - \sin(\omega t)\mathsf{Im}G(\boldsymbol{x}, t) \Big). \tag{4.14}$$

Simulation Parameters

In these simulations, we always work with a cylinder of circumference $C = 6$ and length $L = 36$. We also use a bond dimension $\chi = 512$. The ground state is obtained using the DMRG [386, 315] working in the zero magnetization sector with the magnetization conserved. The time evolution is performed using single-site TDVP [137, 135, 138, 367, 412] with a time step of $\delta t = 0.1$, and a maximum time $T_{\max} = 40$. The simulations are performed in real-space, and the Fourier transform to $\boldsymbol{q}$ and ω is performed using Eq. (4.14), with a Gaussian broadening factor as in Eq. (4.12). The broadening width η used is $\eta^2 = 0.03$ for the square lattice, and $\eta^2 = 0.02$ for the triangular lattice in the 120° and QSL phases, and $\eta^2 = 0.05$ in the striped antiferromagnetic phase. For the triangular lattice, we use the XC geometry as described in Sec. 4.1.2. Our simulations utilize the ITensor library [108].
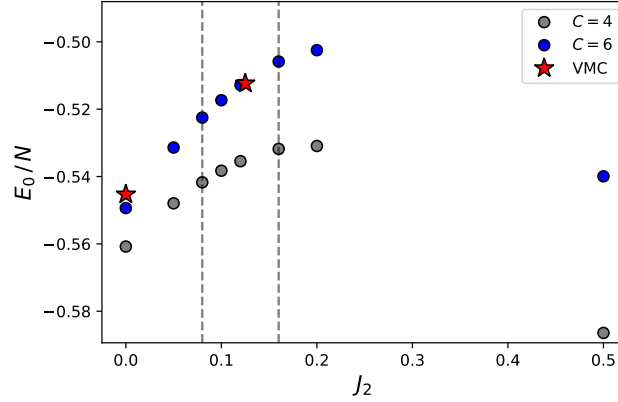
Figure 4.3: Ground state energy per site for the $J_1 - J_2$ Heisenberg model on the triangular lattice for the J_2 values examined in this study. To find the ground state, we used DMRG with a bond dimension $\chi = 512$. We use a cylindrical geometry with circumference C and length $L = C^2$. The stars represent the best estimate of the infinite system ground states, using variational QMC, reported in Ref. [174].

In Fig. 4.3 we show the ground state energy per site as a metric for the accuracy of the ground state. We note that with only two circumferences, a finite size scaling analysis is difficult. However, we also show the best estimates for the infinite system energy density for $J_2 = 0$ and $J_2 = 0.125$ reported in Ref. [174] as a reference.

4.1.3 Quantum Spin Liquid Signatures

There are currently three dominant predictions about the nature of quantum spin liquid ground state of the $J_1 - J_2$ Heisenberg model on the triangular lattice, given by Eq. (4.1). These predictions are a gapped $\mathbb{Z}_2$ spin liquid [434, 299, 163, 117, 186], a gapless $U(1)$ Dirac spin liquid [174, 104, 160], and a spinon Fermi surface [123]. In this work, we will focus on the signatures in the dynamical structure factor, $S(\boldsymbol{q}, \omega)$ in Eq. (4.2), for these three spin liquids. For all three spin liquid states, the low-energy theory is formulated in terms of spinons, which can be understood from the parton construction [305]. In this formalism, the spin operator is written as

$$\boldsymbol{S} = \frac{1}{2} f_\alpha^\dagger \boldsymbol{\sigma}_{\alpha\beta} f_\beta, \quad f_\alpha^\dagger f_\alpha = 1 \tag{4.15}$$

where f_α are spin-1/2 fermions, α, β represent either spin up or spin down, and repeated indices are summed over. This construction has an inherent $\mathbb{Z}_2$ and $U(1)$ redundancy. Because of this, the low-energy theory can be promoted to fermions coupled to either a $\mathbb{Z}_2$ or $U(1)$ gauge field, producing the associated quantum spin liquid state. In the case of gapped $\mathbb{Z}_2$ spin liquids, the spinons can be bosons, but a gapless state is unstable to boson condensation [305]. The signatures for each spin

Spin liquid state	Signature in $S(\boldsymbol{q}, \omega)$
Gapped $\mathbb{Z}_2$	∘ At the 120° transition, gap closes at only $\boldsymbol{q} = K$.
Gapless $U(1)$ Dirac	∘ gapless at $\boldsymbol{q} = K$ and $\boldsymbol{q} = M$.
Spinon Fermi surface	∘ V-shape at $\boldsymbol{q} = \Gamma$. ∘ Broad continuum. ∘ $S(\boldsymbol{q}, \omega = 0^+) > 0 \ \forall \boldsymbol{q}$.

Table 4.1: Table of the three spin liquid candidates, and their corresponding signatures in the dynamical structure factor, $S(\boldsymbol{q}, \omega)$, defined by Eq. (4.2).

liquid state is summarized in Table 4.1, and we provide an explanation for these predictions in this section.

First let us look at the $\mathbb{Z}_2$ spin liquid. In Ref. [380], the authors discuss two possibilities for a gapped $\mathbb{Z}_2$ spin liquid on the triangular lattice, called the zero-flux and π-flux states. In the zero-flux state, the spinon dispersion relation is minimized at the corner of the Brillouin zone, $\boldsymbol{q} = K$. The magnons, which are two-spinon bound states, thus order at $\boldsymbol{q} = 2K = K$. For the π-flux state, the spinon dispersion relation is minimized at $\boldsymbol{q} = Y$, and thus the magnon ordering wave-vector is $\boldsymbol{q} = 2Y = M$. As the next nearest neighbor coupling is tuned, the gap closes, leading to magnon-condensation and a continuous transition into an ordered state. Via this process, the zero-flux state leads to the 120° state, and the π-flux state leads to the stripe ordered phase. Recent neutron scattering experiments in KYbSe$_2$ suggest that the transition from the 120° to the spin liquid phase is second order [313]. This is also observed in a prior variational QMC study [174], and the authors also find that the striped to spin liquid phase transition is first order. These findings are not consistent with the π-flux state. Moreover, if the ground state is the zero-flux gapped $\mathbb{Z}_2$ QSL, then a signature to look for is the spectrum being gapless at $\boldsymbol{q} = K$, and only $\boldsymbol{q} = K$, at the transition point from the 120° to the spin liquid phase. We note that precisely this prediction was observed with the Schwinger-boson formalism starting from the 120° phase [313, 117].

Next, let us examine the $U(1)$ Dirac spin liquid state. The low-energy theory on the triangular lattice is $N_f = 4 \, \text{QED}_3$ [345]. In this theory, there are four spin-1/2 Dirac fermions (with two spin and two 'valley' labels), which correspond to two Dirac cones at $\boldsymbol{q} = \pm Y$ in the spinon dispersion relation. This theory permits two distinct types of gapless modes, fermion bilinears, and monopoles [345, 344, 151, 11]. There are in total 16 fermion bilinears [150], which produce gapless spin singlets and spin triplets at both $\boldsymbol{q} = \Gamma$ and $\boldsymbol{q} = M$ [345]. As for the monopoles, they produce spin-singlets at $\boldsymbol{q} = Y_1$, and spin-triplets at $\boldsymbol{q} = K$ [345, 344]. The dynamical structure factor probes spin-1 excitations, and thus can not detect the fermion bilinears and monopoles that are spin-singlets. Also, due to the $U(1)$ symmetry in Eq. (4.1), it follows that $S(\boldsymbol{q} = \Gamma, \omega) = 0$ for all ω, independent of the phase. This leaves that gapless modes should be detected at $\boldsymbol{q} = K$ and $\boldsymbol{q} = M$ if the ground state is a $U(1)$ Dirac spin liquid. This signature has been observed in a prior DMRG

calculation, where they looked at where the correlation length diverges under flux insertion [160]. We want to note that within mean field theory for the $U(1)$ Dirac spin liquid, without enforcing the half-filling constraint in Eq. (4.15), the spectrum is gapped at $q = K$ [326, 88]. However, enforcing the constraint via variational Monte Carlo has a dramatic effect on the spectrum, and produces a gapless mode at $q = K$ as expected [104]. The free fermion mean-field theory and the effect of the half-filling constraint on the spectrum can be seen in Fig. 8 of Ref. [104].

The last spin liquid state to talk about is the state with a spinon Fermi surface. The idea here is that the low-energy theory is described by a metallic state with a half-filled band, leading to a Fermi surface, and many low energy excitations [326, 212]. In Ref. [212], they start with a mean-field Hamiltonian for free fermions at half-filling of the form

$$
\begin{aligned}
H_{\text{MFT}} = -t_1 \sum_{\langle i,j \rangle, \alpha} f^{\dagger}_{i\alpha} f_{j\alpha} - t_2 \sum_{\langle\langle i,j \rangle\rangle, \alpha} f^{\dagger}_{i\alpha} f_{j\alpha} \\
-\mu \sum_{i,\alpha} f^{\dagger}_{i\alpha} f_{i\alpha}
\end{aligned}
\tag{4.16}
$$

This Hamiltonian is quadratic, and thus diagonalizable, and the chemical potential enforces half-filling. Then, the dynamical structure factor is given by Eq. (4.2), with

$$
G(\boldsymbol{x}, t) = \langle \Omega | S^{-}_{\boldsymbol{x}}(t) S^{+}_{\boldsymbol{c}}(0) | \Omega \rangle,
\tag{4.17}
$$

In terms of the fermion operators, we have

$$
S^{+}_{\boldsymbol{q}} = \sum_{\boldsymbol{k}} f^{\dagger}_{[\boldsymbol{k}+\boldsymbol{q}]\uparrow} f_{\boldsymbol{k}\downarrow}
\tag{4.18}
$$

This means that $S(\boldsymbol{q}, \omega = 0^{+}) > 0$ if $\boldsymbol{q}$ can be written as $\boldsymbol{k}_1 + \boldsymbol{k}_2$, with $\boldsymbol{k}_1, \boldsymbol{k}_2$ located at the Fermi-surface. Due to the half-filling constraint, this is actually possible for every $\boldsymbol{q}$. This model makes three predictions about the dynamical structure factor: (i) $S(\boldsymbol{q}, \omega = 0+) > 0 \ \forall \boldsymbol{q}$, (ii) a V-shape upper excitation edge near $\boldsymbol{q} = \Gamma$, and (iii) a broad continuum throughout the Brillouin zone, with no sharp magnon branches [326, 212, 305]. These features can be observed in Extended Data Figure 5 of Ref. [326], and Fig. 2 of Ref. [328]. Although we do not expect the spin liquid phase of the $J_1 - J_2$ Heisenberg model to be described by such a state, we discuss this state due to reported signatures of this state in neutron scattering experiments in YbMgGaO$_4$ [326, 328], as well as in NaYbSe$_2$ [74].

4.1.4 $J_1 - J_2$ Spectral Functions

The $J_1 - J_2$ Heisenberg model on the triangular lattice hosts three distinct phase as we tune the coupling constant J_2. For intermediate values of J_2, there is a quantum spin liquid phase, and the exact nature of this phase is an active area of current research [434, 163, 174, 299, 389, 124, 160]. Because of this, there is a great interest in reliable simulations in this region. On the experimental side, the material KYbSe$_2$ is a promising candidate to realize this QSL phase [313] (see Sec. 4.2

for more details). In that study, it was observed that KYbSe$_2$ is well modelled by Eq. (4.1), with $J_2/J_1 \sim 0.05$, which is close to the boundary of the QSL phase which is approximately $J_2/J_1 \sim 0.08$ [174]. Applying pressure to this material could push it into the QSL phase, and so signatures of the QSL phase are desired from the theory side. We explore the full phase diagram of the $J_1 - J_2$ Heisenberg model here.

The $120°$ Magnetic Long-Range Ordered Phase

The $J_2 = 0$ phase of the triangular lattice Heisenberg model has a rich history starting back with Anderson postulating the ground state as a candidate for a resonating valence bond state [14], but more recently evidence suggests the state realizes a 120° ordering antiferromagnetic state [167, 188, 338, 66, 27, 52, 430, 387]. In Fig. 4.4 a) we show the static structure factor obtained from DMRG, and see ordering at $q = K$ as expected. In Fig. 4.4 b), we show the full spectrum, the dispersion relation obtained using

$$\epsilon(q) := \underset{\omega}{\mathrm{argmax}}\ S(q, \omega), \tag{4.19}$$

as well as the dispersion relation from SWT [63], for path 1 in Fig. 4.2. The discontinuity in $\epsilon(q)$ in the middle of the path from $q = \Gamma \rightarrow K$ we believe to be an artifact of the definition in Eq. (4.19), as there are two branches of near equal spectral weight in this momentum range. We also note that near $q = K$, we anticipate $\epsilon(q)$ to overestimate the real dispersion relation due to finite size effects, and reduced resolution for small ω due to finite time.

Despite the overestimation of the dispersion relation, we compute the velocity of excitations, which would be robust to a systematic overestimation of the dispersion relation. Near $q = K$ we anticipate the velocity to be independent of the direction, and so we take the direction from $q = K \rightarrow \Gamma$, as this has the most allowed q values in the linear region of SWT. We show the comparison of our MPS results with SWT in Fig. 4.4 c). We see an almost uniform increase of the dispersion relation compared to SWT. We fit the data to a line of the form $vq + \Delta$, which provides an estimate to the velocity, as well as the gap. Again we do not include the value at $q = K$, as this is the least accurate point since we expect gapless modes from SWT. We find the velocity is close to SWT, with a slight decrease. The fit parameter Δ, as well as the value of $\epsilon(q = K)$ provide an estimate to the gap, but this should be viewed as an upper bound rather than a quantitatively accurate result. Analogously to the square lattice case, there is a finite-size gap that we expect to scale as $\Delta \sim 1/LC$, as well as minimum frequency resolution on the order of $\omega_{\min} \sim \eta \approx 0.14$, making the gap challenging to resolve accurately.

We look at the dispersion relation for the entire Brillouin zone in Fig. 4.4 d). It has been previously seen that there is a reduction from the linear spin wave theory results most noticeably at the $q = M$ and $q = Y_1$ points in the Brillouin zone [368, 104]. This reduction in the dispersion relation at $q = Y_1$ leads to a surprising stabilization of quasi-particles, preventing their decay [368]. The reduction is not as clear here when looking at the dispersion relation in Fig. 4.4 d). However, in Fig. 4.4 b) and e), we can clearly see a low energy roton mode near $q = M$, and low energy spectral weight at $q = Y_1$, as expected. These low energy peaks are also visible in Fig. 4.4 f). Since
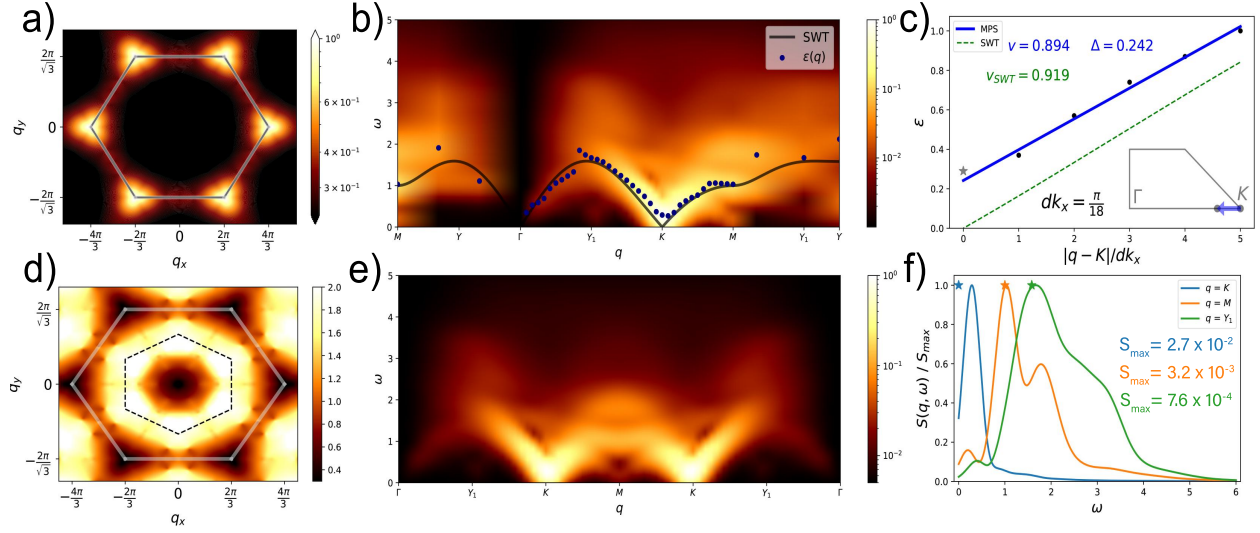
Figure 4.4: Results for the nearest-neighbor antiferromagnetic Heisenberg model on the triangular lattice, defined by Eq. (4.1) with $J_2 = 0$. We show the static structure factor $S(\boldsymbol{q})$ defined by Eq. (4.4) in a). In b) and e) we show the dynamical structure factor $S(\boldsymbol{q}, \omega)$ defined by Eq. (4.2) for path 1 and path 2 shown in Fig. 4.2 respectively. We show the dispersion relation using Eq. (4.19) for momentum values near $\boldsymbol{q} = K = (4\pi/3, 0)$ on the path towards $\boldsymbol{q} = \Gamma = \mathbf{0}$ in c). We fit these points to a line of the form $vq + \Delta$ shown in blue, and the dispersion relation and velocity from linear SWT in green [63]. The dispersion relation using Eq. (4.19) is shown in d). Lastly, We show the frequency dependence of $S(\boldsymbol{q}, \omega)$ at fixed high symmetry momentum values in f), and compare with the SWT results at those momenta shown with a star. We divide the values by the maximum intensity S_{max} to view all three points on the same axis. For both the static structure factor and the dispersion relation, we restore the 6-fold rotational symmetry of the lattice in the thermodynamic limit, as discussed in Sec. 4.1.2.

these low energy branches are not the maximum intensity frequency at these momentum values, our definition of the dispersion relation does not pick them out. However, if we do not damp the data with a Gaussian factor, then these low energy peaks do become the frequency with the maximum intensity. We note that in Fig. 4.4 f), it appears this low energy branch near $\boldsymbol{q} = M$ peaks at a frequency lower than the peak at $\boldsymbol{q} = K$, suggesting a smaller gap at $\boldsymbol{q} = M$. However, with perfect frequency resolution, the gap is better defined as the value of ω where the spectral weight becomes non-zero. Since the spectral weight at $\boldsymbol{q} = K$ is at least one order of magnitude larger than at $\boldsymbol{q} = M$, it is unlikely that the gap would be lower at $\boldsymbol{q} = M$.

We show the dynamical structure factor in Fig. 4.4 e) for path 2 in Fig. 4.2, to easily compare with recent neutron scattering results in $Ba_3CoSb_2O_9$ [176, 237], PEPS results [64], and Schwinger-boson theory [117]. We find the maximum spectral weight resides at $\boldsymbol{q} = K$, and we also see the low energy roton-like mode at $\boldsymbol{q} = M$ seen in prior simulations [368, 104, 64], as well as neutron
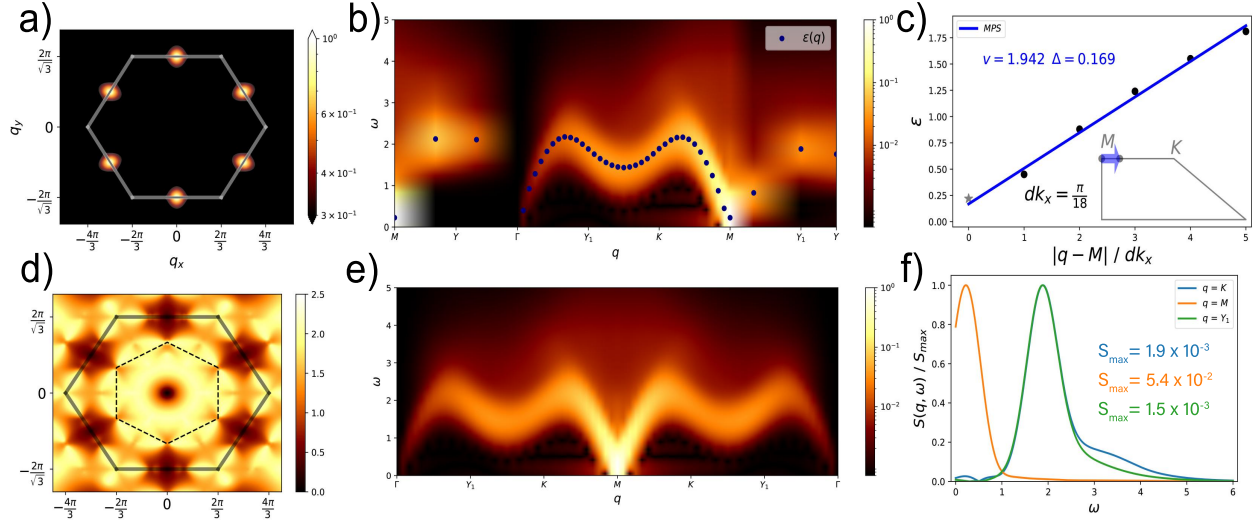
Figure 4.5: Results for the $J_1 - J_2$ Heisenberg model on the triangular lattice, defined by Eq. (4.1) with $J_2/J_1 = 0.5$. We show the static structure factor $S(\boldsymbol{q})$ defined by Eq. (4.4) in a). In b) and e) we show the dynamical structure factor $S(\boldsymbol{q}, \omega)$ defined by Eq. (4.2) for path 1 and path 2 shown in Fig. 4.2 respectively. We show the dispersion relation using Eq. (4.19) for momentum values near $\boldsymbol{q} = M = (0, 2\pi/\sqrt{3})$ on the path towards $\boldsymbol{q} = K = (2\pi/3, 2\pi/\sqrt{3})$ in c). We fit these points to a line of the form $vq + \Delta$ shown in blue. The dispersion relation using Eq. (4.19) is shown in d). Lastly, We show the frequency dependence of $S(\boldsymbol{q}, \omega)$ at fixed high symmetry momentum values in f). We divide the values by the maximum intensity S_{max} to view all three points on the same axis. For both the static structure factor and the dispersion relation, we restore the 6-fold rotational symmetry of the lattice in the thermodynamic limit, as discussed in Sec. 4.1.2.

scattering experiments in $Ba_3CoSb_2O_9$ [176, 237] and $KYbSe_2$ [313]. We note that the roton-like mode is not fully captured in the Schwinger-boson formalism, but the behavior near $\boldsymbol{q} = K$ appears to be well captured.

The Stripe Ordered Phase

For large, J_2/J_1, the Hamiltonian given by Eq. (4.1) exhibits a striped antiferromagnetic ground state. We use $J_2/J_1 = 0.5$ to study this phase. We show the full spectrum given in Fig. 4.5 b) and e) for the paths shown in Fig. 4.2. We also show the dispersion relation from Eq. (4.19) in Fig. 4.5 d). For both the static structure factor and the dispersion relation, we restore the 6-fold rotational symmetry of the lattice in the thermodynamic limit, as discussed in Sec. 4.1.2. The striped phase does in fact break this symmetry, and so this would illustrate the symmetric state formed as a superposition of the three symmetry broken states.

We show the velocity near $\boldsymbol{q} = M$ in Fig. 4.5 c), as well as the gap determined from the linear fit. Again we omit the value of $\epsilon(\boldsymbol{q} = M)$ from the fit, and can compare the value with the value

Δ obtained in the fit. Similarly, we anticipate the largest deviations to be near where we expect gapless excitations, which is at $q = M$ in the striped phase. In the previous systems discussed earlier, we found that the dispersion relation away from these gapless points had good quantitative agreement with SWT and/or QMC, and so we anticipate the same here. We also show the frequency dependence at $q = K, M$, and Y_1 in Fig. 4.5 f) for reference.

The Quantum Spin Liquid Phase

Lastly, we examined the quantum spin liquid phase, with $J_2/J_1 = 0.12$, which is right in the middle of the two boundaries of the QSL phase as predicted by Ref. [174]. We find the maximum intensity is spread across the Brillouin zone boundary in the static structure factor shown in Fig. 4.6 a), a feature also present in kagome lattice spin liquid systems [84, 332, 433, 281, 144]. We show the full spectrum in Fig. 4.6 b) and e), along the paths through the Brillouin zone illustrate in Fig. 4.2. We note the low energy spectral weight lies along the entire Brillouin zone boundary, seen in the path from $q = K \to M$. This is indicative of a competition between the 120° and the stripe ordered phases, which order at $q = K$ and $q = M$, respectively. In Fig. 4.6 b) we see a faint high-energy branch near $q = \Gamma$, in agreement with Ref. [104]. However, we find a continuum extending to higher energies, and this branch lies fully within this continuum as opposed to being isolated. We believe this difference is because our simulations do not rely on an ansatz for the excitations, and can probe the full spectrum.

We also see the low energy spectral weight along the Brillouin zone boundary by looking at the dispersion relation shown in Fig. 4.6 d), obtained using Eq. (4.19). It is more accurate to call this just the maximum intensity as a function of momentum q. The dispersion relation interpretation assumes well define magnon modes, which we do not expect in the QSL phase. Nevertheless, it does indicate that there is low energy spectral weight across the Brillouin zone boundary, but low energy spectral weight is absent near the center of the Brillouin zone. We note that in Fig. 7 e), the spectrum looks flat from $q = K \to M$, but this is an artifact of the frequency resolution and using color to display the spectrum. If we look at Fig. 4.7, we see that there is structure between these two points. Lastly we show the frequency dependence of $S(q, \omega)$ at the high symmetry q points in Fig. 4.6 f). We want to emphasize the similarity between $q = K$ and $q = M$, which is unique to the QSL phase. We also note that the maximum intensity is suppressed as compared to the 120° phase in Fig. 4.4 f), and the striped phase in Fig. 4.5 f).

Let us now examine what these results have to say about the nature of the QSL ground state. First, we show in Fig. 4.6 c) the spectrum with a similar colormap and momentum path as Fig. 4 in Ref [74] for easy comparison. We see the V-shape spectrum near $q = \Gamma$, as is observed in previous neutron scattering experiments in NaYbSe$_2$ [74], and in YbMgGaO$_4$ [326, 328]. This is a hallmark of a QSL with a spinon Fermi surface, as discussed in Sec. 4.1.3. However, we also see that near $q = \Gamma$ there is a small gap $\Delta \approx 0.25$ in the spectrum which is not seen in the experiments. If NaYbSe$_2$ is similar to KYbSe$_2$, which has been shown to be well modelled by a $J_1 - J_2$ Heisenberg model with $J_1 \approx 0.56$ meV [313], then the gap would be $\Delta \approx 0.14$ meV, which is below the lowest frequency $\omega_{min} \approx 0.2$ meV accesible in Ref. [74]. This discrepancy means that either these materials are not well modelled by the $J_1 - J_2$ Heisenberg model, or that the lowest
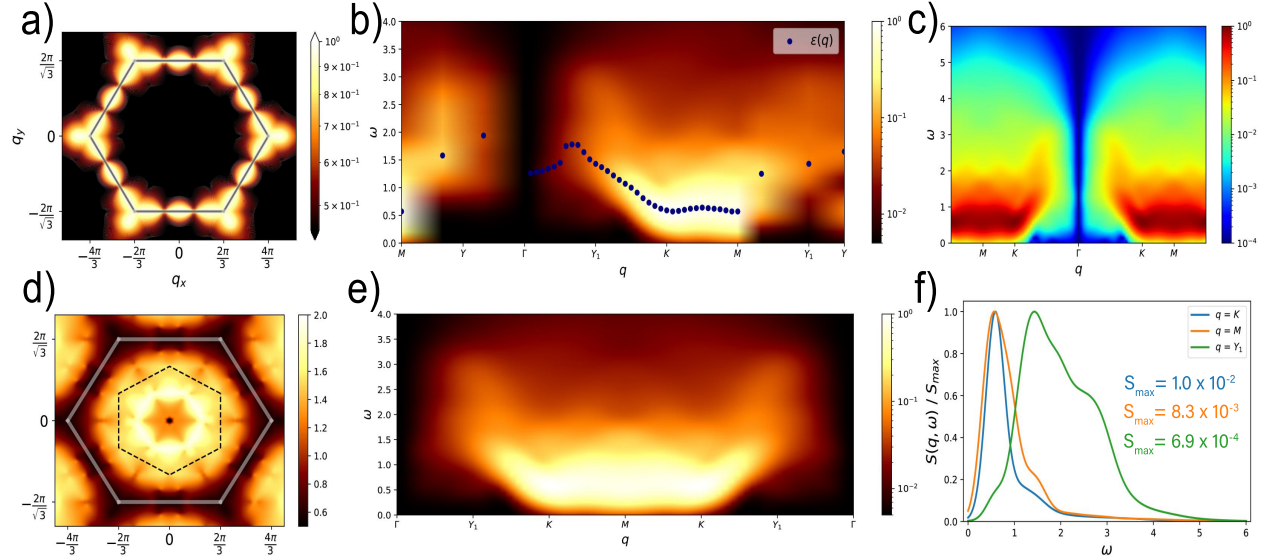
Figure 4.6: Results for the $J_1 - J_2$ Heisenberg model on the triangular lattice, defined by Eq. (4.1) with $J_2/J_1 = 0.12$. We show the static structure factor $S(\boldsymbol{q})$ defined by Eq. (4.4) in a). In b) and e) we show the dynamical structure factor $S(\boldsymbol{q}, \omega)$ defined by Eq. (4.2) for path 1 and path 2 shown in Fig. 4.2 respectively. In c) we show the spectral function using a similar path and color map as Fig. 4 in Ref. [74] for easy comparison. The maximum intensity using Eq. (4.19) is shown in d). Lastly, we show the frequency dependence of $S(\boldsymbol{q}, \omega)$ at fixed high symmetry momentum values in f). We divide the values by the maximum intensity S_{max} to view all three points on the same axis. For both the static structure factor and the dispersion relation, we restore the 6-fold rotational symmetry of the lattice in the thermodynamic limit, as discussed in Sec. 4.1.2.

energies accessible in these experiments is not low enough to probe this gap on the order of $J_1/4$. In either case, the presence of the gap in the spectrum rules out the spinon Fermi surface state as ground state of this model.

Next we wish to distinguish the gapped $\mathbb{Z}_2$ from the gapless $U(1)$ Dirac spin liquid. To do this, we look at how the full spectrum changes as we tune J_2 through all three phases, illustrated in Fig. 4.7. As discussed in Sec. 4.1.3, we want to look at what happens at $\boldsymbol{q} = K$ and $\boldsymbol{q} = M$, as we approach the QSL phase from the 120° phase. What we find is that there is a sharp low energy magnon branch near $\boldsymbol{q} = M$ that softens and decreases as the critical point is approached, and remains this way into the QSL phase. This feature has also been observed in a recent variational QMC study [104]. This is a key signature of a gapless $U(1)$ Dirac QSL, suggesting the spectrum is gapless at both $\boldsymbol{q} = K$ and $\boldsymbol{q} = M$ in the QSL phase, in agreement with a recent DMRG study [160]. This feature is not captured within the Schwinger-boson formalism [313, 117], which finds that the gap $\boldsymbol{q} = M$ remains gapped as J_2 is tuned towards the critical point. This suggests that Schwinger-
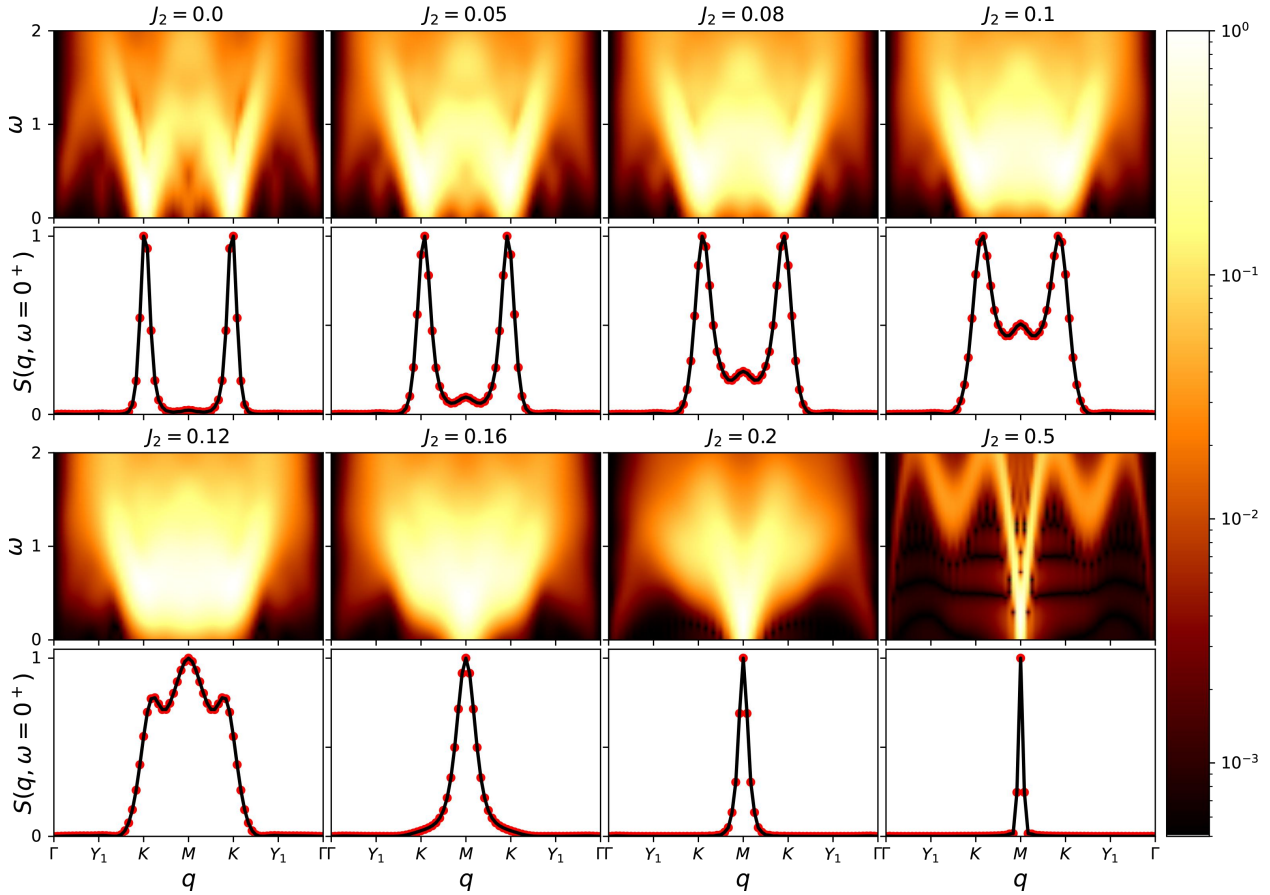
Figure 4.7: The dynamical structure factor given by Eq. (4.2) for the $J_1 - J_2$ Heisenberg model on the triangular lattice defined by Eq. (4.1) along path 2 shown in Fig. 4.2. We show multiple J_2 values across the entire phase diagram. This model is in the spin liquid phase for $0.08 \lesssim J_2 \lesssim 0.16$ [174]. We use a Gaussian broadening defined by Eq. (4.12), with $\eta^2 = 0.02$. The first and third rows show the spectral function, and the second and last row show low frequency cuts of the spectral function. The cuts are obtained by integrating the frequency from 0 to 0.1, and then normalize so that the maximum intensity is 1. The black line is just to help with visualizing the data points in red.

boson theory does not capture the QSL phase well, even though it has remarkable agreement with PEPS [64], and the neutron spectrum of $Ba_3CoSb_2O_9$ [176, 237], near the $J_2 = 0$ point.

To further examine the behavior at $\boldsymbol{q} = K$ and $\boldsymbol{q} = M$ across all three phases, we show $S(\boldsymbol{q}, \omega = 0^+)$ as well in Fig. 4.7. To compute $S(\boldsymbol{q}, \omega = 0^+)$ we integrate $S(\boldsymbol{q}, \omega)$ for $\omega_{\min} \leq \omega \leq \omega_{\max}$, with $\omega_{\min} = 0$, and $\omega_{\max} = 0.1$. We also adjusted the integration window, with $\omega_{\min} \in [0, 0.1]$, and $\omega_{\max} \in [0, 0.2]$, as well as just using the value at $\omega = 0$, with no qualitative difference. Thus, the low frequency cuts are robust and not just probing frequencies lower than can be resolved

numerically. If this quantity is non-zero, then this would mean that there are gapless modes in the spectrum, which produce spectral weight down to the lowest energies. We find that deep in the $120°$ phase, that the low energy spectral weight is near zero, except at $q = K$. As J_2 increases, low energy spectral weight develops at $q = M$. Inside the QSL phase, we find appreciable weight at both $q = K$ and $q = M$, suggesting the spectrum is gapless at both these momenta, implying a gapless $U(1)$ Dirac spin liquid. Moreover, through all three phases, the spectral weight near $q = \Gamma$ is zero, within machine precision. This provides further evidence against a spinon Fermi surface state, which would be non-zero everywhere within the QSL phase[305].

We want to note that separating zero from small is a challenging task numerically, and so we cannot definitively rule out the gapped $\mathbb{Z}_2$ or spinon Fermi surface spin liquid states. However, we believe the most likely interpretation of our data in the QSL phase is that the spectral weight is localized around $q = K$ and $q = M$, and broadened to yield non-zero weight along the full Brillouin zone boundary. These results are most consistent with a $U(1)$ Dirac QSL ground state.

4.1.5 Conclusions

Summary

In this work we examine the dynamical structure factor for the full phase diagram of the $J_1 - J_2$ Heisenberg model on the triangular lattice. We also look at the square lattice for the same model with $J_2 = 0$ as a benchmark for our method. For the square lattice, we compute the full spectrum, $S(q, \omega)$, and find great qualitative agreement with the results from QMC in Ref. [324]. From this, we extract the magnon dispersion relation $\epsilon(q)$ using Eq. (4.19), and then we compare this quantitatively with QMC [324] and SWT [170]. We find great agreement, except for wave-vectors q close to gapless modes. Nevertheless, we were able to extract the magnon velocity near $q = M$ from the dispersion relation, and found excellent agreement with the velocity in Ref. [321], which uses highly accurate methods based on static properties. The success on the square lattice provides confidence on utilizing this method to study the triangular lattice.

In the $120°$ magnetic long-range ordered phase, we compare our results against linear SWT [63]. We find low energy branches at frequencies much lower than the SWT prediction, at $q = M$ and $q = Y_1$. This reduction in the energy has been linked to avoided quasi-particle decay [368], and also observed in variational QMC [104]. This produces a roton-like mode at $q = M$ which is not captured by linear SWT, and has been observed in neutron scattering experiments in $Ba_3CoSb_2O_9$ [176, 237], and $KYbSe_2$ [313], as well as simulations using PEPS [64]. Away from $q = M$ and $q = Y_1$, we also find good agreement with Schwinger-boson theory [117].

In the stripe ordered phase, we show the spectral function, dispersion relation, and velocity near $q = M$ as a reference for future work. As far as we know, there are no other simulations of the full spectrum in this phase to compare against. In the static structure factor, we find ordering at $q = M$, as observed previously [163].

In the QSL phase, we find from the static structure factor that there is no unique ordering wave-vector. The maximal intensity occurs at both $q = K$ and $q = M$, which are the ordering wave-vectors for the $120°$ and striped phase respectively. This demonstrates frustration in the system, as

it struggles to satisfy simultaneously the J_1 and J_2 interactions, which is precisely what is expected to give rise to a QSL phase.

We look for the signatures in the low energy spectrum predicted by the three dominant phases, which are summarized in Table 4.1. We find a V-shape spectrum near $q = \Gamma$, a key signature of a spinon Fermi surface. However, we find at low energies, a gap opens near $q = \Gamma$, in contrast to the spinon Fermi-surface which is gapless everywhere [305, 212]. This V-shape pattern has been observed in neutron scattering experiments in $NaYbSe_2$ [74], and in $YbMgGaO_4$ [326, 328], which has been attributed to a spinon Fermi surface. If $NaYbSe_2$ is similar to $KYbSe_2$, which has been shown to be well modelled by a $J_1 - J_2$ Heisenberg model with $J_1 \approx 0.56\,\text{meV}$ [313], then the gap would be $\Delta \approx 0.14\,\text{meV}$, which is below the lowest frequency $\omega_{\min} \approx 0.2\,\text{meV}$ accesible in Ref. [74]. The absense of a low energy gap developing near $q = \Gamma$ in these experiments means one of two things. Either, these materials are not well modelled by the $J_1 - J_2$ Heisenberg model, and spin anisotropies or longer range interactions lead to different QSL phases than what is found in the $J_1 - J_2$ Heisenberg model. Or, the gap appears at energies lower than what was accessible in these experiments. This calls for future neutron scattering experiments at lower energies, as well as ab-initio calculations, to elucidate the underlying microscopic models of these materials, and associated energy scales.

As we increase J_2/J_1 up from 0, we find that the low energy branch near $q = M$ softens, and eventually leads to the gap closing at the critical point, ruling out a gapped $\mathbb{Z}_2$ QSL. This finding is consistent with the variational QMC study in Ref. [104]. We also find the high-energy branch near the Γ point observed in their work. However, we find a continuum extending to higher energies, and this branch lies fully within this continuum as opposed to being isolated. We believe this difference is due to our method probing the full spectrum, and does not assume an ansatz for the excitations. The gap closing at $q = M$ as the critical point is approached was not observed in the Schwinger-boson formalism [313, 117]. We note that recent neutron scattering experiments in $KYbSe_2$ suggest it is well modelled by a $J_1 - J_2$ Heisenberg model near the quantum critical point [313]. By applying hydrostatic pressure to $KYbSe_2$, and possibly the other triangular lattice materials, neutron scattering experiments may be able to give insights into what is happening near $q = M$ as the material approaches quantum criticality.

Due to finite resolution in our simulations, we cannot definitively rule out a small gap at $q = M$, which would imply a $\mathbb{Z}_2$ spin liquid, as recently claimed [313, 117, 186]. We also cannot definitively distinguish zero spectral weight from small spectral weight near $q = \Gamma$, as expected in a spinon Fermi surface state [212, 305], and recently seen in neutron scattering experiments [74, 326, 328]. However, the most likely interpretation of our results is that there are gapless modes localized at $q = K$ and $q = M$, implying a gapless $U(1)$ Dirac spin liquid, in agreement with Ref. [160].

Perspectives

Distinguishing the gapped $\mathbb{Z}_2$ from a gapless Dirac spin liquid remains a challenging task. Our results favor the gapless case, but future studies are needed to provide a definitive answer to this question. Perhaps looking at level crossings in the low energy spectrum could shed light on this, as

was done for the $J_1 - J_2$ Heisenberg model on the square lattice [381], and the Shastry-Sutherland model [410, 382].

We could also possibly gain insight to this question from cold atom experiments. Recently, a quantum spin liquid was realized in a quantum simulator of Rydberg atoms on the kagome lattice [320]. Triangular optical lattices have been proposed [404], and constructed [411, 403] to study frustrated quantum magnets. This may be a future direction to study the ground state properties of the $J_1 - J_2$ Heisenberg model.

Quantum criticality can also be further explored by the Kibble-Zurek mechanism [194, 195, 49]. This procedure time-evolves a ground state with a time-dependent Hamiltonian in proximity to a quantum critical point. Adiabaticity is lost as the gap closes, and the excitations generated are specified by the rate at which the Hamiltonian changes, and the critical exponents of the quantum critical point. Recent neutron scattering experiments in $KYbSe_2$ have found critical scaling with an unexplained critical exponent [313]. Such a Kibble-Zurek process may be able to shed light on this observed criticality. Moreover, such Kibble-Zurek processes are ideal for use on quantum computers, on which unitary dynamics is easily programmed. If a quantum critical point is continuously connected to a product state, then a quantum computer may be useful in probing the critical point, as was done recently in the one-dimensional quantum Ising model [91]. Such small scale quantum computing devices are, in principle, not prone to the challenges of long-range interactions like MPS calculations are, for studying two-dimensional dynamics. Future work in this direction could provide insight into the nature of the QSL in the $J_1 - J_2$ Heisenberg model, and simultaneously provide a problem where quantum computers extend beyond what is possible with classical simulations.

4.2 Proximate Spin Liquid and Fractionalization in KYbSe$_2$

4.2.1 Introduction

In the last decade, Yb^{3+} based materials have become popular as QSL candidates because of the Yb^{3+} effective $S = 1/2$ state. Most recently, a class of delafossite materials have been proposed as relatively disorder-free QSL candidates, including $NaYbO_2$ [85, 33, 289], $NaYbS_2$ [18, 303], $NaYbSe_2$ [287, 74] and $CsYbSe_2$ [393]. Each of these materials shows diffuse excitations and no long-range magnetic order down to 0.4 K or lower, but because neither are unique to QSL states (both are also caused by spin glass [421], random singlet phases [435], or 2D magnetic order only in the zero temperature limit), they remain QSL candidates only.

Here we investigate a new member of the Yb^{3+} delafossite family: KYbSe$_2$[1] which forms a layered triangular lattice of magnetic Yb^{3+} ions, see Fig. 4.8(a). This material shows no long-range order above 400 mK [398], and finite-field ordered phases similar to $NaYbO_2$ [33] and $NaYbS_2$ [303]. Thus it appears promising as a quantum spin liquid candidate. Using a combination of Onsager reaction field theory, Schwinger bosons, and matrix product state (MPS) approaches to model KYbSe$_2$, we find that its physics is well-captured by a microscopic spin-1/2 Hamiltonian with nearest and next-nearest neighbor Heisenberg interactions on the triangular lattice in proximity to the QSL phase [see Fig. 4.8(b)]. Finally, the neutron spectrum displays signatures of quantum criticality and fractionalized spinon quasiparticles. Together, these results show KYbSe$_2$ to be proximate to a spin liquid phase.

4.2.2 Microscopic Modeling

To better understand the features observed in KYbSe$_2$, and find a microscopic model for the compound, we use a combination of theoretical techniques, the Onsager reaction field, Schwinger bosons, and MPS simulations.

Onsager reaction field: estimating the exchange ratios

First, we employ the Onsager reaction field (ORF) [263] to fit the energy-integrated paramagnetic scattering shown in Fig. 4.9. This approach neglects quantum fluctuations, but in the paramagnetic regime it is accurate up to a temperature-dependent energy scale normalization [166] which in our case is unknown. Despite this limitation, ORF does give relative anisotropy and ratios between exchanges. Using the g-tensor derived from crystal electric field fits and allowing for first and second neighbor exchange, we find the off-diagonal anisotropic exchange is small and the nearest neighbor exchange is isotropic to within uncertainty [see Sec. 4.4.1] making KYbSe$_2$ a very good approximation to a triangular lattice Heisenberg antiferromagnet described by the microscopic

---

[1]The experiments of KYbSe$_2$ were conducted by my collaborators at Oak Ridge National Lab. See Ref. [309] for more information about the researchers and their contributions.
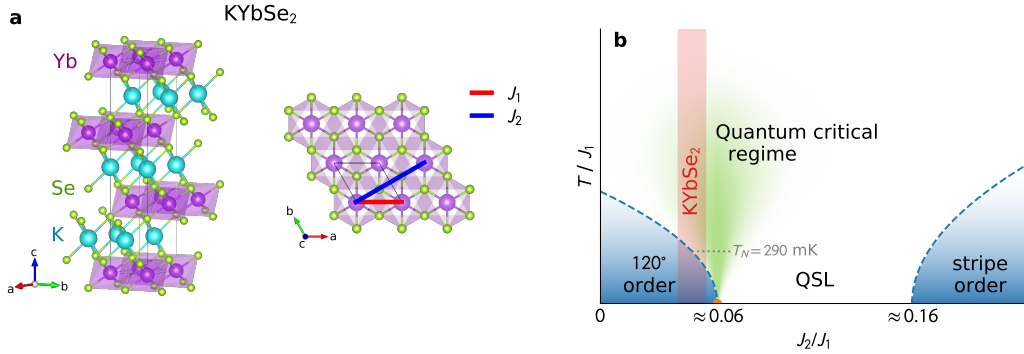
Figure 4.8: **Crystal structure and phase diagram of KYbSe$_2$.** Panel **a** shows the crystal structure with a side view of the stacked triangular layers and a top view showing the Yb^{3+} triangular lattice mediated by Se^{2-} ions. Panel **b** shows a schematic phase diagram of the triangular lattice Heisenberg antiferromagnet as a function of second neighbor exchange strength J_2. This includes a zero temperature 120° ordered phase for $J_2/J_1 \lesssim 0.06$, a zero temperature stripe ordered phase for $J_2/J_1 \gtrsim 0.16$, and an intermediate QSL phase [434, 163, 175, 299, 389, 124, 161]. Near the quantum critical points we expect quantum critical regime extending at finite temperature.

$J_1 - J_2$ Hamiltonian,

$$\hat{\mathcal{H}} = J_1 \sum_{\langle i,j \rangle} \hat{\boldsymbol{S}}_i \cdot \hat{\boldsymbol{S}}_j + J_2 \sum_{\langle\langle i,j \rangle\rangle} \hat{\boldsymbol{S}}_i \cdot \hat{\boldsymbol{S}}_j. \tag{4.20}$$

What is more, the fitted $J_2/J_1 = 0.047(7)$. This is extremely close to the predicted phase boundary between 120° magnetic order and a QSL phase on the triangular lattice Heisenberg antiferromagnet: $J_2/J_1 \approx 0.06$ [434, 163, 175, 299, 389, 124, 161]. Thus, ORF fits show KYbSe$_2$ has nearly isotropic Heisenberg exchange and is very close to a quantum spin liquid phase.

Schwinger bosons: comparing the neutron spectrum

To understand the inelastic neutron spectrum, we turn to a Schwinger Boson (SB) theory beyond the mean field level [15, 16, 116]. This is a parton formulation where the Heisenberg model is expressed in terms of interacting spin-1/2 bosons or spinons, whose condensation leads to long-range magnetic ordering [15, 16]. For details, see the Methods section.

The dynamical spin structure factor $S(\boldsymbol{q}, \omega)$ at $T = 0$ using SB [116] for $J_2/J_1 = 0.05$ is shown in Fig. 4.9(d). On a qualitative level, this result captures the features seen in the experimental data: the strong dispersive cone emanating from K, the continuum scattering at higher energies, the diffuse high-energy feature at M, and the pronounced low-energy "roton-like" mode at M. We note that the downturn of the roton-like mode is much less pronounced in the SB result because of the lack of $1/N$ corrections to the internal vertices and the single-spinon propagator [116]. However, the most remarkable aspect of this comparison is that the SB approach captures the intensity modulation of the continuum scattering at higher energies, which is determined by the
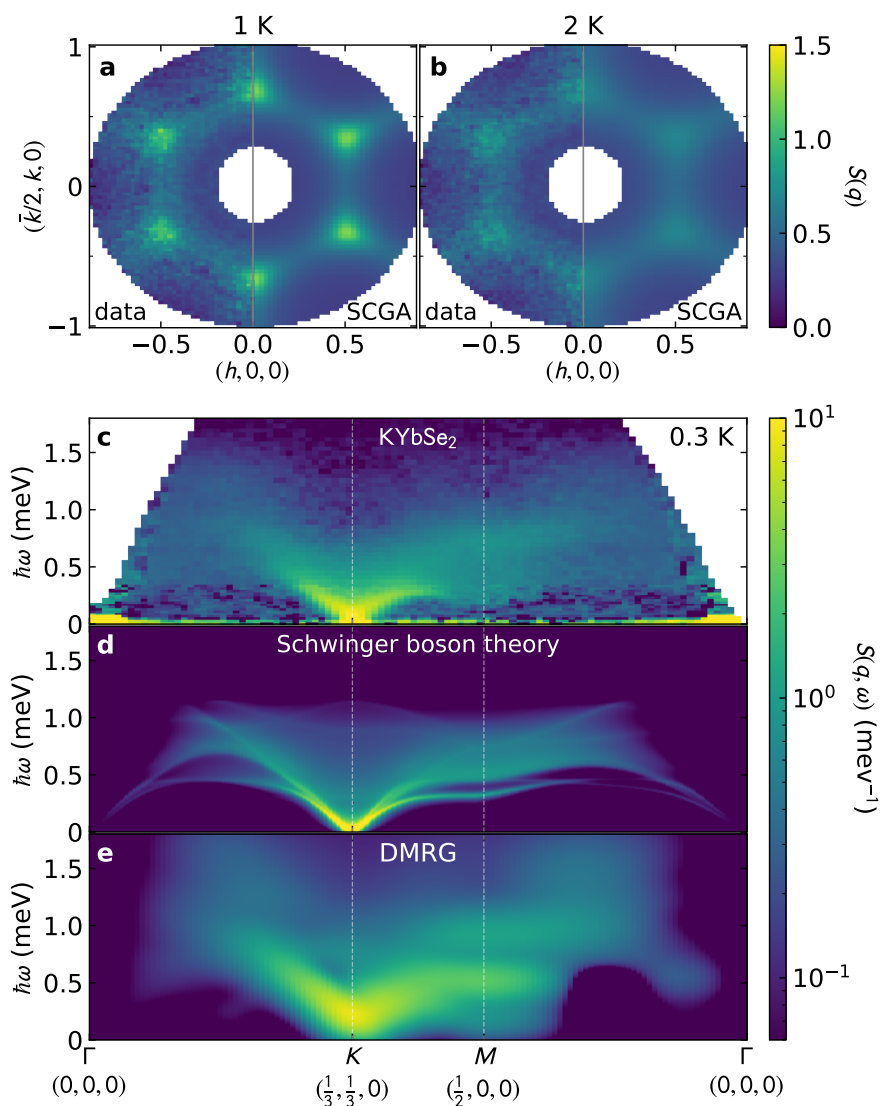
Figure 4.9: **Comparison between experimental KYbSe$_2$ scattering and theoretical simulations.** Panels **a** and **b** show Onsager reaction field (ORF) fits to energy-integrated paramagnetic KYbSe$_2$ scattering at 1 K and 2 K. In each panel, the data is on the left and the fit is on the right. Panels **c-e** show neutron scattering along high-symmetry directions. **c** shows the experimental data for KYbSe$_2$ and **d** shows the zero-temperature simulated spectrum from Schwinger boson calculations with $J_1 = 0.56(3)$ meV and $J_2/J_1 = 0.05$. Panel **e** shows tensor network simulations of a triangular lattice with the same J_1 and J_2 on a cylinder with a circumference of 6 sites and length 36 sites. On a qualitative level, the theory captures the continuum excitations observed in experiment.

two-spinon continuum of the SB theory. This correspondence points to the continuum scattering in KYbSe$_2$ originating from its proximity to a deconfined spin liquid state with fractionalized spinon excitations.

The measured continuum scattering extends up to higher energies than SB predicts: ≈ 1.6 meV, approximately three times the fitted $J_1 = 0.56(3)$ meV (see Sec. 4.4.1). We attribute this discrepancy to the lack of 4-spinon contributions arising from Feynman diagrams which have not been included in the SB calculation [116]. Note that the KYbSe$_2$ continuum extent does match the predicted continuum extent near the $J_2/J_1 \approx 0.06$ transition point as calculated by Gutzwiller projected variational Monte Carlo [105].

Simulations and comparison

The third technique we use to model the diffuse inelastic neutron scattering is using the MPS technique discussed in Sec. 4.1.2. A related approach was recently used to interpret and describe the scattering of CsYbSe$_2$ [393], and provides a full quantum picture of the neutron spectrum. The downside to this technique is finite size effects, which cause broadened modes and gaps in the low energy spectrum. Nevertheless, qualitative comparisons can be made.

The simulated data along high symmetry directions of the Brillouin zone for $J_2/J_1 = 0.05$ is shown in Fig. 4.9(e). The overall features of the experimental data are reproduced in the simulations: the asymmetric dispersive modes emanating from K, the diffuse continuum extending to high energies, and even the broad 1 meV feature at M. This shows that the triangular lattice Heisenberg J_1-J_2 model is indeed an appropriate model for KYbSe$_2$. Further microscopic simulations show that most of the high energy scattering remains unchanged as J_2 is increased and the system enters the QSL phase, showing that the high-energy scattering can be interpreted as bound spinons of a proximate spin liquid.

4.2.3   Critical Scaling

So far, the theoretical comparisons indicate that KYbSe$_2$ is close to the J_2/J_1 QSL quantum critical point. If this is true, we should see quantum critical scaling in the finite temperature neutron spectrum [205, 318, 57, 302]. Plotting scattered intensity times $(k_B T)^\alpha$ versus $\hbar\omega/k_B T$, shown in Fig. 4.10, we see a critical exponent $\alpha = 1.73(12)$ over more than a decade in ω/T. Theoretically, the semiclassical spin wave scattering from an ordered Heisenberg triangular lattice predicts an exponent $\alpha = 1$. The observed scattering is unquestionably inconsistent with this [Fig. 4.10(a)]. Thus this scaling shows that the KYbSe$_2$ inelastic spectrum goes beyond a simple magnon description, suggesting fractionalized spinon excitations, a hallmark of a QSL state.

Elastic Bragg scattering and heat capacity show a transition to long range magnetic order below $T_N = 290$ mK (see Sec. 4.4.1), showing that KYbSe$_2$ is on the 120° side of the phase boundary. Nevertheless, the critical scaling is strong evidence that KYbSe$_2$ is within the quantum critical regime at finite T.
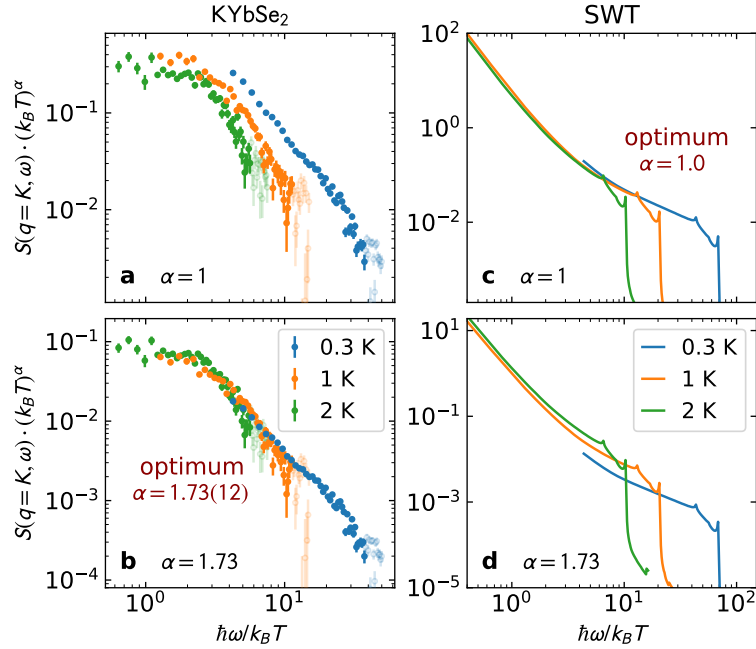
Figure 4.10: **Critical scaling in KYbSe$_2$, showing data at the K point at three different temperatures scaled by $\hbar\omega/k_B T$ and $S(q = K, \omega)(k_B T)^\alpha$.** Measured KYbSe$_2$ spectra are on the left column, and calculated spin wave theory (SWT) are on the right column. When $\alpha = 1.73(12)$, the KYbSe$_2$ data from the three temperatures follow the same curve, suggesting quantum critical scaling. SWT spectra, meanwhile, overlap when $\alpha = 1.0$. This suggests fundamentally different behavior in KYbSe$_2$ that cannot be captured by non-interacting magnons. (Fitted energy range was $\hbar\omega \leq 1.3$ meV; data above this are plotted in lighter colors.)

The critical scaling suggests that KYbSe$_2$ is in close proximity to a second order phase transition. This is consistent with theoretical studies of the $J_1 - J_2$ Heisenberg model [174], which find a second order phase transition between the 120° and QSL phases. This further implies that KYbSe$_2$ is well modelled by the $J_1 - J_2$ Heisenberg model.

4.2.4 Conclusion

These results show that KYbSe$_2$ is within the quantum critical fan of a quantum spin liquid state. CEF fits show an isotropic $J = 1/2$ doublet with strong quantum effects, and ORF simulations show a J_2/J_1 ratio within the 120° ordered phase but very close to the QSL quantum critical point $J_2/J_1 \approx 0.06$. Finally, there are strong signs of quantum criticality in the neutron spectrum: (i) the majority spectral weight in the continuum, (ii) the sharp lower continuum bound reminiscent of the 1D spinon spectrum, (iii) strong correspondence to SB and MPS simulations near the transition to a spin liquid, and (iv) critical scaling incompatible with semiclassical excitations all indicate that

the KYbSe$_2$ excitations are fractionalized spinons of a QSL phase. Thus, despite the existence of magnetic order at the lowest temperature, we propose KYbSe$_2$ as a model for triangular lattice QSL physics at finite energies and temperatures (exactly like many 1D spin chains—c.f. KCuF$_3$ [205]).

These results have implications beyond just this material. As noted earlier, triangular lattice CsYbSe$_2$ and NaYbSe$_2$ also show features of a QSL phase: with CsYbSe$_2$ possibly more toward the $J_2 = 0$ limit [393], and NaYbSe$_2$ J_2/J_1 possibly within the QSL phase (Yb site disorder notwithstanding) [74]. This suggests that the periodic table can be used to "tune" J_2/J_1 such that the delafossite lattice can be brought into and out of a QSL phase depending on the A-site element. This gives a remarkably controlled way to study QSL materials. Another possible way to "tune" J_2/J_1 could be through hydrostatic pressure—there are even reports of superconductivity in NaYbSe$_2$ under pressure [185, 427], which suggests pressure does more than just shift magnetic exchange constants.

The family of Yb^{3+} delafossites are a remarkable platform for 2D triangular lattice Heisenberg systems. By controlling J_2/J_1, we are able to systematically approach a QSL from the 120° ordered phase, which gives a clear pathway towards an experimentally verifiable QSL state. Scaling behavior in $\hbar\omega/k_B T$ with a nontrivial exponent, i.e., a value inconsistent with gapless spin wave excitations, is observed in the spin correlations down to the lowest temperature measured (0.3 K), with a correlation length of at least ten unit cells.

While a weakly first-order transition with a long correlation length is possible, the natural interpretation of the results in this work is that the phase transition from 120° to a QSL is second order, which combines with previous theoretical work to constrain strongly the nature of the QSL. One of the frontiers in quantum condensed matter physics is to understand the possible phase transitions between topological and broken-symmetry phases, and the combined experimental and theoretical analysis of KYbSe$_2$ helps clarify one piece of this frontier.

4.3 Realization of U(1) Dirac Quantum Spin Liquid in YbZn$_2$GaO$_5$

4.3.1 Introduction

In recent years, two-dimensional triangular lattice systems with rare-earth ions carrying effective spin-1/2 moments have presented promising opportunities in realizing QSL states, given the presence of spin-orbit coupling, crystal electric fields, and strong quantum fluctuations. Among these systems, the Yb-based YbMgGaO$_4$ has been intensively studied due to the absence of magnetic ordering and the observed continuum-like inelastic neutron scattering (INS) spectra, making it a promising candidate for QSL[218, 223, 220, 327, 264, 436, 197]. However, the presence of chemical disorder in YbMgGaO$_4$, caused by the inherently mixed occupancies of magnesium and gallium atoms on the same crystallographic site, has made the interpretation of the results challenging [436, 216, 197]. Specifically, a theoretical study suggests that the chemical disorder may imitate the continuous INS spectra [436]. Further studies on a sister compound, YbZnGaO$_4$, have proposed the presence of a spin-glass ground state attributed to the coexistence of chemical disorder and quantum fluctuation [236]. Therefore, eliminating chemical disorder and accessing the intrinsic physics of an ideal triangular lattice of effective spin-1/2 moments is highly desired. As such, a potential candidate for hosting a QSL state is another class of Yb-based triangular lattice rocksalt-type compounds that do not have significant intrinsic chemical disorder: AYbX$_2$ (A = Li, Na, K, Rb, Cs and X = O, S, Se) [34, 86, 35, 134, 290, 75, 288, 424, 426, 395, 310]. Nevertheless, the task of obtaining high-quality single-crystal samples for this particular family has posed significant challenges. As a result, most of the reported results have been derived from powder samples or small single crystals, rendering the interpretation of data quite challenging. Furthermore, it is worth noting that in this compound family, the inter-layer Yb-Yb distance is relatively shorter, which introduces a more three-dimensional magnetic structure. Thus, the crucial step toward unraveling the enigma of the QSL state in these systems lies in the design and synthesis of single crystal samples for a novel class of Yb-based triangular lattice compounds that lack intrinsic chemical disorder and exhibit quasi-two-dimensional magnetic structures.

To that end, we present a new Yb-based compound, YbZn$_2$GaO$_5$ shown in Fig. 4.11, that features an ideal triangular lattice of effective spin-1/2 moments without any intrinsic chemical disorder. Experiments aimed at elucidating the nature of the possible triangular lattice QSL in YbZn$_2$GaO$_5$ are of great importance. Thus, we grew a large and high-quality single crystal of YbZn$_2$GaO$_5$ (see Sec. 4.4.2) using the optical floating-zone technique to facilitate such experiments [2]. Our heat capacity measurements indicate that at ultra-low temperatures, the heat capacity displays a ~ T^2 dependence, indicating a U(1) Dirac QSL behavior [286, 162]. In addition to the heat capacity measurements, we conducted an INS investigation, comparing matrix product state (MPS) simulations, on YbZn$_2$GaO$_5$ which reveals gapless, continuum-like spectra at the high-symmetry M and K points, but not throughout the Brillouin zone, and in particular not at the Γ point. This

---

[2]The experiments of YbZn$_2$GaO$_5$ were conducted by my collaborators at Duke University. See Ref. [399] for more information about the researchers and their contributions.
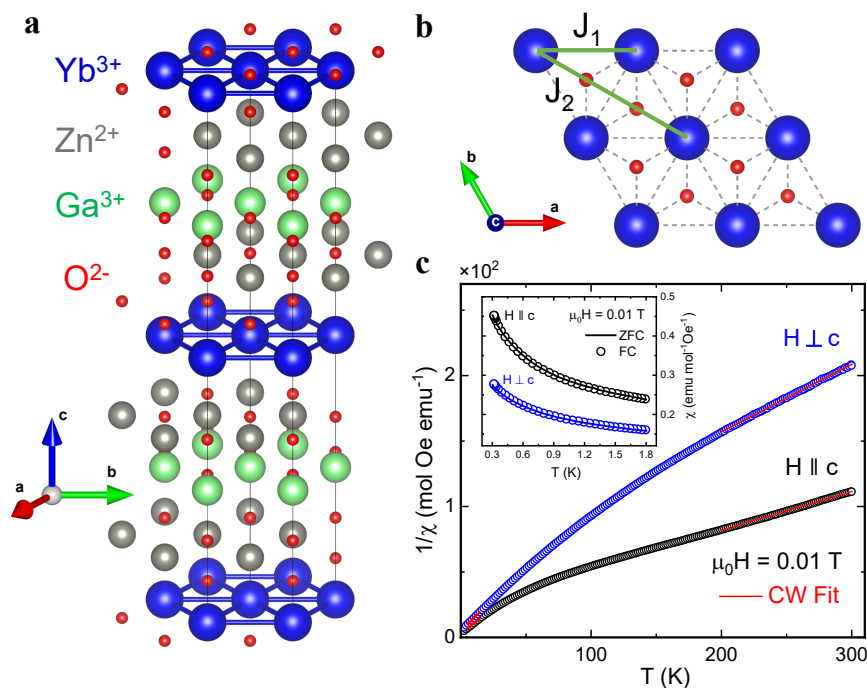
Figure 4.11: **Crystal structure and magnetic susceptibility a**. Crystal structure of $YbZn_2GaO_5$; Yb-O planes are well separated by non-magnetic Zn-O, Ga-O, and Zn-O layers along crystallographic *c*-direction. **b**. The Yb^{3+} (blue sphere) forms a triangular lattice. The nearest neighbor couplings J_1 and next-nearest neighbor couplings J_2 are shown by green solid lines. **c**. The inverse magnetic susceptibility, $1/\chi$ ($H\|c$ and $H\perp c$) data collected on single crystal sample of $YbZn_2GaO_5$ from 2 to 300 K. The red solid lines are the Curie-Weiss (CW) Fit at the low-temperature range from 5 - 15 K and at high-temperature range from 200 - 300 K. The inset shows no splitting between zero-field-cooling (ZFC) and field cooling (FC) magnetic susceptibility data of $YbZn_2GaO_5$ crystal down to 0.3 K. The measurements were conducted under an applied magnetic field of 0.01 T parallel and perpendicular to crystallographic *c* - direction.

particular pattern of low-energy spinon excitations is expected for the U(1) Dirac QSL phase [331, 89] and not for a spinon Fermi surface state, as discussed in Sec. 4.1.3. Hence the heat capacity scaling and INS spectra independently are best explained by low-energy spinon excitations with Dirac-like spectrum.

4.3.2 Microscopic Model

For comparison with the INS spectra, we performed MPS based simulations, analogous to the methods discussed in Sec. 4.1.2. To identify the model, we seek the simplest model that recovers the essential features of the experimental data. We find that the experimental spectrum (shown in

Fig. 4.14) has a similar structure to the spectrum shown in the QSL phase of the $J_1 - J_2$ model, displayed in Fig. 4.6. One difference however is the relative intensity of the spectral peaks present at K and M points in the low energy spectral weight. To treat this theoretically, we introdce an anisotropy into the model, defining the $J_1 - J_2$ XXZ model with Hamiltonian

$$H = J_1 \sum_{\langle i,j \rangle} \left(\Delta S_i^z S_j^z + S_i^x S_j^x + S_i^y S_j^y \right) \tag{4.21}$$

$$+ J_2 \sum_{\langle\langle i,j \rangle\rangle} \left(\Delta S_i^z S_j^z + S_i^x S_j^x + S_i^y S_j^y \right), \tag{4.22}$$

where S_i^α are spin-1/2 operators, and $\langle i, j \rangle$ and $\langle\langle i, j \rangle\rangle$ denote nearest- and next-nearest neighbor pairs, respectively.

We take $J_2/J_1 = 0.12$, the same value used in Fig. 4.6, which lies in the middle of the QSL phase [174]. To determine the value of Δ, we look at the relative intensity of the low-energy spectrum at K and M, and choose Δ so that it best reproduces the experimental data. This is displayed in Fig. 4.12, and we find that the best choice is $\Delta = 1.35$.

4.3.3 Results & Discussion

Before discussing the results further, we would like to review briefly the key signatures that differentiate a spinon Fermi surface state from a U(1) Dirac spin liquid. First, let us start with the spinon Fermi surface state. In such a state, the low temperature heat capacity is predicted to scale as $\sim T$ [432] at the mean-field level, possibly becoming $T^{2/3}$ if emergent gauge fluctuations dominate. As for the spectrum, mean-field theory predicts a V-shape spectrum near the Γ point and gapless excitations throughout the entire Brillouin zone [327, 213, 306]. These signatures have been observed in YbMgGaO$_4$ [327, 329], and NaYbSe$_2$ [75]. For the U(1) Dirac spin liquid, the heat capacity is expected to scale as $\sim T^2$ because of the Dirac nodes [286, 384]. The low-energy theory on the triangular lattice is quantum electrodynamics (QED$_3$) with 4 Dirac fermions ($N_f = 4$), which predicts gapless excitations at both the M and K wavevectors [346]. The main signature to distinguish this from a spinon Fermi surface state is the presence of a gap away from these points, such as near the Γ point, as observed in recent simulations of the $J_1 - J_2$ Heisenberg model on the triangular lattice [104, 331, 89] (as discussed in Sec. 4.1).

Returning to the discussion of YbZn$_2$GaO$_5$, we demonstrate in Fig. 4.11a the hexagonal crystal structure of YbZn$_2$GaO$_5$, with the space group P6$_3$mmc. This is in contrast to YbMgGaO$_4$ and YbZnGaO$_4$ which crystallize in the R$\bar{3}$m space group. In YbZn$_2$GaO$_5$, the P6$_3$mmc space group provides unique Wyckoff positions for gallium and zinc, therefore, YbZn$_2$GaO$_5$ does not display any intrinsic chemical site mixing. The phase purity of our sample is confirmed through a Rietveld refinement analysis performed on the powder X-ray diffraction pattern obtained from a crushed YbZn$_2$GaO$_5$ single crystal (see Fig. 4.26). We further performed the single-crystal X-ray diffraction measurement on YbZn$_2$GaO$_5$ crystal and observed no discernible chemical disorder within the limit of our experimental accuracy (see Table 4.4). It is noteworthy to add that in YbZn$_2$GaO$_5$,
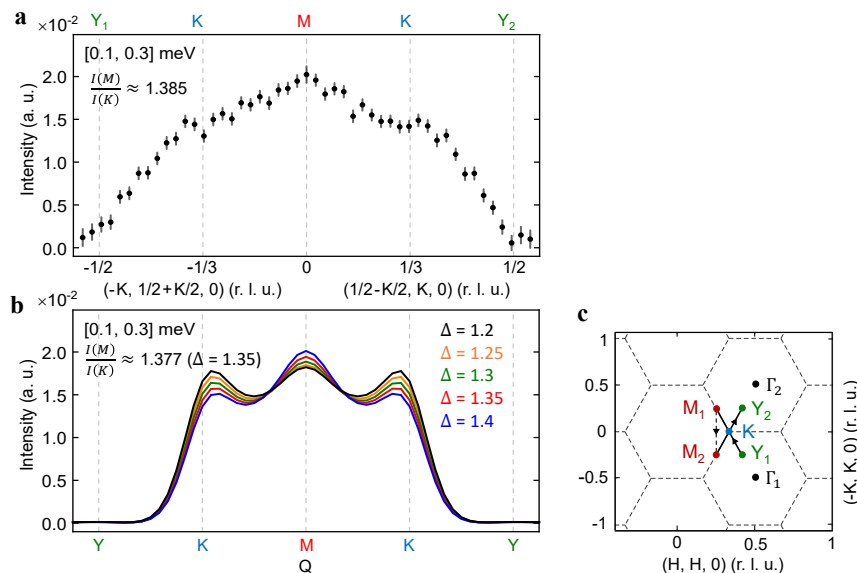
Figure 4.12: **Line cut along high-symmetry points and theoretical calculation with different Δ values**. We present an investigation of the anisotropy effect in the low-energy INS spectrum. **a**. A line cut traveling through high symmetry points (as depicted in c.): Y_1, K, M_1/M_2, K, Y_2. The background-subtracted intensity was integrated between energy intervals [0.1, 0.3] meV and a small q window perpendicular to the high-symmetry path. The ratio of spectral weights between M and K points is around 1.385. **b**. Theoretical calculations of the spectral weights along the same path using different Δ values (Δ = 1.2, 1.25, 1.3, 1.35, 1.4). The ratios between spectral weights at the M and K points for different Delta were calculated, and we find that the ratio of the Δ = 1.35 case provides the best agreement with our experimental data. **c**. A schematic for the high symmetry path of the line cut is shown in a and b.

an additional non-magnetic Zn-O layer is introduced along the crystallographic c-direction, which increases the distance between magnetic Yb-O planes from 8.38 (YbZnGaO$_4$) to 10.98, enhancing the two-dimensionality and quantum fluctuations in this compound compared to previously reported Yb-based triangular lattice QSL candidates [264, 236, 34, 86]. The nearest neighbor Yb^{3+} ions are arranged in a perfect triangular pattern with a distance of 3.37 between them, as illustrated in Fig. 4.11b. This distance is comparable to that in the previously reported Yb-based triangular lattice compounds proposed to host QSL state [223, 218].

We illustrate in Fig. 4.11c the temperature-dependent magnetic susceptibility data collected on the single crystal of YbZn$_2$GaO$_5$ along both directions parallel and perpendicular to the crystallographic c-axis, in the presence of an applied magnetic field of 0.01 T. The inset of Fig. 4.11c highlights the low-temperature susceptibility region down to 0.3 K, confirming the absence of magnetic ordering down to this temperature. The inverse magnetic susceptibility data are fitted to Curie-Weiss law: $1/\chi = (T - \theta_{CW})/C$, (where θ_{CW} is the Curie-Weiss temperature, and C is the
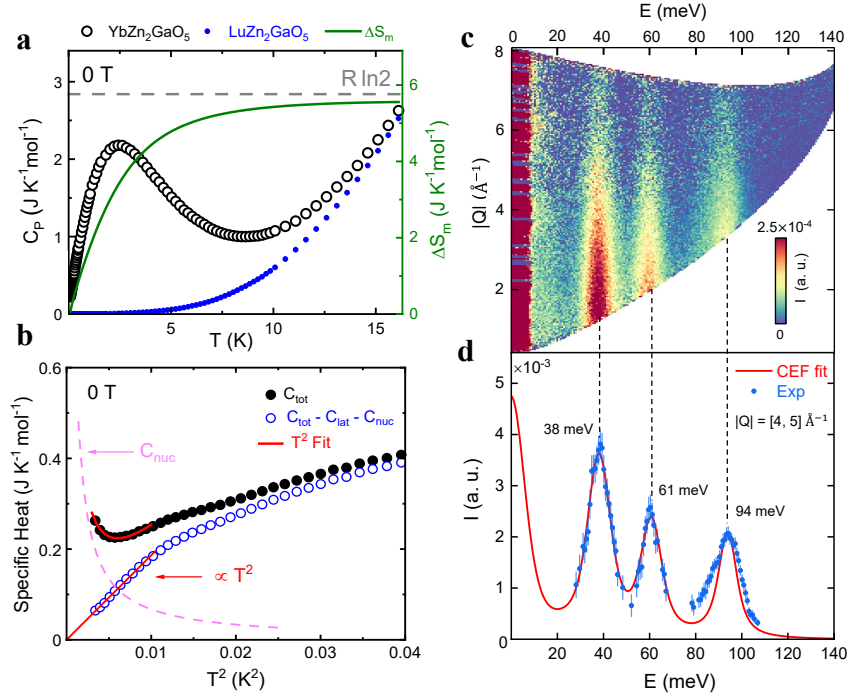
Figure 4.13: **Heat capacity and crystal electric field levels. a**. Heat capacity data of $YbZn_2GaO_5$ single crystal and $LuZn_2GaO_5$ powder sample collected under zero field and down to 0.06 K are shown. The calculated magnetic entropy (right Y-axis) of $YbZn_2GaO_5$ saturates to Rln2, indicating the effective spin-1/2 ground state. **b**. Heat capacity vs T^2 plot: Low-temperature total heat capacity ($C_{tot} = C_{lat} + C_{nuc} + C_{mag}$) shows an upturn below 0.1 K. Using an isostructural nonmagnetic $LuZn_2GaO_5$ and a fitted Schottky model ($C_{nuc} \simeq AT^{-2}$), the lattice and nuclear contributions were removed. The magnetic heat capacity data (C_{mag}) after subtraction is presented as open circles and fitted with a solid red straight line that exhibits a quadratic T-dependence ($C_{mag} \simeq \gamma T^2$). The quadratic T-dependence fit yields an adjusted R-square value of 0.9583, indicating excellent agreement between the model and experimental data. The T^2 dependency of magnetic heat capacity data for $T \to 0$ implies $YbZn_2GaO_5$ is a U(1) Dirac QSL candidate. **c** Inelastic neutron scattering (INS) spectra of $YbZn_2GaO_5$ reveal three crystal electric field (CEF) bands. The phononic contribution is subtracted using an isostructural nonmagnetic sample $LuZn_2GaO_5$. **d** The single-ion CEF fitting shows energy levels at 38 meV, 61 meV, and 94 meV.

Curie constant) at two different temperature regimes. The obtained effective moment ($\mu_{eff} \simeq 4.36$ μ_B) at a high-temperature range agrees with the expected theoretical value of free Yb^{3+} ion ($\simeq 4.54$ μ_B). The Curie-Weiss temperatures obtained for $YbZn_2GaO_5$ in the low-temperature range (5 - 15 K) are slightly higher ($\theta_{CW,\parallel} = -3.77$ K and $\theta_{CW,\perp} = -5.22$ K) than those of Yb(Mg, Zn)GaO$_4$ [218, 223, 327, 401, 236]. This observation suggests a stronger antiferromagnetic coupling between Yb^{3+} ions in $YbZn_2GaO_5$. The collected isothermal magnetization data along both directions up to 14 T
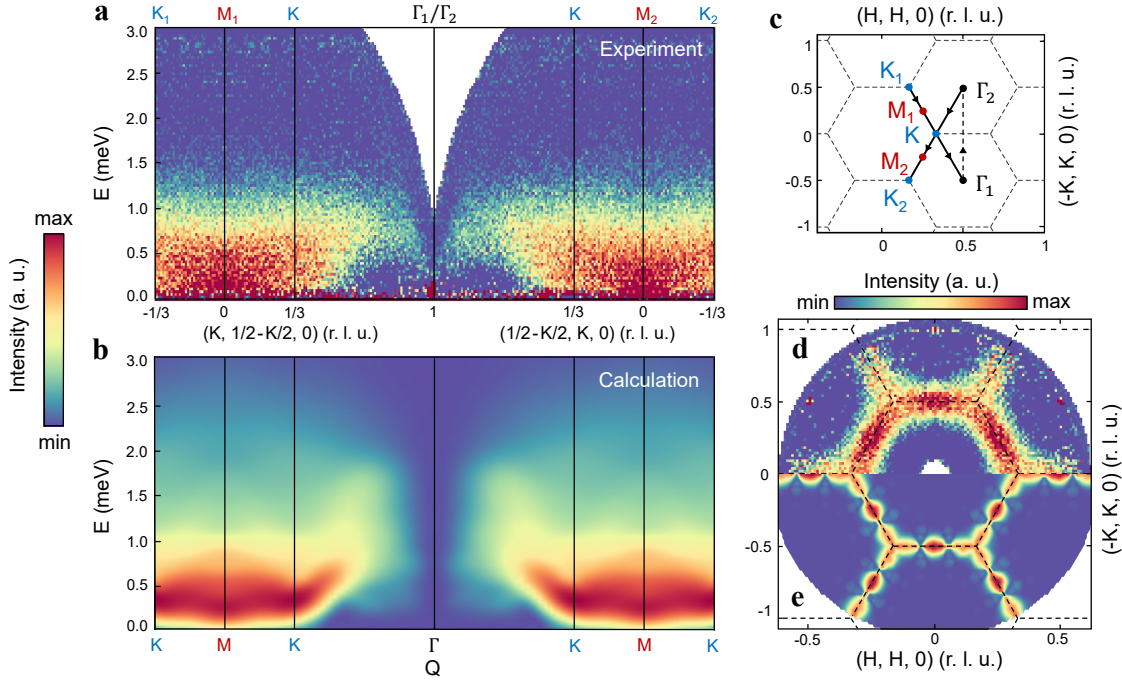
Figure 4.14: **Inelastic Neutron scattering data under zero applied magnetic field a**. Energy dependence of the magnetic excitation spectrum along high symmetry points measured at 0.1 K. The background is subtracted using the high temperature (45 K) spectrum (See Sec. 4.4.2 for details). The contour path travels along the high symmetry points K_1-M_1-K-Γ_1/Γ_2-K-M_2-K_2, which is illustrated by the black solid curve in c. **b**. Calculated spectrum using matrix product states for the $J_1 - J_2$ XXZ model on the triangular lattice, with $J_2/J_1 = 0.12$ and $\Delta = 1.35$ (see Methods section for details). We use $J_1 = 0.5$ meV to adjust the scale of the y-axis for better comparison of the experimental data. **c**. A schematic of the high symmetry path used in a,b. The dashed lines show the boundary of the Brillouin zones. **d**. Background-subtracted low energy slice of the magnetic excitation spectrum collected at 0.1 K. The energy integration range is [0.1, 0.3] meV. **e**. The calculated spectrum of the $J_1 - J_2$ XXZ model with the same parameters as in b. We integrate the spectrum in the energy range [0.1, 0.3] meV for comparison with d.

of applied magnetic field provides anisotropic Landé-g factors ($g_\parallel \simeq 3.44$ and $g_\perp \simeq 3.04$), which are found to be in agreement with those reported earlier for YbZnGaO$_4$ [236] (see Fig. S1).

We show in Fig. 4.13a zero-field heat capacity measurement performed on YbZn$_2$GaO$_5$ single crystal sample down to 0.06 K, confirming the absence of any long-range magnetic ordering. The contribution of phonons is subtracted using the isostructural non-magnetic sample of LuZn$_2$GaO$_5$. In Fig. 4.13b, we highlight the low-temperature behavior of the heat capacity data below 0.2 K, which is particularly intriguing. The heat capacity of YbZn$_2$GaO$_5$ at low temperature has multiple contributions denoted by $C_{tot} = C_{lat} + C_{nuc} + C_{mag}$. C_{lat} represents the lattice (phononic)

contribution that is negligible below 0.1 K. C_{nuc} accounts for the nuclear Schottky contribution due to the hyperfine splitting of the nuclear energy levels resulting from the interaction between nuclear spins and electrons [126]. The nuclear contribution ($C_{nuc} \simeq AT^{-2}$) is subtracted by fitting the heat capacity data below 0.1 K and the fitting coefficient value ($A = 6.72(4) \times 10^{-4}$ JKmol^{-1}) is consistent with that reported for other Yb-based compounds [288]. The subtracted magnetic heat capacity data (C_{mag}) displays a $\sim T^2$ dependence (red solid straight line in Fig. 4.13b) with a coefficient of $\gamma = C_{mag}/T^2 = 18.6(1)$ JK^{-3}mol^{-1} below 0.1 K. We also attempted to fit the magnetic heat capacity data with a linear dependence ($C_{mag} \sim T$), but this fitting approach did not provide a satisfactory result (see Fig. S3). The magnetic heat capacity data exhibiting a $\sim T^2$ dependence for T $\rightarrow$ 0 and the lack of any long-range magnetic ordering down to the lowest temperature of 0.06 K imply that the ground state of YbZn$_2$GaO$_5$ is a U(1) Dirac QSL candidate [286, 384].

To obtain a better understanding of the ground state of YbZn$_2$GaO$_5$, an INS experiment was conducted on a high-purity powder sample at 5 K, as shown in Fig. 4.13c,d. The single-ion crystal electric field (CEF) fitting results revealed three distinct crystal field excitations at 38 meV, 61 meV, and 94 meV, which agree with those observed in other previously reported Yb-based triangular lattice systems [216, 86, 304, 75, 425, 352]. Based on our analysis of the CEF levels, we have determined that the first excited state of YbZn$_2$GaO$_5$ is separated from the ground state by a gap of over 441 K (38 meV). This suggests a Kramer's doublet ground state for the Yb^{3+} ions with an effective spin-1/2. Our CEF fitting scheme, which is consistent with the heat capacity data, supports this conclusion. In particular, the calculated magnetic entropy of YbZn$_2$GaO$_5$ saturates at Rln2, indicating an effective spin-1/2 ground state, as shown in Fig. 4.13a (see Tables S2 and S3 for further details on the CEF fitting scheme).

Furthermore, we conducted INS experiments on a high-quality single crystal of YbZn$_2$GaO$_5$. These experiments were designed to probe the low-energy excitations of the material. An incident neutron energy of 3.32 meV was used and the excitation spectrum under zero-field was collected at a base temperature of 0.1 K. Scans performed at a high temperature of 45 K were used for background subtraction (see Fig. S2). We show in Fig.4.14a the scattering intensity as a function of energy transfer, with a path taken through the high-symmetry points of K_1-M_1-K-Γ_1/Γ_2-K-M_2-K_2, as illustrated in Fig.4.14c. A broad continuum extending over an energy scale of approximately 1.4 meV was observed, with the spectrum weight gradually decreasing at higher energy. We observed a clear gap in the spectra of YbZn$_2$GaO$_5$ near the Γ point, while the excitation remained gapless between M and K points within the instrumental energy resolution of approximately 0.06 meV, as shown in Fig. 4.14a. Our theoretical calculation shows promising agreement with our experimental data, with J$_2$/J$_1$ = 0.12 and an anisotropy value of Δ = 1.35 (see Fig. 4.14b). In contrast to YbZn$_2$GaO$_5$, other reported Yb-based triangular systems, such as the delafossite material NaYbSe$_2$, display a continuum spectrum without a gap at all Q. This observation is consistent with a spinon Fermi surface state [75, 213]. However, in YbZn$_2$GaO$_5$, the observed energy gap near Γ along with the gapless continuum spectra observed at Q = K and M are indicative of a U(1) Dirac QSL state [331]. The thermodynamics measurements are consistent with this spectrum, as the magnetic heat capacity data (C_{mag}) exhibits a $\sim T^2$ dependence for T $\rightarrow$ 0, which is also indicative of a U(1) Dirac QSL.

In Fig. 4.14d, we demonstrate the experimental dispersion of the neutron scattering intensities through constant energy slice integrated from 0.1 to 0.3 meV. We observe that at low energy, spectral weights are localized at the edge of the Brillouin zone, with higher intensities at the M points than at the K points. As the energy increases, the difference in intensities between M and K points becomes less prominent, and the intensities disperse throughout the Brillouin zone, as shown in Fig. 4.28. Moreover, the theoretical calculations in Fig. 4.14e agree with our experimental observations in similar energy ranges. The agreement between theory and experiment suggests that INS spectra of $YbZn_2GaO_5$ are sufficiently well described by the $J_1 - J_2$ XXZ model without additional couplings. The presence of gapless modes at K and M while having a gap near Γ strongly favors a U(1) Dirac QSL ground state over either a spinon Fermi surface or the effects of disorder.

4.3.4 Conclusions

In conclusion, high-quality single crystals of $YbZn_2GaO_5$,a Yb-based triangular lattice system without any intrinsic chemical disorder, have been successfully synthesized and characterized. These results reveal that the magnetic heat capacity data at ultra-low temperatures follow a T^2 dependence, providing experimental evidence for the realization of U(1) Dirac QSL on a triangular lattice in $YbZn_2GaO_5$. Additionally, our INS investigation of $YbZn_2GaO_5$ demonstrates gapless, continuum-like spectra at the high-symmetry M and K points but *not* at the Γ point, confirming the possibility of a U(1) Dirac QSL ground state in this compound. Therefore, we suggest that $YbZn_2GaO_5$ is a highly promising candidate for the long-sought U(1) Dirac QSL and warrants further investigations with other techniques.

Figure 4.15: $KYbSe_2$ sample used to measure the low-energy spin excitations on CNCS. 20 crystals were coaligned and glued to two aluminum plates (top) which were then screwed to a copper rod (bottom). The different crystals are different shades of red because of their different thicknesses.

4.4   Appendix

4.4.1   Experimental details for $KYbSe_2$

In this section of the appendix, I discuss additional information regarding the experiment conducted in $KYbSe_2$ by my collaborators at Oak Ridge National Lab. I was not involved directly with conducting the experiments, but this is an important part of my thesis, and so I include details about the setup here.

CNCS experiment

We measured the low-energy spin excitations with the CNCS spectrometer at Oak Ridge National Laboratory's Spallation Neutron Source. The sample for this experiment consisted of 20 coaligned plate-like crystals glued to aluminum discs (see Fig. 4.15), for a total mass of 200 mg $KYbSe_2$ in the $(hk0)$ scattering plane. The sample was mounted in a ^{3}He refrigerator and measured with double-disc chopper frequency 300.0 Hz (high-flux mode, 9 degree opening on the double disk). All CNCS data were corrected for the isotropic Yb^{3+} form factor [41].

The spectrum was measured over $180°$ rotation at $E_i = 3.32$ meV and $E_i = 1.55$ meV at base temperature and at 12 K. At 1 K and 2 K, we measured only over $60°$ and used $-3m$ crystal symmetry to fold the scattering over and cover the full range of reciprocal space. In comparing intensity of nuclear Bragg peaks, we did find some degree of obverse-reverse twinning of the crystal array, such that some crystal planes were rotated $60°$ from those below. This did not affect the in-plane scattering due to the lack of scattering dependence upon ℓ. The sample thermometer at base temperature read 270 mK, but because this thermometer was not exactly on the sample we round up the effective base temperature to 300 mK. To probe a possible gap at K, we also measured
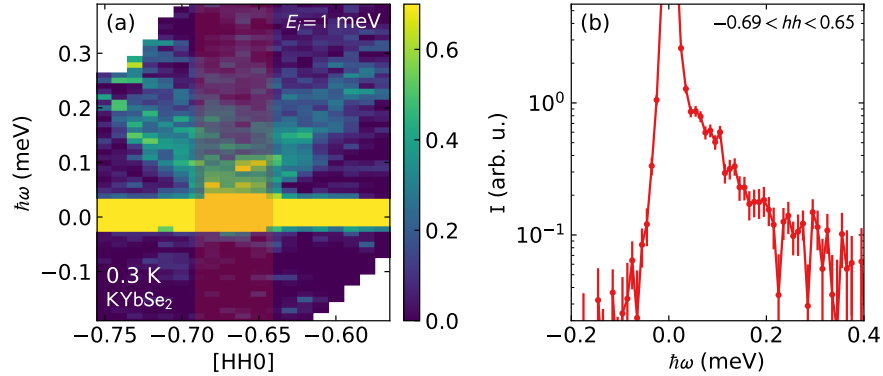
Figure 4.16: High resolution KYbSe$_2$ scattering at $(1/3, 1/3, 0)$. Panel (a) shows a slice through the data showing the gapless dispersion. Panel (b) shows a 1D cut indicated by the faint vertical red bar in panel (a). Both plots show the dispersion to be gapless at 0.3 K to within 0.04 meV.

a rotation scan over 15° at $E_i = 1.0$ meV, for a resolution FWHM of 20 μeV at $\hbar\omega = 0$. These data are shown in Fig. 4.16, and reveal a gapless excitation spectrum at 0.3 K to within 40 μeV.

Background subtraction — For the CNCS experiment, a phenomenological background was created and subtracted using the 12 K scattering data. At 12 K, the spin excitations become totally diffuse paramagnetic excitations. To model and eliminate these, we took the median intensity at each constant energy slice to be the approximate value of paramagnetic intensity, and subtracted this value from each pixel at that energy transfer. Then, we set any negative intensities to zero, and subtracted this background from the data. This median-value subtraction was not done for elastic scattering because paramagnetic intensity has negligible elastic contributions. Thus, for elastic data the 12 K was directly subtracted from lower temperatures. We find that this procedure effectively eliminates artifacts in the data while leaving magnetic intensity unchanged, as shown in Fig. 4.17. Finally, because entanglement witnesses require a total sum rule satisfying $S(S + 1) = 0.75$ for an effective $J = 1/2$ system, we normalized the background-subtracted 300 mK KYbSe$_2$ scattering such that the total scattering is $\langle S^2 \rangle = 0.75$.

Critical scaling fits — To fit the critical exponent in Fig. 4.10, we used data at $\hbar\omega/k_B T$ above the "knee" where the power law behavior starts. Using this data range, we minimized the χ^2 of the scaled data fitted to a power law in $(\hbar\omega/k_B T)^\alpha$, varying α and rescaling the data in each iteration. This resulted in a fitted $\alpha = 1.73(12)$.

ARCS experiment

The sample for the ARCS measurement was 3 g of plate-like crystals ground into a powder. We measured the inelastic neutron scattering at incident energies $E_i = 35$ meV, 50 meV, and 130 meV and at temperatures 7 K, 100 K, 200 K, and 300 K (for $E_i = 50$ meV only).
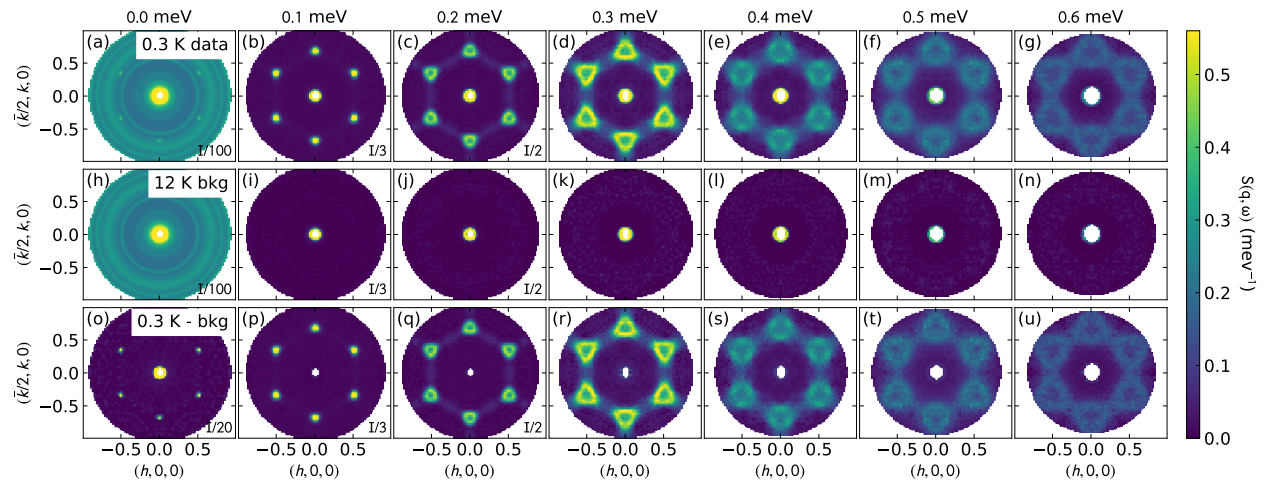
Figure 4.17: $KYbSe_2$ background subtraction for CNCS data. The top row shows the raw data at 0.3 K. The middle row shows the phenomenological background generated from the 12 K scattering data. The bottom row shows the data with the background subtracted, eliminating artifacts near $Q = 0$ and $\hbar\omega = 0$.

Low temperature magnetic order

Diffuse scattering Hamiltonian fits predicted that $KYbSe_2$ is within the 120° ordered phase, so that it should order magnetically at the lowest temperatures. To test this, we measured the specific heat of $KYbSe_2$ using quasi-adiabatic method in a dilution refrigerator. Heater was mounted on one side of the sapphire stage, with one large single sample (1.19 mg) mounted on the other side with GE varnish. Ruthenium oxide resistance thermometer was glued on the top of the samples. A heat pulse is delivered to heat capacity stage, and the temperature of the thermometer is measured as a function of time. The results are shown in Fig. 4.18(a). A clear kink is visible at 290 mK consistent with an ordering transition.

To evaluate any possible sample-dependent properties, we remeasured heat capacity of a collection of 11 small pieces (2.33 mg) [see the grey data in Fig. 4.18(a)], which shows a somewhat broadened transition. Neither sample had a measurable amount of crystalline disorder, suggesting that an appreciable amount of crystalline disorder may suppress the transition entirely.

More clear evidence of static magnetism comes from the upturn at the lowest temperatures. We fit this with a nuclear Schottky anomaly using the hyperfine parameters for Yb^{3+} in Ref. [31]. As shown by the colored lines in Fig. 4.18(a), the Yb moment size is well-constrained by the data, giving a fitted $\mu = (0.579 \pm 0.010)\,\mu_B$. This method of determining the magnetic moment has the advantage of (a) being a local probe and insensitive to the particular type of magnetic order, and (b) is a fit extrapolated to zero temperature, and thus is an estimate of the $T = 0$ ordered moment.

We also measured the neutron diffraction of $KYbSe_2$ using the CTAX spectrometer at the Oak Ridge National Laboratory HFIR reactor, using the same sample and sample mount as used in the
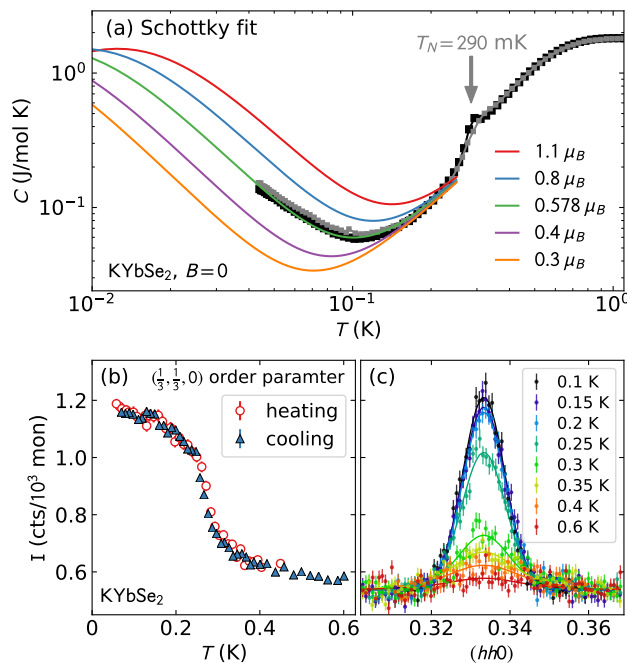
Figure 4.18: Evidence of magnetic order in $KYbSe_2$. (a) Zero field heat capacity of a large (black) and small (grey) sample, showing a kink at 290 mK. An upturn at low temperatures is fitted with a nuclear Schottky anomaly, which uniquely constrains the local ordered Yb^{3+} moment as shown by the colored curves.

CNCS experiment, but mounted in a dilution refrigerator. We measured with $E_i = E_f = 4.8$ meV neutrons focusing on the $Q = (1/3, 1/3, 0)$ point, the wavevector associated with 120° order. This data is shown in Fig. 4.18(b), and shows a clear onset of elastic scattering at around 300 mK. Panel (c) shows cuts along the $(hh0)$ direction at several different temperatures, showing the emergence of the Bragg intensity. The steepest part of the order parameter curve is at 290 mK, confirming that the bump observed in heat capacity is indeed the transition to 120° magnetic order. Additionally, the agreement between the heat capacity and neutron order parameter curves shows that the sample mount used for the neutron experiments provides adequate thermal equilibration down to at least 290 mK. In summary, both heat capacity and neutron diffraction confirm that the $KYbSe_2$ J_2/J_1 ratio is indeed within the 120° ordered phase.

Crystal characterization

To investigate the quality of the $KYbSe_2$ crystals used in this experiment, we measured the single crystal X-ray diffraction using a Bruker Quest D8 single-crystal X-ray diffractometer. The data were collected at room temperature utilizing a Mo Kα radiation, $\lambda = 0.71073$. The crystal diffraction images were collected using ϕ and ω-scans. The diffractometer was equipped with an Incoatec
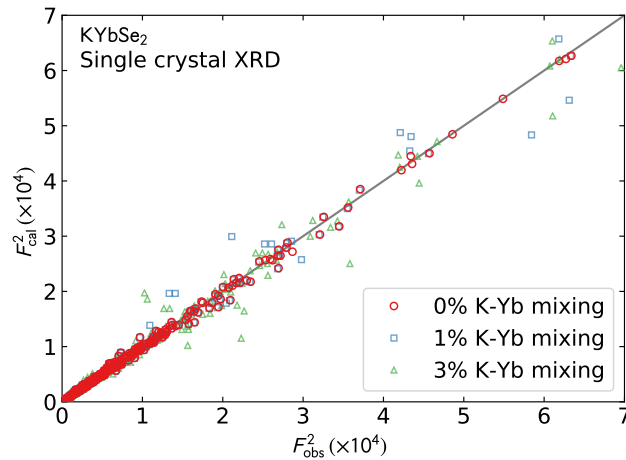
Figure 4.19: Single crystal $KYbSe_2$ X-ray diffraction, showing the observed peak intensities versus the peak intensities of a calculated model with no site mixing or disorder (red circles), 1% Yb-K site mixing (blue squares), and 3% Yb-K site mixing (green triangles). The 0% site mixing visibly fits the data the best, indicating very high crystal quality.

IμS source using the APEXIII software suite for data setup, collection, and processing [42]. The structure was resolved using intrinsic phasing and full-matrix least square methods with refinement on F2. Structure refinements were performed using the SHELXTL software suite [325]. All atoms were first refined with isotropic displacement parameters and then they were refined anisotropically. The final refinement was confirmed with *CheckCif* [347]. A refinement with no site mixing fits the data extremely well.

If we allow site mixing between K and Yb, similar to what was observed in $NaYbSe_2$ [74], the K-Yb site mixing in $KYbSe_2$ refines to (0.2 ± 0.3)%, where the error bar indicates one standard deviation uncertainty as calculated by reduced χ^2 contour. This is a full order of magnitude less site mixing than the 3% site disorder found in $NaYbSe_2$ [74]. If we force the refined model to have a site-mixing greater than 1%, as shown in Fig. 4.19, we find a worse *R*-value and a visibly worse fit. Thus, to within uncertainty, $KYbSe_2$ has no K-Yb site mixing and can be considered as an ideal 2D triangular lattice.

Fitting the Roton Mode

To quantify the extent and the gap of the roton-like mode, we fitted the intensity vs energy of many constant-*Q* cuts as shown in Fig. 4.20. We used an asymmetric Gaussian to model the mode, and with the exception of two data points near *M*, it picks out the peak maximum very well. We then fitted these data points to a sinusoidal function $A\sin(Q) + B\sin(3Q) + C$ to estimate the mode maximum and minimum. These fits show a mode maximum of 0.288(12) meV, a roton minimum 0.200(13) meV, and a fitted gap of 0.059(7) meV. The fitted gap may be an artifact of the mode's
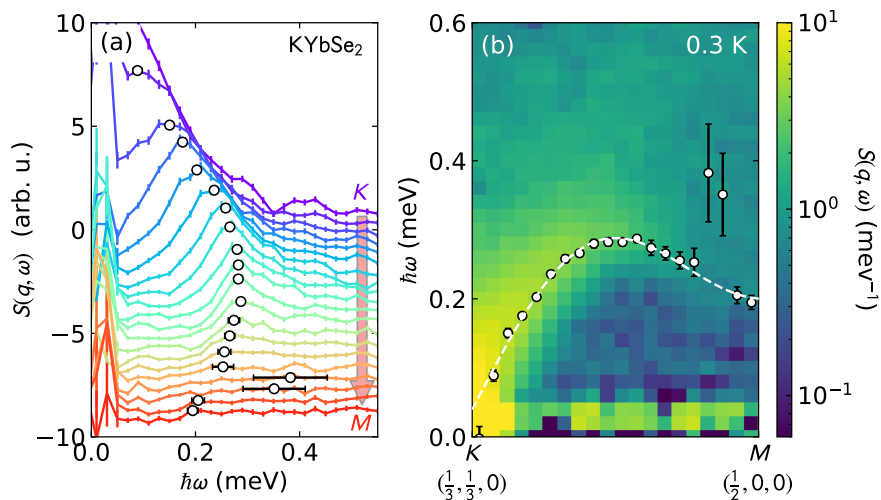
Figure 4.20: Fits to the KYbSe$_2$ roton mode. (a) shows constant Q cuts between K and M, and the fitted mode maximum. Each constant Q slice is offset on the y axis, and the colors show the variation from K and M. (b) shows the mode maximum overplotted on the colormap data, along with a fitted sinusoidal dispersion function.

deviation from the idealized sin function rather than an actual gap—the higher resolution scan in Fig. 8 of the main text do not reveal a clear gap above 40 μeV.

We also fitted the low-energy intense mode emanating from K toward Γ in order to match energy scales between theory and experiment, shown in Fig. 4.21. We fit constant Q cuts to Gaussian curves to define the center of the mode in both KYbSe$_2$ scattering data and Schwinger boson simulations. We then fit these fitted points to a sinusoidal curve between Γ and K, and scaled the slope of the sin curves at K so that theory matched experiment. This led to a fitted energy scale $J_1 = 0.56(3)$ meV. The Schwinger boson simulations show the fitted maxima extrapolating toward $\hbar\omega = 0$ at K, but the KYbSe$_2$ mode maxima appear to have a nonzero intercept. Allowing for a gap in the fitted sin function, we estimate a KYbSe$_2$ fitted gap of 0.030(5) meV—too small to be directly resolved using these data.

We can cross-check this fitted J_1 value by comparing to the saturation magnetization. Although saturation magnetization has not been measured for KYbSe$_2$, it has been measured for the sister compound NaYbSe$_2$, which has an ab-plane saturation magnetization of $\sim$ 12 T [287]. Assuming the KYbSe$_2$ value to be close to 12 T, this gives an exchange energy scale of J_1 = 5.36 K = 0.462 meV.

Crystal electric field fits

Here we describe the procedure used, and the results from the crystal electric field (CEF) fits to the KYbSe$_2$ ARCS data.
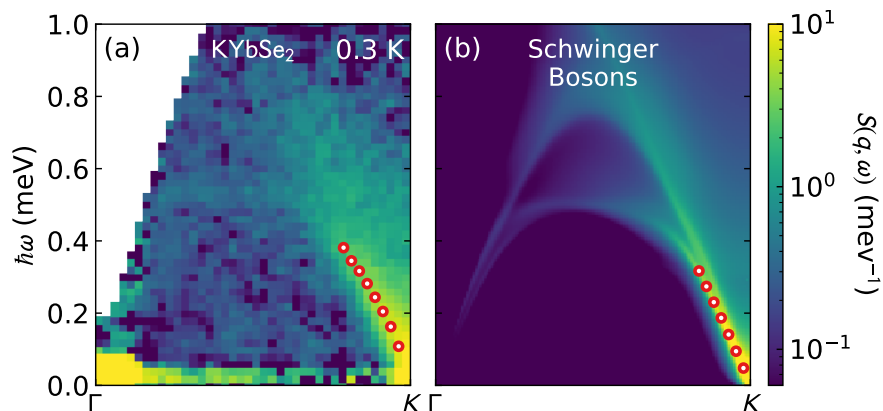
Figure 4.21: Fits to the mode maximum between Γ and K for both (a) KYbSe$_2$ and (b) Schwinger boson simulations. The red dots show the center of a fitted Gaussian, the slope of which was used to determine the energy scale for Schwinger boson simulations. The experimental slope appears to have a nonzero $\hbar\omega$ intercept, but is too small to be directly resolved with this experiment.

Because of the three-fold Yb^{3+} rotational symmetry in KYbSe$_2$, there are six nonzero crystal field parameters in the Stevens operator formalism for the Yb^{3+} ion: B_2^0, B_4^0, B_4^3, B_6^0, B_6^3, B_6^6 [168]. The effective $J = 7/2$ of Yb^{3+} allows for four energetically-distinct Kramers doublet states, which means three crystal field excitation peaks should be visible in the neutron spectrum.

The crystal field excitations in Fig. 4.22 can be distinguished from the phonon background by the dependence upon Q: phonon intensity grows with Q while magnetic intensity decreases with Q according to the magnetic form factor. Three of the latter excitations are visible: one near 32 meV, one near 23 meV, and one near 17 meV. Unfortunately, as shown in Fig. 4.22, the 17 meV mode sits atop an intense flat phonon band which extends to low Q (it is clearly a phonon because its intensity grows with both temperature and $|Q|$), which potentially indicates coupling between phonons and the CEF excitation. (Alternatively, flat-band phonons can have $Q = 0$ intensity from multiple scattering [5].) To verify that the low-energy mode is indeed the third CEF excited level, we measured the CEF spectrum up to 130 meV [Fig. 4.23], and found no additional visible CEF levels. Furthermore, the observed energies are close to (i) point charge calculations which predict excited modes at 6.4 meV, 18.4 meV, and 33.0 meV, and (ii) measured crystal field excitations of sister compound NaYbSe$_2$ of 15.8 meV, 24.3 meV, and 30.5 meV [423]. Therefore, we are confident that the 17 meV, 23 meV, and 32 meV peaks are the three excited Yb^{3+} CEF levels.

Fitting procedure

To fit the six crystal field parameters to the data, we started with a point-charge model calculation of the crystal field levels, which predicts energies at 6.4 meV, 18.4 meV, and 33.0 meV. We then used *PyCrystalField* [311] to fit the model to the neutron scattering data between 1 Å^{-1} and 2 Å^{-1} using the point charge model as starting values.
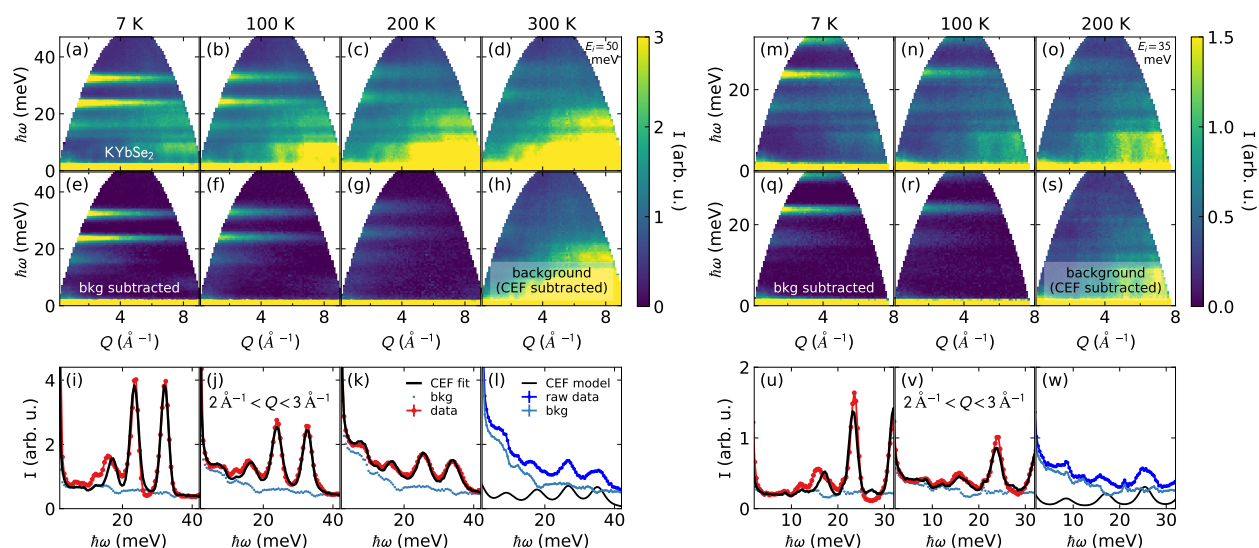
Figure 4.22: KYbSe$_2$ crystal field fit. The top row shows the raw data measured with $E_i = 50$ meV (left section) and $E_i = 35$ meV neutrons (right section). The middle row shows the background subtracted data, with the model-subtracted backgrounds shown in panels (h) and (s). The bottom row shows the fitted data between 2 Å^{-1} and 3 Å^{-1}. Red data shows the raw data, light blue data shows the rescaled high-temperature background. The black line shows the CEF model plus the fitted background. The backgrounds are shown in panels (l) and (w).
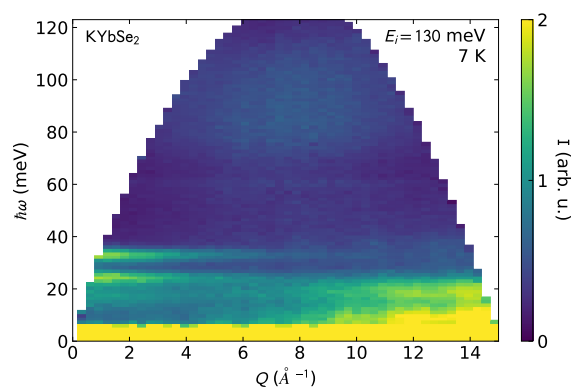
Figure 4.23: Crystal field spectrum of KYbSe$_2$ measured with $E_i = 130$ meV neutrons. No crystal field excitations are visible above 40 meV, confirming the model derived in this study.

In order to isolate the crystal field excitations from the phonon background, we employed a self-consistent background subtraction scheme. We used the highest temperature data (300 K for $E_i = 50$ meV and 200 K for $E_i = 35$ meV) as background, but subtracted off the simulated CEF intensities and then rescaled the subtracted data to match the lower-temperature phonons. This way, the background improves as the CEF model improves, such that the best fit CEF model subtracts off the visible CEF excitations at high temperatures. Because the frequencies of the phonon spectrum are not precisely known, we created a phenomenological energy-dependent scale function to apply the background to lower temperatures. It was a step function of the form

$$\frac{a}{\exp[(\hbar\omega - \mu)/k_B T] + 1} + b$$

where a, b, and μ were fitted to the ratio of high-T to low-T scattering data at energy transfers where no crystal electric excitations are present. As shown in Fig. 4.22, it produces a reasonable background for the fits.

As in NaYbSe$_2$ [423], the crystal field levels broaden in energy and shift to higher energies as temperature increases, as shown in Fig. 4.24. The broadening indicates a shorter excitation lifetime, and is typical for crystal field levels at high temperatures. The shift in energy indicates CEF-phonon coupling, which is not surprising given that the lowest energy CEF mode is at nearly the same energy as an intense phonon band. To account for this in our fits, we applied an ad-hoc shift to the higher temperature energy eigenvalues so that they match the data. In theory, these shifts occur because of slight shifts in the CEF Hamiltonian and require a separate CEF fit—but in order to constrain the low-temperature Hamiltonian it was necessary to include the higher temperature data. Thus we assume that the slight shift in energy indicates a negligible change in the mode intensities, and the resulting fit matches the data very well.

We simulated the crystal field excitations with a Voigt profile, with a temperature-dependent Lorentzian width to account for finite lifetime and a Gaussian width to account for instrumental resolution. The Lorentzian widths were fitted to the two highest peaks for each temperature prior to the Hamiltonian fit and were kept fixed throughout the fit. The resolution function was treated as a fitted parameter, and was allowed to vary linearly as a function of energy transfer but not temperature. The fitted resolution was allowed to vary between $E_i = 50$ meV and $E_i = 35$ meV. Also, an overall scale factor was fitted to the data, one for each incident energy. We simultaneously fit the 7 K, 100 K, and 200 K $E_i = 50$ meV data and the 7 K and 100 K $E_i = 35$ meV data. χ^2 minimization was performed with Powell's method [279] as implemented by Scipy [378]. The best fit crystal field parameter values are given in Table 4.2, and the resulting crystal field Hamiltonian eigenstates are listed in Table 4.3. The best fit calculated g-tensor is given in the main text.

We calculated the uncertainty for these parameters by using a Monte Carlo stochastic search method to map out the χ^2 contour around the best fit model [312]. Using a series of Markov chains, we generated several thousand solutions within $\Delta\chi^2 = 1$ of the best fit minimum $\chi^2_{red} = 65.86$. This search was aided by principal component analysis of the valid solutions using Scikit [269], such that the random guesses were more along principal component axes. The CEF parameter, g-tensor, and eigenvector uncertainties were calculated from the range of valid values in this set.
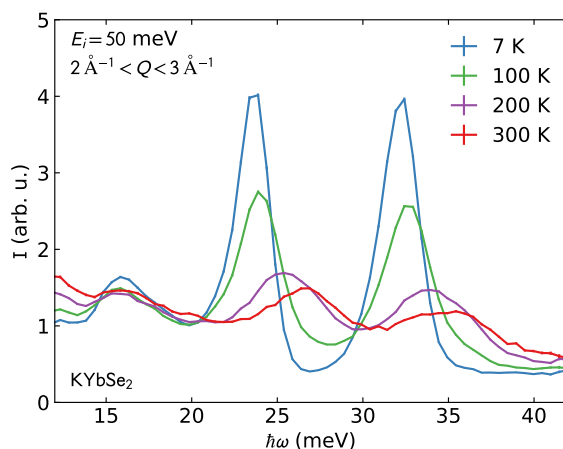
Figure 4.24: KYbSe$_2$ crystal field excitations as a function of temperature. The top two peaks noticeably shift to higher energies as temperature increases, while the bottom level stays constant. This effect was accounted for in the model fit.

Table 4.2: Best fit crystal field parameters for KYbSe$_2$. The middle column gives the nearest neighbor point charge model for KYbSe$_2$ and the right column shows the best fit values.

Crystal field parameter	Point charge model	Best fit
B_0^0	-0.556	-0.16(2)
B_0^0	0.0088	0.004(2)
B_3^3	-0.281	-0.15(2)
B_0^0	0.00005	0.00038(5)
B_3^3	0.0002	0.0143(5)
B_6^6	0.00043	0.0103(5)

Table 4.3: Eigenvectors and eigenvalues for the best fit KYbSe$_2$ CEF Hamiltonian. Numbers in parenthesis are one standard deviation uncertainty.

E (meV)	$\lvert -\frac{7}{2}\rangle$	$\lvert -\frac{5}{2}\rangle$	$\lvert -\frac{3}{2}\rangle$	$\lvert -\frac{1}{2}\rangle$	$\lvert \frac{1}{2}\rangle$	$\lvert \frac{3}{2}\rangle$	$\lvert \frac{5}{2}\rangle$	$\lvert \frac{7}{2}\rangle$
0.0	0.0	0.78(3)	0.0	0.0	-0.44(4)	0.0	0.0	-0.44(3)
0.0	-0.44(3)	0.0	0.0	0.44(4)	0.0	0.0	0.78(3)	0.0
17.1(3)	0.0	-0.09(3)	0.0	0.0	0.61(3)	0.0	0.0	-0.79(2)
17.1(3)	-0.79(2)	0.0	0.0	-0.61(3)	0.0	0.0	-0.09(3)	0.0
23.24(5)	0.0	0.0	1.0	0.0	0.0	0.0	0.0	0.0
23.24(5)	0.0	0.0	0.0	0.0	0.0	1.0	0.0	0.0
31.93(5)	0.43(3)	0.0	0.0	-0.66(4)	0.0	0.0	0.62(4)	0.0
31.93(5)	0.0	0.62(4)	0.0	0.0	0.66(4)	0.0	0.0	0.43(3)
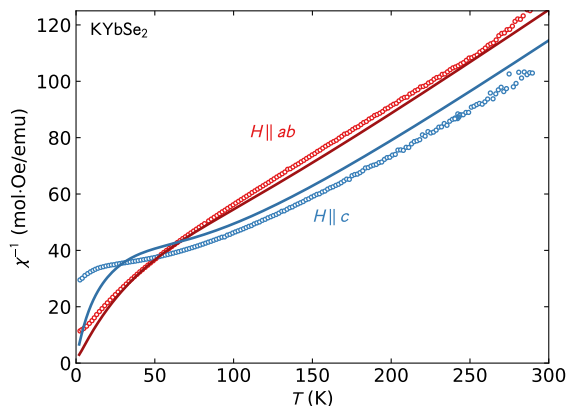
Figure 4.25: KYbSe$_2$ susceptibility compared to best fit CEF calculated single crystal susceptibility. Qualitatively, the simulation matches experiment, though the experiments show a higher susceptibility in the *c* direction.

It is often the case that crystal field fits to neutron data are underconstrained, and wildly different Hamiltonians can fit the data equally well [312, 307]. The same is true here: two different models emerged from the fits, one with easy-axis magnetism and one with easy-plane. To select the correct Hamiltonian, we compared the calculated single-ion susceptibility to the measured susceptibility in Fig. 4.25. Measured susceptibility clearly shows an easy-plane magnetism at low temperature shifting to easy-axis magnetism at high temperature. The easy-plane model matches this behavior very well, and thus we select it as the correct model. However, this highlights the need to cross-check any fitted Hamiltonian with a different measure of magnetic anisotropy.

Although the calculated susceptibility qualitatively matches the measured susceptibility, the correspondence is not perfect (especially in the *c* direction). Although this discrepancy is within error bars of the fitted Hamiltonian, two additional complications may also prevent perfect agreement: (i) magnetic exchange which shifts measured susceptibility values, and (ii) a shifting CEF Hamiltonian as a function of temperature. Because of these effects, we did not use susceptibility data to constrain the fit itself.

One final cross-check of the crystal field model can be made by comparing the calculated saturation magnetization to the measured KYbSe$_2$ 1/3 magnetization plateau. According to ref. [398], the 0.42 K 1/3 magnetization plateau occurs at $\mu_0 H = 4.2$ T, $M = 0.569\,\mu_B$. However, this value is offset by Van Vleck susceptibility which at low fields adds a linear offset to the ground state CEF magnetization. According to the fitted KYbSe$_2$ CEF model, the Van Vleck susceptibility is $0.0176\,\mu_B$/T at 0.42 K—which means we must subtract $(0.0176\,\mu_B/\text{T})(4.2\,\text{T}) = 0.074\,\mu_B$ from the measured plateau magnetization for a true 1/3 magnetization of $0.495\,\mu_B$. This is one third of the CEF predicted *ab*-plane saturation magnetization 1.48(9) μ_B. Thus we have high confidence that our fitted CEF model and associated *g*-tensor is correct.

Onsager reaction field fits

The magnetic diffuse scattering from the CNCS experiment was analyzed using the Onsager reaction field approach of Ref. [263]. Fits to the single-crystal diffuse-scattering data sets were performed using the Migrad algorithm in the MINUIT program [180]. The fitted data sets comprised the $(hk0)$, $(h0l)$ and (hhl) scattering planes measured at 1 K and 2 K. All data were energy-integrated over $E > 0.05$ meV. We minimize the sum of squared residuals, defined as

$$\chi^2 = \sum_d \sum_{i \in d} \left(\frac{I_i^{\text{data}} - s I_i^{\text{calc}} - B}{\sigma_i} \right)^2, \tag{4.23}$$

where d denotes a data set, I_i^{data} is the intensity of data point i, I_i^{calc} is the corresponding calculated intensity [see the next section], σ_i is the corresponding uncertainty, and s and B denote, respectively, fitted intensity scale and offset factors determined at each iteration using linear-least-squares relations.

The $J_{\alpha\beta}(\mathbf{Q})$ are elements of an interaction matrix given by

$$\mathsf{J}(\mathbf{Q}) = - \begin{pmatrix} a J_X + b J_A & c J_A & 0 \\ c J_A & a J_X - b J_A & 0 \\ 0 & 0 & a J_Z \end{pmatrix}, \tag{4.24}$$

in which

$$a = 2[\cos 2\pi(h+k) + \cos 2\pi h + \cos 2\pi k], \tag{4.25}$$

$$b = 2\cos 2\pi(h+k) - \cos 2\pi h - \cos 2\pi k, \tag{4.26}$$

$$c = \sqrt{3}(\cos 2\pi k - \cos 2\pi h), \tag{4.27}$$

where h and k are noninteger Miller indices. We find a best fit Hamiltonian

$$J_X = 2.33(10) \text{ K} \qquad J_Z = 2.28(10) \text{ K}$$
$$J_A = -0.018(8) \text{ K} \qquad J_2 = 0.11(2) \text{ K} \tag{4.28}$$

where J_X and J_Z are the ab-plane and c-axis nearest neighbor exchange respectively, J_A is off-diagonal exchange [263], J_2 is second neighbor Heisenberg exchange, and spins have been treated as classical vectors of unit length. These values show off-diagonal exchange J_A being much smaller than the Heisenberg terms J_X and J_Y, showing that KYbSe$_2$ can be effectively modeled by the $J_1 - J_2$ Heisenberg model of Eq. (4.29) in the main text.

To check the robustness of the results, we performed three checks. First, to check for the possibility of local χ^2 minima, we performed 20 separate fits initialized with different parameter values in the range $[-1 : 1]$ K. No local minima were found to give acceptable agreement with the experimental data, and the parameters reported in the text correspond to the minimum χ^2 we obtained. Second, we considered the effect of including an additional symmetry-allowed off-diagonal exchange interaction, J_B [263]. This parameter refined to a zero value within uncertainty, and has negligible effect on the results. Third, we considered the effect of the obverse-reverse twinning of the crystal array, and found that including this effect in the calculation had negligible effect on the fit quality or parameter values.

Onsager reaction field: calculated intensity

Here we outline the Onsager reaction field (ORF) approach for completeness. We consider the spin Hamiltonian

$$\mathcal{H} = \sum_{\langle i,j \rangle} \Big\{ J_X \left(S_i^x S_j^x + S_i^y S_j^y \right) + J_Z S_i^z S_j^z$$
$$+ J_A \left[(S_i^x S_j^x - S_i^y S_j^y) \cos \phi_{ij} - (S_i^x S_j^y + S_i^y S_j^x) \sin \phi_{ij} \right],$$
(4.29)

in which $\alpha \in \{x, y, z\}$ denote spin components with respect to Cartesian axes $\mathbf{x}, \mathbf{y}, \mathbf{z}$, and $\phi_{ij} \in \{\frac{2\pi}{3}, -\frac{2\pi}{3}, 0\}$ as specified in Ref. [263]. We use the Onsager reaction-field (ORF) approach [40, 156, 392] to calculate magnetic diffuse scattering patterns. The Fourier transform of the interactions is given by

$$J_{\alpha\beta}(\mathbf{Q}) \equiv - \sum_{\mathbf{R}} J_{\alpha\beta}(\mathbf{R}) e^{-i\mathbf{Q} \cdot \mathbf{R}},$$
(4.30)

where $J_{\alpha\beta}(\mathbf{R})$ is the coefficient of $S_i^\alpha S_j^\beta$ in Eq. (4.29) for sites i and j separated by a lattice vector $\mathbf{R}$.

The magnetic diffuse scattering intensity is given, in the reaction-field approximation, by

$$I_{\mathrm{ORF}}(\mathbf{Q}) \propto [f(Q)]^2 \sum_{\mu=1}^{3} \frac{|\mathbf{s}_\mu(\mathbf{Q})|^2}{1 - \chi_0(\lambda_\mu(\mathbf{Q}) - \lambda)},$$
(4.31)

where $\chi_0 = 1/3T$ is the Curie susceptibility and λ_μ denotes the eigenvalues of the interaction matrix, where μ labels its 3 eigenmodes. The structure factor

$$\mathbf{s}_\mu(\mathbf{Q}) = \sum_\alpha (\hat{\mathbf{n}}_\alpha - \mathbf{Q}\,\hat{\mathbf{n}}_\alpha \cdot \mathbf{Q}/Q^2) g_\alpha U_\mu^\alpha,$$
(4.32)

where $\hat{\mathbf{n}}_\alpha \in \{\mathbf{x}, \mathbf{y}, \mathbf{z}\}$, g_α denotes components of the diagonal g-tensor, and U_μ^α denotes the eigenvector components of the interaction matrix. At each temperature, we obtain the reaction field λ self-consistently by enforcing that $\sum_{\mu,\mathbf{q}}[1 - \chi_0(\lambda_\mu(\mathbf{q}) - \lambda)]^{-1} = 3N_{\mathbf{q}}$ for a grid of $N_{\mathbf{q}} = 40^3$ wavevectors in the Brillouin zone. The best fit values are given in the methods section of the main text.

We also performed the fit including the off-diagonal J_B component. [263]. This quantity is difficult to determine because it depends upon distinguishing K from K', and there is some degree of twinning in KYbSe$_2$ which means we can only fit the magnitude of J_B. Nevertheless, for completeness we performed the ORF fit assuming a twinning model and found

$$J_X = 2.33(10) \text{ K} \qquad J_Z = 2.28(10) \text{ K}$$
$$J_A = -0.018(8) \text{ K} \qquad J_2 = 0.11(2) \text{ K} \tag{4.33}$$
$$|J_B| = 0.00(5) \text{ K}. \tag{4.34}$$

The error bar indicates $|J_B|$ could be larger than $|J_A|$, but this is still much smaller than J_X and J_Y, indicating that the Heisenberg model is still appropriate for KYbSe$_2$.

4.4.2 Experimental details for $YbZn_2GaO_5$

In this section of the appendix, I discuss additional information regarding the experiment conducted in $YbZn_2GaO_5$ by my collaborators at Duke University. I was not involved directly with conducting the experiments, but this is an important part of my thesis, and so I include details about the setup here.

Sample preparation and single crystal growth

The poly-crystalline sample of $YbZn_2GaO_5$ was synthesized using a solid-state reaction route. The high-purity precursors of Yb_2O_3 (99.9%), Ga_2O_3 (99.9%), and ZnO (99.9%) with 5% excess ZnO were used and mixed thoroughly and then pressed into a pellet. The pellets were sintered at $1275°C$ for 36 hours with intermediate grinding to obtain a pure phase of $YbZn_2GaO_5$. The phase purity is confirmed using Powder X-ray diffraction (PXRD) (see Fig. S1). The pure powder sample and around 10% excess of ZnO were mixed and pressed into a cylindrical rod using a hydrostatic pressure of 700 bar. Single crystals of $YbZn_2GaO_5$ were grown using the optical floating-zone technique in the presence of a 10-bar oxygen atmosphere. A transparent single-grain crystal was successfully obtained, with a cleaved facet plane along [001] which was confirmed from Laue X-ray diffraction (see Fig. 4.26).

Single crystal X-ray diffraction

The single crystal X-ray diffraction (SCXRD) is performed on $YbZn_2GaO_5$ single crystal sample at the Department of Chemistry, University of North Carolina. A colorless transparent crystal piece (approximate dimensions $0.020 \times 0.010 \times 0.010 \ mm^3$) was harvested by an X-ray transparent loop made by MiTeGen and mounted on a Bruker D8 VENTURE diffractometer and measured at 150 K. The data collection was carried out using Mo-Kα radiation (graphite monochromator) with a frame time of 0.4 seconds and a detector distance of 4 cm. Data is displayed in Table 4.4

Heat capacity measurements

Zero field heat capacity measurements were carried out on a single crystal of $YbZn_2GaO_5$ and a powder sample of $LuZn_2GaO_5$ using Helium-4 (1.8 K $\leq$ T $\leq$ 300 K) and dilution refrigeration (0.06 K $\leq$ T $\leq$ 2 K) set up attached to Quantum Design (QD) Physical Property Measurement System (PPMS). A representative single-crystal sample of $YbZn_2GaO_5$ mounted on a heat capacity measurement platform is shown in Fig. 4.27.

Magnetic measurements

Temperature-dependent magnetic susceptibility was measured using a 7 Tesla Cryogenic Ltd SQUID (superconducting quantum interference device) magnetometer with a Helium-3 probe from 0.3 K to 2 K and with a Helium-4 probe from 2 K to 300 K. For the Helium-3 measurements, a small crystalline $YbZn_2GaO_5$ sample of 1.04 mg was mounted on a silver sample holder and
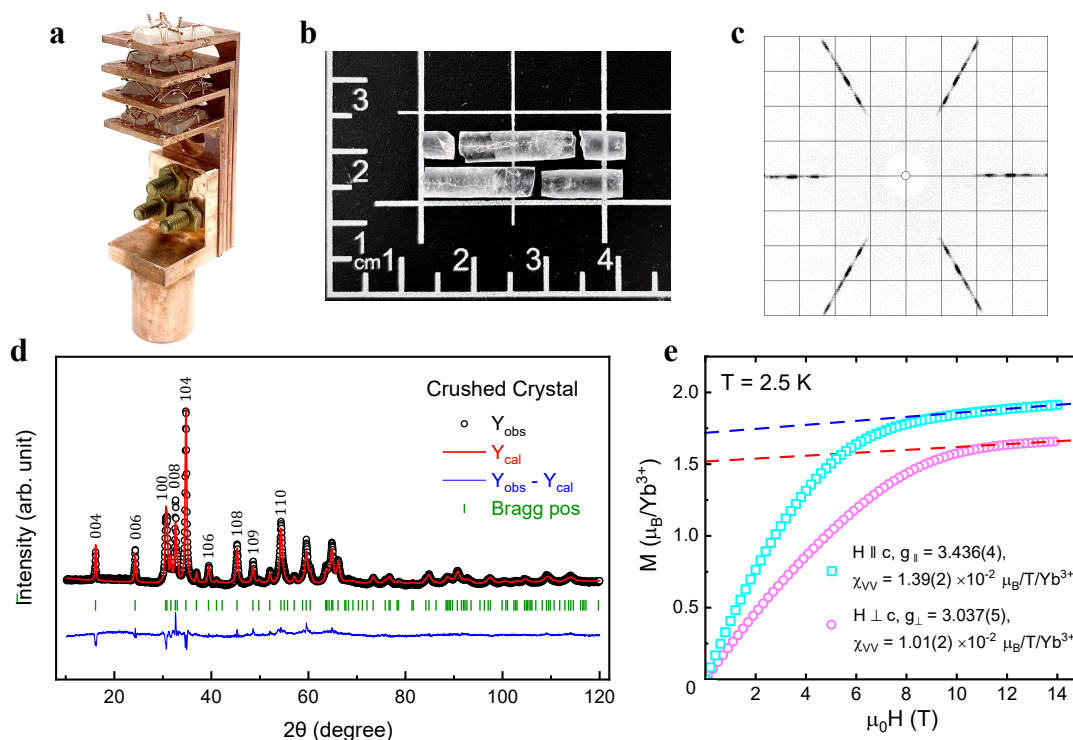
Figure 4.26: **Pictures, Laue pattern, powder X-ray diffraction pattern, and isothermal magnetization**. **a**. A picture of co-aligned single crystals of $YbZn_2GaO_5$ on a neutron sample mount. 10 selected high-quality single crystals with a total mass of ~ 1.8 grams were aligned and bound on an oxygen-free Cu sample mount with Cu wire. **b**. A representative image of the grown single crystals sample of $YbZn_2GaO_5$, the transparency of the crystal indicates its high quality. **c**. Sharp Laue Back-scattered X-ray pattern with an incident beam along the c-axis. **d**. Rietveld refinement performed on powder X-ray diffraction (PXRD) pattern of the ground single crystal of $YbZn_2GaO_5$. **e**. Field-dependent isothermal magnetization of $YbZn_2GaO_5$ single crystal collected at 2.5 K. The magnetic field was applied parallel and perpendicular to the crystallographic c-axis. The obtained gyromagnetic ratios g and Van-Vleck contribution χ_{VV} from the fit (red and blue dashed lines) are shown.

the Helium-4 measurement, 11.90 mg of $YbZn_2GaO_5$ single crystal was used. The crystals were oriented using the Laue diffraction method and the regular shape of the single crystals was obtained using a wire saw. The magnetic measurements were performed under an applied magnetic field parallel ($H\|c$) and perpendicular ($H\perp c$) to the crystallographic c-directions of $YbZn_2GaO_5$. The isothermal magnetization measurements along both directions of $YbZn_2GaO_5$ single crystal sample were performed using a VSM (vibration sample magnetometer) in PPMS up to 14 Tesla of the applied magnetic field (see Fig. 4.26).

Table 4.4: The refinement parameters of the single crystal X-ray diffraction (SCXRD) data collected at 150 K. The atomic coordinates and equivalent isotropic displacement parameters suggest no chemical site mixing in $YbZn_2GaO_5$. U(eq) is defined as one-third of the trace of the orthogonalized U^{ij} tensor.

$YbZn_2GaO_5$ SCXRD ($T = 150$ K, MoK_α, $\lambda = 0.71073$ Å)						
Space group	$P6_3mmc$ (No.194)					
Cell parameters	$a = b = 3.3678(2)$ Å, $c = 21.951(2)$ Å					
	$\alpha = \beta = 90°$, $\gamma = 120°$					
Fit quality	$R1 = 0.0779$, $wR2 = 0.1895$, $GooF = 1.0612$					
Atom	**Site**	**x(Å)**	**y(Å)**	**z(Å)**	**U(eq)(Å^2)**	**Occ**
Yb1	$2a$	0.0000	0.0000	0.5000	0.0024	1.000
Ga1	$2b$	0.0000	0.0000	0.7500	0.0018	1.000
Zn1	$4f$	0.6667	0.3333	0.6372(1)	0.0018	1.000
O1	$4f$	0.6667	0.3333	0.5494(10)	0.00018	1.000
O2	$2c$	-	-	0.7500	0.0032	1.000
		0.3333	0.6667			
O3	$4e$	0.0000	0.0000	0.6546(11)	0.0020	1.000

Inelastic neutron scattering

The inelastic neutron scattering (INS) experiments were performed on the Fine-Resolution Fermi Chopper Spectrometer (SEQUOIA) [131] and the Cold Neutron Chopper Spectrometer (CNCS) [101] at the Spallation Neutron Source (SNS), Oak Ridge National Laboratory. For the SEQUOIA experiment, 6.5 g of pure powder samples of $YbZn_2GaO_5$ and $LuZn_2GaO_5$ were used with incident neutron energies of $E_i = 80$ and 120 meV at temperatures of $T = 5$ and 100 K. The phonon contributions in the $YbZn_2GaO_5$ spectrum were subtracted using isostructural non-magnetic $LuZn_2GaO_5$. For the CNCS experiment, 10 pieces of high-quality single crystal samples of $YbZn_2GaO_5$ with a total mass of ~ 1.8 g were co-aligned within 1.5° using a Laue X-ray back-scattering diffractometer and mounted along ($hk0$) scattering plane on an oxygen-free copper sample holder (see Fig. 4.26). The measurements were carried out in a dilution refrigerator with a base temperature of 0.1 K. A neutron-absorbing Cd foil was placed at the bottom of the holder to reduce the background from the sample holder. The measurements were conducted at the base temperature and 45 K under zero-field with an incident neutron energy of E_i =3.32 meV. The sample was rotated with an increment of 1°, with a range of -180° to 180°. The data were analyzed using the HORACE software and were folded 3 times along the high symmetry axis [0H0], [$\bar{H}H$0], and [H00] into a 60° sector in the reciprocal space to improve statistics. For the constant energy slice, the folded data were cut, duplicated, and recombined to restore 360° coverage for the purpose of presentation. To better extract the magnetic signal of interest, a comparative analysis was conducted between the 0.1 K and 45 K spectra. The 45 K spectrum was normalized to 0.1 K data and used as background which then was subtracted from the 0.1 K spectrum.
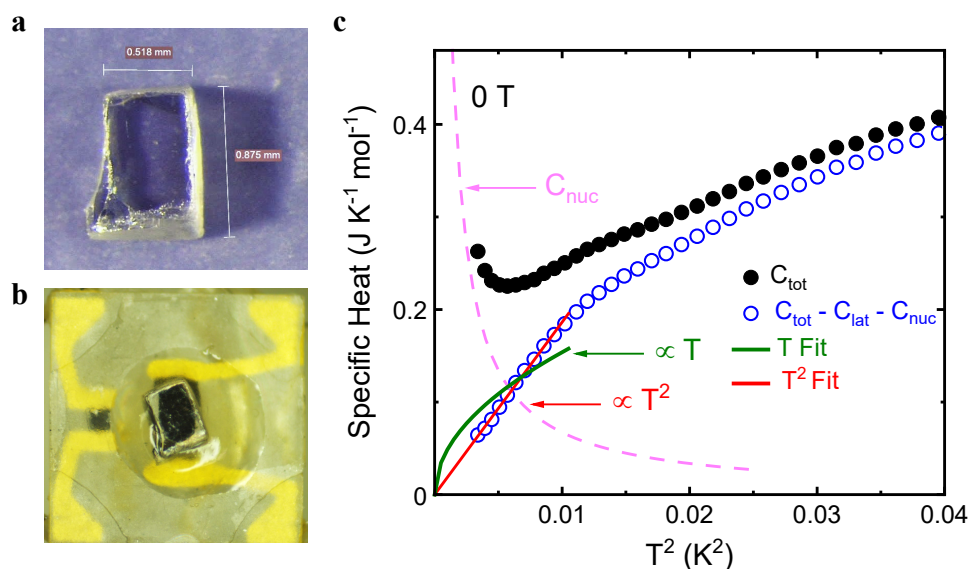
Figure 4.27: **Heat capacity data fitted with linear and quadratic T models**. **a**. Microscopic image of $YbZn_2GaO_5$ single crystal sample used for heat capacity measurement. **b**. The mounted single crystal sample on a heat capacity platform of the Dilution Refrigerator set up of PPMS. The transparency of the single crystal sample of $YbZn_2GaO_5$ indicates the crystal quality. **c**. The filled black circles display the total heat capacity which can be written as $C_{tot} = C_{nuc} + C_{lat} + C_{mag}$. C_{nuc} is expressed as AT^{-2}; and C_{lat} is subtracted using the heat capacity of the non-magnetic $LuZn_2GaO_5$ sample. The light-magenta dash line indicates the nuclear contribution obtained from the fit. The blue circles show the data after subtracting the nuclear and lattice contribution. The green and red solid lines show the results of subtracted magnetic heat capacity data fitted using a linear ($C_{mag} \sim T$) and a quadratic ($C_{mag} \sim T^2$) models. The linear T dependence is expected for the spinon Fermi surface quantum spin liquid, while the quadratic behavior for $T \rightarrow 0$ corresponds to U(1) Dirac quantum spin liquid model.

Crystal electric field fits
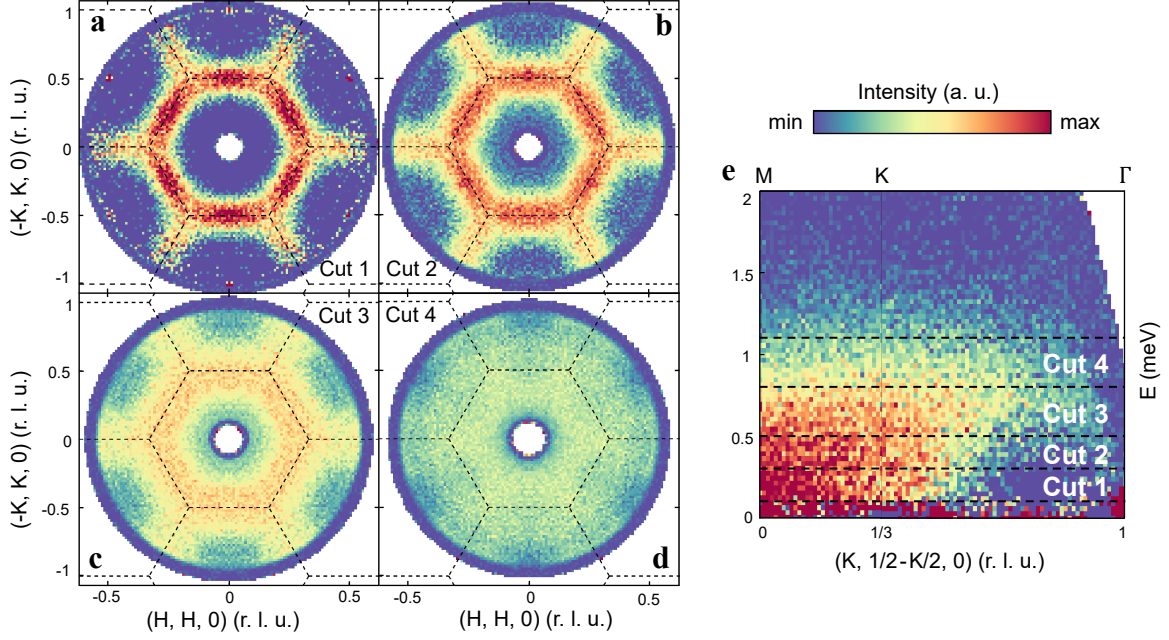
Figure 4.28: **Momentum dependence of the magnetic excitation**. **a-d**. Background-subtracted constant energy slices of the magnetic excitation spectra collected at 0.1 K. The energy integration ranges are [0.1, 0.3], [0.3, 0.5], [0.5, 0.8], and [0.8, 1.1] meV. The spectra were folded along high symmetry directions to increase statistics and the folded data was duplicated and recombined to restore full coverage for presentation, as explained in the Methods section. The spectral weights are expressed by the same color map scale for better comparison. **e**. $S(q,\omega)$ plot along high symmetry path M-K-Γ. The dash lines indicate the energy integration intervals of cuts 1-4 for direct visualization.

Table 4.5: Fitted CEF parameters for $YbZn_2GaO_5$.

B_n^m	Fit values (meV)
B_0^2	-1.008×10^0
B_0^4	1.459×10^{-2}
B_3^4	-6.427×10^{-1}
B_0^6	5.446×10^{-4}
B_3^6	-3.284×10^{-2}
B_6^6	2.232×10^{-2}

Table 4.6: Eigenvalues and eigenvectors of the CEF Hamiltonian for $YbZn_2GaO_5$.

Eigenvalues (meV)	Eigenvectors
0.00	$-0.758\left|-\frac{7}{2}\right\rangle + 0.402\left|-\frac{1}{2}\right\rangle + 0.512\left|\frac{5}{2}\right\rangle$
0.00	$-0.513\left|-\frac{5}{2}\right\rangle + 0.402\left|\frac{1}{2}\right\rangle + 0.758\left|\frac{7}{2}\right\rangle$
38.14	$-0.834\left|-\frac{5}{2}\right\rangle - 0.444\left|\frac{1}{2}\right\rangle - 0.329\left|\frac{7}{2}\right\rangle$
38.14	$-0.329\left|-\frac{7}{2}\right\rangle + 0.444\left|-\frac{1}{2}\right\rangle - 0.834\left|\frac{5}{2}\right\rangle$
60.88	$\left|-\frac{3}{2}\right\rangle$
60.88	$\left|\frac{3}{2}\right\rangle$
94.00	$0.204\left|-\frac{5}{2}\right\rangle - 0.801\left|\frac{1}{2}\right\rangle + 0.563\left|\frac{7}{2}\right\rangle$
94.00	$-0.563\left|-\frac{7}{2}\right\rangle - 0.801\left|-\frac{1}{2}\right\rangle - 0.204\left|\frac{5}{2}\right\rangle$

Chapter 5

Critical Dynamics with Matrix Product States

In this chapter I discuss the effect that representing a state with a matrix product state (MPS) has on quantum dynamics near criticality, by looking at a Kibble-Zurek process [194, 195, 439, 49]. In this process, a ground state is slowly time-evolved under a time dependent Hamiltonian to a quantum critical point. At the critical point, the gap closes, and so adiabaticity is lost for any finite rate of the changing Hamiltonian. This causes excitations in the system, which have a simple description in terms of properties of the underlying conformal field theory describing the quantum critical point. The density λ of these excitations gives rise to a length scale in the problem $\xi_{KZ} \sim \rho^{-1}$.

A dominant technique in modern condensed matter physics, as well as in this thesis, relies on simulating many-body systems using a matrix product state (MPS) (see Chapter 2). The MPS ansatz places a restriction on the entanglement of the state it is representing, leading to an approximation for critical systems with diverging entanglement. The result is that the use of an MPS introduces a length into the problem ξ_χ (see Sec. 2.4.2 for more details). This provides a useful testing ground for exploring how representing a state by an MPS modifies the results of a dynamical process. If $\xi_\chi \gg \xi_{KZ}$, then the expectation is that representing the state as an MPS through the entire process will have a negligible effect, where when $\xi_\chi \ll \xi_{KZ}$, the entanglement restriction will be noticeable.

In Sec. 5.1, I look at a Kibble-Zurek process for the transverse field Ising model, and the 3-state Potts model, using an MPS to represent the state for all times. I show that the deviations from the exact evolution is fully specified by a dimensionless scaling function of the ratio ξ_χ/ξ_{KZ}. I then demonstrate this result numerically, by looking at the excitation energy density, and the fidelity density.

5.1 Universality of Critical Dynamics With Finite Entanglement

5.1.1 Introduction

The long-time dynamics of a many-body quantum system is challenging to study on classical computers even if the system is initialized in a weakly entangled state, as the entanglement entropy will generically grow linearly in time [48, 65, 196, 153]. At the same time, this regime of dynamically produced entanglement is of great interest in modern research, as it contains insights into such fundamental questions as how apparently non-reversible thermalization emerges from unitary dynamics in isolated quantum systems [293, 73]. The dynamical aspect is particularly important in quantum simulation on current quantum computers, on which preparing a nontrivial ground state is often harder than performing coherent evolution. Yet, compared to static properties, non-equilibrium time evolution is less understood in terms of either conceptual guiding principles or effective methods of calculation.

An exception is the dynamics of a system swept slowly through a quantum critical point, when universal properties are known to emerge in the limit of long times and distances via the quantum Kibble-Zurek (KZ) mechanism. We focus on this mechanism as an example of universal out-of-equilibrium dynamics that is theoretically fundamental and also used in experiments to probe quantum criticality in emerging platforms that maintain quantum coherence well but have difficulty in reaching thermal equilibrium [97]. The modification of quantum criticality by limits on observation time or system size is of renewed interest in light of these new efforts to study such criticality on quantum computers and emulators. Another, more challenging, kind of modification arises from noise or other effects in the system that act to limit quantum entanglement. The goal of the present work is to capture how the quantum Kibble-Zurek mechanism is universally modified in systems with finite entanglement.

Quantum critical points are of particular interest because of their emergent universal properties: their large-scale behavior is insensitive to some "irrelevant" microscopic details and is the same across vast groups of models known as universality classes. However, certain other microscopic perturbations are "relevant" and change the universality class, and indeed finite entanglement will turn out to be such a perturbation. Despite having a degree of robustness to irrelevant perturbations, quantum critical points are also well known to be challenging for computational methods on classical computers, for reasons such as requiring large system sizes that also apply to new efforts on quantum computers. Indeed, finite size can be viewed as a relevant perturbation to criticality, and this insight underlies the successful theory of finite-size scaling [53].

Dynamically, the most straightforward manifestation of universality is the (classical or quantum) Kibble-Zurek scaling. It describes the number and energy of excitations produced in a system that is driven through a second-order phase transition. The scaling of the corresponding density with the drive rate is determined by combinations of standard critical exponents. This behavior is often one of the first phenomena probed on new quantum simulation platforms [26, 420, 91], which has also motivated numerical studies of this process [285, 154]. We derive forms for the fidelity and

excitation energy produced by the sweep based on the existence of two relevant scales: the KZ length ξ_{KZ} arising from falling out of adiabaticity with a nonzero sweep rate, and one ξ_χ arising from the restricted entanglement.

We test the resulting theory using an example of entanglement restriction that is familiar on classical computers: restriction of the bond dimension of a tensor network. The emergence of this length scale ξ_χ is a widely used tool in understanding calculations based on Matrix Product States (MPS), and as these calculations are among the most used to model the experimental platforms above, we review their use briefly.

MPSs originally emerged as the output of the density matrix renormalization group (DMRG) algorithm [386, 315], which provides an approximation to the ground states of 1D local Hamiltonians. The efficiency of this algorithm in many cases is underpinned by the area law of entanglement entropy in gapped one-dimensional systems [147] which implies that the exact ground state can be represented efficiently by an MPS [369, 260]. Later, MPSs inspired the development of other tensor networks, including the multiscale entanglement renormalization ansatz (MERA) for critical states [373, 372] and projected entanglement pair states (PEPS) [370, 259, 68, 67]. MPS applications extend beyond ground state properties to include excited states [261, 294, 139, 136, 417, 135] and quantum dynamics [137, 135, 138, 367, 267, 414, 76].

MPSs have also found applications beyond classical simulations of quantum systems. There is a direct mapping between an MPS and certain quantum circuits [317, 109, 140]. In such mappings the physical qubits are coupled to some χ-dimensional ancillary system, such as an optical cavity [317], or other qubits [109, 140].Recent work has also demonstrated a mapping between tensor networks and neural networks, the main architecture for machine learning (ML) and artificial intelligence [58, 210], allowing for deep learning architectures to be understood from an entanglement perspective [209]. Tensor networks have been successfully used for ML applications, such as image classification [60, 228, 99, 379, 145, 59, 95].

For a periodic (or infinite) MPS (iMPS), the expressive power of the ansatz is fully specified by the dimension of the matrices χ, called the bond dimension, which is related to the entanglement entropy of the state [315]. However, if the entanglement is unbounded, the existence of an efficient representation of the state with finite χ is no longer guaranteed. This applies whether the MPS is approximating a critical ground state or the entanglement was dynamically generated. Here we consider dynamics where, as in many practical computations, the state is represented by an MPS at finite χ during the full time evolution. We focus on dynamics near a quantum critical point and the goal is to gain insight about properties of the time-evolved state; using the universality of critical behavior, we are able to predict how observables scale with χ and controllably approach the $\chi = \infty$ state from finite-χ data.

We begin with a time evolution protocol known as a Kibble-Zurek sweep [194, 195, 439, 49]. We then show that finite χ dynamics is well-defined, in that different procedures for time evolution produce the same result in the appropriate limits. A subtlety is that different definitions that all give the exact ground state are no longer equivalent at finite χ, and how algorithms resolve this ambiguity. We then demonstrate our results by examining the transverse-field Ising model (TFIM) and the 3-state Potts model, verifying our finite χ scaling hypothesis in detail.

5.1.2   Kibble-Zurek Scaling

We consider an extended quantum system described by a Hamiltonian $H(\lambda)$ with some parameter λ. We further assume that $\lambda = \lambda_0$ corresponds to an isolated quantum critical point. For the correlation length ξ and time τ in the vicinity of the critical point we expect [301]

$$\xi \sim |\lambda - \lambda_0|^{-\nu}, \tau \sim |\lambda - \lambda_0|^{-z\nu}, \tag{5.1}$$

where ν and z are the corresponding critical exponents.

Let us now consider the evolution of the system initiated in the ground state (that we assume to be non-degenerate) far away from the critical point with the parameter changing in time as $\lambda(t) = \lambda_0 + vt$. We assume that v is slow compared to the bandwidth and t runs from $-\infty$ to 0. Far from the critical point the gap is large compared to v and the adiabatic theorem applies. Because the breakdown of adiabaticity only occurs close to the critical point, properties of the resulting state will obey universal scaling laws, the KZ scaling [194, 195, 439, 49].

The scaling exponents can be deduced from a simple reasoning. The adiabaticity is lost when $t \approx -\tau$, where τ is determined by Eq. (5.1); this corresponds to

$$\tau_{KZ} \sim v^{-\frac{\nu z}{1+\nu z}}, \ \xi_{KZ} \sim v^{-\frac{\nu}{1+\nu z}}, \tag{5.2}$$

thus defining the Kibble-Zurek time and length, correspondingly. Since the adiabaticity is restored after $t = \tau$ and we expect the generated exitations to freeze out and the average density of excitations and energy will be (in one spatial dimension)

$$n_{ex} \sim 1/\xi_{KZ} \sim v^{\frac{\nu}{1+z\nu}}, \tag{5.3}$$

$$\epsilon_{ex} \sim 1/\xi_{KZ}^2 \sim v^{\frac{2\nu}{1+z\nu}}. \tag{5.4}$$

This scaling has been verified by extensive numerics [77, 296] as well as experiments [69, 26, 420]. There exists also an exact solution for the transverse-field Ising model [96, 61].

In Eq. (5.3), ϵ_{ex} is the energy above the ground state divided by the volume and n_{ex} needs to be defined with care when particle number is not well-defined. We propose to use fidelity density, which is given by

$$f(t) = -\frac{1}{N} \log \left(|\langle \psi(t) | \psi_0 \rangle|^2 \right), \tag{5.5}$$

where $|\psi_0\rangle$ is the ground state, $|\psi(t)\rangle$ the time evolved state, and N is the total number of sites in the system. $f(t)$ has the same scaling as we expect for n_{ex} [78, 77], and is proportional to it at low densities when the system has a free fermion description, as we explain in Sec. 5.2.2.

5.1.3   MPS Dynamics and Finite Bond Dimension

The time evolution of a state under a Hamiltonian $H(t)$ is given by

$$|\psi(t)\rangle = U(t) |\psi(0)\rangle \tag{5.6}$$

$$U(T) = \mathcal{T} \exp \left(-i \int_0^T dt \, H(t) \right) \tag{5.7}$$

where $\mathcal{T}(\cdot)$ is the time ordering operator. If we write $t_n = n\Delta t$, and $T = t_N$, then this is equivalent to writing

$$U(t) = \lim_{N \to \infty} \left[e^{-iH(t_N)\Delta t} \cdots e^{-iH(t_0)\Delta t} \right]. \tag{5.8}$$

Conceptually, this amounts to treating the Hamiltonian as piecewise constant over an interval of size Δt, and the exact time evolution is found in the limit that $\Delta t \to 0$. For finite Δt, treating the Hamiltonian as piecewise constant produces an error of order $O(\Delta t)$. To implement time evolution using an MPS, if Δt is sufficiently small, it is sufficient to define time evolution for a constant Hamiltonian over a time Δt. We demonstrate in Sec. 5.2.1 that finite χ dynamics is independent of the algorithm used as $\Delta t \to 0$.

Now we turn to how KZ scaling is modified when the state is represented at all times by an MPS with a fixed finite bond dimension χ. The effect of finite bond dimension is to limit the amount of entanglement in the system. And since close to conformal critical points entanglement is related to the correlation length by the celebrated expression [46]

$$S = \frac{c}{6} \log \xi, \tag{5.9}$$

for fast sweeps, when ξ_{KZ} is small, the effect of χ will be small, whereas for slower sweeps, when ξ_{KZ} is large, the number of excitations will be suppressed compared to Eq. (5.3).

This situation is similar to the one studied in [285], where the KZ scaling in the TFIM was studied in the presence of a symmetry breaking bias $g_{||}$ that kept the gap finite at all times during the sweep. It was numerically verified that the effect of $g_{||}$ could be described by a single length scale $\xi_{||} = g_{||}^{-\nu_{||}}$ where $\nu_{||}$ is the corresponding critical exponent, and all KZ scaling laws were modified by scaling function that depended on the ratio $\xi_{||}/\xi_{KZ}$. We also expect the scaling behavior to occur for finite system size, in which case the argument of the scaling function would be L/ξ_{KZ} with L, the system size.

Returning to the case of finite bond dimension, we conjecture its effect to be describable by a single length scale ξ_χ. Thus, we expect that the $\chi = \infty$ result is modulated by a dimensionless scaling function, similar to the scaling theory of entanglement entropy [50]. In particular, we expect

$$O(v, \chi) = O(v, \chi = \infty) f_O(\xi_{KZ}/\xi_\chi) \tag{5.10}$$

where f_O is some scaling function for the observable O. Here, we look at the fidelity density f from Eq. (5.5) and the excitation energy ϵ_{ex}. the fidelity density f is computed via the largest eigenvalue of the transfer matrix formed by the full contraction of both states (see Sec. 5.2.2). Both of these quantities require the ground state at finite χ, where equivalent definitions of the $\chi = \infty$ ground state are no longer equivalent. See Sec. 5.2.3 for more details on choosing the relevant finite χ ground state.

The length scale ξ_χ has been previously studied for ground state properties and the scaling given by $\xi_\chi \sim \chi^\kappa$ was observed in [357]. The conformal field theory (CFT) entanglement spectrum was used to obtain a form for the exponent [277]

$$\kappa = \frac{6}{c \left(\sqrt{\frac{12}{c}} + 1 \right)} \tag{5.11}$$

in surprisingly good agreement with numerical data [357, 277, 274]. Looking ahead, we will find that the same critical exponent governs the dynamical problem of Kibble-Zurek scaling.

5.1.4 Numerical Verification

We look at two models in this study. First, the transverse-field Ising model (TFIM), defined by the Hamiltonian

$$H = -J \sum_n \sigma_n^z \sigma_{n+1}^z - g \sum_n \sigma_n^x, \tag{5.12}$$

where σ_n^i is the i-th Pauli matrix at site n. Eq. (5.12) has a Z_2 symmetry $\bigotimes_i \sigma_i^x$. This system has a quantum phase transition at $g = J$ that separates a disordered phase with a unique GS for $g > J$ and an ordered phase with a two-fold degenerate GS for $0 < g < J$. The CFT describing the critical point is the minimal model with $c = 1/2$ and the critical correlation length critical exponent is given by $\nu = 1$ [110]. Thus, for the KZ scaling we expect

$$n_{ex} \sim v^{1/2}, \; \epsilon_{ex} \sim v. \tag{5.13}$$

The coupling constants have a v dependence given by

$$\begin{aligned} J(t) &= 1 + vt \\ g(t) &= 1 - vt \end{aligned} \quad t : -\frac{1}{v} \to 0 \tag{5.14}$$

The initial coupling is given by $J = 0$, and $g = 2$. The ground state at this point is a simple product state given by $|\psi_0\rangle = |\rightarrow\rangle^{\otimes N}$. We then time evolve this state with the time dependent Hamiltonian using the time-evolution block-decimation (TEBD) algorithm [76, 315]. We use a fourth order Trotter decomposition [22], with a timestep of $dt = 0.005$.

We enforce the $\mathbb{Z}_2$ symmetry during the ground state search, and time evolution, producing a $\mathbb{Z}_2$ symmetric state in both cases. For different values of the bond dimension χ, we calculate f and ϵ_{ex}, and show the results in Fig. 5.1. The black line illustrates the $\chi = \infty$ result. We see that for large v, the effect of finite bond dimension is minimal, but as we decrease the speed, the deviations become dramatic. The systematic nature of the deviations is a focus of the present work.

In Fig. 5.2, we show the scaling function collapse assuming the scaling hypothesis in Eq. (5.10). We expect the scaling hypothesis to be valid for large χ but it already begins to work for $\chi \geq 4$, with the exponent κ specified by Eq. 5.11.

The second model we explore is the 3-state Potts model defined by the Hamiltonian [342]

$$H = -J \sum_n \left(\eta_n^\dagger \eta_{n+1} + \eta_n \eta_{n+1}^\dagger \right) - g \sum_n \left(\tau_n + \tau_n^\dagger \right) \tag{5.15}$$

$$\eta = \begin{bmatrix} 1 & & \\ & e^{i\frac{2\pi}{3}} & \\ & & e^{-i\frac{2\pi}{3}} \end{bmatrix}, \; \tau = \begin{bmatrix} 0 & 1 & 0 \\ 0 & 0 & 1 \\ 1 & 0 & 0 \end{bmatrix} \tag{5.16}$$
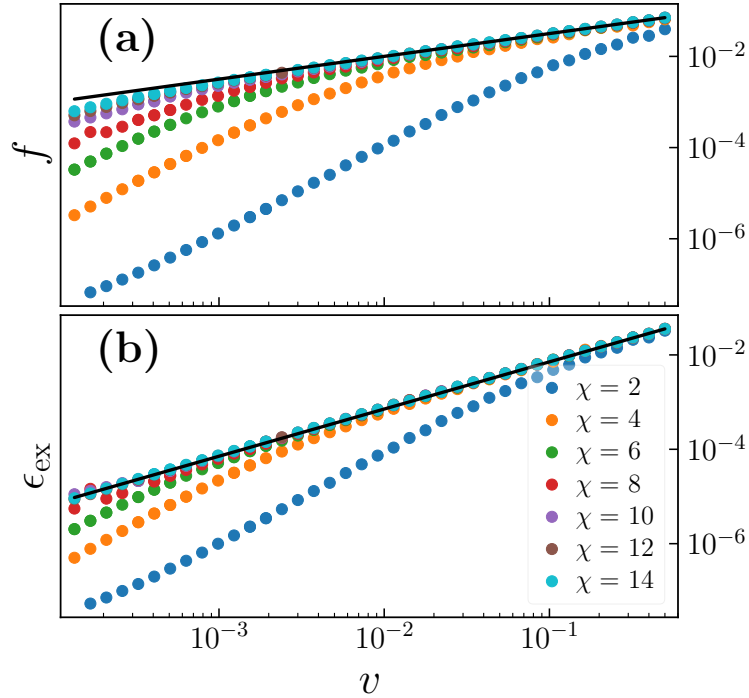
Figure 5.1: The fidelity and excitation energy densities after a Kibble Zurek sweep performed at speed v for the TFIM. We show the results for different maximum bond dimensions χ. We show a black line illustrating the scaling prediction for $\chi = \infty$.

Eq. (5.15) enjoys S_3 symmetry comprised of all permutation of the basis states on all sites. However, we explicitly enforce the only $\mathbb{Z}_3 \subset S_3$ symmetry containing cyclic permutations.

Analogously to the TFIM, at $g = J$ there is a critical point that separates a Z_3 symmetric phase for $g > J$ and a Z_3 ordered phase for $0 < g < J$. The CFT is similarly a minimal model (Z_3 parafermion) with $c = 4/5$ and $\nu = 5/6$ [110]. Accordingly, the KZ scaling is

$$n_{ex} \sim v^{5/11}, \quad \epsilon_{ex} \sim v^{10/11}. \tag{5.17}$$

For the dynamics, we use the same time dependent coupling used for the TFIM, given in Eq. (5.14). We again use TEBD with a fourth order Trotter decomposition, except with a timestep of $dt = 0.01$. The excitation energy, and fidelity density, are qualitatively identical to the TFIM, except with different scaling exponents with v (see Sec. 5.2.4). We do show the scaling function collapse in Fig. 5.3. Again we see a clear collapse of the data, further confirming the scaling hypothesis of Eq. (5.10).

Figure 5.2: The scaling function collapse for the fidelity density and excitation energy in the TFIM. The length scale introduced by the bond dimension, ξ_χ, follows a power law with exponent given by Eq. (5.11), with a central charge of $c = 1/2$.

5.1.5 Conclusions

We found that a Kibble-Zurek sweep through a one-dimensional quantum critical point is modified by finite entanglement, i.e., fixed finite bond dimension χ for an iMPS, in a way similar to relevant perturbations of the Hamiltonian, even though finite χ is not equivalent to any local Hamiltonian perturbation. Properly defined, the sweep-induced differences from an adiabatically defined ground state are captured by a universal scaling function that unusually involves both scaling dimensions and central charge. The scaling function involves the ratio of two length scales ξ_{KZ} and ξ_χ and the essential features are independent of the specific implementation of the dynamics, suggesting that the finite-entanglement scaling form for dynamics will have similar utility in practice as the form for ground states, by enabling systematic extrapolation from finite-χ results (see Sec. 5.2.5 for further details).

Whether bond dimension can be treated as a relevant perturbation in an even more general setting, and whether other non-Hamiltonian perturbations to quantum dynamics can similarly be captured by scaling functions, remains an open question. The way matrix product states implement finite entanglement is via the restriction on bond dimension and therefore Schmidt rank: the relevant ground state here was the lowest-energy state within a specified symmetry sector and Schmidt rank.
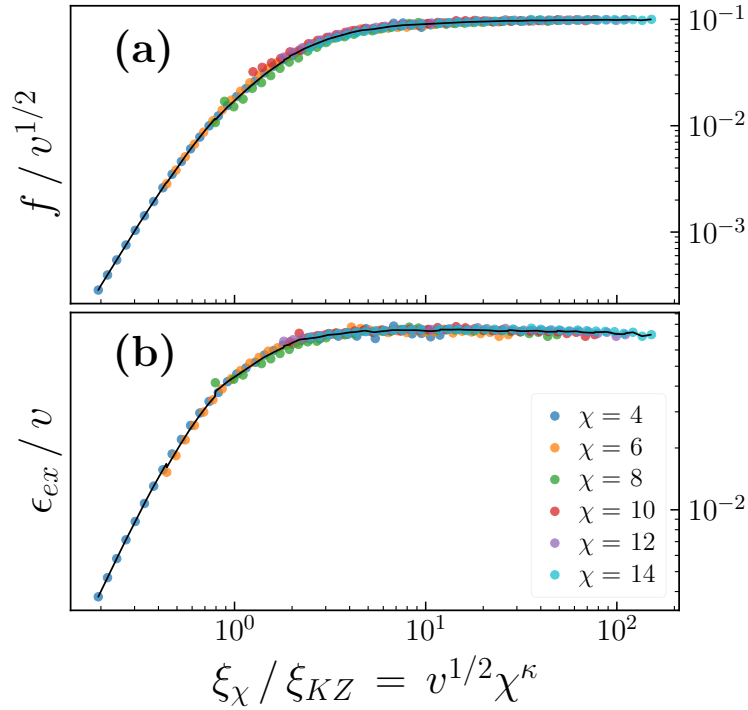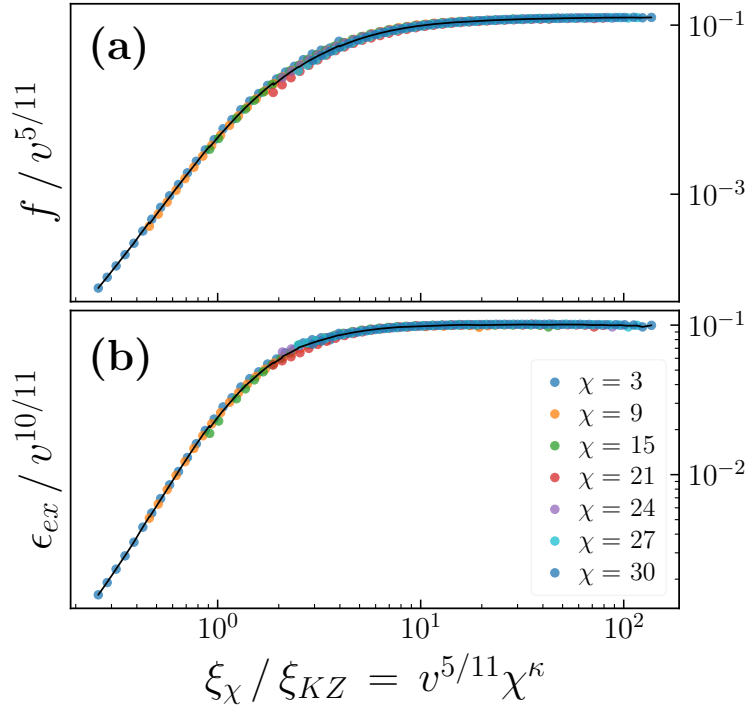
Figure 5.3: The scaling function collapse for the fidelity density and excitation energy in the 3-state Potts model. The length scale introduced by the bond dimension, ξ_χ is a power law with exponent given by Eq. (5.11), with a central charge of $c = 4/5$.

It would be worthwhile to generalize the scaling theory to (pure or mixed) states approximating criticality that arise via other mechanisms that also put a limit on entanglement, such as some non-unitary processes arising from environmental interactions in quantum hardware, and to understand how these approximate states compare to MPS. It would also be interesting to see if our analysis applies beyond Kibble-Zurek scaling to the more general finite-time scaling [125, 165]. Lastly, the finite χ scaling of dynamical observables opens up an interesting application of quantum computers in the NISQ era. Since quantum circuits can represent MPSs with a physically relevant bond dimension [317, 109, 140], running such simulations at different bond dimensions could enable a novel way to extract the central charge of critical theories. This procedure is well suited for quantum computers, on which unitary dynamics are easily programmed.

5.2 Appendix

5.2.1 Equivalence of different time evolution procedures at finite χ.

In practice, the time evolution of a state is implemented in one of three ways. Most commonly used when studying a nearest-neighbor Hamiltonian is the Time Evolution Block Decimation (TEBD) algorithm [76, 315], which is based on a Suzuki-Trotter decomposition of the time evolution operator. One can also calculate a matrix product operator (MPO) representation of the matrix exponential itself [414], known as the WII method. For both of these methods, a time evolution step will generically increase the entanglement of the system, increasing the bond dimension χ. Thus a procedure is required to project the resulting state down to a state with a bond dimension $\chi_{\max}$. The last notable time evolution procedure, the time-dependent variational principle (TDVP) [137, 135, 138, 367], projects the dynamics on the states in the manifold of $\chi \leq \chi_{\max}$. Often we are interested in the limit of both $\chi \to \infty$ and $\Delta t \to 0$, corresponding to the exact solution of the time-dependent Schrodinger equation. In this work, we hold χ finite and discuss just the limit $\Delta t \to 0$. Here, we will show that these three methods of time evolution produce the same state when χ is fixed and $\Delta t \to 0$.

Let us consider the following. Starting with an MPS $|\Psi(A)\rangle$ with bond dimension χ, we perform one step of time evolution, corresponding to a time step dt, that increases the bond dimension to χ'. Finite χ' can be achieved by considering an arbitrary but finite number of Trotter-Suzuki steps. We denote the new MPS as $|\Psi(A + B)\rangle$, where B has bond dimension χ', and we can enlarge A with zeros to make the sum $A + B$ well defined. We wish to understand whether the different ways of compressing this state back to bond dimension χ become equivalent when we take $dt \to 0$. In this limit B can be thought of as a tangent vector [367].

Let us denote the compressed state $|\Psi(A + B')\rangle$ where B' is an MPS of bond dimension χ. The difference between TEBD and WII MPO/TDVP can be thought of as the difference in how truncation is performed. The TEBD projection of $A + B$ to the subspace of bond dimension χ corresponds to the truncation of the SVD spectrum [377, 371]. This would be an optimal compression in terms of vector distance $||\Psi(A + B')\rangle - |\Psi(A + B)\rangle|^2$ if we were only changing the tensor from $A + B$ to $A + B'$ at one site [315], but is not optimal for a global change. Meanwhile for the WII MPO method the globally optimal $||\Psi(A + B')\rangle - |\Psi(A + B)\rangle|^2$ [414] is achieved and the TDVP is the infinitesimal version of that [367].

Let us now show that both compression are equivalent to the linear order in B, B'. We expand the states to the linear order in B, B', obtaining

$$|\Psi(A + B)\rangle \approx |\Psi(A)\rangle + \sum_i \ldots \boxed{A}_{|i-2} \boxed{A}_{|i-1} \boxed{B}_{|i} \boxed{A}_{|i+1} \boxed{A}_{|i+2} \ldots \qquad (5.18)$$

Thus to the first order, the difference of the states to be minimized is

$$|\Psi(A + B)\rangle - |\Psi(A + B')\rangle \approx \sum_i \ldots \boxed{A}_{|i-2} \boxed{A}_{|i-1} \boxed{B-B'}_{|i} \boxed{A}_{|i+1} \boxed{A}_{|i+2} \ldots \qquad (5.19)$$

The last step is to contract it with itself. For definiteness work with the left gauge for the tangent vector B, in which case

$$\text{(5.20)}$$

With that gauge, the contraction of the difference with itself will only have diagonal components, where A's are contracted with A's and $B - B'$ is contracted with itself at site i:

$$||\Psi(A+B)\rangle - |\Psi(A+B')\rangle|^2 \approx \sum_i \ldots \qquad \ldots$$

This is the same as what we would obtain if we just wanted to truncate a nonuniform MPS

$$|\Psi(A, B, i)\rangle = \ldots \qquad \ldots \qquad \text{(5.21)}$$

(no sum over i!) at a single site, where we know the truncation of the SVD spectrum is optimal. This proves that both ways of truncation are equivalent when $dt \to 0$ and, thus, TEBD, TDVP and WII MPO are also equivalent in this limit.

We also demonstrate the equivalence between these methods numerically, see Fig. 5.4. We work at $\chi = 16$, starting with the ground state of the critical TFIM, Eq. 12 in the main text, with $(J, g) = (1, 1)$. We then time evolve this state using the coupling $(J, g) = (0.1, 1)$, for $t = J$. As dt decreases, we see that all three methods converge.

5.2.2 Fidelity and Excitation Density

In this section, we will use the exact solution of the Kibble-Zurek (KZ) sweep for the transverse-field Ising model (TFIM) [96] to show that the fidelity density reduces to the excitation density in the low-density limit. Let $|\psi(t)\rangle$ be the time evolved state after a Kibble-Zurek sweep, and $|\psi_0\rangle$ the ground state. Then, using the free fermion representation from [96], the time-evolved state can be written as

$$|\psi(t)\rangle = \prod_{k>0}(\alpha_k(t)|\text{no pair}\rangle_k + \beta_k(t)|\text{ pair}\rangle_k), \qquad \text{(5.22)}$$

where $|\text{pair}\rangle_k$ denotes the state with quasipartice of momenta k and $-k$ present above the ground state. The probability of finding the $k, -k$ pair in this state is $P_k = |\beta_k(t)|^2$. The expected number of particles in $|\psi(t)\rangle$ is $N_{ex} = 2\sum_{k>0} P_k$ and for the fidelity we find

$$|\langle\psi_0|\psi(t)\rangle|^2 = \prod_k |\langle\psi_k^{(0)}|\psi_k(t)\rangle|^2 = \exp\left(\sum_{k>0}\log(1-P_k)\right) \approx \exp\left(-\sum_{k>0}P_k\right) = e^{-N_{ex}/2}, \quad \text{(5.23)}$$

Figure 5.4: The energy of the time evolved state obtained from TEBD and TDVP, for different values of the timestep dt used in TEBD. To prepare the state, we started with the $\chi = 16$ ground state of the critical TFIM $(J, g) = (1, 1)$, and then time evolved with the the the TFIM with $(J, g) = (0.1, 1)$ for $t = J$. The TDVP data was obtained using a timestep of 10^{-3}, and a 2-site iTDVP algorithm. Maybe cat state issues with other quantities, could try a different time evolution process.

where we have used that the excitation density is low $P_k \ll 1$ (but not $\sum_{k>0} P_k \ll 1$). Now, defining the excitation density as $n_{ex} = N_{ex}/L$, and we find that the fidelity density is given by

$$f(t) := -\frac{1}{N} \log \left(|\langle \psi_0 | \psi(t) \rangle|^2 \right) \approx n_{ex}/2 \qquad (5.24)$$

This approximation becomes exact in the limit of low-density of excitations. In the context of a Kibble-Zurek sweep, this limit corresponds to $v \to 0$.

To compute this quantity using uniform MPSs, we note

$$\langle \psi_0 | \psi(t) \rangle = \text{tr} \left(\left[\begin{array}{c} T \end{array} \right]^L \right), \qquad (5.25)$$

where

$$T = \begin{array}{c} A(t) \\ \bar{A}_0 \end{array} . \qquad (5.26)$$

If λ is the magnitude of the largest eigenvalue of T, then in the thermodynamic limit we have

$$|\langle \psi_0 | \psi(t) \rangle|^2 = \lambda^{2L}, \qquad (5.27)$$

and thus

$$f = -2 \log |\lambda|. \tag{5.28}$$

5.2.3 Relevant finite χ ground state

We want to discuss what is meant by a finite χ ground state. In particular, different definitions for the ground state no longer are equivalent when working at finite χ. A simple example is an Ising ferromagnet, where the ground state is given by all spin point up, or pointing down. Then, any state of the form

$$|\psi\rangle = \alpha \, |\uparrow \cdots\rangle + \beta \, |\downarrow \cdots\rangle \tag{5.29}$$

would also be a ground state with the same energy. This is not the case at fixed finite χ. In particular, the cat state, with $\alpha = \beta$, requires a bond-dimension of $\chi = 2$, but the states where $\alpha = 0$ or $\beta = 0$ require only $\chi = 1$. This means that the lowest energy state at fixed χ would be a symmetry broken state, not a symmetric, cat like, state. However, in the thermodynamic limit, both the symmetric and symmetry broken state would have the same energy.

In a Kibble-Zurek sweep, we calculate the state $|\psi(v, t)\rangle$ (see the main text for more details). Another definition for the ground state is given by

$$|\psi_0(\lambda(t = 0))\rangle := \lim_{v \to 0} |\psi(v, t = 0)\rangle. \tag{5.30}$$

One property that we seek when deciding which ground state we use is that the excitation energy density $\epsilon_{\text{ex}}(v) \to 0$ as $v \to 0$. At $\chi = \infty$, this is the case whether or not we take the symmetric or symmetry broken state for the ground state. However, at finite χ, since the symmetric and symmetry broken states no longer have the same energy, this is not the case. The preferred definition of the ground state, when calculating the fidelity density and the excitation energy density, is the one given by Eq. (5.30). Since we can not take the limit of $v \to 0$ numerically, we wish to perform a ground state search that yields this state.

Since unitary time evolution does not spontaneously break any symmetries, the state in Eq. (5.30) will have all symmetries that are shared by the initial state and Hamiltonian, Thus we enforce the symmetries of the resulting time-evolved state when we perform the ground state optimization, to ensure we obtain the correct state.

When looking at the TFIM, the result of a KZ sweep will be a cat state with a global $\mathbb{Z}_2$ symmetry. Such states can only be represented with bond-dimension that is divisible by two. We believe for larger, discrete, symmetries, the bond-dimension must be a multiple of the number of elements in the symmetry group, to represent a fully symmetric state exactly. However this remains to be seen in full generality. In this work, we also look at the 3-state Potts model, which has a full S_3 symmetry. Our numerical simulations do not implement non-abelian symmetries, and so we can not enforce the fully symmetric state in our ground state calculation. However, we do enforce a $\mathbb{Z}_3$ symmetry. We have found that this is sufficient in the Potts model when working with a bond-dimension that is divisible by three, but not by six. This result is what makes us believe that a symmetric state requires a bond-dimension that is a multiple of the number of elements in the symmetry group, as S_3 has six elements. This discrepancy is most noticeable at small v, where the

deviations due to finite χ are most apparent, and because of this, we omit $\chi = 6, 12, 18$ for the 3-state Potts model.

5.2.4 Best fit to extract κ

In the main text, the scaling function collapse depended on the length scale introduced by working at finite bond dimension. In previous work, it was demonstrated that the length scale is takes the form of $\xi_\chi \sim \chi^\kappa$ with κ given by Eq. (5.11). Here, we find κ by the best fit for the scaling function collapse for both the fidelity and excitation energy densities. Generically, the scaling ansatz for a Kibble-Zurek sweep at finite χ is given by Eq. 10 in the main text. If one fixes χ and v, then

$$f_O(\xi_{KZ}/\xi_\chi) = O(v, \chi)/O(v, \chi = \infty) \tag{5.31}$$

For simplicity, define the right hand side as y_χ, and the argument $x_\kappa := \xi_{KZ}/\xi_\chi$. Then, for each χ, our numerical data gives an interval I_χ for calculated values of x. We then interpolate the values for $y_\chi(x_\kappa)$ for $x_\kappa \in I_\chi$. Call the interpolated function $\tilde{y}_\chi$. To find κ, we define a cost function

$$C(\kappa) = \sum_{\chi_i > \chi_j} \|\tilde{y}_{\chi_i}(x_\kappa) - \tilde{y}_{\chi_j}(x_\kappa)\|^2, \quad x_\kappa \in I_{\chi_i} \cap I_{\chi_j} \tag{5.32}$$

Conceptually, the cost function is given by the sum of the differences between all pairs of $\tilde{y}_{\chi_i}, \tilde{y}_{\chi_j}$, along the interval where x_κ is defined for both. We then find κ by minimizing $C(\kappa)$. We show in Fig. 5.5 the results of the best fit scaling function, as well as the extracted κ values, for the Ising and 3-state Potts models. Note that for both models the difference between best-fit and theoretical values is small, and comparable to the differences between best-fit κ values taken from fidelity and energy results, which (unless KZ scaling is incorrect) should ultimately be the same in the $\chi \to \infty$ limit. For the Ising case, the cost-function measure of error is essentially the same between the best fit and the theoretical value.

5.2.5 Extrapolation to $\chi = \infty$

One major benefit of the realization that observables satisfy the scaling relation in Eq. 10 of the main text, is that it provides a means to extrapolate systematically to $\chi = \infty$ from finite-χ data. To see this, we can write

$$O(v, \chi = \infty) = O(v, \chi) / f_O(\xi_{KZ}/\xi_\chi). \tag{5.33}$$

The quantity $O(v, \chi)$ is what is computed in the simulations. As for f_O, this is computed by finding the function that the data collapses onto for different values of χ. Where the collapse is not exact, we opt for the average over the different χ values. Then, the ratio of these two values yields the $\chi = \infty$ result, computed for each value of χ. The resulting fidelity and excitation energy densities are shown in Fig. 5.6, for both the TFIM, and the 3-state Potts model.
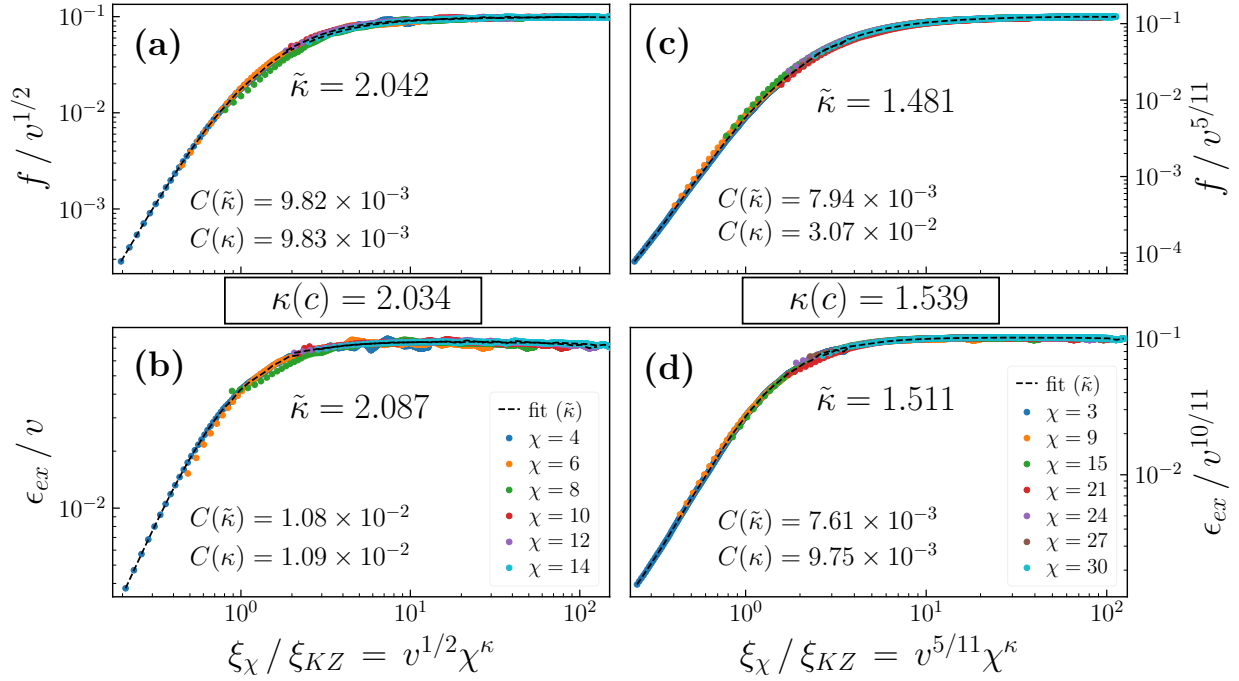
Figure 5.5: The best fit scaling function collapse for the fidelity and excitation energy densities, for the TFIM in (a) and (b), and the 3-state Potts model in (c) and (d). The value $\tilde{\kappa}$ is shown on the plots, and the scaling functions are drawn using that value of κ. The theoretical values are shown between the subplots as a reference. The values for the cost function of Eq. (5.32) are shown for the theoretical and best-fit values of κ.

5.2.6 Kibble-Zurek Sweep starting point dependence

Here we wish to show how the results in the main text depend on the starting location of the Kibble-Zurek sweep. In the main text, we start at $(g_0, J_0) = (2, 0)$ and end at $(1, 1)$. This is equivalent to start infinitely far away from the critical point, and time evolving up to the critical point. However, so long as v is sufficiently small, then the results should not depend on where we start the time evolution, since adiabatic evolution will ensure we stay in the ground state until the gap begins to close.

In Fig. 5.7, we show the fidelity density and the excitation energy as a function of v for different starting points defined by g_0. We only show $\chi = 14$ and the TFIM, but similar results are available for different values of χ, and also in the Potts model. To perform the simulations, we fix g_0, and set $J_0 = 2 - g_0$, so we evolve along the same path towards the critical point as was used in the main text.
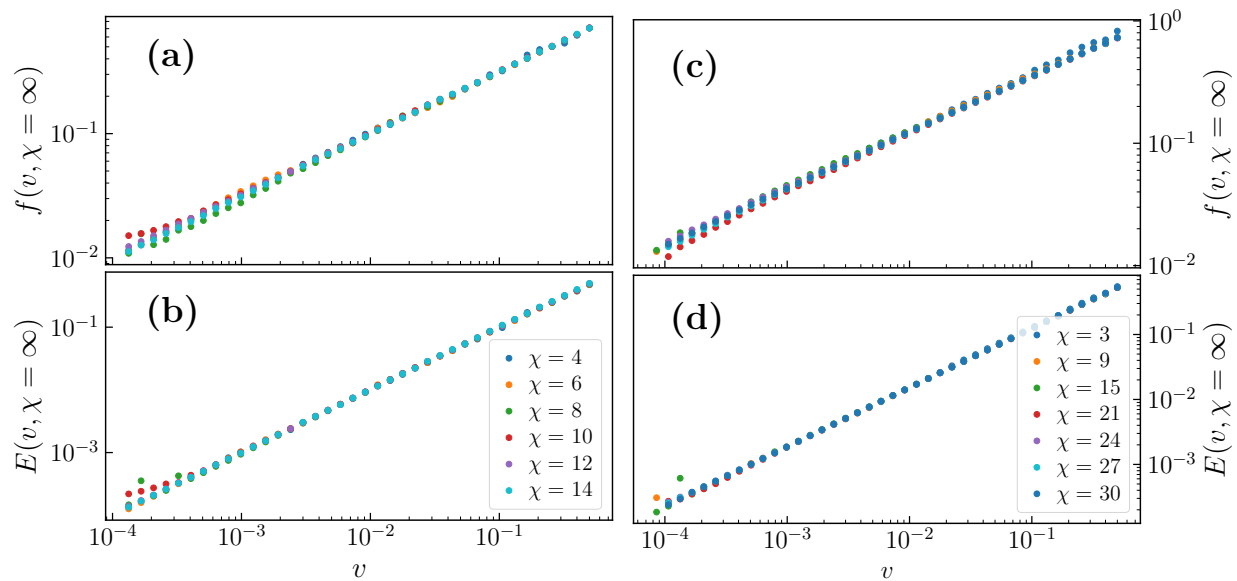
Figure 5.6: The extrapolated $\chi = \infty$ result for the fidelity and excitation energy densities, for the TFIM in (a) and (b), and the 3-state Potts model in (c) and (d). The extrapolation is computed using Eq. (5.33).
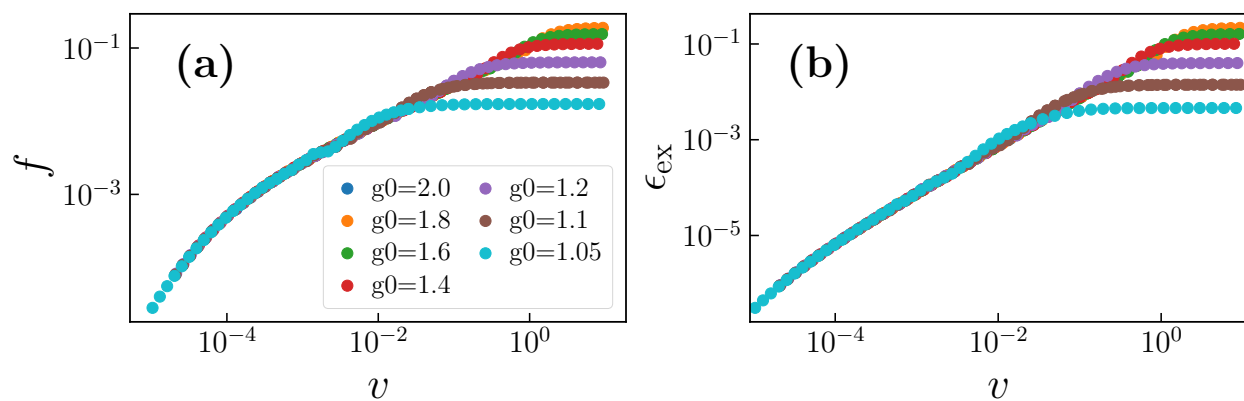

Figure 5.7: Fidelity density, and excitation energy density as a function of the sweep rate v in the TFIM. The different colors correspond to different starting points in the Kibble-Zurek sweep. All starting points are along the line connecting $(g, J) = (2, 0) \rightarrow (1, 1)$. The simulations were performed with a bond-dimension $\chi = 14$.

To calculate these results, there are two ways to think about what v means here to compare different starting points. In the main text, the time dependence of the coupling constants is given by

$$g(t) = 1 + vt \atop J(t) = 1 - vt, \quad t : -\frac{1}{v} \to 0. \tag{5.34}$$

If v is sufficiently small, then starting at t closer to 0 should not change the result. One can think about the results in Fig. 5.7 as starting the simulations at t_0 such that the initial coupling constant g_0 is given by the key in the legend. However, what we actually do is still enforce that $t : -\frac{1}{v} \to 0$, but then modify $v \to v(g_0 - 1)$. These two methods are equivalent.

When talking about v being sufficiently small, there are two relevant scales in the problem to define this. There is a length scale introduced by time evolving with a finite velocity. This scale for the TFIM is given by

$$\xi_{KZ} \sim v^{1/2}. \tag{5.35}$$

As the critical point is approached, the gap in the system starts to close, corresponding to a diverging correlation length ξ_{GS}. In particular

$$\xi_{GS} \quad \sim \frac{1}{|\log(g/J)|} \tag{5.36}$$

Therefore, when v is small enough, such that $\xi_{KZ} \ll \xi_{GS}$, then the starting point does not matter. In the other limit, for large v, the results are sensitive to the starting point, as adiabaticity is lost. This is seen in Fig. 5.7 where all the starting points align for small v, but differ at large v.

Chapter 6

Conclusion

In this work, I have utilized matrix product state (MPS) simulations to identify experimentally relevant signatures of novel quantum materials. First, I examined an anomalous transport observed in one-dimensional magnets known as Kardar-Parisi-Zhang hydrodynamics. Second, I looked at the $J_1 - J_2$ Heisenberg model on the triangular lattice, which hosts a quantum spin liquid (QSL) phase. I discussed key signatures of the QSL phase in the low-energy spectrum that are relevant for neutron scattering experiments. These simulations require large-scale MPS simulations of quantum dynamics, which are challenging, and require approximations to be performed. In particular the MPS ansatz restricts the total entanglement in the state. Lastly, we looked at how this entanglement restriction modifies the evolution of states near criticality. I will detail out the highlights of this work, as well as discuss future directions.

In Chapter 3, we looked at the hydrodynamical behavior of the antiferromagnetic Heisenberg spin chain. It had been previously discovered that at infinite temperature, this model exhibits KPZ hydrodynamics [229]. We demonstrated that KPZ hydrodynamics persists down to experimentally relevant temperatures, and can be detected in the low-energy neutron scattering cross-section. In collaboration with the neutron scattering group at Oak Ridge National Lab, this signature was detected, finding KPZ hydrodynamics in the first quantum mechanical system. What is especially surprising about this is that this is a high temperature phenomena, which historically had been thought to be fairly trivial and predominately governed by classical physics. However, KPZ hydrodynamics is only present in the spin$-1/2$ Heisenberg model, and is not present in the classical Heisenberg spin chain, making this fundamentally a quantum effect present at high temperatures. The low temperature physics of this model is described by the Tomonaga-Luttinger liquid (TLL) [119], which does not possess KPZ hydrodynamics. We showed that there is a spatio-temporal crossover from the TLL physics to KPZ hydrodynamics as temperature is increased. At intermediate temperatures, KPZ hydrodynamics is present at the longest time scale, but the TLL physics is observed for intermediate times. The time scale separating TLL physics from KPZ hydrodynamics is determined by the thermal correlation length $\xi_T \sim 1/T$.

Several questions regarding KPZ hydrodynamics still remain open questions. One main question is understanding why KPZ emerges in the Heisenberg chain. To this end, numerical simulations seem to suggest that KPZ hydrodynamics requires integrability, as well as an enhanced symmetry

such as rotational invariance [92], or possibly any non-abelian symmetry [413]. How robust is the KPZ hydrodynamics to perturbations that break integrability, or the enhanced symmetry, is still an open question. From the experiments in $KCuF_3$ [308], we expect that KPZ hydrodynamics must have some stability against integrability breaking, as a real material will not be integrable. Similar to the crossover from TLL to KPZ as temperature is tuned, we might expect a crossover from KPZ to diffusion as an integrability breaking term is introduced into the model. In such a case, at the longest times, we would expect diffusive transport, but for intermediate times, KPZ transport is likely present. Characterizing this crossover would be an interesting question to address.

In Chapter 4, we looked at the $J_1 - J_2$ Heisenberg model, and studied the dynamical structure factor. This model is known to have a QSL phase at intermediate values of J_2/J_1. However, despite extensive work over decades, the exact nature of the ground state has remained elusive. The three main QSL ground state candidates are a gapped $\mathbb{Z}_2$, a gapless U(1) Dirac, and spinon fermi surface quantum spin liquid state. We discussed key signatures in the dynamical structure factor that distinguish these three phases for triangular lattice systems. Using MPS simulations, we calculated the dynamical structure factor across the full phase diagram of the $J_1 - J_2$ Heisenberg model, and argued that our results are most consistent with a U(1) Dirac spin liquid. These simulations also enabled comparisons in the triangular lattice compounds $KYbSe_2$ and $YbZn_2GaO_5$. From these comparisons, we demonstrated that $KYbSe_2$ is well modelled by the $J_1 - J_2$ Heisenberg model, and in close proximity to the QSL phase. In $YbZn_2GaO_5$, we saw that the spectrum looks very similar to the QSL phase of the $J_1 - J_2$ model, suggesting it is a realization of a U(1) Dirac spin liquid. Introducing an easy axis anisotropy reproduced the relative spectral weight between the K and M points, suggesting that $YbZn_2GaO_5$is well modelled by a $J_1 - J_2$ XXZ model.

Only very recently has dynamical simulations of two-dimensional systems been possible within the MPS framework. Using the technique described in Chapter 4, simulations of spectral functions for other QSL systems would be interesting to pursue. For example, the Hubbard model on the triangular lattice has shown evidence of a chiral spin liquid [356], which also emerges with the introduction of four-spin terms into the $J_1 - J_2$ Heisenberg model [72]. Examining the dynamical structure factor of such models could produce signatures for such an exotic phase that could be realized experimentally.

Lastly, in Chapter 5, we looked at how the Kibble-Zurek mechanism is modified when considering the finite entanglement restrictions present during MPS simulations. We found that the effect of finite bond-dimension χ was to introduce a length scale ξ_χ into the problem, similar to the case of ground state properties of critical theories [357]. We conjectured that the Kibble-Zurek predictions for quantities such as the energy and fidelity densities would be modulated by a scaling function of the ratio of the Kibble-Zurek length scale ξ_{KZ} and ξ_χ. We demonstrated this hypothesis for the quantum Ising model and the 3-state Potts. This enabled us to extract ξ_χ, and found that it is given by a power law with the same power as derived in Ref. [277]. This conjecture also provides a means to extrapolate to $\chi = \infty$, and we showed this reproduces the exact Kibble-Zurek prediction well.

Understanding the effect that finite entanglement has on critical states is relatively unexplored. One question is whether or not finite entanglement can be interpreted as a relevant perturbation, similarly to the effect of finite size [53]. One way to address this question is to use MPS simulations

to calculate the ground state of a critical theory. Using something such as the density matrix renormalization group (DMRG), we find the state that satisfies

$$\min_{|\psi_\chi\rangle \in \mathcal{H}_\chi} \langle \psi_\chi | H_c | \psi_\chi \rangle \tag{6.1}$$

where $\mathcal{H}_\chi$ is the subset of Hilbert space that can be written as an MPS with bond-dimension at most χ, and H_c is a critical Hamiltonian. We could ask if this state is also the solution of an unconstrained minimization problem of a different Hamiltonian $\tilde{H}(\chi)$. If so, is $\tilde{H}(\chi)$ related to H_c by a relevant perturbation? We would expect that as $\chi \to \infty$ we have that $\tilde{H}(\chi) \to H_c$, suggesting that

$$\tilde{H}(\chi) = H_c + \delta H(\chi) \tag{6.2}$$

It would be interesting to understand the term $\delta H(\chi)$ for a particular model, and to see if there are universal features to this term that behave similarly to a relevant perturbation.

Bibliography

[1] We use a Trotter step $\delta = 0.1$ leading to a negligible discretization error $O\left(\delta^5\right)$.

[2] Including first-order log corrections would change Eq. (3.12) to $t^\star(x = 0, T) = A + B\left[1 + C \left/ \ln(T/D)\right.\right]^{-1}\left/T\right.$ with fitting parameters A, B, C, and D. The limited data of Fig. 3.8(a) do not allow us to reliably use this enhance functional form. The spatial dependence of $t^\star(x, T)$ for $x \neq 0$ would remain unchanged.

[3] Majed Abdel-Jawad et al. "Anomalous dielectric response in the dimer Mott insulator $\kappa-(\mathrm{BEDT-TTF})_2\mathrm{Cu}_2(\mathrm{CN})_3$". In: *Phys. Rev. B* 82 (12 Sept. 2010), p. 125119. DOI: 10.1103/PhysRevB.82.125119. URL: https://link.aps.org/doi/10.1103/PhysRevB.82.125119.

[4] Anatole Abragam and HY Carr. *The principles of nuclear magnetism*. Clarendon Press, Oxford, UK, 1961.

[5] Adam A Aczel et al. "Quantum oscillations of nitrogen atoms in uranium nitride". In: *Nature communications* 3.1 (2012), pp. 1–7. URL: https://doi.org/10.1038/ncomms2117.

[6] I Affleck et al. "Critical behaviour of spin-s Heisenberg antiferromagnetic chains: analytic and numerical results". In: *J. Phys. A* 22.5 (Mar. 1989), pp. 511–529. DOI: 10.1088/0305-4470/22/5/015. URL: https://doi.org/10.1088/0305-4470/22/5/015.

[7] Ian Affleck. "Exact correlation amplitude for the Heisenberg antiferromagnetic chain". In: *J. Phys. A* 31.20 (May 1998), pp. 4573–4581. DOI: 10.1088/0305-4470/31/20/002. URL: https://doi.org/10.1088/0305-4470/31/20/002.

[8] Amir M Aghaei et al. *Efficient matrix-product-state preparation of highly entangled trial states: Weak Mott insulators on the triangular lattice revisited*. 2020. DOI: 10.48550/ARXIV.2009.12435. URL: https://arxiv.org/abs/2009.12435.

[9] Utkarsh Agrawal, Sarang Gopalakrishnan, and Romain Vasseur. "Generalized hydrodynamics, quasiparticle diffusion, and anomalous local relaxation in random integrable spin chains". In: *Phys. Rev. B* 99 (17 May 2019), p. 174203. DOI: 10.1103/PhysRevB.99.174203. URL: https://link.aps.org/doi/10.1103/PhysRevB.99.174203.

[10] Utkarsh Agrawal et al. "Anomalous low-frequency conductivity in easy-plane XXZ spin chains". In: *Phys. Rev. B* 101 (22 June 2020), p. 224415. DOI: 10.1103/PhysRevB.101.224415. URL: https://link.aps.org/doi/10.1103/PhysRevB.101.224415.

[11] Jason Alicea. "Monopole quantum numbers in the staggered flux spin liquid". In: *Phys. Rev. B* 78 (3 July 2008), p. 035126. DOI: 10.1103/PhysRevB.78.035126. URL: https://link.aps.org/doi/10.1103/PhysRevB.78.035126.

[12] L. Amico et al. "Divergence of the entanglement range in low-dimensional quantum systems". In: *Phys. Rev. A* 74 (2 Aug. 2006), p. 022322. DOI: 10.1103/PhysRevA.74.022322. URL: https://link.aps.org/doi/10.1103/PhysRevA.74.022322.

[13] Luigi Amico et al. "Dynamics of entanglement in one-dimensional spin systems". In: *Phys. Rev. A* 69 (2 Feb. 2004), p. 022304. DOI: 10.1103/PhysRevA.69.022304. URL: https://link.aps.org/doi/10.1103/PhysRevA.69.022304.

[14] P.W. Anderson. "Resonating valence bonds: A new kind of insulator?" In: *Materials Research Bulletin* 8.2 (1973), pp. 153–160. ISSN: 0025-5408. DOI: https://doi.org/10.1016/0025-5408(73)90167-0. URL: https://www.sciencedirect.com/science/article/pii/0025540873901670.

[15] Daniel P. Arovas and Assa Auerbach. "Functional integral theories of low-dimensional quantum Heisenberg models". In: *Phys. Rev. B* 38 (1 July 1988), pp. 316–332. DOI: 10.1103/PhysRevB.38.316. URL: https://link.aps.org/doi/10.1103/PhysRevB.38.316.

[16] Assa Auerbach. *Interacting electrons and quantum magnetism*. New York: Springer-Verlag, 1994.

[17] Sebastian Bachus et al. "Field evolution of the spin-liquid candidate $YbMgGaO_4$". In: *Phys. Rev. B* 102 (10 Sept. 2020), p. 104433. DOI: 10.1103/PhysRevB.102.104433. URL: https://link.aps.org/doi/10.1103/PhysRevB.102.104433.

[18] M. Baenitz et al. "$NaYbS_2$: A planar spin-$\frac{1}{2}$ triangular-lattice magnet and putative spin liquid". In: *Phys. Rev. B* 98 (22 Dec. 2018), p. 220409. DOI: 10.1103/PhysRevB.98.220409. URL: https://link.aps.org/doi/10.1103/PhysRevB.98.220409.

[19] J. Bardeen, L. N. Cooper, and J. R. Schrieffer. "Microscopic Theory of Superconductivity". In: *Phys. Rev.* 106 (1 Apr. 1957), pp. 162–164. DOI: 10.1103/PhysRev.106.162. URL: https://link.aps.org/doi/10.1103/PhysRev.106.162.

[20] S M Barnett and B J Dalton. "Liouville space description of thermofields and their generalisations". In: *Journal of Physics A: Mathematical and General* 20.2 (Feb. 1987), pp. 411–418. DOI: 10.1088/0305-4470/20/2/026. URL: https://doi.org/10.1088%2F0305-4470%2F20%2F2%2F026.

[21] Fabrizio Baroni et al. "Two-spin entanglement distribution near factorized states". In: *Journal of Physics A: Mathematical and Theoretical* 40.32 (July 2007), pp. 9845–9857. DOI: 10.1088/1751-8113/40/32/010. URL: https://doi.org/10.1088/1751-8113/40/32/010.

[22] Thomas Barthel and Yikang Zhang. "Optimized Lie–Trotter–Suzuki decompositions for two and three non-commuting terms". In: *Annals of Physics* 418 (July 2020), p. 168165. DOI: 10.1016/j.aop.2020.168165. URL: https://doi.org/10.1016%2Fj.aop.2020.168165.

[23] Victor Barzykin. "NMR relaxation rates in a spin-$\frac{1}{2}$ antiferromagnetic chain". In: *Phys. Rev. B* 63 (14 Mar. 2001), 140412(R). DOI: 10.1103/PhysRevB.63.140412. URL: https://link.aps.org/doi/10.1103/PhysRevB.63.140412.

[24] Victor Barzykin. "Temperature-dependent logarithmic corrections in the spin-1/2 Heisenberg chain". In: *J. Condens. Matter Phys.* 12.9 (Feb. 2000), pp. 2053–2059. DOI: 10.1088/0953-8984/12/9/309. URL: https://doi.org/10.1088/0953-8984/12/9/309.

[25] H. Benthien, F. Gebhard, and E. Jeckelmann. "Spectral Function of the One-Dimensional Hubbard Model away from Half Filling". In: *Phys. Rev. Lett.* 92 (25 June 2004), p. 256401. DOI: 10.1103/PhysRevLett.92.256401. URL: https://link.aps.org/doi/10.1103/PhysRevLett.92.256401.

[26] Hannes Bernien et al. "Probing many-body dynamics on a 51-atom quantum simulator". In: *Nature* 551.7682 (2017), pp. 579–584. DOI: 10.1038/nature24622. URL: https://doi.org/10.1038/nature24622.

[27] B. Bernu et al. "Exact spectra, spin susceptibilities, and order parameter of the quantum Heisenberg antiferromagnet on the triangular lattice". In: *Phys. Rev. B* 50 (14 Oct. 1994), pp. 10048–10062. DOI: 10.1103/PhysRevB.50.10048. URL: https://link.aps.org/doi/10.1103/PhysRevB.50.10048.

[28] Claude Berthier et al. "Nuclear magnetic resonance in high magnetic field: Application to condensed matter physics". In: *C. R. Phys.* 18.5 (2017), pp. 331–348. DOI: https://doi.org/10.1016/j.crhy.2017.09.009. URL: https://www.sciencedirect.com/science/article/pii/S1631070517300658.

[29] B. Bertini et al. "Finite-temperature transport in one-dimensional quantum lattice models". In: *Rev. Mod. Phys.* 93 (2 May 2021), p. 025003. DOI: 10.1103/RevModPhys.93.025003. URL: https://link.aps.org/doi/10.1103/RevModPhys.93.025003.

[30] Bruno Bertini et al. "Transport in Out-of-Equilibrium *XXZ* Chains: Exact Profiles of Charges and Currents". In: *Phys. Rev. Lett.* 117 (20 Nov. 2016), p. 207201. DOI: 10.1103/PhysRevLett.117.207201. URL: https://link.aps.org/doi/10.1103/PhysRevLett.117.207201.

[31] B. Bleaney. "Hyperfine interactions in rare-earth metals". In: *Journal of Applied Physics* 34.4 (1963), pp. 1024–1031. DOI: 10.1063/1.1729355. URL: https://doi.org/10.1063/1.1729355.

[32] Andrew Boothroyd. *Principles of Neutron Scattering from Condensed Matter*. Oxford University Press, USA, 2020.

[33] Mitchell M. Bordelon et al. "Field-tunable quantum disordered ground state in the triangular-lattice antiferromagnet $NaYbO_2$". In: *Nature Physics* 15.10 (2019), pp. 1058–1064. DOI: 10.1038/s41567-019-0594-5. URL: https://doi.org/10.1038/s41567-019-0594-5.

[34] Mitchell M. Bordelon et al. "Field-tunable quantum disordered ground state in the triangular-lattice antiferromagnet NaYbO2". In: *Nature physics* 15 (2019), pp. 1058–1064. DOI: https://doi.org/10.1038/s41567-019-0594-5.

[35] Mitchell M. Bordelon et al. "Spin excitations in the frustrated triangular lattice antiferromagnet $NaYbO_2$". In: *Phys. Rev. B* 101 (22 June 2020), p. 224427. DOI: 10.1103/PhysRevB.101.224427. URL: https://link.aps.org/doi/10.1103/PhysRevB.101.224427.

[36] Pierre Bouillot et al. "Statics and dynamics of weakly coupled antiferromagnetic spin-$\frac{1}{2}$ ladders in a magnetic field". In: *Phys. Rev. B* 83 (5 Feb. 2011), p. 054407. DOI: 10.1103/PhysRevB.83.054407. URL: https://link.aps.org/doi/10.1103/PhysRevB.83.054407.

[37] P. Bourgeois-Hope et al. "Thermal Conductivity of the Quantum Spin Liquid Candidate $EtMe_3Sb[Pd(dmit)_2]_2$: No Evidence of Mobile Gapless Excitations". In: *Phys. Rev. X* 9 (4 Dec. 2019), p. 041051. DOI: 10.1103/PhysRevX.9.041051. URL: https://link.aps.org/doi/10.1103/PhysRevX.9.041051.

[38] C. Broholm et al. "Quantum spin liquids". In: *Science* 367.6475 (2020). ISSN: 0036-8075. DOI: 10.1126/science.aay0668. URL: https://science.sciencemag.org/content/367/6475/eaay0668.

[39] C. Broholm et al. "Quantum spin liquids". In: *Science* 367.6475 (2020), eaay0668. DOI: 10.1126/science.aay0668. URL: https://www.science.org/doi/abs/10.1126/science.aay0668.

[40] R. Brout and H. Thomas. "Molecular field theory, the Onsager reaction field and the spherical model". In: *Physics Physique Fizika* 3 (6 Dec. 1967), pp. 317–329. DOI: 10.1103/PhysicsPhysiqueFizika.3.317. URL: https://link.aps.org/doi/10.1103/PhysicsPhysiqueFizika.3.317.

[41] P. J. Brown. *Magnetic Form Factors*. The Cambridge Crystallographic Subroutine Library. 1998. URL: https://www.ill.eu/sites/ccsl/ffacts/.

[42] Bruker. *Apex3*. Madison, WI, 2015.

[43] Časlav Brukner, Vlatko Vedral, and Anton Zeilinger. "Crucial role of quantum entanglement in bulk properties of solids". In: *Phys. Rev. A* 73 (1 Jan. 2006), p. 012110. DOI: 10.1103/PhysRevA.73.012110. URL: https://link.aps.org/doi/10.1103/PhysRevA.73.012110.

[44] Vir B. Bulchandani. "Kardar-Parisi-Zhang universality from soft gauge modes". In: *Phys. Rev. B* 101 (4 Jan. 2020), p. 041411. DOI: 10.1103/PhysRevB.101.041411. URL: https://link.aps.org/doi/10.1103/PhysRevB.101.041411.

[45] Vir B. Bulchandani et al. "Bethe-Boltzmann hydrodynamics and spin transport in the XXZ chain". In: *Phys. Rev. B* 97 (4 Jan. 2018), p. 045407. DOI: 10.1103/PhysRevB.97.045407. URL: https://link.aps.org/doi/10.1103/PhysRevB.97.045407.

[46] Pasquale Calabrese and John Cardy. "Entanglement entropy and conformal field theory". In: *Journal of Physics A: Mathematical and Theoretical* 42.50 (Dec. 2009), p. 504005. DOI: 10.1088/1751-8113/42/50/504005. URL: https://dx.doi.org/10.1088/1751-8113/42/50/504005.

[47] Pasquale Calabrese and John Cardy. "Entanglement entropy and quantum field theory". In: *Journal of Statistical Mechanics: Theory and Experiment* 2004.06 (June 2004), P06002. DOI: 10.1088/1742-5468/2004/06/P06002. URL: https://dx.doi.org/10.1088/1742-5468/2004/06/P06002.

[48] Pasquale Calabrese and John Cardy. "Evolution of entanglement entropy in one-dimensional systems". In: *Journal of Statistical Mechanics: Theory and Experiment* 2005.04 (Apr. 2005), P04010. DOI: 10.1088/1742-5468/2005/04/P04010. URL: https://dx.doi.org/10.1088/1742-5468/2005/04/P04010.

[49] Adolfo del Campo and Wojciech H Zurek. "Universality of phase transition dynamics: Topological defects from symmetry breaking". In: *Int. J. Mod. Phys. A* 29.08 (Mar. 2014), p. 1430018. URL: https://www.worldscientific.com/doi/abs/10.1142/S0217751X1430018X.

[50] Xuanmin Cao, Qijun Hu, and Fan Zhong. "Scaling theory of entanglement entropy in confinements near quantum critical points". In: *Phys. Rev. B* 98 (24 Dec. 2018), p. 245124. DOI: 10.1103/PhysRevB.98.245124. URL: https://link.aps.org/doi/10.1103/PhysRevB.98.245124.

[51] Sylvain Capponi et al. "NMR relaxation in the spin-1 Heisenberg chain". In: *Phys. Rev. B* 100 (9 Sept. 2019), p. 094411. DOI: 10.1103/PhysRevB.100.094411. URL: https://link.aps.org/doi/10.1103/PhysRevB.100.094411.

[52] Luca Capriotti, Adolfo E. Trumper, and Sandro Sorella. "Long-Range Néel Order in the Triangular Heisenberg Model". In: *Phys. Rev. Lett.* 82 (19 May 1999), pp. 3899–3902. DOI: 10.1103/PhysRevLett.82.3899. URL: https://link.aps.org/doi/10.1103/PhysRevLett.82.3899.

[53] "1 - Introduction to Theory of Finite-Size Scaling". In: *Finite-Size Scaling*. Ed. by John L. CARDY. Vol. 2. Current Physics–Sources and Comments. Elsevier, 1988, pp. 1–7. DOI: https://doi.org/10.1016/B978-0-444-87109-1.50006-6. URL: https://www.sciencedirect.com/science/article/pii/B9780444871091500066.

[54] Olalla A. Castro-Alvaredo, Benjamin Doyon, and Takato Yoshimura. "Emergent Hydrodynamics in Integrable Quantum Systems Out of Equilibrium". In: *Phys. Rev. X* 6 (4 Dec. 2016), p. 041065. DOI: 10.1103/PhysRevX.6.041065. URL: https://link.aps.org/doi/10.1103/PhysRevX.6.041065.

[55] Jean-Sébastien Caux and Rob Hagemans. "The four-spinon dynamical structure factor of the Heisenberg chain". In: *Journal of Statistical Mechanics: Theory and Experiment* 2006.12 (Dec. 2006), P12013–P12013. DOI: 10.1088/1742-5468/2006/12/p12013. URL: https://doi.org/10.1088%2F1742-5468%2F2006%2F12%2Fp12013.

[56] Sudip Chakravarty, Bertrand I. Halperin, and David R. Nelson. "Two-dimensional quantum Heisenberg antiferromagnet at low temperatures". In: *Phys. Rev. B* 39 (4 Feb. 1989), pp. 2344–2371. DOI: 10.1103/PhysRevB.39.2344. URL: https://link.aps.org/doi/10.1103/PhysRevB.39.2344.

[57] Sudip Chakravarty, Bertrand I. Halperin, and David R. Nelson. "Two-dimensional quantum Heisenberg antiferromagnet at low temperatures". In: *Phys. Rev. B* 39 (4 Feb. 1989), pp. 2344–2371. DOI: 10.1103/PhysRevB.39.2344. URL: https://link.aps.org/doi/10.1103/PhysRevB.39.2344.

[58] Jing Chen et al. "Equivalence of restricted Boltzmann machines and tensor network states". In: *Phys. Rev. B* 97 (8 Feb. 2018), p. 085104. DOI: 10.1103/PhysRevB.97.085104. URL: https://link.aps.org/doi/10.1103/PhysRevB.97.085104.

[59] Song Cheng, Lei Wang, and Pan Zhang. "Supervised learning with projected entangled pair states". In: *Phys. Rev. B* 103 (12 Mar. 2021), p. 125117. DOI: 10.1103/PhysRevB.103.125117. URL: https://link.aps.org/doi/10.1103/PhysRevB.103.125117.

[60] Song Cheng et al. "Tree tensor networks for generative modeling". In: *Phys. Rev. B* 99 (15 Apr. 2019), p. 155131. DOI: 10.1103/PhysRevB.99.155131. URL: https://link.aps.org/doi/10.1103/PhysRevB.99.155131.

[61] R. W. Cherng and L. S. Levitov. "Entropy and correlation functions of a driven quantum spin chain". In: *Phys. Rev. A* 73 (4 Apr. 2006), p. 043614. DOI: 10.1103/PhysRevA.73.043614. URL: https://link.aps.org/doi/10.1103/PhysRevA.73.043614.

[62] A. L. Chernyshev and M. E. Zhitomirsky. "Magnon Decay in Noncollinear Quantum Antiferromagnets". In: *Phys. Rev. Lett.* 97 (20 Nov. 2006), p. 207202. DOI: 10.1103/PhysRevLett.97.207202. URL: https://link.aps.org/doi/10.1103/PhysRevLett.97.207202.

[63] A. L. Chernyshev and M. E. Zhitomirsky. "Spin waves in a triangular lattice antiferromagnet: Decays, spectrum renormalization, and singularities". In: *Phys. Rev. B* 79 (14 Apr. 2009), p. 144416. DOI: 10.1103/PhysRevB.79.144416. URL: https://link.aps.org/doi/10.1103/PhysRevB.79.144416.

[64] Run-Ze Chi et al. *Spin excitation spectra of the spin-1/2 triangular Heisenberg antiferromagnets from tensor networks*. 2022. DOI: 10.48550/ARXIV.2201.12121. URL: https://arxiv.org/abs/2201.12121.

[65] Gabriele De Chiara et al. "Entanglement entropy dynamics of Heisenberg chains". In: *Journal of Statistical Mechanics: Theory and Experiment* 2006.03 (Mar. 2006), P03001. DOI: 10.1088/1742-5468/2006/03/P03001. URL: https://dx.doi.org/10.1088/1742-5468/2006/03/P03001.

[66] A V Chubukov, S Sachdev, and T Senthil. "Large-S expansion for quantum antiferromagnets on a triangular lattice". In: *Journal of Physics: Condensed Matter* 6.42 (Oct. 1994), pp. 8891–8902. DOI: `10.1088/0953-8984/6/42/019`. URL: `https://doi.org/10.1088/0953-8984/6/42/019`.

[67] J. Ignacio Cirac et al. "Matrix product states and projected entangled pair states: Concepts, symmetries, theorems". In: *Rev. Mod. Phys.* 93 (4 Dec. 2021), p. 045003. DOI: `10.1103/RevModPhys.93.045003`. URL: `https://link.aps.org/doi/10.1103/RevModPhys.93.045003`.

[68] Juan Ignacio Cirac, José Garre-Rubio, and David Pérez-Garcia. "Mathematical open problems in projected entangled pair states". In: *Revista Matemática Complutense* 32.3 (2019), pp. 579–599. URL: `https://link.springer.com/article/10.1007/s13163-019-00318-x`.

[69] Logan W. Clark, Lei Feng, and Cheng Chin. "Universal space-time scaling symmetry in the dynamics of bosons across a quantum phase transition". In: *Science* 354.6312 (2016), pp. 606–610. DOI: `10.1126/science.aaf9657`. eprint: `https://www.science.org/doi/pdf/10.1126/science.aaf9657`. URL: `https://www.science.org/doi/abs/10.1126/science.aaf9657`.

[70] Valerie Coffman, Joydip Kundu, and William K. Wootters. "Distributed entanglement". In: *Phys. Rev. A* 61 (5 Apr. 2000), p. 052306. DOI: `10.1103/PhysRevA.61.052306`. URL: `https://link.aps.org/doi/10.1103/PhysRevA.61.052306`.

[71] E. Coira et al. "Temperature dependence of the NMR spin-lattice relaxation rate for spin-$\frac{1}{2}$ chains". In: *Phys. Rev. B* 94 (14 Oct. 2016), p. 144408. DOI: `10.1103/PhysRevB.94.144408`. URL: `https://link.aps.org/doi/10.1103/PhysRevB.94.144408`.

[72] Tessa Cookmeyer, Johannes Motruk, and Joel E. Moore. "Four-Spin Terms and the Origin of the Chiral Spin Liquid in Mott Insulators on the Triangular Lattice". In: *Phys. Rev. Lett.* 127 (8 Aug. 2021), p. 087201. DOI: `10.1103/PhysRevLett.127.087201`. URL: `https://link.aps.org/doi/10.1103/PhysRevLett.127.087201`.

[73] Luca D'Alessio et al. "From quantum chaos and eigenstate thermalization to statistical mechanics and thermodynamics". In: *Advances in Physics* 65.3 (2016), pp. 239–362. DOI: `10.1080/00018732.2016.1198134`. eprint: `https://doi.org/10.1080/00018732.2016.1198134`. URL: `https://doi.org/10.1080/00018732.2016.1198134`.

[74] Peng-Ling Dai et al. "Spinon Fermi Surface Spin Liquid in a Triangular Lattice Antiferromagnet NaYbSe$_2$". In: *Phys. Rev. X* 11 (2 May 2021), p. 021044. DOI: `10.1103/PhysRevX.11.021044`. URL: `https://link.aps.org/doi/10.1103/PhysRevX.11.021044`.

[75] Peng-Ling Dai et al. "Spinon Fermi Surface Spin Liquid in a Triangular Lattice Antiferromagnet NaYbSe$_2$". In: *Phys. Rev. X* 11 (2 May 2021), p. 021044. DOI: `10.1103/PhysRevX.11.021044`. URL: `https://link.aps.org/doi/10.1103/PhysRevX.11.021044`.

[76] A J Daley et al. "Time-dependent density-matrix renormalization-group using adaptive effective Hilbert spaces". In: *Journal of Statistical Mechanics: Theory and Experiment* 2004.04 (Apr. 2004), P04005. DOI: 10.1088/1742-5468/2004/04/P04005. URL: https://dx.doi.org/10.1088/1742-5468/2004/04/P04005.

[77] C. De Grandi and A. Polkovnikov. "Adiabatic Perturbation Theory: From Landau–Zener Problem to Quenching Through a Quantum Critical Point". In: *Quantum Quenching, Annealing and Computation*. Ed. by Anjan Kumar Chandra, Arnab Das, and Bikas K. Chakrabarti. Berlin, Heidelberg: Springer Berlin Heidelberg, 2010, pp. 75–114. ISBN: 978-3-642-11470-0. DOI: 10.1007/978-3-642-11470-0_4. URL: https://doi.org/10.1007/978-3-642-11470-0_4.

[78] C. De Grandi, A. Polkovnikov, and A. W. Sandvik. "Universal nonequilibrium quantum dynamics in imaginary time". In: *Phys. Rev. B* 84 (22 Dec. 2011), p. 224303. DOI: 10.1103/PhysRevB.84.224303. URL: https://link.aps.org/doi/10.1103/PhysRevB.84.224303.

[79] Jacopo De Nardis, Denis Bernard, and Benjamin Doyon. "Hydrodynamic Diffusion in Integrable Systems". In: *Phys. Rev. Lett.* 121 (16 Oct. 2018), p. 160603. DOI: 10.1103/PhysRevLett.121.160603. URL: https://link.aps.org/doi/10.1103/PhysRevLett.121.160603.

[80] Jacopo De Nardis et al. "Anomalous Spin Diffusion in One-Dimensional Antiferromagnets". In: *Phys. Rev. Lett.* 123 (18 Oct. 2019), p. 186601. DOI: 10.1103/PhysRevLett.123.186601. URL: https://link.aps.org/doi/10.1103/PhysRevLett.123.186601.

[81] Jacopo De Nardis et al. "Stability of Superdiffusion in Nearly Integrable Spin Chains". In: *Phys. Rev. Lett.* 127 (5 July 2021), p. 057201. DOI: 10.1103/PhysRevLett.127.057201. URL: https://link.aps.org/doi/10.1103/PhysRevLett.127.057201.

[82] Jacopo De Nardis et al. "Superdiffusion from Emergent Classical Solitons in Quantum Spin Chains". In: *Phys. Rev. Lett.* 125 (7 Aug. 2020), p. 070601. DOI: 10.1103/PhysRevLett.125.070601. URL: https://link.aps.org/doi/10.1103/PhysRevLett.125.070601.

[83] Jacopo De Nardis et al. "Universality Classes of Spin Transport in One-Dimensional Isotropic Magnets: The Onset of Logarithmic Anomalies". In: *Phys. Rev. Lett.* 124 (21 May 2020), p. 210605. DOI: 10.1103/PhysRevLett.124.210605. URL: https://link.aps.org/doi/10.1103/PhysRevLett.124.210605.

[84] Stefan Depenbrock, Ian P. McCulloch, and Ulrich Schollwöck. "Nature of the Spin-Liquid Ground State of the $S = 1/2$ Heisenberg Model on the Kagome Lattice". In: *Phys. Rev. Lett.* 109 (6 Aug. 2012), p. 067201. DOI: 10.1103/PhysRevLett.109.067201. URL: https://link.aps.org/doi/10.1103/PhysRevLett.109.067201.

[85] Lei Ding et al. "Gapless spin-liquid state in the structurally disorder-free triangular anti-ferromagnet NaYbO$_2$". In: *Phys. Rev. B* 100 (14 Oct. 2019), p. 144432. DOI: 10.1103/PhysRevB.100.144432. URL: https://link.aps.org/doi/10.1103/PhysRevB.100.144432.

[86] Lei Ding et al. "Gapless spin-liquid state in the structurally disorder-free triangular anti-ferromagnet NaYbO$_2$". In: *Phys. Rev. B* 100 (14 Oct. 2019), p. 144432. DOI: 10.1103/PhysRevB.100.144432. URL: https://link.aps.org/doi/10.1103/PhysRevB.100.144432.

[87] Zhaofeng Ding et al. "Persistent spin dynamics and absence of spin freezing in the $H-T$ phase diagram of the two-dimensional triangular antiferromagnet YbMgGaO$_4$". In: *Phys. Rev. B* 102 (1 July 2020), p. 014428. DOI: 10.1103/PhysRevB.102.014428. URL: https://link.aps.org/doi/10.1103/PhysRevB.102.014428.

[88] Markus Drescher et al. *Dynamical Signatures of Symmetry Broken and Liquid Phases in an S = 1/2 Heisenberg Antiferromagnet on the Triangular Lattice*. 2022. DOI: 10.48550/ARXIV.2209.03344. URL: https://arxiv.org/abs/2209.03344.

[89] Markus Drescher et al. *Dynamical Signatures of Symmetry Broken and Liquid Phases in an S = 1/2 Heisenberg Antiferromagnet on the Triangular Lattice*. 2022. DOI: https://doi.org/10.48550/arXiv.2209.03344. arXiv: 2209.03344 [cond-mat.str-el].

[90] Maxime Dupont, Sylvain Capponi, and Nicolas Laflorencie. "Temperature dependence of the NMR relaxation rate $1/T_1$ for quantum spin chains". In: *Phys. Rev. B* 94 (14 Oct. 2016), p. 144409. DOI: 10.1103/PhysRevB.94.144409. URL: https://link.aps.org/doi/10.1103/PhysRevB.94.144409.

[91] Maxime Dupont and Joel E. Moore. "Quantum criticality using a superconducting quantum processor". In: *Phys. Rev. B* 106 (4 July 2022), p. L041109. DOI: 10.1103/PhysRevB.106.L041109. URL: https://link.aps.org/doi/10.1103/PhysRevB.106.L041109.

[92] Maxime Dupont and Joel E. Moore. "Universal spin dynamics in infinite-temperature one-dimensional quantum magnets". In: *Phys. Rev. B* 101 (12 Mar. 2020), p. 121106. DOI: 10.1103/PhysRevB.101.121106. URL: https://link.aps.org/doi/10.1103/PhysRevB.101.121106.

[93] Maxime Dupont, Nicholas E. Sherman, and Joel E. Moore. "Spatiotemporal Crossover between Low- and High-Temperature Dynamical Regimes in the Quantum Heisenberg Magnet". In: *Phys. Rev. Lett.* 127 (10 Aug. 2021), p. 107201. DOI: 10.1103/PhysRevLett.127.107201. URL: https://link.aps.org/doi/10.1103/PhysRevLett.127.107201.

[94] Maxime Dupont et al. "Dynamical response and dimensional crossover for spatially anisotropic antiferromagnets". In: *Phys. Rev. B* 98 (9 Sept. 2018), p. 094403. DOI: 10.1103/PhysRevB.98.094403. URL: https://link.aps.org/doi/10.1103/PhysRevB.98.094403.

[95]   Anatoly Dymarsky and Kirill Pavlenko. "Tensor network to learn the wave function of data". In: *Phys. Rev. Res.* 4 (4 Nov. 2022), p. 043111. DOI: 10.1103/PhysRevResearch.4.043111. URL: https://link.aps.org/doi/10.1103/PhysRevResearch.4.043111.

[96]   Jacek Dziarmaga. "Dynamics of a Quantum Phase Transition: Exact Solution of the Quantum Ising Model". In: *Phys. Rev. Lett.* 95 (24 Dec. 2005), p. 245701. DOI: 10.1103/PhysRevLett.95.245701. URL: https://link.aps.org/doi/10.1103/PhysRevLett.95.245701.

[97]   Sepehr Ebadi et al. "Quantum phases of matter on a 256-atom programmable quantum simulator". In: *Nature* 595.7866 (2021), pp. 227–232. DOI: 10.1038/s41586-021-03582-4. URL: https://doi.org/10.1038/s41586-021-03582-4.

[98]   S F Edwards and P W Anderson. "Theory of spin glasses". In: *Journal of Physics F: Metal Physics* 5.5 (May 1975), pp. 965–974. DOI: 10.1088/0305-4608/5/5/017. URL: https://doi.org/10.1088/0305-4608/5/5/017.

[99]   Stavros Efthymiou, Jack Hidary, and Stefan Leichenauer. *TensorNetwork for Machine Learning*. 2019. DOI: 10.48550/ARXIV.1906.06329. URL: https://arxiv.org/abs/1906.06329.

[100]   Sebastian Eggert, Ian Affleck, and Minoru Takahashi. "Susceptibility of the spin 1/2 Heisenberg antiferromagnetic chain". In: *Phys. Rev. Lett.* 73 (2 July 1994), pp. 332–335. DOI: 10.1103/PhysRevLett.73.332. URL: https://link.aps.org/doi/10.1103/PhysRevLett.73.332.

[101]   Georg Ehlers et al. "The new cold neutron chopper spectrometer at the Spallation Neutron Source: Design and performance". In: *Review of Scientific Instruments* 82.8 (2011), p. 085108. DOI: https://doi.org/10.1063/1.3626935.

[102]   Sebastian Elsässer et al. "Power-law dependence of the optical conductivity observed in the quantum spin-liquid compound $\kappa-(BEDT-TTF)_2Cu_2(CN)_3$". In: *Phys. Rev. B* 86 (15 Oct. 2012), p. 155150. DOI: 10.1103/PhysRevB.86.155150. URL: https://link.aps.org/doi/10.1103/PhysRevB.86.155150.

[103]   Quentin Faure et al. "Topological quantum phase transition in the Ising-like antiferromagnetic spin chain $BaCo_2V_2O_8$". In: *Nature Physics* 14.7 (July 2018), pp. 716–722. ISSN: 1745-2481. DOI: 10.1038/s41567-018-0126-8. URL: https://doi.org/10.1038/s41567-018-0126-8.

[104]   Francesco Ferrari and Federico Becca. "Dynamical Structure Factor of the $J_1 - J_2$ Heisenberg Model on the Triangular Lattice: Magnons, Spinons, and Gauge Fields". In: *Phys. Rev. X* 9 (3 Aug. 2019), p. 031026. DOI: 10.1103/PhysRevX.9.031026. URL: https://link.aps.org/doi/10.1103/PhysRevX.9.031026.

[105]   Francesco Ferrari and Federico Becca. "Dynamical Structure Factor of the $J_1 - J_2$ Heisenberg Model on the Triangular Lattice: Magnons, Spinons, and Gauge Fields". In: *Phys. Rev. X* 9 (3 Aug. 2019), p. 031026. DOI: 10.1103/PhysRevX.9.031026. URL: https://link.aps.org/doi/10.1103/PhysRevX.9.031026.

[106] Francesco Ferrari and Federico Becca. "Spectral signatures of fractionalization in the frustrated Heisenberg model on the square lattice". In: *Phys. Rev. B* 98 (10 Sept. 2018), p. 100405. DOI: 10.1103/PhysRevB.98.100405. URL: https://link.aps.org/doi/10.1103/PhysRevB.98.100405.

[107] Adolf Fick. "Ueber Diffusion". In: *Annalen der Physik* 170.1 (1855), pp. 59–86. DOI: https://doi.org/10.1002/andp.18551700105. eprint: https://onlinelibrary.wiley.com/doi/pdf/10.1002/andp.18551700105. URL: https://onlinelibrary.wiley.com/doi/abs/10.1002/andp.18551700105.

[108] Matthew Fishman, Steven R. White, and E. Miles Stoudenmire. "The ITensor Software Library for Tensor Network Calculations". In: *SciPost Phys. Codebases* (2022), p. 4. DOI: 10.21468/SciPostPhysCodeb.4. URL: https://scipost.org/10.21468/SciPostPhysCodeb.4.

[109] Michael Foss-Feig et al. "Holographic quantum algorithms for simulating correlated spin systems". In: *Physical Review Research* 3.3 (2021), p. 033002.

[110] Philippe Francesco, Pierre Mathieu, and David Sénéchal. *Conformal field theory*. Springer Science & Business Media, 2012.

[111] Aaron J. Friedman, Sarang Gopalakrishnan, and Romain Vasseur. "Diffusive hydrodynamics from integrability breaking". In: *Phys. Rev. B* 101 (18 May 2020), 180302(R). DOI: 10.1103/PhysRevB.101.180302. URL: https://link.aps.org/doi/10.1103/PhysRevB.101.180302.

[112] Tetsuya Furukawa et al. "Quasi-continuous transition from a Fermi liquid to a spin liquid in $\kappa-(ET)_2Cu_2(CN)_3$". In: *Nature Communications* 9.1 (Jan. 2018), p. 307. ISSN: 2041-1723. DOI: 10.1038/s41467-017-02679-7. URL: https://doi.org/10.1038/s41467-017-02679-7.

[113] Juan José García-Ripoll. "Time evolution of Matrix Product States". In: *New Journal of Physics* 8.12 (Dec. 2006), pp. 305–305. DOI: 10.1088/1367-2630/8/12/305. URL: https://doi.org/10.1088%2F1367-2630%2F8%2F12%2F305.

[114] Elena Gati et al. "Insights from experiment and ab initio calculations into the glasslike transition in the molecular conductor $\kappa-(BEDT-TTF)_2Hg(SCN)_2Cl$". In: *Phys. Rev. B* 97 (7 Feb. 2018), p. 075115. DOI: 10.1103/PhysRevB.97.075115. URL: https://link.aps.org/doi/10.1103/PhysRevB.97.075115.

[115] Q. Q. Ge et al. "Angle-resolved photoemission study of the electronic structure of the quantum spin liquid $EtMe_3Sb[Pd(dmit)_2]_2$". In: *Phys. Rev. B* 89 (7 Feb. 2014), p. 075105. DOI: 10.1103/PhysRevB.89.075105. URL: https://link.aps.org/doi/10.1103/PhysRevB.89.075105.

[116] E. A. Ghioldi et al. "Dynamical structure factor of the triangular antiferromagnet: Schwinger boson theory beyond mean field". In: *Phys. Rev. B* 98 (18 Nov. 2018), p. 184403. DOI: 10.1103/PhysRevB.98.184403. URL: https://link.aps.org/doi/10.1103/PhysRevB.98.184403.

[117] E. A. Ghioldi et al. *Evidence of Two-Spinon Bound States in the Magnetic Spectrum of* $Ba_3CoSb_2O_9$. 2022. DOI: `10.48550/ARXIV.2201.13369`. URL: `https://arxiv.org/abs/2201.13369`.

[118] T. Giamarchi. "SOME EXPERIMENTAL TESTS OF TOMONAGA–LUTTINGER LIQ-UIDS". In: *Int. J. Mod. Phys. B* 26.22 (2012), p. 1244004. DOI: `10.1142/S02179792124 40043`. URL: `https://doi.org/10.1142/S0217979212440043`.

[119] Thierry Giamarchi. *Quantum physics in one dimension*. Vol. 121. Clarendon press, Oxford, 2003.

[120] Thierry Giamarchi. *Quantum physics in one dimension*. Oxford: Clarendon press, 2004.

[121] Thierry Giamarchi, Christian Rüegg, and Oleg Tchernyshyov. "Bose–Einstein condensation in magnetic insulators". In: *Nature Physics* 4.3 (Mar. 2008), pp. 198–204. ISSN: 1745-2481. DOI: `10.1038/nphys893`. URL: `https://doi.org/10.1038/nphys893`.

[122] Jan de Gier et al. "Kardar-Parisi-Zhang universality of the Nagel-Schreckenberg model". In: *Phys. Rev. E* 100 (5 Nov. 2019), p. 052111. DOI: `10.1103/PhysRevE.100.052111`. URL: `https://link.aps.org/doi/10.1103/PhysRevE.100.052111`.

[123] Shou-Shu Gong et al. "Chiral spin liquid with spinon Fermi surfaces in the spin-$\frac{1}{2}$ triangular Heisenberg model". In: *Phys. Rev. B* 100 (24 Dec. 2019), p. 241111. DOI: `10.1103/PhysRevB.100.241111`. URL: `https://link.aps.org/doi/10.1103/PhysRevB.100.241111`.

[124] Shou-Shu Gong et al. "Global phase diagram and quantum spin liquids in a spin-$\frac{1}{2}$ triangular antiferromagnet". In: *Phys. Rev. B* 96 (7 Aug. 2017), p. 075116. DOI: `10.1103/PhysRevB.96.075116`. URL: `https://link.aps.org/doi/10.1103/PhysRevB.96.075116`.

[125] Shurong Gong et al. "Finite-time scaling via linear driving". In: *New Journal of Physics* 12.4 (Apr. 2010), p. 043036. DOI: `10.1088/1367-2630/12/4/043036`. URL: `https://dx.doi.org/10.1088/1367-2630/12/4/043036`.

[126] Erode Gopal. *Specific heats at low temperatures*. Springer Science & Business Media, 2012.

[127] Sarang Gopalakrishnan and Romain Vasseur. "Kinetic Theory of Spin Diffusion and Superdiffusion in XXZ Spin Chains". In: *Phys. Rev. Lett.* 122 (12 Mar. 2019), p. 127202. DOI: `10.1103/PhysRevLett.122.127202`. URL: `https://link.aps.org/doi/10.1103/PhysRevLett.122.127202`.

[128] Sarang Gopalakrishnan, Romain Vasseur, and Brayden Ware. "Anomalous relaxation and the high-temperature structure factor of XXZ spin chains". In: *Proc. Natl. Acad. Sci.* 116.33 (2019), pp. 16250–16255. ISSN: 0027-8424. DOI: `10.1073/pnas.1906914116`. URL: `https://www.pnas.org/content/116/33/16250`.

[129] Sarang Gopalakrishnan et al. "Hydrodynamics of operator spreading and quasiparticle diffusion in interacting integrable systems". In: *Phys. Rev. B* 98 (22 Dec. 2018), 220303(R). DOI: 10.1103/PhysRevB.98.220303. URL: https://link.aps.org/doi/10.1103/PhysRevB.98.220303.

[130] G. E. Granroth, D. H. Vandergriff, and S. E. Nagler. "SEQUOIA: A fine resolution chopper spectrometer at the SNS". In: *Physica B-Condensed Matter* 385-86 (NOV 15 2006), 1104–1106. DOI: {10.1016/j.physb.2006.05.379}. URL: https://doi.org/10.1016/j.physb.2006.05.379.

[131] GE Granroth et al. "SEQUOIA: a newly operating chopper spectrometer at the SNS". In: *Journal of Physics: Conference Series*. Vol. 251. 1. IOP Publishing. 2010, p. 012058. DOI: 10.1088/1742-6596/251/1/012058. URL: https://iopscience.iop.org/article/10.1088/1742-6596/251/1/012058.

[132] J. E. Gubernatis et al. "Quantum Monte Carlo simulations and maximum entropy: Dynamics from imaginary-time data". In: *Phys. Rev. B* 44 (12 Sept. 1991), pp. 6011–6029. DOI: 10.1103/PhysRevB.44.6011. URL: https://link.aps.org/doi/10.1103/PhysRevB.44.6011.

[133] Jie Guo et al. "Magnetic-field and composition tuned antiferromagnetic instability in the quantum spin-liquid candidate $NaYbO_2$". In: *Phys. Rev. Materials* 4 (6 June 2020), p. 064410. DOI: 10.1103/PhysRevMaterials.4.064410. URL: https://link.aps.org/doi/10.1103/PhysRevMaterials.4.064410.

[134] Jie Guo et al. "Magnetic-field and composition tuned antiferromagnetic instability in the quantum spin-liquid candidate $NaYbO_2$". In: *Phys. Rev. Mater.* 4 (6 June 2020), p. 064410. DOI: 10.1103/PhysRevMaterials.4.064410. URL: https://link.aps.org/doi/10.1103/PhysRevMaterials.4.064410.

[135] Jutho Haegeman, Tobias J. Osborne, and Frank Verstraete. "Post-matrix product state methods: To tangent space and beyond". In: *Phys. Rev. B* 88 (7 Aug. 2013), p. 075133. DOI: 10.1103/PhysRevB.88.075133. URL: https://link.aps.org/doi/10.1103/PhysRevB.88.075133.

[136] Jutho Haegeman et al. "Elementary Excitations in Gapped Quantum Spin Systems". In: *Phys. Rev. Lett.* 111 (8 Aug. 2013), p. 080401. DOI: 10.1103/PhysRevLett.111.080401. URL: https://link.aps.org/doi/10.1103/PhysRevLett.111.080401.

[137] Jutho Haegeman et al. "Time-Dependent Variational Principle for Quantum Lattices". In: *Phys. Rev. Lett.* 107 (7 Aug. 2011), p. 070601. DOI: 10.1103/PhysRevLett.107.070601. URL: https://link.aps.org/doi/10.1103/PhysRevLett.107.070601.

[138] Jutho Haegeman et al. "Unifying time evolution and optimization with matrix product states". In: *Phys. Rev. B* 94 (16 Oct. 2016), p. 165116. DOI: 10.1103/PhysRevB.94.165116. URL: https://link.aps.org/doi/10.1103/PhysRevB.94.165116.

[139] Jutho Haegeman et al. "Variational matrix product ansatz for dispersion relations". In: *Phys. Rev. B* 85 (10 Mar. 2012), p. 100408. DOI: 10.1103/PhysRevB.85.100408. URL: https://link.aps.org/doi/10.1103/PhysRevB.85.100408.

[140] Reza Haghshenas et al. "Variational Power of Quantum Circuit Tensor Networks". In: *Phys. Rev. X* 12 (1 Mar. 2022), p. 011047. DOI: 10.1103/PhysRevX.12.011047. URL: https://link.aps.org/doi/10.1103/PhysRevX.12.011047.

[141] F D M Haldane. "'Luttinger liquid theory' of one-dimensional quantum fluids. I. Properties of the Luttinger model and their extension to the general 1D interacting spinless Fermi gas". In: *Journal of Physics C: Solid State Physics* 14.19 (July 1981), p. 2585. DOI: 10.1088/0022-3719/14/19/010. URL: https://dx.doi.org/10.1088/0022-3719/14/19/010.

[142] F. D. M. Haldane. "Nonlinear Field Theory of Large-Spin Heisenberg Antiferromagnets: Semiclassically Quantized Solitons of the One-Dimensional Easy-Axis Néel State". In: *Phys. Rev. Lett.* 50 (15 Apr. 1983), pp. 1153–1156. DOI: 10.1103/PhysRevLett.50.1153. URL: https://link.aps.org/doi/10.1103/PhysRevLett.50.1153.

[143] F. D. M. Haldane. "Nonlinear Field Theory of Large-Spin Heisenberg Antiferromagnets: Semiclassically Quantized Solitons of the One-Dimensional Easy-Axis Néel State". In: *Phys. Rev. Lett.* 50 (15 Apr. 1983), pp. 1153–1156. DOI: 10.1103/PhysRevLett.50.1153. URL: https://link.aps.org/doi/10.1103/PhysRevLett.50.1153.

[144] Tian-Heng Han et al. "Fractionalized excitations in the spin-liquid state of a kagome-lattice antiferromagnet". In: *Nature* 492.7429 (Dec. 2012), pp. 406–410. ISSN: 1476-4687. DOI: 10.1038/nature11659. URL: https://doi.org/10.1038/nature11659.

[145] Zhao-Yu Han et al. "Unsupervised Generative Modeling Using Matrix Product States". In: *Phys. Rev. X* 8 (3 July 2018), p. 031012. DOI: 10.1103/PhysRevX.8.031012. URL: https://link.aps.org/doi/10.1103/PhysRevX.8.031012.

[146] Steffi Hartmann et al. "Thermal Expansion Studies on the Spin-Liquid-Candidate System $\kappa-(\text{BEDT-TTF})_2\text{Ag}_2(\text{CN})_3$". In: *physica status solidi (b)* 256.9 (2019), p. 1800640. DOI: https://doi.org/10.1002/pssb.201800640. URL: https://onlinelibrary.wiley.com/doi/abs/10.1002/pssb.201800640.

[147] M B Hastings. "An area law for one-dimensional quantum systems". In: *Journal of Statistical Mechanics: Theory and Experiment* 2007.08 (Aug. 2007), P08024–P08024. DOI: 10.1088/1742-5468/2007/08/p08024. URL: https://doi.org/10.1088/1742-5468/2007/08/p08024.

[148] Naomichi Hatano and Masuo Suzuki. "Finding Exponential Product Formulas of Higher Orders". In: *Quantum Annealing and Other Optimization Methods*. Ed. by Arnab Das and Bikas K. Chakrabarti. Berlin, Heidelberg: Springer Berlin Heidelberg, 2005, pp. 37–68. ISBN: 978-3-540-31515-5. DOI: 10.1007/11526216_2. URL: https://doi.org/10.1007/11526216_2.

[149] Philipp Hauke et al. "Measuring multipartite entanglement through dynamic susceptibilities". In: *Nature Physics* 12.8 (Aug. 2016), pp. 778–782. ISSN: 1745-2481. DOI: 10.1038/nphys3700. URL: https://doi.org/10.1038/nphys3700.

[150] Michael Hermele, T. Senthil, and Matthew P. A. Fisher. "Algebraic spin liquid as the mother of many competing orders". In: *Phys. Rev. B* 72 (10 Sept. 2005), p. 104404. DOI: 10.1103/PhysRevB.72.104404. URL: https://link.aps.org/doi/10.1103/PhysRevB.72.104404.

[151] Michael Hermele et al. "Properties of an algebraic spin liquid on the kagome lattice". In: *Phys. Rev. B* 77 (22 June 2008), p. 224413. DOI: 10.1103/PhysRevB.77.224413. URL: https://link.aps.org/doi/10.1103/PhysRevB.77.224413.

[152] Kinshiro Hirakawa and Yukihisa Kurogi. "One-Dimensional Antiferromagnetic Properties of KCuF3". In: *Progress of Theoretical Physics Supplement* 46 (June 1970), pp. 147–161. ISSN: 0375-9687. DOI: 10.1143/PTPS.46.147. eprint: https://academic.oup.com/ptps/article-pdf/doi/10.1143/PTPS.46.147/5301207/46-147.pdf. URL: https://doi.org/10.1143/PTPS.46.147.

[153] Wen Wei Ho and Dmitry A. Abanin. "Entanglement dynamics in quantum many-body systems". In: *Phys. Rev. B* 95 (9 Mar. 2017), p. 094302. DOI: 10.1103/PhysRevB.95.094302. URL: https://link.aps.org/doi/10.1103/PhysRevB.95.094302.

[154] Kristóf Hódsági and Marton Kormos. "Kibble–Zurek mechanism in the Ising Field Theory". In: *SciPost Phys.* 9 (2020), p. 055. DOI: 10.21468/SciPostPhys.9.4.055. URL: https://scipost.org/10.21468/SciPostPhys.9.4.055.

[155] P. C. Hohenberg. "Existence of Long-Range Order in One and Two Dimensions". In: *Phys. Rev.* 158 (2 June 1967), pp. 383–386. DOI: 10.1103/PhysRev.158.383. URL: https://link.aps.org/doi/10.1103/PhysRev.158.383.

[156] Dietmar Hohlwein, Jens-Uwe Hoffmann, and Rainer Schneider. "Magnetic interaction parameters from paramagnetic diffuse neutron scattering in MnO". In: *Phys. Rev. B* 68 (14 Oct. 2003), p. 140408. DOI: 10.1103/PhysRevB.68.140408. URL: https://link.aps.org/doi/10.1103/PhysRevB.68.140408.

[157] Andreas Holzner et al. "Chebyshev matrix product state approach for spectral functions". In: *Phys. Rev. B* 83 (19 May 2011), p. 195115. DOI: 10.1103/PhysRevB.83.195115. URL: https://link.aps.org/doi/10.1103/PhysRevB.83.195115.

[158] Mladen Horvatić and Claude Berthier. "NMR Studies of Low-Dimensional Quantum Antiferromagnets". In: *High Magnetic Fields*. Ed. by C. Berthier, L. P. Lévy, and G. Martinez. Lecture Notes in Physics 595. Springer Berlin Heidelberg, 2002, pp. 191–210. URL: http://link.springer.com/chapter/10.1007/3-540-45649-X_7 (visited on 06/27/2016).

[159] Mladen Horvatić, Martin Klanjšek, and Edmond Orignac. "Direct determination of the Tomonaga-Luttinger parameter K in quasi-one-dimensional spin systems". In: *Phys. Rev. B* 101 (22 June 2020), 220406(R). DOI: 10.1103/PhysRevB.101.220406. URL: https://link.aps.org/doi/10.1103/PhysRevB.101.220406.

[160] Shijie Hu et al. "Dirac Spin Liquid on the Spin-1/2 Triangular Heisenberg Antiferromagnet". In: *Phys. Rev. Lett.* 123 (20 Nov. 2019), p. 207203. DOI: 10.1103/PhysRevLett.123.207203. URL: https://link.aps.org/doi/10.1103/PhysRevLett.123.207203.

[161] Shijie Hu et al. "Dirac Spin Liquid on the Spin-1/2 Triangular Heisenberg Antiferromagnet". In: *Phys. Rev. Lett.* 123 (20 Nov. 2019), p. 207203. DOI: 10.1103/PhysRevLett.123.207203. URL: https://link.aps.org/doi/10.1103/PhysRevLett.123.207203.

[162] Shijie Hu et al. "Dirac Spin Liquid on the Spin-1/2 Triangular Heisenberg Antiferromagnet". In: *Phys. Rev. Lett.* 123 (20 Nov. 2019), p. 207203. DOI: 10.1103/PhysRevLett.123.207203. URL: https://link.aps.org/doi/10.1103/PhysRevLett.123.207203.

[163] Wen-Jun Hu et al. "Competing spin-liquid states in the spin-$\frac{1}{2}$ Heisenberg model on the triangular lattice". In: *Phys. Rev. B* 92 (14 Oct. 2015), p. 140403. DOI: 10.1103/PhysRevB.92.140403. URL: https://link.aps.org/doi/10.1103/PhysRevB.92.140403.

[164] Jun-Han Huang, Guang-Ming Zhang, and Dao-Xin Yao. "Dynamical spin excitations of the topological Haldane gapped phase in the $S = 1$ Heisenberg antiferromagnetic chain with single-ion anisotropy". In: *Phys. Rev. B* 103 (2 Jan. 2021), p. 024403. DOI: 10.1103/PhysRevB.103.024403. URL: https://link.aps.org/doi/10.1103/PhysRevB.103.024403.

[165] Yingyi Huang et al. "Kibble-Zurek mechanism and finite-time scaling". In: *Phys. Rev. B* 90 (13 Oct. 2014), p. 134108. DOI: 10.1103/PhysRevB.90.134108. URL: https://link.aps.org/doi/10.1103/PhysRevB.90.134108.

[166] T Huberman et al. "A study of the quantum classical crossover in the spin dynamics of the 2DS= 5/2 antiferromagnet Rb2MnF4: neutron scattering, computer simulations and analytic theories". In: *Journal of Statistical Mechanics: Theory and Experiment* 2008.05 (May 2008), P05017. DOI: 10.1088/1742-5468/2008/05/p05017. URL: https://doi.org/10.1088/1742-5468/2008/05/p05017.

[167] David A. Huse and Veit Elser. "Simple Variational Wave Functions for Two-Dimensional Heisenberg Spin-½ Antiferromagnets". In: *Phys. Rev. Lett.* 60 (24 June 1988), pp. 2531–2534. DOI: 10.1103/PhysRevLett.60.2531. URL: https://link.aps.org/doi/10.1103/PhysRevLett.60.2531.

[168] M.T. Hutchings. "Point-Charge Calculations of Energy Levels of Magnetic Ions in Crystalline Electric Fields". In: Solid State Physics 16 (1964). Ed. by Frederick Seitz and David Turnbull, pp. 227–273. ISSN: 0081-1947. DOI: https://doi.org/10.1016/S0081-1947(08)60517-2. URL: http://www.sciencedirect.com/science/article/pii/S0081194708605172.

[169] Philipp Hyllus et al. "Fisher information and multiparticle entanglement". In: *Phys. Rev. A* 85 (2 Feb. 2012), p. 022321. DOI: 10.1103/PhysRevA.85.022321. URL: https://link.aps.org/doi/10.1103/PhysRevA.85.022321.

[170] Jun-ichi Igarashi and Tatsuya Nagao. "$1/S$-expansion study of spin waves in a two-dimensional Heisenberg antiferromagnet". In: *Phys. Rev. B* 72 (1 July 2005), p. 014403. DOI: 10.1103/PhysRevB.72.014403. URL: https://link.aps.org/doi/10.1103/PhysRevB.72.014403.

[171] E. Ilievski et al. "Complete Generalized Gibbs Ensembles in an Interacting Theory". In: *Phys. Rev. Lett.* 115 (15 Oct. 2015), p. 157201. DOI: 10.1103/PhysRevLett.115.157201. URL: https://link.aps.org/doi/10.1103/PhysRevLett.115.157201.

[172] Enej Ilievski et al. "Superdiffusion in One-Dimensional Quantum Lattice Models". In: *Phys. Rev. Lett.* 121 (23 Dec. 2018), p. 230602. DOI: 10.1103/PhysRevLett.121.230602. URL: https://link.aps.org/doi/10.1103/PhysRevLett.121.230602.

[173] Enej Ilievski et al. "Superuniversality of Superdiffusion". In: *Phys. Rev. X* 11 (3 July 2021), p. 031023. DOI: 10.1103/PhysRevX.11.031023. URL: https://link.aps.org/doi/10.1103/PhysRevX.11.031023.

[174] Yasir Iqbal et al. "Spin liquid nature in the Heisenberg $J_1 - J_2$ triangular antiferromagnet". In: *Phys. Rev. B* 93 (14 Apr. 2016), p. 144411. DOI: 10.1103/PhysRevB.93.144411. URL: https://link.aps.org/doi/10.1103/PhysRevB.93.144411.

[175] Yasir Iqbal et al. "Spin liquid nature in the Heisenberg $J_1 - J_2$ triangular antiferromagnet". In: *Phys. Rev. B* 93 (14 Apr. 2016), p. 144411. DOI: 10.1103/PhysRevB.93.144411. URL: https://link.aps.org/doi/10.1103/PhysRevB.93.144411.

[176] Saya Ito et al. "Structure of the magnetic excitations in the spin-1/2 triangular-lattice Heisenberg antiferromagnet $Ba_3CoSb_2O_9$". In: *Nature Communications* 8.1 (Aug. 2017), p. 235. ISSN: 2041-1723. DOI: 10.1038/s41467-017-00316-x. URL: https://doi.org/10.1038/s41467-017-00316-x.

[177] K. Itoh et al. "Narrowing of phonon spectrum induced by ultrafast charge fluctuations in an organic dimer Mott insulator". In: *Phys. Rev. B* 88 (12 Sept. 2013), p. 125101. DOI: 10.1103/PhysRevB.88.125101. URL: https://link.aps.org/doi/10.1103/PhysRevB.88.125101.

[178] T Itou et al. "^{13}C NMR study of the spin-liquid state in the triangular quantum antiferromagnet $EtMe_3Sb[Pd(dmit)_2]_2$". In: *Journal of Physics: Conference Series* 145 (Jan. 2009), p. 012039. DOI: 10.1088/1742-6596/145/1/012039. URL: https://doi.org/10.1088/1742-6596/145/1/012039.

[179] T. Itou et al. "Quantum spin liquid in the spin-1/2 triangular antiferromagnet $EtMe_3Sb[Pd(dmit)_2]_2$". In: *Phys. Rev. B* 77 (10 Mar. 2008), p. 104413. DOI: 10.1103/PhysRevB.77.104413. URL: https://link.aps.org/doi/10.1103/PhysRevB.77.104413.

[180] F. James and M. Roos. "Minuit - a system for function minimization and analysis of the parameter errors and correlations". In: *Comp. Phys. Commun.* 10.6 (1975), pp. 343–367. ISSN: 0010-4655. DOI: https://doi.org/10.1016/0010-4655(75)90039-9. URL: http://www.sciencedirect.com/science/article/pii/0010465575900399.

[181] Mark Jarrell and J.E. Gubernatis. "Bayesian inference and the analytic continuation of imaginary-time quantum Monte Carlo data". In: *Physics Reports* 269.3 (1996), pp. 133–195. ISSN: 0370-1573. DOI: https://doi.org/10.1016/0370-1573(95)00074-7. URL: https://www.sciencedirect.com/science/article/pii/0370157395000747.

[182] M. Jeong et al. "Attractive Tomonaga-Luttinger Liquid in a Quantum Spin Ladder". In: *Phys. Rev. Lett.* 111 (10 Sept. 2013), p. 106404. DOI: 10.1103/PhysRevLett.111.106404. URL: https://link.aps.org/doi/10.1103/PhysRevLett.111.106404.

[183] M. Jeong et al. "Dichotomy between Attractive and Repulsive Tomonaga-Luttinger Liquids in Spin Ladders". In: *Phys. Rev. Lett.* 117 (10 Sept. 2016), p. 106402. DOI: 10.1103/PhysRevLett.117.106402. URL: https://link.aps.org/doi/10.1103/PhysRevLett.117.106402.

[184] Paul Niklas Jepsen et al. "Spin transport in a tunable Heisenberg model realized with ultracold atoms". In: *Nature* 588.7838 (2020), pp. 403–407. DOI: 10.1038/s41586-020-3033-y. URL: https://doi.org/10.1038/s41586-020-3033-y.

[185] Ya-Ting Jia et al. "Mott Transition and Superconductivity in Quantum Spin Liquid Candidate NaYbSe2". In: *Chinese Physics Letters* 37.9 (Sept. 2020), p. 097404. DOI: 10.1088/0256-307x/37/9/097404. URL: https://doi.org/10.1088/0256-307x/37/9/097404.

[186] Yi-Fan Jiang and Hong-Chen Jiang. *Nature of quantum spin liquids of the S=1/2 Heisenberg antiferromagnet on the triangular lattice: A parallel DMRG study*. 2022. DOI: 10.48550/ARXIV.2203.10216. URL: https://arxiv.org/abs/2203.10216.

[187] Hong-Chen Jiang. "Superconductivity in the doped quantum spin liquid on the triangular lattice". In: *npj Quantum Materials* 6.1 (Aug. 2021), p. 71. ISSN: 2397-4648. DOI: 10.1038/s41535-021-00375-w. URL: https://doi.org/10.1038/s41535-021-00375-w.

[188] Th. Jolicoeur and J. C. Le Guillou. "Spin-wave results for the triangular Heisenberg antiferromagnet". In: *Phys. Rev. B* 40 (4 Aug. 1989), pp. 2727–2729. DOI: 10.1103/PhysRevB.40.2727. URL: https://link.aps.org/doi/10.1103/PhysRevB.40.2727.

[189] Y. Kamiya et al. "The nature of spin excitations in the one-third magnetization plateau phase of $Ba_3CoSb_2O_9$". In: *Nature Communications* 9.1 (July 2018), p. 2666. ISSN: 2041-1723. DOI: 10.1038/s41467-018-04914-1. URL: https://doi.org/10.1038/s41467-018-04914-1.

[190] Mehran Kardar, Giorgio Parisi, and Yi-Cheng Zhang. "Dynamic Scaling of Growing Interfaces". In: *Phys. Rev. Lett.* 56 (9 Mar. 1986), pp. 889–892. DOI: 10.1103/PhysRevLett.56.889. URL: https://link.aps.org/doi/10.1103/PhysRevLett.56.889.

[191] C. Karrasch, J. H. Bardarson, and J. E. Moore. "Finite-Temperature Dynamical Density Matrix Renormalization Group and the Drude Weight of Spin-1/2 Chains". In: *Phys. Rev. Lett.* 108 (22 May 2012), p. 227206. DOI: 10.1103/PhysRevLett.108.227206. URL: https://link.aps.org/doi/10.1103/PhysRevLett.108.227206.

[192] C. Karrasch et al. "Drude weight of the spin-$\frac{1}{2}$ XXZ chain: Density matrix renormalization group versus exact diagonalization". In: *Phys. Rev. B* 87 (24 June 2013), p. 245128. DOI: 10.1103/PhysRevB.87.245128. URL: https://link.aps.org/doi/10.1103/PhysRevB.87.245128.

[193] Reizo Kato et al. "A Discrepancy in Thermal Conductivity Measurement Data of Quantum Spin Liquid β'-EtMe$_3$Sb[Pd(dmit)$_2$]$_2$ (dmit = 1,3-Dithiol-2-thione-4,5-dithiolate)". In: *Crystals* 12.1 (2022). ISSN: 2073-4352. DOI: 10.3390/cryst12010102. URL: https://www.mdpi.com/2073-4352/12/1/102.

[194] T W B Kibble. "Topology of cosmic domains and strings". In: *Journal of Physics A: Mathematical and General* 9.8 (Aug. 1976), pp. 1387–1398. DOI: 10.1088/0305-4470/9/8/029. URL: https://doi.org/10.1088/0305-4470/9/8/029.

[195] T.W.B. Kibble. "Some implications of a cosmological phase transition". In: *Physics Reports* 67.1 (1980), pp. 183–199. ISSN: 0370-1573. DOI: https://doi.org/10.1016/0370-1573(80)90091-5. URL: https://www.sciencedirect.com/science/article/pii/0370157380900915.

[196] Hyungwon Kim and David A. Huse. "Ballistic Spreading of Entanglement in a Diffusive Nonintegrable System". In: *Phys. Rev. Lett.* 111 (12 Sept. 2013), p. 127205. DOI: 10.1103/PhysRevLett.111.127205. URL: https://link.aps.org/doi/10.1103/PhysRevLett.111.127205.

[197] Itamar Kimchi, Adam Nahum, and T. Senthil. "Valence Bonds in Random Quantum Magnets: Theory and Application to YbMgGaO$_4$". In: *Phys. Rev. X* 8 (3 July 2018), p. 031028. DOI: 10.1103/PhysRevX.8.031028. URL: https://link.aps.org/doi/10.1103/PhysRevX.8.031028.

[198] A.Yu. Kitaev. "Fault-tolerant quantum computation by anyons". In: *Annals of Physics* 303.1 (2003), pp. 2–30. ISSN: 0003-4916. DOI: https://doi.org/10.1016/S0003-4916(02)00018-0. URL: https://www.sciencedirect.com/science/article/pii/S0003491602000180.

[199] M. Klanjšek et al. "Controlling Luttinger Liquid Physics in Spin Ladders under a Magnetic Field". In: *Phys. Rev. Lett.* 101 (13 Sept. 2008), p. 137207. DOI: 10.1103/PhysRevLett.101.137207. URL: https://link.aps.org/doi/10.1103/PhysRevLett.101.137207.

[200] J. Knolle and R. Moessner. "A Field Guide to Spin Liquids". In: *Annu. Rev. Condens. Matter Phys.* 10.1 (2019), pp. 451–472. DOI: 10.1146/annurev-conmatphys-031218-013401. URL: https://doi.org/10.1146/annurev-conmatphys-031218-013401.

[201] T. Kobayashi et al. "Charge disproportionation in the spin-liquid candidate $\kappa - (ET)_2Cu_2(CN)_3$ at 6 K revealed by ^{63}Cu NQR measurements". In: *Phys. Rev. Research* 2 (4 Oct. 2020), p. 042023. DOI: 10.1103/PhysRevResearch.2.042023. URL: https://link.aps.org/doi/10.1103/PhysRevResearch.2.042023.

[202] G. Koutroulakis et al. "Quantum phase diagram of the $S = \frac{1}{2}$ triangular-lattice antiferromagnet $Ba_3CoSb_2O_9$". In: *Phys. Rev. B* 91 (2 Jan. 2015), p. 024410. DOI: 10.1103/PhysRevB.91.024410. URL: https://link.aps.org/doi/10.1103/PhysRevB.91.024410.

[203] Manas Kulkarni, David A. Huse, and Herbert Spohn. "Fluctuating hydrodynamics for a discrete Gross-Pitaevskii equation: Mapping onto the Kardar-Parisi-Zhang universality class". In: *Phys. Rev. A* 92 (4 Oct. 2015), p. 043612. DOI: 10.1103/PhysRevA.92.043612. URL: https://link.aps.org/doi/10.1103/PhysRevA.92.043612.

[204] B. Lake et al. "Multispinon Continua at Zero and Finite Temperature in a Near-Ideal Heisenberg Chain". In: *Phys. Rev. Lett.* 111 (13 Sept. 2013), p. 137205. DOI: 10.1103/PhysRevLett.111.137205. URL: https://link.aps.org/doi/10.1103/PhysRevLett.111.137205.

[205] Bella Lake et al. "Quantum criticality and universal scaling of a quantum antiferromagnet". In: *Nat. Mater.* 4.4 (2005), pp. 329–334. ISSN: 1476-4660. DOI: 10.1038/nmat1327. URL: https://doi.org/10.1038/nmat1327.

[206] Cornelius Lanczos. "An iteration method for the solution of the eigenvalue problem of linear differential and integral operators". In: (1950).

[207] L. D. Landau and E. M. Lifshitz. *Fluid Mechanics*. 2nd ed. Oxford: Butterworth-Heinemann, 1987.

[208] T. Le et al. "Disorder and slowing magnetic dynamics in $\kappa-(BEDT-TTF)_2Hg(SCN)_2Br$". In: *Phys. Rev. B* 102 (18 Nov. 2020), p. 184417. DOI: 10.1103/PhysRevB.102.184417. URL: https://link.aps.org/doi/10.1103/PhysRevB.102.184417.

[209] Yoav Levine et al. *Deep Learning and Quantum Entanglement: Fundamental Connections with Implications to Network Design*. 2017. DOI: 10.48550/ARXIV.1704.01552. URL: https://arxiv.org/abs/1704.01552.

[210] Yoav Levine et al. "Quantum Entanglement in Deep Learning Architectures". In: *Phys. Rev. Lett.* 122 (6 Feb. 2019), p. 065301. DOI: 10.1103/PhysRevLett.122.065301. URL: https://link.aps.org/doi/10.1103/PhysRevLett.122.065301.

[211] M. Li et al. "Magnetoelastic coupling and the magnetization plateau in $Ba_3CoSb_2O_9$". In: *Phys. Rev. B* 99 (9 Mar. 2019), p. 094408. DOI: 10.1103/PhysRevB.99.094408. URL: https://link.aps.org/doi/10.1103/PhysRevB.99.094408.

[212] Yao-Dong Li and Gang Chen. "Detecting spin fractionalization in a spinon Fermi surface spin liquid". In: *Phys. Rev. B* 96 (7 Aug. 2017), p. 075105. DOI: 10.1103/PhysRevB.96.075105. URL: https://link.aps.org/doi/10.1103/PhysRevB.96.075105.

[213] Yao-Dong Li and Gang Chen. "Detecting spin fractionalization in a spinon Fermi surface spin liquid". In: *Phys. Rev. B* 96 (7 Aug. 2017), p. 075105. DOI: 10.1103/PhysRevB.96.075105. URL: https://link.aps.org/doi/10.1103/PhysRevB.96.075105.

[214] Yao-Dong Li, Yuan-Ming Lu, and Gang Chen. "Spinon Fermi surface $U(1)$ spin liquid in the spin-orbit-coupled triangular-lattice Mott insulator YbMgGaO$_4$". In: *Phys. Rev. B* 96 (5 Aug. 2017), p. 054445. DOI: 10.1103/PhysRevB.96.054445. URL: https://link.aps.org/doi/10.1103/PhysRevB.96.054445.

[215] Yuesheng Li et al. "Crystalline Electric-Field Randomness in the Triangular Lattice Spin-Liquid YbMgGaO$_4$". In: *Phys. Rev. Lett.* 118 (10 Mar. 2017), p. 107202. DOI: 10.1103/PhysRevLett.118.107202. URL: https://link.aps.org/doi/10.1103/PhysRevLett.118.107202.

[216] Yuesheng Li et al. "Crystalline Electric-Field Randomness in the Triangular Lattice Spin-Liquid YbMgGaO$_4$". In: *Phys. Rev. Lett.* 118 (10 Mar. 2017), p. 107202. DOI: 10.1103/PhysRevLett.118.107202. URL: https://link.aps.org/doi/10.1103/PhysRevLett.118.107202.

[217] Yuesheng Li et al. "Gapless quantum spin liquid ground state in the two-dimensional spin-1/2 triangular antiferromagnet YbMgGaO$_4$". In: *Scientific Reports* 5.1 (Nov. 2015), p. 16419. ISSN: 2045-2322. DOI: 10.1038/srep16419. URL: https://doi.org/10.1038/srep16419.

[218] Yuesheng Li et al. "Gapless quantum spin liquid ground state in the two-dimensional spin-1/2 triangular antiferromagnet YbMgGaO4". In: *Scientific reports* 5.1 (2015), p. 16419. DOI: https://doi.org/10.1038/srep16419.

[219] Yuesheng Li et al. "Muon Spin Relaxation Evidence for the U(1) Quantum Spin-Liquid Ground State in the Triangular Antiferromagnet YbMgGaO$_4$". In: *Phys. Rev. Lett.* 117 (9 Aug. 2016), p. 097201. DOI: 10.1103/PhysRevLett.117.097201. URL: https://link.aps.org/doi/10.1103/PhysRevLett.117.097201.

[220] Yuesheng Li et al. "Muon Spin Relaxation Evidence for the U(1) Quantum Spin-Liquid Ground State in the Triangular Antiferromagnet YbMgGaO$_4$". In: *Phys. Rev. Lett.* 117 (9 Aug. 2016), p. 097201. DOI: 10.1103/PhysRevLett.117.097201. URL: https://link.aps.org/doi/10.1103/PhysRevLett.117.097201.

[221] Yuesheng Li et al. "Nearest-neighbour resonating valence bonds in YbMgGaO$_4$". In: *Nature Communications* 8.1 (June 2017), p. 15814. ISSN: 2041-1723. DOI: 10.1038/ncomms15814. URL: https://doi.org/10.1038/ncomms15814.

[222] Yuesheng Li et al. "Rare-Earth Triangular Lattice Spin Liquid: A Single-Crystal Study of YbMgGaO$_4$". In: *Phys. Rev. Lett.* 115 (16 Oct. 2015), p. 167203. DOI: 10.1103/PhysRevLett.115.167203. URL: https://link.aps.org/doi/10.1103/PhysRevLett.115.167203.

[223] Yuesheng Li et al. "Rare-Earth Triangular Lattice Spin Liquid: A Single-Crystal Study of YbMgGaO$_4$". In: *Phys. Rev. Lett.* 115 (16 Oct. 2015), p. 167203. DOI: 10.1103/PhysRevLett.115.167203. URL: https://link.aps.org/doi/10.1103/PhysRevLett.115.167203.

[224] Yuesheng Li et al. "Rearrangement of Uncorrelated Valence Bonds Evidenced by Low-Energy Spin Excitations in YbMgGaO$_4$". In: *Phys. Rev. Lett.* 122 (13 Apr. 2019), p. 137201. DOI: 10.1103/PhysRevLett.122.137201. URL: https://link.aps.org/doi/10.1103/PhysRevLett.122.137201.

[225] Elliott H. Lieb. "Exact Analysis of an Interacting Bose Gas. II. The Excitation Spectrum". In: *Phys. Rev.* 130 (4 May 1963), pp. 1616–1624. DOI: 10.1103/PhysRev.130.1616. URL: https://link.aps.org/doi/10.1103/PhysRev.130.1616.

[226] Elliott H. Lieb and Werner Liniger. "Exact Analysis of an Interacting Bose Gas. I. The General Solution and the Ground State". In: *Phys. Rev.* 130 (4 May 1963), pp. 1605–1616. DOI: 10.1103/PhysRev.130.1605. URL: https://link.aps.org/doi/10.1103/PhysRev.130.1605.

[227] Jiao YY Lin et al. "MCViNE–An object oriented Monte Carlo neutron ray tracing simulation package". In: *Nuclear Instruments and Methods in Physics Research Section A: Accelerators, Spectrometers, Detectors and Associated Equipment* 810 (2016), pp. 86–99. DOI: 10.1016/j.nima.2015.11.118. URL: https://doi.org/10.1016/j.nima.2015.11.118.

[228] Ding Liu et al. "Machine learning by unitary tensor network of hierarchical tree structure". In: *New Journal of Physics* 21.7 (July 2019), p. 073059. DOI: 10.1088/1367-2630/ab31ef. URL: https://dx.doi.org/10.1088/1367-2630/ab31ef.

[229] Marko Ljubotina, Marko Žnidarič, and Tomač Prosen. "Kardar-Parisi-Zhang Physics in the Quantum Heisenberg Magnet". In: *Phys. Rev. Lett.* 122 (21 May 2019), p. 210602. DOI: 10.1103/PhysRevLett.122.210602. URL: https://link.aps.org/doi/10.1103/PhysRevLett.122.210602.

[230] E. Y. Loh et al. "Sign problem in the numerical simulation of many-electron systems". In: *Phys. Rev. B* 41 (13 May 1990), pp. 9301–9307. DOI: 10.1103/PhysRevB.41.9301. URL: https://link.aps.org/doi/10.1103/PhysRevB.41.9301.

[231] Javier Lopez-Piqueres et al. "Hydrodynamics of nonintegrable systems from a relaxation-time approximation". In: *Phys. Rev. B* 103 (6 Feb. 2021), p. L060302. DOI: 10.1103/PhysRevB.103.L060302. URL: https://link.aps.org/doi/10.1103/PhysRevB.103.L060302.

[232] J. M. Luttinger. "An Exactly Soluble Model of a Many-Fermion System". In: *Journal of Mathematical Physics* 4.9 (Dec. 2004), pp. 1154–1162. ISSN: 0022-2488. DOI: 10.1063/1.1704046. eprint: https://pubs.aip.org/aip/jmp/article-pdf/4/9/1154/8169124/1154_1_online.pdf. URL: https://doi.org/10.1063/1.1704046.

[233] J. Ma et al. "Static and Dynamical Properties of the Spin-1/2 Equilateral Triangular-Lattice Antiferromagnet $Ba_3CoSb_2O_9$". In: *Phys. Rev. Lett.* 116 (8 Feb. 2016), p. 087201. DOI: 10.1103/PhysRevLett.116.087201. URL: https://link.aps.org/doi/10.1103/PhysRevLett.116.087201.

[234] Zhen Ma et al. "Disorder-induced broadening of the spin waves in the triangular-lattice quantum spin liquid candidate $YbZnGaO_4$". In: *Phys. Rev. B* 104 (22 Dec. 2021), p. 224433. DOI: 10.1103/PhysRevB.104.224433. URL: https://link.aps.org/doi/10.1103/PhysRevB.104.224433.

[235] Zhen Ma et al. "Spin-Glass Ground State in a Triangular-Lattice Compound $YbZnGaO_4$". In: *Phys. Rev. Lett.* 120 (8 Feb. 2018), p. 087201. DOI: 10.1103/PhysRevLett.120.087201. URL: https://link.aps.org/doi/10.1103/PhysRevLett.120.087201.

[236] Zhen Ma et al. "Spin-Glass Ground State in a Triangular-Lattice Compound $YbZnGaO_4$". In: *Phys. Rev. Lett.* 120 (8 Feb. 2018), p. 087201. DOI: 10.1103/PhysRevLett.120.087201. URL: https://link.aps.org/doi/10.1103/PhysRevLett.120.087201.

[237] David Macdougal et al. "Avoided quasiparticle decay and enhanced excitation continuum in the spin-$\frac{1}{2}$ near-Heisenberg triangular antiferromagnet $Ba_3CoSb_2O_9$". In: *Phys. Rev. B* 102 (6 Aug. 2020), p. 064421. DOI: 10.1103/PhysRevB.102.064421. URL: https://link.aps.org/doi/10.1103/PhysRevB.102.064421.

[238] Mayukh Majumder et al. "Persistent spin dynamics in the pressurized spin-liquid candidate $YbMgGaO_4$". In: *Phys. Rev. Research* 2 (2 May 2020), p. 023191. DOI: 10.1103/PhysRevResearch.2.023191. URL: https://link.aps.org/doi/10.1103/PhysRevResearch.2.023191.

[239] Neel Malvania et al. "Generalized hydrodynamics in strongly interacting 1D Bose gases". In: *arXiv:2009.06651* (2020). URL: https://arxiv.org/abs/2009.06651.

[240] R. S. Manna et al. "Lattice Effects and Entropy Release at the Low-Temperature Phase Transition in the Spin-Liquid Candidate $\kappa-(BEDT-TTF)_2Cu_2(CN)_3$". In: *Phys. Rev. Lett.* 104 (1 Jan. 2010), p. 016403. DOI: 10.1103/PhysRevLett.104.016403. URL: https://link.aps.org/doi/10.1103/PhysRevLett.104.016403.

[241] Rudra Sekhar Manna et al. "Lattice effects in the quasi-two-dimensional valence-bond-solid Mott insulator $EtMe_3P[Pd(dmit)_2]_2$". In: *Phys. Rev. B* 89 (4 Jan. 2014), p. 045113. DOI: 10.1103/PhysRevB.89.045113. URL: https://link.aps.org/doi/10.1103/PhysRevB.89.045113.

[242] Rudra Sekhar Manna et al. "Low-Temperature Lattice Effects in the Spin-Liquid Candidate $\kappa-(BEDT-TTF)_2Cu_2(CN)_3$". In: *Crystals* 8.2 (2018). ISSN: 2073-4352. URL: https://www.mdpi.com/2073-4352/8/2/87.

[243] Daniel Manzano. "A short introduction to the Lindblad master equation". In: *AIP Advances* 10.2 (Feb. 2020), p. 025106. ISSN: 2158-3226. DOI: 10.1063/1.5115323. eprint: https://pubs.aip.org/aip/adv/article-pdf/doi/10.1063/1.5115323/12881278/025106_1_online.pdf. URL: https://doi.org/10.1063/1.5115323.

[244] T. E. Mason et al. "The Spallation Neutron Source in Oak Ridge: A powerful tool for materials research". In: *Physica B: Condensed Matter* 385 (2006), pp. 955–960. URL: https://doi.org/10.1016/j.physb.2006.05.281.

[245] N. D. Mermin and H. Wagner. "Absence of Ferromagnetism or Antiferromagnetism in One- or Two-Dimensional Isotropic Heisenberg Models". In: *Phys. Rev. Lett.* 17 (22 Nov. 1966), pp. 1133–1136. DOI: 10.1103/PhysRevLett.17.1133. URL: https://link.aps.org/doi/10.1103/PhysRevLett.17.1133.

[246] L Michel and I. P. McCulloch. "Schur Forms of Matrix Product Operators in the Infinite Limit". In: *arXiv preprint arXiv:1008.4667* (2021). URL: https://arxiv.org/abs/1008.4667.

[247] Björn Miksch et al. "Gapped magnetic ground state in quantum spin liquid candidate $\kappa-(\text{BEDT-TTF})_2\text{Cu}_2(\text{CN})_3$". In: *Science* 372.6539 (2021), pp. 276–279. DOI: 10.1126/science.abc6363. eprint: https://www.science.org/doi/pdf/10.1126/science.abc6363. URL: https://www.science.org/doi/abs/10.1126/science.abc6363.

[248] Tsutomu Momoi. "Quantum fluctuations in quantum lattice systems with continuous symmetry". In: *J. Stat. Phys.* 85.1 (1996), pp. 193–210. DOI: 10.1007/BF02175562. URL: https://doi.org/10.1007/BF02175562.

[249] M. Mourigal et al. "Dynamical structure factor of the triangular-lattice antiferromagnet". In: *Phys. Rev. B* 88 (9 Sept. 2013), p. 094407. DOI: 10.1103/PhysRevB.88.094407. URL: https://link.aps.org/doi/10.1103/PhysRevB.88.094407.

[250] Gerhard Müller et al. "Quantum spin dynamics of the antiferromagnetic linear chain in zero and nonzero magnetic field". In: *Phys. Rev. B* 24 (3 Aug. 1981), pp. 1429–1467. DOI: 10.1103/PhysRevB.24.1429. URL: https://link.aps.org/doi/10.1103/PhysRevB.24.1429.

[251] Y Muraoka et al. "AC heat capacities of $\kappa-(\text{BEDT-TTF})_2\text{Cu}_2(\text{CN})_3$ measured by microchip calorimeter". In: *Journal of Physics: Conference Series* 320 (Sept. 2011), p. 012027. DOI: 10.1088/1742-6596/320/1/012027. URL: https://doi.org/10.1088/1742-6596/320/1/012027.

[252] Adam Nahum et al. "Quantum Entanglement Growth under Random Unitary Dynamics". In: *Phys. Rev. X* 7 (3 July 2017), p. 031016. DOI: 10.1103/PhysRevX.7.031016. URL: https://link.aps.org/doi/10.1103/PhysRevX.7.031016.

[253] Saori Nakajima et al. "Microscopic Phase Separation in Triangular-Lattice Quantum Spin Magnet $\kappa-(\text{BEDT-TTF})_2\text{Cu}_2(\text{CN})_3$ Probed by Muon Spin Relaxation". In: *Journal of the Physical Society of Japan* 81.6 (2012), p. 063706. DOI: 10.1143/JPSJ.81.063706. URL: https://doi.org/10.1143/JPSJ.81.063706.

[254] Jacopo De Nardis, Denis Bernard, and Benjamin Doyon. "Diffusion in generalized hydrodynamics and quasiparticle scattering". In: *SciPost Phys.* 6 (4 2019), p. 49. DOI: 10.21468/SciPostPhys.6.4.049. URL: https://scipost.org/10.21468/SciPostPhys.6.4.049.

[255] K Naruse et al. "Thermal Conductivity in the Triangular-Lattice Antiferromagnet Ba$_3$CoSb$_2$O$_9$". In: *Journal of Physics: Conference Series* 568.4 (Dec. 2014), p. 042014. DOI: 10.1088/1742-6596/568/4/042014. URL: https://doi.org/10.1088/1742-6596/568/4/042014.

[256] A. Nocera and G. Alvarez. "Spectral functions with the density matrix renormalization group: Krylov-space approach for correction vectors". In: *Phys. Rev. E* 94 (5 Nov. 2016), p. 053308. DOI: 10.1103/PhysRevE.94.053308. URL: https://link.aps.org/doi/10.1103/PhysRevE.94.053308.

[257] Tetsuya Nomoto et al. "Systematic study on thermal conductivity of organic triangular lattice systems β'-X[Pd(dmit)$_2$]$_2$". In: *Phys. Rev. B* 105 (24 June 2022), p. 245133. DOI: 10.1103/PhysRevB.105.245133. URL: https://link.aps.org/doi/10.1103/PhysRevB.105.245133.

[258] Kiyohide Nomura and Miki Yamada. "Thermal Bethe-ansatz study of the correlation length of the one-dimensional S=1/2 Heisenberg antiferromagnet". In: *Phys. Rev. B* 43 (10 Apr. 1991), pp. 8217–8223. DOI: 10.1103/PhysRevB.43.8217. URL: https://link.aps.org/doi/10.1103/PhysRevB.43.8217.

[259] Román Orús. "A practical introduction to tensor networks: Matrix product states and projected entangled pair states". In: *Annals of Physics* 349 (2014), pp. 117–158. ISSN: 0003-4916. DOI: https://doi.org/10.1016/j.aop.2014.06.013. URL: https://www.sciencedirect.com/science/article/pii/S0003491614001596.

[260] Tobias J. Osborne. "Ground state of a class of noncritical one-dimensional quantum spin systems can be approximated efficiently". In: *Phys. Rev. A* 75 (4 Apr. 2007), p. 042306. DOI: 10.1103/PhysRevA.75.042306. URL: https://link.aps.org/doi/10.1103/PhysRevA.75.042306.

[261] Stellan Östlund and Stefan Rommer. "Thermodynamic Limit of Density Matrix Renormalization". In: *Phys. Rev. Lett.* 75 (19 Nov. 1995), pp. 3537–3540. DOI: 10.1103/PhysRevLett.75.3537. URL: https://link.aps.org/doi/10.1103/PhysRevLett.75.3537.

[262] Joseph A. M Paddison et al. "Continuous excitations of the triangular-lattice quantum spin liquid YbMgGaO$_4$". In: *Nature Physics* 13.2 (2017), pp. 117–122. ISSN: 1745-2481. DOI: 10.1038/nphys3971. URL: https://doi.org/10.1038/nphys3971.

[263] Joseph A. M. Paddison. "Scattering Signatures of Bond-Dependent Magnetic Interactions". In: *Phys. Rev. Lett.* 125 (24 Dec. 2020), p. 247202. DOI: 10.1103/PhysRevLett.125.247202. URL: https://link.aps.org/doi/10.1103/PhysRevLett.125.247202.

[264] Joseph AM Paddison et al. "Continuous excitations of the triangular-lattice quantum spin liquid YbMgGaO4". In: *Nature Physics* 13.2 (2017), pp. 117–122. DOI: https://doi.org/10.1038/nphys3971.

[265] K.G. Padmalekha et al. "ESR studies on the spin-liquid candidate $\kappa-(\text{BEDT-TTF})_2\text{Cu}_2(\text{CN})_3$: Anomalous response below T=8K". In: *Physica B: Condensed Matter* 460 (2015). Special Issue on Electronic Crystals (ECRYS-2014), pp. 211–213. ISSN: 0921-4526. DOI: https://doi.org/10.1016/j.physb.2014.11.073. URL: https://www.sciencedirect.com/science/article/pii/S0921452614009077.

[266] Sebastian Paeckel et al. "Time-evolution methods for matrix-product states". In: *Annals of Physics* 411 (2019), p. 167998. ISSN: 0003-4916. DOI: https://doi.org/10.1016/j.aop.2019.167998. URL: https://www.sciencedirect.com/science/article/pii/S0003491619302532.

[267] Sebastian Paeckel et al. "Time-evolution methods for matrix-product states". In: *Annals of Physics* 411 (2019), p. 167998. ISSN: 0003-4916. DOI: https://doi.org/10.1016/j.aop.2019.167998. URL: https://www.sciencedirect.com/science/article/pii/S0003491619302532.

[268] B. L. Pan et al. "Specific heat and thermal conductivity of the triangular-lattice rare-earth material $\text{KBaYb}(\text{BO}_3)_2$ at ultralow temperature". In: *Phys. Rev. B* 103 (10 Mar. 2021), p. 104412. DOI: 10.1103/PhysRevB.103.104412. URL: https://link.aps.org/doi/10.1103/PhysRevB.103.104412.

[269] Fabian Pedregosa et al. "Scikit-learn: Machine Learning in Python". In: *Journal of Machine Learning Research* 12.85 (2011), pp. 2825–2830. URL: http://jmlr.org/papers/v12/pedregosa11a.html.

[270] Rodrigo G. Pereira. "LONG TIME CORRELATIONS OF NONLINEAR LUTTINGER LIQUIDS". In: *Int. J. Mod. Phys. B* 26.22 (2012), p. 1244008. DOI: 10.1142/S0217979212440080. URL: https://doi.org/10.1142/S0217979212440080.

[271] Rodrigo G. Pereira, Steven R. White, and Ian Affleck. "Exact Edge Singularities and Dynamical Correlations in Spin-1/2 Chains". In: *Phys. Rev. Lett.* 100 (2 Jan. 2008), p. 027206. DOI: 10.1103/PhysRevLett.100.027206. URL: https://link.aps.org/doi/10.1103/PhysRevLett.100.027206.

[272] Ho N. Phien, Guifré Vidal, and Ian P. McCulloch. "Infinite boundary conditions for matrix product state calculations". In: *Phys. Rev. B* 86 (24 Dec. 2012), p. 245107. DOI: 10.1103/PhysRevB.86.245107. URL: https://link.aps.org/doi/10.1103/PhysRevB.86.245107.

[273] M. Pinterić et al. "Anisotropic charge dynamics in the quantum spin-liquid candidate $\kappa-(\text{BEDT-TTF})_2\text{Cu}_2(\text{CN})_3$". In: *Phys. Rev. B* 90 (19 Nov. 2014), p. 195139. DOI: 10.1103/PhysRevB.90.195139. URL: https://link.aps.org/doi/10.1103/PhysRevB.90.195139.

[274] B. Pirvu et al. "Matrix product states for critical spin chains: Finite-size versus finite-entanglement scaling". In: *Phys. Rev. B* 86 (7 Aug. 2012), p. 075117. DOI: 10.1103/PhysRevB.86.075117. URL: https://link.aps.org/doi/10.1103/PhysRevB.86.075117.

[275] Mario Poirier et al. "Magnetodielectric effects and spin-charge coupling in the spin-liquid candidate $\kappa-(\text{BEDT-TTF})_2\text{Cu}_2(\text{CN})_3$". In: *Phys. Rev. B* 85 (13 Apr. 2012), p. 134444. DOI: 10.1103/PhysRevB.85.134444. URL: https://link.aps.org/doi/10.1103/PhysRevB.85.134444.

[276] Mario Poirier et al. "Ultrasonic investigation of the transition at 6 K in the spin-liquid candidate $\kappa-(\text{BEDT}-\text{TTF})_2\text{Cu}_2(\text{CN})_3$". In: *Phys. Rev. B* 89 (4 Jan. 2014), p. 045138. DOI: 10.1103/PhysRevB.89.045138. URL: https://link.aps.org/doi/10.1103/PhysRevB.89.045138.

[277] Frank Pollmann et al. "Theory of Finite-Entanglement Scaling at One-Dimensional Quantum Critical Points". In: *Phys. Rev. Lett.* 102 (25 June 2009), p. 255701. DOI: 10.1103/PhysRevLett.102.255701. URL: https://link.aps.org/doi/10.1103/PhysRevLett.102.255701.

[278] Frank Pollmann et al. "Theory of Finite-Entanglement Scaling at One-Dimensional Quantum Critical Points". In: *Phys. Rev. Lett.* 102 (25 June 2009), p. 255701. DOI: 10.1103/PhysRevLett.102.255701. URL: https://link.aps.org/doi/10.1103/PhysRevLett.102.255701.

[279] M. J. D. Powell. "An efficient method for finding the minimum of a function of several variables without calculating derivatives". In: *The Computer Journal* 7.2 (1964), pp. 155–162. DOI: 10.1093/comjnl/7.2.155.

[280] Michael Prähofer and Herbert Spohn. "Exact Scaling Functions for One-Dimensional Stationary KPZ Growth". In: *J. Stat. Phys.* 115.1 (2004), pp. 255–279. DOI: 10.1023/B:JOSS.0000019810.21828.fc. URL: https://doi.org/10.1023/B:JOSS.0000019810.21828.fc.

[281] P. Prelovšek et al. "Dynamical spin correlations of the kagome antiferromagnet". In: *Phys. Rev. B* 103 (1 Jan. 2021), p. 014431. DOI: 10.1103/PhysRevB.103.014431. URL: https://link.aps.org/doi/10.1103/PhysRevB.103.014431.

[282] Tomaž Prosen. "Open XXZ Spin Chain: Nonequilibrium Steady State and a Strict Bound on Ballistic Transport". In: *Phys. Rev. Lett.* 106 (21 May 2011), p. 217206. DOI: 10.1103/PhysRevLett.106.217206. URL: https://link.aps.org/doi/10.1103/PhysRevLett.106.217206.

[283] Yan Qi Qin et al. "Amplitude Mode in Three-Dimensional Dimerized Antiferromagnets". In: *Phys. Rev. Lett.* 118 (14 Apr. 2017), p. 147207. DOI: 10.1103/PhysRevLett.118.147207. URL: https://link.aps.org/doi/10.1103/PhysRevLett.118.147207.

[284] G. Quirion et al. "Magnetic phase diagram of $\text{Ba}_3\text{CoSb}_2\text{O}_9$ as determined by ultrasound velocity measurements". In: *Phys. Rev. B* 92 (1 July 2015), p. 014414. DOI: 10.1103/PhysRevB.92.014414. URL: https://link.aps.org/doi/10.1103/PhysRevB.92.014414.

[285] Marek M. Rams, Jacek Dziarmaga, and Wojciech H. Zurek. "Symmetry Breaking Bias and the Dynamics of a Quantum Phase Transition". In: *Phys. Rev. Lett.* 123 (13 Sept. 2019), p. 130603. DOI: 10.1103/PhysRevLett.123.130603. URL: https://link.aps.org/doi/10.1103/PhysRevLett.123.130603.

[286] Ying Ran et al. "Projected-Wave-Function Study of the Spin-1/2 Heisenberg Model on the Kagomé Lattice". In: *Phys. Rev. Lett.* 98 (11 Mar. 2007), p. 117205. DOI: 10.1103/PhysRevLett.98.117205. URL: https://link.aps.org/doi/10.1103/PhysRevLett.98.117205.

[287] K. M. Ranjith et al. "Anisotropic field-induced ordering in the triangular-lattice quantum spin liquid NaYbSe$_2$". In: *Phys. Rev. B* 100 (22 Dec. 2019), p. 224417. DOI: 10.1103/PhysRevB.100.224417. URL: https://link.aps.org/doi/10.1103/PhysRevB.100.224417.

[288] K. M. Ranjith et al. "Anisotropic field-induced ordering in the triangular-lattice quantum spin liquid NaYbSe$_2$". In: *Phys. Rev. B* 100 (22 Dec. 2019), p. 224417. DOI: 10.1103/PhysRevB.100.224417. URL: https://link.aps.org/doi/10.1103/PhysRevB.100.224417.

[289] K. M. Ranjith et al. "Field-induced instability of the quantum spin liquid ground state in the $J_{\text{eff}} = \frac{1}{2}$ triangular-lattice compound NaYbO$_2$". In: *Phys. Rev. B* 99 (18 May 2019), p. 180401. DOI: 10.1103/PhysRevB.99.180401. URL: https://link.aps.org/doi/10.1103/PhysRevB.99.180401.

[290] K. M. Ranjith et al. "Field-induced instability of the quantum spin liquid ground state in the $J_{\text{eff}} = \frac{1}{2}$ triangular-lattice compound NaYbO$_2$". In: *Phys. Rev. B* 99 (18 May 2019), p. 180401. DOI: 10.1103/PhysRevB.99.180401. URL: https://link.aps.org/doi/10.1103/PhysRevB.99.180401.

[291] X. Rao et al. "Survival of itinerant excitations and quantum spin state transitions in YbMgGaO$_4$ with chemical disorder". In: *Nature Communications* 12.1 (Aug. 2021), p. 4949. ISSN: 2041-1723. DOI: 10.1038/s41467-021-25247-6. URL: https://doi.org/10.1038/s41467-021-25247-6.

[292] Heiko Rieger and A. Peter Young. "Quantum spin glasses". In: *Complex Behaviour of Glassy Systems*. Ed. by Miguel Rubí and Conrado Pérez-Vicente. Berlin, Heidelberg: Springer Berlin Heidelberg, 1997, pp. 256–265. ISBN: 978-3-540-69123-5. URL: https://link.springer.com/chapter/10.1007/BFb0104832.

[293] Marcos Rigol, Vanja Dunjko, and Maxim Olshanii. "Thermalization and its mechanism for generic isolated quantum systems". In: *Nature* 452.7189 (2008), pp. 854–858. DOI: 10.1038/nature06838. URL: https://doi.org/10.1038/nature06838.

[294] Stefan Rommer and Stellan Östlund. "Class of ansatz wave functions for one-dimensional spin systems and their relation to the density matrix renormalization group". In: *Phys. Rev. B* 55 (4 Jan. 1997), pp. 2164–2181. DOI: 10.1103/PhysRevB.55.2164. URL: https://link.aps.org/doi/10.1103/PhysRevB.55.2164.

[295] Tommaso Roscilde et al. "Studying Quantum Spin Systems through Entanglement Estimators". In: *Phys. Rev. Lett.* 93 (16 Oct. 2004), p. 167203. DOI: 10.1103/PhysRevLett.93.167203. URL: https://link.aps.org/doi/10.1103/PhysRevLett.93.167203.

[296] Davide Rossini and Ettore Vicari. "Coherent and dissipative dynamics at quantum phase transitions". In: *Physics Reports* 936 (2021). Coherent and dissipative dynamics at quantum phase transitions, pp. 1–110. ISSN: 0370-1573. DOI: https://doi.org/10.1016/j.physrep.2021.08.003. URL: https://www.sciencedirect.com/science/article/pii/S0370157321003380.

[297] R. Rösslhuber et al. "Phase coexistence at the first-order Mott transition revealed by pressure-dependent dielectric spectroscopy of $\kappa-(\text{BEDT-TTF})_2\text{Cu}_2(\text{CN})_3$". In: *Phys. Rev. B* 103 (12 Mar. 2021), p. 125111. DOI: 10.1103/PhysRevB.103.125111. URL: https://link.aps.org/doi/10.1103/PhysRevB.103.125111.

[298] Yousef Saad. *Iterative methods for sparse linear systems*. SIAM, 2003.

[299] S. N. Saadatmand and I. P. McCulloch. "Symmetry fractionalization in the topological phase of the spin-$\frac{1}{2}$ J_1–J_2 triangular Heisenberg model". In: *Phys. Rev. B* 94 (12 Sept. 2016), p. 121111. DOI: 10.1103/PhysRevB.94.121111. URL: https://link.aps.org/doi/10.1103/PhysRevB.94.121111.

[300] Subir Sachdev. "Quantum magnetism and criticality". In: *Nature Physics* 4.3 (Mar. 2008), pp. 173–185. ISSN: 1745-2481. DOI: 10.1038/nphys894. URL: https://doi.org/10.1038/nphys894.

[301] Subir Sachdev. "Quantum phase transitions". In: *Physics world* 12.4 (1999), p. 33.

[302] Subir Sachdev and Jinwu Ye. "Universal quantum-critical dynamics of two-dimensional antiferromagnets". In: *Phys. Rev. Lett.* 69 (16 Oct. 1992), pp. 2411–2414. DOI: 10.1103/PhysRevLett.69.2411. URL: https://link.aps.org/doi/10.1103/PhysRevLett.69.2411.

[303] R. Sarkar et al. "Quantum spin liquid ground state in the disorder free triangular lattice NaYbS_2". In: *Phys. Rev. B* 100 (24 Dec. 2019), p. 241116. DOI: 10.1103/PhysRevB.100.241116. URL: https://link.aps.org/doi/10.1103/PhysRevB.100.241116.

[304] R. Sarkar et al. "Quantum spin liquid ground state in the disorder free triangular lattice NaYbS_2". In: *Phys. Rev. B* 100 (24 Dec. 2019), p. 241116. DOI: 10.1103/PhysRevB.100.241116. URL: https://link.aps.org/doi/10.1103/PhysRevB.100.241116.

[305] Lucile Savary and Leon Balents. "Quantum spin liquids: a review". In: *Rep. Prog. Phys.* 80.1 (Nov. 2016), p. 016502. DOI: 10.1088/0034-4885/80/1/016502. URL: https://doi.org/10.1088/0034-4885/80/1/016502.

[306] Lucile Savary and Leon Balents. "Quantum spin liquids: a review". In: *Reports on Progress in Physics* 80.1 (Nov. 2016), p. 016502. DOI: 10.1088/0034-4885/80/1/016502. URL: https://dx.doi.org/10.1088/0034-4885/80/1/016502.

[307] A. Scheie et al. "Crystal-field Hamiltonian and anisotropy in KErSe$_2$ and CsErSe$_2$". In: *Phys. Rev. B* 101 (14 Apr. 2020), p. 144432. DOI: 10.1103/PhysRevB.101.144432. URL: https://link.aps.org/doi/10.1103/PhysRevB.101.144432.

[308] A. Scheie et al. "Detection of Kardar–Parisi–Zhang hydrodynamics in a quantum Heisenberg spin-1/2 chain". In: *Nature Physics* 17.6 (June 2021), pp. 726–730. ISSN: 1745-2481. DOI: 10.1038/s41567-021-01191-6. URL: https://doi.org/10.1038/s41567-021-01191-6.

[309] A. Scheie et al. "Witnessing entanglement in quantum magnets using neutron scattering". In: *Phys. Rev. B* 103 (22 June 2021), p. 224434. DOI: 10.1103/PhysRevB.103.224434. URL: https://link.aps.org/doi/10.1103/PhysRevB.103.224434.

[310] A. O. Scheie et al. *Witnessing quantum criticality and entanglement in the triangular antiferromagnet KYbSe$_2$*. 2023. DOI: https://doi.org/10.48550/arXiv.2109.11527. arXiv: 2109.11527 [cond-mat.str-el].

[311] Allen Scheie. "PyCrystalField: software for calculation, analysis and fitting of crystal electric field Hamiltonians". In: *Journal of Applied Crystallography* 54.1 (2021). URL: https://doi.org/10.1107/S160057672001554X.

[312] Allen Scheie. "Quantifying uncertainties in crystal electric field Hamiltonian fits to neutron data". In: *arXiv preprint arXiv:2107.14164* (2021). URL: https://arxiv.org/abs/2107.14164.

[313] AO Scheie et al. "Witnessing quantum criticality and entanglement in the triangular antiferromagnet KYbSe$_2$". In: *arXiv preprint arXiv:2109.11527* (2021). URL: https://arxiv.org/abs/2109.11527.

[314] M. Schemmer et al. "Generalized Hydrodynamics on an Atom Chip". In: *Phys. Rev. Lett.* 122 (9 Mar. 2019), p. 090601. DOI: 10.1103/PhysRevLett.122.090601. URL: https://link.aps.org/doi/10.1103/PhysRevLett.122.090601.

[315] Ulrich Schollwock. "The density-matrix renormalization group in the age of matrix product states". In: *Annals of Physics* 326.1 (2011). January 2011 Special Issue, pp. 96–192. ISSN: 0003-4916. DOI: https://doi.org/10.1016/j.aop.2010.09.012. URL: https://www.sciencedirect.com/science/article/pii/S0003491610001752.

[316] Ulrich Schollwöck. "The density-matrix renormalization group in the age of matrix product states". In: *Annals of Physics* 326.1 (2011). January 2011 Special Issue, pp. 96–192. ISSN: 0003-4916. DOI: https://doi.org/10.1016/j.aop.2010.09.012. URL: https://www.sciencedirect.com/science/article/pii/S0003491610001752.

[317] C. Schön et al. "Sequential Generation of Entangled Multiqubit States". In: *Phys. Rev. Lett.* 95 (11 Sept. 2005), p. 110503. DOI: 10.1103/PhysRevLett.95.110503. URL: https://link.aps.org/doi/10.1103/PhysRevLett.95.110503.

[318] A Schröder et al. "Onset of antiferromagnetism in heavy-fermion metals". In: *Nature* 407.6802 (2000), pp. 351–355. DOI: 10.1038/35030039. URL: https://doi.org/10.1038/35030039.

[319] Katrin Sedlmeier et al. "Absence of charge order in the dimerized κ-phase BEDT−TTF salts". In: *Phys. Rev. B* 86 (24 Dec. 2012), p. 245103. DOI: 10.1103/PhysRevB.86.245103. URL: https://link.aps.org/doi/10.1103/PhysRevB.86.245103.

[320] G. Semeghini et al. "Probing topological spin liquids on a programmable quantum simulator". In: *Science* 374.6572 (2021), pp. 1242–1247. DOI: 10.1126/science.abi8794. URL: https://www.science.org/doi/abs/10.1126/science.abi8794.

[321] Arnab Sen, Hidemaro Suwa, and Anders W. Sandvik. "Velocity of excitations in ordered, disordered, and critical antiferromagnets". In: *Phys. Rev. B* 92 (19 Nov. 2015), p. 195145. DOI: 10.1103/PhysRevB.92.195145. URL: https://link.aps.org/doi/10.1103/PhysRevB.92.195145.

[322] V. R. Shaginyan et al. "Theoretical and experimental developments in quantum spin liquid in geometrically frustrated magnets: a review". In: *J. Mater. Sci.* 55.6 (2020), pp. 2257–2290. DOI: 10.1007/s10853-019-04128-w. URL: https://doi.org/10.1007/s10853-019-04128-w.

[323] Hui Shao and Anders W. Sandvik. "Progress on stochastic analytic continuation of quantum Monte Carlo data". In: *2202.09870* (2022). URL: https://arxiv.org/abs/2202.09870.

[324] Hui Shao et al. "Nearly Deconfined Spinon Excitations in the Square-Lattice Spin-1/2 Heisenberg Antiferromagnet". In: *Phys. Rev. X* 7 (4 Dec. 2017), p. 041072. DOI: 10.1103/PhysRevX.7.041072. URL: https://link.aps.org/doi/10.1103/PhysRevX.7.041072.

[325] George M Sheldrick. "A short history of SHELX". In: *Acta Crystallographica Section A: Foundations of Crystallography* 64.1 (2008), pp. 112–122. DOI: 10.1107/S010876730704 3930. URL: https://doi.org/10.1107/S0108767307043930.

[326] Yao Shen et al. "Evidence for a spinon Fermi surface in a triangular-lattice quantum-spin-liquid candidate". In: *Nature* 540.7634 (2016), pp. 559–562. ISSN: 1476-4687. DOI: 10.1038/nature20614. URL: https://doi.org/10.1038/nature20614.

[327] Yao Shen et al. "Evidence for a spinon Fermi surface in a triangular-lattice quantum-spin-liquid candidate". In: *Nature* 540.7634 (2016), pp. 559–562. DOI: https://doi.org/10.1038/nature20614.

[328] Yao Shen et al. "Fractionalized excitations in the partially magnetized spin liquid candidate YbMgGaO$_4$". In: *Nature Communications* 9.1 (Oct. 2018), p. 4138. ISSN: 2041-1723. DOI: 10.1038/s41467-018-06588-1. URL: https://doi.org/10.1038/s41467-018-06588-1.

[329] Yao Shen et al. "Fractionalized excitations in the partially magnetized spin liquid candidate YbMgGaO$_4$". In: *Nature Communications* 9.1 (Oct. 2018), p. 4138. ISSN: 2041-1723. DOI: 10.1038/s41467-018-06588-1. URL: https://doi.org/10.1038/s41467-018-06588-1.

[330] Nicholas E. Sherman, Alexander Avdoshkin, and Joel E. Moore. *Universality of critical dynamics with finite entanglement*. 2023. arXiv: 2301.09681 [quant-ph].

[331] Nicholas E. Sherman, Maxime Dupont, and Joel E. Moore. "Spectral function of the $J_1 - J_2$ Heisenberg model on the triangular lattice". In: *Phys. Rev. B* 107 (16 Apr. 2023), p. 165146. DOI: 10.1103/PhysRevB.107.165146. URL: https://link.aps.org/doi/10.1103/PhysRevB.107.165146.

[332] Nicholas E. Sherman and Rajiv R. P. Singh. "Structure factors of the kagome-lattice Heisenberg antiferromagnets at finite temperatures". In: *Phys. Rev. B* 97 (1 Jan. 2018), p. 014423. DOI: 10.1103/PhysRevB.97.014423. URL: https://link.aps.org/doi/10.1103/PhysRevB.97.014423.

[333] Yasuhiro Shimizu et al. "Pressure-Tuned Exchange Coupling of a Quantum Spin Liquid in the Molecular Triangular Lattice $\kappa-(ET)_2Ag_2(CN)_3$". In: *Phys. Rev. Lett.* 117 (10 Aug. 2016), p. 107203. DOI: 10.1103/PhysRevLett.117.107203. URL: https://link.aps.org/doi/10.1103/PhysRevLett.117.107203.

[334] Yutaka Shirata et al. "Experimental Realization of a Spin-1/2 Triangular-Lattice Heisenberg Antiferromagnet". In: *Phys. Rev. Lett.* 108 (5 Jan. 2012), p. 057205. DOI: 10.1103/PhysRevLett.108.057205. URL: https://link.aps.org/doi/10.1103/PhysRevLett.108.057205.

[335] Yu-Rong Shu et al. "Dynamical properties of the $S = \frac{1}{2}$ random Heisenberg chain". In: *Phys. Rev. B* 97 (10 Mar. 2018), p. 104424. DOI: 10.1103/PhysRevB.97.104424. URL: https://link.aps.org/doi/10.1103/PhysRevB.97.104424.

[336] Jörg Sichelschmidt et al. "Electron spin resonance on the spin-1/2 triangular magnet NaYbS2". In: *Journal of Physics: Condensed Matter* 31.20 (Mar. 2019), p. 205601. DOI: 10.1088/1361-648x/ab071d. URL: https://doi.org/10.1088%2F1361-648x%2Fab071d.

[337] R. N. Silver, D. S. Sivia, and J. E. Gubernatis. "Maximum-entropy method for analytic continuation of quantum Monte Carlo data". In: *Phys. Rev. B* 41 (4 Feb. 1990), pp. 2380–2389. DOI: 10.1103/PhysRevB.41.2380. URL: https://link.aps.org/doi/10.1103/PhysRevB.41.2380.

[338] Rajiv R. P. Singh and David A. Huse. "Three-sublattice order in triangular- and Kagomé-lattice spin-half antiferromagnets". In: *Phys. Rev. Lett.* 68 (11 Mar. 1992), pp. 1766–1769. DOI: 10.1103/PhysRevLett.68.1766. URL: https://link.aps.org/doi/10.1103/PhysRevLett.68.1766.

[339] J. Sirker. "Spin diffusion and the anisotropic spin-$\frac{1}{2}$ Heisenberg chain". In: *Phys. Rev. B* 73 (22 June 2006), p. 224424. DOI: 10.1103/PhysRevB.73.224424. URL: https://link.aps.org/doi/10.1103/PhysRevB.73.224424.

[340] J. Sirker, R. G. Pereira, and I. Affleck. "Conservation laws, integrability, and transport in one-dimensional quantum systems". In: *Phys. Rev. B* 83 (3 Jan. 2011), p. 035115. DOI: 10.1103/PhysRevB.83.035115. URL: https://link.aps.org/doi/10.1103/PhysRevB.83.035115.

[341] Charles P Slichter. *Principles of magnetic resonance*. Vol. 1. Springer Science & Business Media, Berlin, Heidelberg, 2013.

[342] J. Sólyom and P. Pfeuty. "Renormalization-group study of the Hamiltonian version of the Potts model". In: *Phys. Rev. B* 24 (1 July 1981), pp. 218–229. DOI: 10.1103/PhysRevB.24.218. URL: https://link.aps.org/doi/10.1103/PhysRevB.24.218.

[343] A. M. Somoza, M. Ortuño, and J. Prior. "Universal Distribution Functions in Two-Dimensional Localized Systems". In: *Phys. Rev. Lett.* 99 (11 Sept. 2007), p. 116602. DOI: 10.1103/PhysRevLett.99.116602. URL: https://link.aps.org/doi/10.1103/PhysRevLett.99.116602.

[344] Xue-Yang Song et al. "From Spinon Band Topology to the Symmetry Quantum Numbers of Monopoles in Dirac Spin Liquids". In: *Phys. Rev. X* 10 (1 Feb. 2020), p. 011033. DOI: 10.1103/PhysRevX.10.011033. URL: https://link.aps.org/doi/10.1103/PhysRevX.10.011033.

[345] Xue-Yang Song et al. "Unifying description of competing orders in two-dimensional quantum magnets". In: *Nature Communications* 10.1 (Sept. 2019), p. 4254. ISSN: 2041-1723. DOI: 10.1038/s41467-019-11727-3. URL: https://doi.org/10.1038/s41467-019-11727-3.

[346] Xue-Yang Song et al. "Unifying description of competing orders in two-dimensional quantum magnets". In: *Nature Communications* 10.1 (Sept. 2019), p. 4254. ISSN: 2041-1723. DOI: 10.1038/s41467-019-11727-3. URL: https://doi.org/10.1038/s41467-019-11727-3.

[347] Anthony L Spek. "Structure validation in chemical crystallography". In: *Acta Crystallographica Section D: Biological Crystallography* 65.2 (2009), pp. 148–155. DOI: 10.1107/S090744490804362X. URL: https://doi.org/10.1107/S090744490804362X.

[348] Herbert Spohn. "Fluctuating hydrodynamics approach to equilibrium time correlations for anharmonic chains". In: *Thermal Transport in Low Dimensions*. Springer, 2016, pp. 107–158. DOI: 10.1007/978-3-319-29261-8_3.

[349] Herbert Spohn. "Nonlinear Fluctuating Hydrodynamics for Anharmonic Chains". In: *J. Stat. Phys.* 154.5 (2014), pp. 1191–1227. DOI: 10.1007/s10955-014-0933-y. URL: https://doi.org/10.1007/s10955-014-0933-y.

[350] G. L. Squires. *Introduction to the Theory of Thermal Neutron Scattering*. 3rd ed. Cambridge University Press, 2012. DOI: 10.1017/CBO9781139107808.

[351] Oleg A. Starykh, Andrey V. Chubukov, and Alexander G. Abanov. "Flat spin-wave dispersion in a triangular antiferromagnet". In: *Phys. Rev. B* 74 (18 Nov. 2006), p. 180403. DOI: 10.1103/PhysRevB.74.180403. URL: https://link.aps.org/doi/10.1103/PhysRevB.74.180403.

[352] William Steinhardt et al. "Phase diagram of YbZnGaO4 in applied magnetic field". In: *npj Quantum Materials* 6.1 (2021), p. 78. DOI: https://doi.org/10.1038/s41535-021-00380-z.

[353] K. Sturm. "Dynamic Structure Factor: An Introduction". In: *Zeitschrift Naturforschung Teil A* 48 (Feb. 1993), pp. 233–242. DOI: 10.1515/zna-1993-1-244.

[354] Takuya Susuki et al. "Magnetization Process and Collective Excitations in the $S=1/2$ Triangular-Lattice Heisenberg Antiferromagnet $Ba_3CoSb_2O_9$". In: *Phys. Rev. Lett.* 110 (26 June 2013), p. 267201. DOI: 10.1103/PhysRevLett.110.267201. URL: https://link.aps.org/doi/10.1103/PhysRevLett.110.267201.

[355] Aaron Szasz and Johannes Motruk. "Phase diagram of the anisotropic triangular lattice Hubbard model". In: *Phys. Rev. B* 103 (23 June 2021), p. 235132. DOI: 10.1103/PhysRevB.103.235132. URL: https://link.aps.org/doi/10.1103/PhysRevB.103.235132.

[356] Aaron Szasz et al. "Chiral Spin Liquid Phase of the Triangular Lattice Hubbard Model: A Density Matrix Renormalization Group Study". In: *Phys. Rev. X* 10 (2 May 2020), p. 021042. DOI: 10.1103/PhysRevX.10.021042. URL: https://link.aps.org/doi/10.1103/PhysRevX.10.021042.

[357] L. Tagliacozzo et al. "Scaling of entanglement support for matrix product states". In: *Phys. Rev. B* 78 (2 July 2008), p. 024410. DOI: 10.1103/PhysRevB.78.024410. URL: https://link.aps.org/doi/10.1103/PhysRevB.78.024410.

[358] Kazumasa A. Takeuchi and Masaki Sano. "Universal Fluctuations of Growing Interfaces: Evidence in Turbulent Liquid Crystals". In: *Phys. Rev. Lett.* 104 (23 June 2010), p. 230601. DOI: 10.1103/PhysRevLett.104.230601. URL: https://link.aps.org/doi/10.1103/PhysRevLett.104.230601.

[359] M. Takigawa et al. "Nuclear relaxation in the spin-1/2 antiferromagnetic chain compound Sr_2CuO_3: Comparison between theories and experiments". In: *Phys. Rev. B* 56 (21 Dec. 1997), pp. 13681–13684. DOI: 10.1103/PhysRevB.56.13681. URL: https://link.aps.org/doi/10.1103/PhysRevB.56.13681.

[360] D. A. Tennant et al. "Unbound spinons in the S=1/2 antiferromagnetic chain $KCuF_3$". In: *Phys. Rev. Lett.* 70 (25 June 1993), pp. 4003–4006. DOI: 10.1103/PhysRevLett.70.4003. URL: https://link.aps.org/doi/10.1103/PhysRevLett.70.4003.

[361] K. R. Thurber et al. "^{17}O NMR Study of $q = 0$ Spin Excitations in a Nearly Ideal $S = \frac{1}{2}$ 1D Heisenberg Antiferromagnet, Sr_2CuO_3, up to 800 K". In: *Phys. Rev. Lett.* 87 (24 Nov. 2001), p. 247202. DOI: 10.1103/PhysRevLett.87.247202. URL: https://link.aps.org/doi/10.1103/PhysRevLett.87.247202.

[362] Alexander C. Tiegel et al. "Matrix product state formulation of frequency-space dynamics at finite temperatures". In: *Phys. Rev. B* 90 (6 Aug. 2014), p. 060406. DOI: `10.1103/PhysRevB.90.060406`. URL: `https://link.aps.org/doi/10.1103/PhysRevB.90.060406`.

[363] Yoshinori Tokura, Masashi Kawasaki, and Naoto Nagaosa. "Emergent functions of quantum materials". In: *Nature Physics* 13.11 (2017), pp. 1056–1068. URL: `https://doi.org/10.1038/nphys4274`.

[364] Sin-itiro Tomonaga. "Remarks on Bloch's Method of Sound Waves applied to Many-Fermion Problems". In: *Progress of Theoretical Physics* 5.4 (July 1950), pp. 544–569. ISSN: 0033-068X. DOI: `10.1143/ptp/5.4.544`. eprint: `https://academic.oup.com/ptp/article-pdf/5/4/544/5430161/5-4-544.pdf`. URL: `https://doi.org/10.1143/ptp/5.4.544`.

[365] Matthias Troyer and Uwe-Jens Wiese. "Computational Complexity and Fundamental Limitations to Fermionic Quantum Monte Carlo Simulations". In: *Phys. Rev. Lett.* 94 (17 May 2005), p. 170201. DOI: `10.1103/PhysRevLett.94.170201`. URL: `https://link.aps.org/doi/10.1103/PhysRevLett.94.170201`.

[366] Léon Van Hove. "Correlations in Space and Time and Born Approximation Scattering in Systems of Interacting Particles". In: *Phys. Rev.* 95 (1 July 1954), pp. 249–262. DOI: `10.1103/PhysRev.95.249`. URL: `https://link.aps.org/doi/10.1103/PhysRev.95.249`.

[367] Laurens Vanderstraeten, Jutho Haegeman, and Frank Verstraete. "Tangent-space methods for uniform matrix product states". In: *SciPost Phys. Lect. Notes* (2019), p. 7. DOI: `10.21468/SciPostPhysLectNotes.7`. URL: `https://scipost.org/10.21468/SciPostPhysLectNotes.7`.

[368] Ruben Verresen, Roderich Moessner, and Frank Pollmann. "Avoided quasiparticle decay from strong quantum interactions". In: *Nature Physics* 15.8 (Aug. 2019), pp. 750–753. ISSN: 1745-2481. DOI: `10.1038/s41567-019-0535-3`. URL: `https://doi.org/10.1038/s41567-019-0535-3`.

[369] F. Verstraete and J. I. Cirac. "Matrix product states represent ground states faithfully". In: *Phys. Rev. B* 73 (9 Mar. 2006), p. 094423. DOI: `10.1103/PhysRevB.73.094423`. URL: `https://link.aps.org/doi/10.1103/PhysRevB.73.094423`.

[370] F. Verstraete and J. I. Cirac. *Renormalization algorithms for Quantum-Many Body Systems in two and higher dimensions*. 2004. DOI: `10.48550/ARXIV.COND-MAT/0407066`. URL: `https://arxiv.org/abs/cond-mat/0407066`.

[371] F. Verstraete, J. J. García-Ripoll, and J. I. Cirac. "Matrix Product Density Operators: Simulation of Finite-Temperature and Dissipative Systems". In: *Phys. Rev. Lett.* 93 (20 Nov. 2004), p. 207204. DOI: `10.1103/PhysRevLett.93.207204`. URL: `https://link.aps.org/doi/10.1103/PhysRevLett.93.207204`.

[372] G. Vidal. "Class of Quantum Many-Body States That Can Be Efficiently Simulated". In: *Phys. Rev. Lett.* 101 (11 Sept. 2008), p. 110501. DOI: 10.1103/PhysRevLett.101.110501. URL: https://link.aps.org/doi/10.1103/PhysRevLett.101.110501.

[373] G. Vidal. "Entanglement Renormalization". In: *Phys. Rev. Lett.* 99 (22 Nov. 2007), p. 220405. DOI: 10.1103/PhysRevLett.99.220405. URL: https://link.aps.org/doi/10.1103/PhysRevLett.99.220405.

[374] G. Vidal et al. "Entanglement in Quantum Critical Phenomena". In: *Phys. Rev. Lett.* 90 (22 June 2003), p. 227902. DOI: 10.1103/PhysRevLett.90.227902. URL: https://link.aps.org/doi/10.1103/PhysRevLett.90.227902.

[375] Guifré Vidal. "Efficient Simulation of One-Dimensional Quantum Many-Body Systems". In: *Phys. Rev. Lett.* 93 (4 July 2004), p. 040502. DOI: 10.1103/PhysRevLett.93.040502. URL: https://link.aps.org/doi/10.1103/PhysRevLett.93.040502.

[376] Guifré Vidal. "Efficient Simulation of One-Dimensional Quantum Many-Body Systems". In: *Phys. Rev. Lett.* 93 (4 July 2004), p. 040502. DOI: 10.1103/PhysRevLett.93.040502. URL: https://link.aps.org/doi/10.1103/PhysRevLett.93.040502.

[377] Guifré Vidal. "Efficient Simulation of One-Dimensional Quantum Many-Body Systems". In: *Phys. Rev. Lett.* 93 (4 July 2004), p. 040502. DOI: 10.1103/PhysRevLett.93.040502. URL: https://link.aps.org/doi/10.1103/PhysRevLett.93.040502.

[378] Pauli Virtanen et al. "SciPy 1.0: fundamental algorithms for scientific computing in Python". In: *Nature Methods* 17.3 (Mar. 2020), pp. 261–272. ISSN: 1548-7105. DOI: 10.1038/s41592-019-0686-2. URL: https://doi.org/10.1038/s41592-019-0686-2.

[379] Michael L. Wall, Matthew R. Abernathy, and Gregory Quiroz. "Generative machine learning with tensor networks: Benchmarks on near-term quantum computers". In: *Phys. Rev. Research* 3 (2 Apr. 2021), p. 023010. DOI: 10.1103/PhysRevResearch.3.023010. URL: https://link.aps.org/doi/10.1103/PhysRevResearch.3.023010.

[380] Fa Wang and Ashvin Vishwanath. "Spin-liquid states on the triangular and Kagomé lattices: A projective-symmetry-group analysis of Schwinger boson states". In: *Phys. Rev. B* 74 (17 Nov. 2006), p. 174423. DOI: 10.1103/PhysRevB.74.174423. URL: https://link.aps.org/doi/10.1103/PhysRevB.74.174423.

[381] Ling Wang and Anders W. Sandvik. "Critical Level Crossings and Gapless Spin Liquid in the Square-Lattice Spin-1/2 $J_1 - J_2$ Heisenberg Antiferromagnet". In: *Phys. Rev. Lett.* 121 (10 Sept. 2018), p. 107202. DOI: 10.1103/PhysRevLett.121.107202. URL: https://link.aps.org/doi/10.1103/PhysRevLett.121.107202.

[382] Ling Wang, Yalei Zhang, and Anders W. Sandvik. "Quantum Spin Liquid Phase in the Shastry-Sutherland Model Detected by an Improved Level Spectroscopic Method". In: *Chinese Physics Letters* 39.7 (June 2022), p. 077502. DOI: 10.1088/0256-307x/39/7/077502. URL: https://doi.org/10.1088/0256-307x/39/7/077502.

[383] Alexander Weiße et al. "The kernel polynomial method". In: *Rev. Mod. Phys.* 78 (1 Mar. 2006), pp. 275–306. DOI: 10.1103/RevModPhys.78.275. URL: https://link.aps.org/doi/10.1103/RevModPhys.78.275.

[384] Xiao-Gang Wen. "Quantum orders and symmetric spin liquids". In: *Phys. Rev. B* 65 (16 Apr. 2002), p. 165113. DOI: 10.1103/PhysRevB.65.165113. URL: https://link.aps.org/doi/10.1103/PhysRevB.65.165113.

[385] Steven R. White. "Density matrix formulation for quantum renormalization groups". In: *Phys. Rev. Lett.* 69 (19 Nov. 1992), pp. 2863–2866. DOI: 10.1103/PhysRevLett.69.2863. URL: https://link.aps.org/doi/10.1103/PhysRevLett.69.2863.

[386] Steven R. White. "Density matrix formulation for quantum renormalization groups". In: *Phys. Rev. Lett.* 69 (19 Nov. 1992), pp. 2863–2866. DOI: 10.1103/PhysRevLett.69.2863. URL: https://link.aps.org/doi/10.1103/PhysRevLett.69.2863.

[387] Steven R. White and A. L. Chernyshev. "Neél Order in Square and Triangular Lattice Heisenberg Models". In: *Phys. Rev. Lett.* 99 (12 Sept. 2007), p. 127004. DOI: 10.1103/PhysRevLett.99.127004. URL: https://link.aps.org/doi/10.1103/PhysRevLett.99.127004.

[388] Keola Wierschem and Pinaki Sengupta. "Characterizing the Haldane phase in quasi-one-dimensional spin-1 Heisenberg antiferromagnets". In: *Mod. Phys. Lett. B* 28.32 (2014), p. 1430017. DOI: 10.1142/S0217984914300178. URL: https://doi.org/10.1142/S0217984914300178.

[389] Alexander Wietek and Andreas M. Läuchli. "Chiral spin liquid and quantum criticality in extended $S = \frac{1}{2}$ Heisenberg models on the triangular lattice". In: *Phys. Rev. B* 95 (3 Jan. 2017), p. 035141. DOI: 10.1103/PhysRevB.95.035141. URL: https://link.aps.org/doi/10.1103/PhysRevB.95.035141.

[390] F. Alexander Wolf et al. "Spectral functions and time evolution from the Chebyshev recursion". In: *Phys. Rev. B* 91 (11 Mar. 2015), p. 115144. DOI: 10.1103/PhysRevB.91.115144. URL: https://link.aps.org/doi/10.1103/PhysRevB.91.115144.

[391] F. Alexander Wolf et al. "Spectral functions and time evolution from the Chebyshev recursion". In: *Phys. Rev. B* 91 (11 Mar. 2015), p. 115144. DOI: 10.1103/PhysRevB.91.115144. URL: https://link.aps.org/doi/10.1103/PhysRevB.91.115144.

[392] G. M. Wysin. "Onsager reaction-field theory for magnetic models on diamond and hcp lattices". In: *Phys. Rev. B* 62 (5 Aug. 2000), pp. 3251–3258. DOI: 10.1103/PhysRevB.62.3251. URL: https://link.aps.org/doi/10.1103/PhysRevB.62.3251.

[393] Tao Xie et al. "Field-Induced Spin Excitations in the Spin-1/2 Triangular-Lattice Antiferromagnet $CsYbSe_2$". In: *arXiv preprint arXiv:2106.12451* (2021). URL: https://arxiv.org/abs/2106.12451.

[394] Jie Xing et al. "Crystal Synthesis and Frustrated Magnetism in Triangular Lattice CsRESe$_2$ (RE = La–Lu): Quantum Spin Liquid Candidates CsCeSe$_2$ and CsYbSe$_2$". In: *ACS Materials Letters* 2.1 (Jan. 2020), pp. 71–75. DOI: 10.1021/acsmaterialslett.9b00464. URL: https://doi.org/10.1021/acsmaterialslett.9b00464.

[395] Jie Xing et al. "Crystal Synthesis and Frustrated Magnetism in Triangular Lattice Cs RE Se2 (RE= La–Lu): Quantum Spin Liquid Candidates CsCeSe2 and CsYbSe2". In: *ACS Materials Letters* 2.1 (2019), pp. 71–75. DOI: https://doi.org/10.1021/acsmaterialslett.9b00464.

[396] Jie Xing et al. "Field-induced magnetic transition and spin fluctuations in the quantum spin-liquid candidate CsYbSe$_2$". In: *Phys. Rev. B* 100 (22 Dec. 2019), p. 220407. DOI: 10.1103/PhysRevB.100.220407. URL: https://link.aps.org/doi/10.1103/PhysRevB.100.220407.

[397] Jie Xing et al. "Synthesis and anisotropic magnetism in quantum spin liquid candidates AYbSe$_2$ (A = K and Rb)". In: *APL Materials* 9.11 (2021), p. 111104. DOI: 10.1063/5.0071161. eprint: https://doi.org/10.1063/5.0071161. URL: https://doi.org/10.1063/5.0071161.

[398] Jie Xing et al. "Synthesis and anisotropic magnetism in quantum spin liquid candidates AYbSe$_2$ (A = K and Rb)". In: *APL Materials* 9.11 (2021), p. 111104. DOI: 10.1063/5.0071161. URL: https://doi.org/10.1063/5.0071161.

[399] Sijie Xu et al. *Realization of U(1) Dirac Quantum Spin Liquid in YbZn2GaO5*. 2023. arXiv: 2305.20040 [cond-mat.str-el].

[400] Y. Xu et al. "Absence of Magnetic Thermal Conductivity in the Quantum Spin-Liquid Candidate YbMgGaO$_4$". In: *Phys. Rev. Lett.* 117 (26 Dec. 2016), p. 267202. DOI: 10.1103/PhysRevLett.117.267202. URL: https://link.aps.org/doi/10.1103/PhysRevLett.117.267202.

[401] Y. Xu et al. "Absence of Magnetic Thermal Conductivity in the Quantum Spin-Liquid Candidate YbMgGaO$_4$". In: *Phys. Rev. Lett.* 117 (26 Dec. 2016), p. 267202. DOI: 10.1103/PhysRevLett.117.267202. URL: https://link.aps.org/doi/10.1103/PhysRevLett.117.267202.

[402] Kyuya Yakushi et al. "Raman Spectroscopy Study of Charge Fluctuation in the Spin-Liquid Candidate $\kappa-$(BEDT-TTF)$_2$Cu$_2$(CN)$_3$". In: *Journal of the Physical Society of Japan* 84.8 (2015), p. 084711. DOI: 10.7566/JPSJ.84.084711. eprint: https://doi.org/10.7566/JPSJ.84.084711. URL: https://doi.org/10.7566/JPSJ.84.084711.

[403] Daisuke Yamamoto, Takeshi Fukuhara, and Ippei Danshita. "Frustrated quantum magnetism with Bose gases in triangular optical lattices at negative absolute temperatures". In: *Communications Physics* 3.1 (Mar. 2020), p. 56. ISSN: 2399-3650. DOI: 10.1038/s42005-020-0323-5. URL: https://doi.org/10.1038/s42005-020-0323-5.

[404]   Daisuke Yamamoto et al. "Magnetism driven by the interplay of fluctuations and frustration in the easy-axis triangular XXZ model with transverse fields". In: *Phys. Rev. B* 100 (14 Oct. 2019), p. 140410. DOI: 10.1103/PhysRevB.100.140410. URL: https://link.aps.org/doi/10.1103/PhysRevB.100.140410.

[405]   M. Yamashita et al. "Presence and absence of itinerant gapless excitations in the quantum spin liquid candidate $EtMe_3Sb[Pd(dmit)_2]_2$". In: *Phys. Rev. B* 101 (14 Apr. 2020), p. 140407. DOI: 10.1103/PhysRevB.101.140407. URL: https://link.aps.org/doi/10.1103/PhysRevB.101.140407.

[406]   Minoru Yamashita. "Boundary-limited and Glassy-like Phonon Thermal Conduction in $EtMe_3Sb[Pd(dmit)_2]_2$". In: *Journal of the Physical Society of Japan* 88.8 (2019), p. 083702. DOI: 10.7566/JPSJ.88.083702. eprint: https://doi.org/10.7566/JPSJ.88.083702. URL: https://doi.org/10.7566/JPSJ.88.083702.

[407]   Minoru Yamashita et al. "Highly Mobile Gapless Excitations in a Two-Dimensional Candidate Quantum Spin Liquid". In: *Science* 328.5983 (2010), pp. 1246–1248. DOI: 10.1126/science.1188200. eprint: https://www.science.org/doi/pdf/10.1126/science.1188200. URL: https://www.science.org/doi/abs/10.1126/science.1188200.

[408]   Minoru Yamashita et al. "Resistivity and thermal conductivity of an organic insulator β'–$EtMe_3Sb[Pd(dmit)_2]_2$". In: *Scientific Reports* 12.1 (June 2022), p. 9187. ISSN: 2045-2322. DOI: 10.1038/s41598-022-13155-8. URL: https://doi.org/10.1038/s41598-022-13155-8.

[409]   Satoshi Yamashita et al. "Thermodynamic properties of a spin-1/2 spin-liquid state in a k-type organic salt". In: *Nature Physics* 4.6 (2008), pp. 459–462. ISSN: 1745-2481. DOI: 10.1038/nphys942. URL: https://doi.org/10.1038/nphys942.

[410]   Jianwei Yang, Anders W. Sandvik, and Ling Wang. "Quantum criticality and spin liquid phase in the Shastry-Sutherland model". In: *Phys. Rev. B* 105 (6 Feb. 2022), p. L060409. DOI: 10.1103/PhysRevB.105.L060409. URL: https://link.aps.org/doi/10.1103/PhysRevB.105.L060409.

[411]   Jin Yang et al. "Site-Resolved Imaging of Ultracold Fermions in a Triangular-Lattice Quantum Gas Microscope". In: *PRX Quantum* 2 (2 June 2021), p. 020344. DOI: 10.1103/PRXQuantum.2.020344. URL: https://link.aps.org/doi/10.1103/PRXQuantum.2.020344.

[412]   Mingru Yang and Steven R. White. "Time-dependent variational principle with ancillary Krylov subspace". In: *Phys. Rev. B* 102 (9 Sept. 2020), p. 094315. DOI: 10.1103/PhysRevB.102.094315. URL: https://link.aps.org/doi/10.1103/PhysRevB.102.094315.

[413]   Bingtian Ye et al. "Universal Kardar-Parisi-Zhang Dynamics in Integrable Quantum Systems". In: *Phys. Rev. Lett.* 129 (23 Nov. 2022), p. 230602. DOI: 10.1103/PhysRevLett.129.230602. URL: https://link.aps.org/doi/10.1103/PhysRevLett.129.230602.

[414] Michael P. Zaletel et al. "Time-evolving a matrix product state with long-ranged interactions". In: *Phys. Rev. B* 91 (16 Apr. 2015), p. 165112. DOI: 10.1103/PhysRevB.91.165112. URL: https://link.aps.org/doi/10.1103/PhysRevB.91.165112.

[415] Igor A Zaliznyak and Seung-Hun Lee. "Magnetic Neutron Scattering". In: *Modern Techniques for Characterizing Magnetic Materials*. Ed. by Yimei Zhu. New York: Springer, 2005, pp. 3–64. ISBN: 14020-8007-7.

[416] Ziba Zangeneh et al. "Single-site magnetic anisotropy governed by interlayer cation charge imbalance in triangular-lattice AYbX_2". In: *Phys. Rev. B* 100 (17 Nov. 2019), p. 174436. DOI: 10.1103/PhysRevB.100.174436. URL: https://link.aps.org/doi/10.1103/PhysRevB.100.174436.

[417] V. Zauner-Stauber et al. "Topological nature of spinons and holons: Elementary excitations from matrix product states with conserved symmetries". In: *Phys. Rev. B* 97 (23 June 2018), p. 235155. DOI: 10.1103/PhysRevB.97.235155. URL: https://link.aps.org/doi/10.1103/PhysRevB.97.235155.

[418] K. Y. Zeng et al. "NMR study of the spin excitations in the frustrated antiferromagnet Yb(BaBO$_3$)$_3$ with a triangular lattice". In: *Phys. Rev. B* 102 (4 July 2020), p. 045149. DOI: 10.1103/PhysRevB.102.045149. URL: https://link.aps.org/doi/10.1103/PhysRevB.102.045149.

[419] Chun Zhang and Tao Li. "Resonating valence bond theory of anomalous spin dynamics of spin-$\frac{1}{2}$ triangular lattice Heisenberg antiferromagnet and its application to Ba$_3$CoSb$_2$O$_9$". In: *Phys. Rev. B* 102 (7 Aug. 2020), p. 075108. DOI: 10.1103/PhysRevB.102.075108. URL: https://link.aps.org/doi/10.1103/PhysRevB.102.075108.

[420] J. Zhang et al. "Observation of a many-body dynamical phase transition with a 53-qubit quantum simulator". In: *Nature* 551.7682 (2017), pp. 601–604. DOI: 10.1038/nature24654. URL: https://doi.org/10.1038/nature24654.

[421] Shu Zhang et al. "Dynamical Structure Factor of the Three-Dimensional Quantum Spin Liquid Candidate NaCaNi$_2$F$_7$". In: *Phys. Rev. Lett.* 122 (16 Apr. 2019), p. 167203. DOI: 10.1103/PhysRevLett.122.167203. URL: https://link.aps.org/doi/10.1103/PhysRevLett.122.167203.

[422] Xinshu Zhang et al. "Hierarchy of Exchange Interactions in the Triangular-Lattice Spin Liquid YbMgGaO$_4$". In: *Phys. Rev. X* 8 (3 July 2018), p. 031001. DOI: 10.1103/PhysRevX.8.031001. URL: https://link.aps.org/doi/10.1103/PhysRevX.8.031001.

[423] Zheng Zhang et al. "Crystalline electric field excitations in the quantum spin liquid candidate NaYbSe$_2$". In: *Phys. Rev. B* 103 (3 Jan. 2021), p. 035144. DOI: 10.1103/PhysRevB.103.035144. URL: https://link.aps.org/doi/10.1103/PhysRevB.103.035144.

[424] Zheng Zhang et al. "Crystalline electric field excitations in the quantum spin liquid candidate NaYbSe$_2$". In: *Phys. Rev. B* 103 (3 Jan. 2021), p. 035144. DOI: 10.1103/PhysRevB.103.035144. URL: https://link.aps.org/doi/10.1103/PhysRevB.103.035144.

[425] Zheng Zhang et al. "Crystalline electric field excitations in the quantum spin liquid candidate NaYbSe$_2$". In: *Phys. Rev. B* 103 (3 Jan. 2021), p. 035144. DOI: 10.1103/PhysRevB.103.035144. URL: https://link.aps.org/doi/10.1103/PhysRevB.103.035144.

[426] Zheng Zhang et al. "Low-energy spin dynamics of the quantum spin liquid candidate NaYbSe$_2$". In: *Phys. Rev. B* 106 (8 Aug. 2022), p. 085115. DOI: 10.1103/PhysRevB.106.085115. URL: https://link.aps.org/doi/10.1103/PhysRevB.106.085115.

[427] Zheng Zhang et al. "Pressure induced metallization and possible unconventional superconductivity in spin liquid *NaYbSe_{2}*". In: *arXiv preprint arXiv:2003.11479* (2020). URL: https://arxiv.org/abs/2003.11479.

[428] Zheng Zhang et al. *Pressure induced metallization and possible unconventional superconductivity in spin liquid* NaYbSe$_2$. 2020. DOI: 10.48550/ARXIV.2003.11479. URL: https://arxiv.org/abs/2003.11479.

[429] Weihong Zheng et al. "Anomalous Excitation Spectra of Frustrated Quantum Antiferromagnets". In: *Phys. Rev. Lett.* 96 (5 Feb. 2006), p. 057201. DOI: 10.1103/PhysRevLett.96.057201. URL: https://link.aps.org/doi/10.1103/PhysRevLett.96.057201.

[430] Weihong Zheng et al. "Excitation spectra of the spin-$\frac{1}{2}$ triangular-lattice Heisenberg antiferromagnet". In: *Phys. Rev. B* 74 (22 Dec. 2006), p. 224420. DOI: 10.1103/PhysRevB.74.224420. URL: https://link.aps.org/doi/10.1103/PhysRevB.74.224420.

[431] Weihong Zheng et al. "Excitation spectra of the spin-$\frac{1}{2}$ triangular-lattice Heisenberg antiferromagnet". In: *Phys. Rev. B* 74 (22 Dec. 2006), p. 224420. DOI: 10.1103/PhysRevB.74.224420. URL: https://link.aps.org/doi/10.1103/PhysRevB.74.224420.

[432] Yi Zhou, Kazushi Kanoda, and Tai-Kai Ng. "Quantum spin liquid states". In: *Rev. Mod. Phys.* 89 (2 Apr. 2017), p. 025003. DOI: 10.1103/RevModPhys.89.025003. URL: https://link.aps.org/doi/10.1103/RevModPhys.89.025003.

[433] W. Zhu, Shou-shu Gong, and D. N. Sheng. "Identifying spinon excitations from dynamic structure factor of spin-1/2 Heisenberg antiferromagnet on the Kagome lattice". In: *Proceedings of the National Academy of Sciences* 116.12 (2019), pp. 5437–5441. DOI: 10.1073/pnas.1807840116. URL: https://www.pnas.org/doi/abs/10.1073/pnas.1807840116.

[434] Zhenyue Zhu and Steven R. White. "Spin liquid phase of the $S = \frac{1}{2}$ $J_1 - J_2$ Heisenberg model on the triangular lattice". In: *Phys. Rev. B* 92 (4 July 2015), p. 041105. DOI: 10.1103/PhysRevB.92.041105. URL: https://link.aps.org/doi/10.1103/PhysRevB.92.041105.

[435] Zhenyue Zhu et al. "Disorder-Induced Mimicry of a Spin Liquid in YbMgGaO$_4$". In: *Phys. Rev. Lett.* 119 (15 Oct. 2017), p. 157201. DOI: 10.1103/PhysRevLett.119.157201. URL: https://link.aps.org/doi/10.1103/PhysRevLett.119.157201.

[436] Zhenyue Zhu et al. "Disorder-Induced Mimicry of a Spin Liquid in YbMgGaO$_4$". In: *Phys. Rev. Lett.* 119 (15 Oct. 2017), p. 157201. DOI: 10.1103/PhysRevLett.119.157201. URL: https://link.aps.org/doi/10.1103/PhysRevLett.119.157201.

[437] Marko Žnidarič. "Spin Transport in a One-Dimensional Anisotropic Heisenberg Model".
       In: *Phys. Rev. Lett.* 106 (22 May 2011), p. 220601. DOI: 10.1103/PhysRevLett.106.
       220601. URL: https://link.aps.org/doi/10.1103/PhysRevLett.106.220601.

[438] X. Zotos, F. Naef, and P. Prelovsek. "Transport and conservation laws". In: *Phys. Rev.
       B* 55 (17 May 1997), pp. 11029–11032. DOI: 10.1103/PhysRevB.55.11029. URL:
       https://link.aps.org/doi/10.1103/PhysRevB.55.11029.

[439] Wojciech H Zurek. "Cosmological experiments in superfluid helium?" In: *Nature* 317.6037
       (1985), pp. 505–508.

[440] Michael Zwolak and Guifré Vidal. "Mixed-State Dynamics in One-Dimensional Quantum
       Lattice Systems: A Time-Dependent Superoperator Renormalization Algorithm". In: *Phys.
       Rev. Lett.* 93 (20 Nov. 2004), p. 207205. DOI: 10.1103/PhysRevLett.93.207205. URL:
       https://link.aps.org/doi/10.1103/PhysRevLett.93.207205.